Identification by inverse method of optical properties of a participating medium - Application to the impact of fog on artificial perception

Ali Krayem

Clermont Auvergne University
Doctoral School of Sciences For Engineering

A thesis submitted in fulfillment of the requirements for the degree of
Doctor from Clermont Auvergne University
Speciality: "Electronics and Systems"
presented by: Ali Krayem

Identification by inverse method of optical properties of a participating medium. Application to the impact of fog on artificial perception.

Supervisor

Frédéric Bernardin and Arnaud Münch

Thesis defended on 14 March 2024 in front of the jury composed of:

Mme. Anabela Da SILVA	Research Director, CNRS, Aix-Marseille University	President of jury
M. Frédéric BERNARDIN	ICTPE HDR, Cerema Centre-Est, Clermont-Ferrand	Supervisor
M. Arnaud MÜNCH	Professor, Clermont Auvergne University	Co-supervisor
M. Jérôme RIEDI	Professor, Lille University	Reviewer
M. Nicolas RIVIERE	Research Director, ONERA	Reviewer
M. Frédéric SZCZAP	Associate Professor HDR, Clermont Auvergne University	Examiner

Acknowledgements

Tout d'abord, je tiens à remercier mon directeur de thèse, Frédéric BERNARDIN, pour sa guidance experte, son soutien constant et ses conseils précieux tout au long de ce projet. Sa passion pour la recherche et son dévouement envers l'excellence académique ont été une source d'inspiration constante. Je tiens également à exprimer ma profonde gratitude envers mon co-directeur de thèse, Arnaud MÜNCH. Sa contribution significative, son expertise complémentaire et son engagement envers mon projet ont grandement enrichi mon expérience de recherche.

Je tiens à exprimer ma profonde gratitude à tous les membres du comité de soutenance pour avoir accepté d'évaluer mon travail de thèse. M. Jérôme RIEDI et M. Nicolas RIVIÈRE pour avoir été rapporteur de cette these. Les contributions apportées à ce manuscrit ont été précieusement enrichies par vos relectures, corrections et remarques. Mme. Anabela Da SILVA et M. Frédéric SZCZAP qui ont accepté d'être les examinateurs de mon projet de thèse. Je tiens à exprimer ma profonde gratitude pour leur engagement dans l'évaluation de mon travail.

Je suis profondément reconnaissant envers mes collègues des laboratoires LMBP et Cerema pour leur précieuse collaboration. Leurs idées novatrices et leur soutien constant ont véritablement enrichi mon expérience de recherche. Travailler avec eux m'a permis de découvrir de nouvelles perspectives, de relever des défis et d'atteindre des objectifs que je n'aurais jamais pu réaliser seul. Leur contribution a été inestimable et je suis reconnaissant de pouvoir compter sur leur expertise et leur amitié tout au long de cette aventure scientifique.

À mes parents, merci du fond du coeur pour tout ce que vous avez accompli et pour vos efforts continus. Vous m'avez inculqué les valeurs de travail, d'intégrité et de compassion qui m'ont guidé à chaque étape de ce voyage. Votre dévouement infaillible et votre amour indéfectible ont illuminé chaque étape de ma vie. Que ce message puisse témoigner de l'amour et de la reconnaissance que je porte dans mon cœur pour vous, mes chers parents. Votre influence positive continuera à m'inspirer et à éclairer mon chemin, aujourd'hui et pour les années à venir.

À ma femme, tu as été ma source constante d'inspiration et de soutien. Ta patience infinie, ton encouragement et ton amour m'ont aidé à traverser les défis de ce parcours académique. Merci d'avoir été à mes côtés, de m'avoir encouragé et soutenu tout au long de ce parcours exigeant. Cette thèse porte aussi ton empreinte, et je suis reconnaissant de partager ce moment de réussite avec toi.

À ma famille, vos encouragements, vos conseils avisés et votre présence constante ont fait de ce parcours une aventure significative. Chacun de vous a contribué à ma réussite à sa manière, et je vous suis profondément reconnaissant.

Enfin, je tiens à remercier toutes les personnes qui, de près ou de loin, ont participé à la réalisation de ce projet. Votre contribution a été précieuse.

Abstract

Optical sensors (cameras, lidars, and radars) are commonly used for perception in automated vehicles. The primary function of these systems is to detect obstacles in order to avoid them. However, adverse weather conditions such as rain or fog can disrupt these information streams, impacting the performance and safety level of autonomous vehicles. The Cerema, through its "PAVIN Fog&Rain" platform, conducts evaluations of these sensors under controlled rain and fog conditions. In order to perform testing in a vitual environment allowing to consider a large variety of scenarios, what can be achieved by developing a digital twin of the platform, it is necessary to develop a robust model of electromagnetic wave propagation in fog whose outputs are close to experimental meaasurements made in the platform. To achieve this modeling, a thorough understanding of the fog droplet size distribution is required. In this thesis, we are devising a method to identify this distribution using radiance data measured in the Cerema's Rain&Fog PAVIN platform.

In this work, radiance propagation modeling is based on the Lorenz-Mie theory. Our goal is to reconstruct the particle size distribution, denoted as N, by inversely solving the radiative transfer equation from radiation measurements at several wavelengths. This approach enables the identification of fog's optical characteristics through the evaluation of coefficients in the radiative transfer equation, including the extinction coefficient, absorption coefficient, scattering coefficient, and the phase function. Indeed, using the Lorenz-Mie theory allows to express these coefficients in terms of the distribution N. The radiative transfer equation (RTE) was originally introduced in astrophysics, nuclear reactors, and atmospheric science. In our work, we focus on the 1D stationary radiative transfer equation, which has a unique solution satisfying certain estimates.

Various authors have explored inverse problems related to radiative transfer equations. The objective of the inverse problem is to reconstruct the absorption and scattering coefficients, as well as the phase function from experimental data. This coefficient reconstruction has been studied by several authors in two and three dimensions for both stationary and non-stationary RTEs.

In our study, we introduce a minimization problem with an objective function that enables the identification of the distribution N. This function quantifies the difference between measured and radiative transfer model-evaluated radiance, with the distribution N as input. We show that the objective function is continuous, differentiable, and strictly convex, ensuring a unique solution for the minimization problem. We then apply the Barzilai-Borwein algorithm to minimize this function by using a gradient descent based method to solve our minimization problem: we will introduce an adjoint problem to the RTE allowing us to easily calculate the cost function gradient. Comparisons with

other minimization algorithms, such as CG-Polak-Ribière and CG-Daniel, have been conducted. Our problem is formulated in two dimensions: x for spatial coordinates and μ for the radiation direction. We approximate both the direct and adjoint problems using the double Legendre polynomial basis decomposition, discretizing x while functionally decomposing on a double Legendre polynomial basis for the μ variable. Code validations have been performed using the explicit solutions provided by Dautray-Lions. Leveraging the Lorenz-Mie theory, we have formulated the inversion problem for the 1D case, validating against the explicit case (where the collision operator is null). Mathematical analysis of the problem subsequently yielded specific results.

Optical characteristics of the medium are evaluated through the inversion of the radiative transfer equation, yielding numerical reconstruction results in various scenarios (direct measurements in front of the light source and inverse measurements of backward-diffused luminance). At present, the droplet size distribution has been reconstructed using synthetic measurements (model outputs) derived from a target granulometry distribution. Simulations have been performed using artificial fog droplet size distributions from the PAVIN platform at Cerema [1], natural distribution [2], and for distribution obtained from the theoretical model as Shettle-Fen [3].

The identification results are obtained by using two different source types which are the Lambertian source and the Collimated source. For both source types, we obtained a good approximation of our DSDs. We also give numerical results of the DSDs identification in the anisotropic case with the Henyey-Greenstein phase function and we do not limit ourselves to the Lorenz-Mie phase function. In all these cases, we obtained a good approximation of the droplet size distribution. Also, we studied in each case the robustness of our identification method by adding several noise levels to our synthetic measurements. The effect of the noise level on the extinction coefficient computed from the approximated DSD and on the visibility is presented in some cases.

Résumé étendu de la thèse

Pour les systèmes de véhicules automatisés, les conditions routières dégradées peuvent poser de sérieuses difficultés. En effet, ces systèmes utilisent un réseau complexe de capteurs optiques comme des caméras, des LiDARs, des RADARs pour comprendre leur environnement et ajuster leur comportement de conduite. Le brouillard en particulier présente plusieurs défis qui pourraient empêcher les voitures autonomes de fonctionner comme prévu. Le brouillard diminue significativement les capacités visuelles des capteurs tels que les caméras et les LiDARs. Pour cette raison, il pourrait être difficile pour ces capteurs de reconnaitre les obstacles et les objets dans leur environnement. La capacité du système autonome à prendre des décisions sécuritaires peut être limitée par la nature incertaine ou partielle des informations reçues par les capteurs. Les signaux générés par les capteurs RADAR et LiDAR peuvent être réfléchis, absorbés ou dispersés par les gouttelettes d'eau en suspension dans l'air. Cela présente un danger pour la sécurité routière, car cela peut entrainer des erreurs de détection, des résultats incorrects, voire une perte totale de détection.

Le développement des véhicules autonomes nécessite l'intégration de nombreuses technologies d'assistance à la conduite qui reposent sur des équipements optiques tels que le RADAR, le LiDAR, les caméras, et d'autres. Ces technologies servent à des fins telles que l'identification des obstacles, la détection des piétons, la reconnaissance des panneaux de signalisation et l'ajustement de la trajectoire. Assurer la sécurité et la fiabilité de ces dispositifs est une préoccupation majeure, car il est largement reconnu que des conditions météorologiques dégradées telles que la pluie, la neige ou le brouillard peuvent perturber leurs performances. Selon les différentes feuilles de route françaises ou européennes [4] sur la mobilité automatisée, la simulation numérique est un outil pertinent à développer pour évaluer la sécurité dans les situations les plus variées possibles, ce qui est difficile à réaliser avec des tests réels. Les simulateurs actuels de capteurs perceptifs sont largement basés sur des modèles simplifiés de l'interaction des rayons lumineux avec le brouillard, ce qui remet en question le réalisme des simulations, pourtant crucial pour faire des simulateurs des outils d'évaluation de la sécurité pour les véhicules automatisés.

La simulation des capteurs perceptifs automobiles dans des conditions de brouillard doit tenir compte de la modélisation de la propagation des ondes électromagnétiques à travers un milieu diffusant. Les caractéristiques optiques de ce milieu doivent être connues pour simuler l'extinction du rayonnement.

Pour évaluer les capteurs perceptifs (caméra, RADAR, LiDAR) ou leurs simulateurs en conditions météorologiques dégradées, la platforme PAVIN Brouilard&Pluie du Cerema est mise à contribution dans de nombreuses études et projets. Cette évaluation doit être garantie par une bonne connaissance de la microphysique des hydrométéores

produits dans la plateforme, notamment pour le cas du brouillard. En effet, les différentes longueurs d'onde dans lesquelles opèrent les capteurs perceptifs (du visible à l'infrarouge thermique) conduisent à des propagations électromagnétiques sensibles à la taille des gouttes de brouillard. Des capteurs analysant la distribution de la taille des gouttes sont utilisés mais ils n'offrent des mesures que très locales et qui peuvent ne pas être assez représentatives d'une distribution "moyenne" du milieu. Une approche pourrait être d'évaluer des modèles de propagation d'ondes basés sur des mesures spectrales de rayonnements issus d'une source de lumière placée dans la plateforme. Notre objectif est de caractériser le brouillard produit par une DSD moyenne compatible à la fois avec les mesures de rayonnement et la modélisation physique de la propagation. Ceci constitue la définition de ce que nous entendons dans notre travail par identification de la distribution de la taille des gouttes du brouillard (DSD), à savoir la recherche d'une DSD compatible avec des mesures expérimentales interprétées par une modélisation donnée. Nous proposons différentes modélisations et différents types de mesures. Par ailleurs, nous évaluons cette identification par une quantification de la proximité des sorties de modèle aux mesures (luminance, éclairement), ainsi que par celle de la proximité portant sur des grandeurs calculées à partir de la DSD comme le coefficient d'extinction ou la visibilité météorologique. La DSD pour le cas du brouillard est un paramètre clé qui régit les caractéristiques optiques en fonction de la longueur d'onde du rayonnement [5]. Une DSD est une fonction $N(r)$ (cm^{-3} $\mu\mathrm{m}^{-1}$) telle que $N(r)\,dr$ représente le nombre de gouttelettes d'eau contenues dans un volume de 1 cm^3 dont les rayons appartiennent à $(r, r + dr)$. La théorie de Lorenz-Mie [6] est utilisée dans ce travail pour exprimer les paramètres optiques grâce à la DSD.

D'autre part, dans les domaines de l'optique et de l'imagerie, la reconstruction des propriétés optiques est un domaine important. Il consiste à extraire et étudier les propriétés significatives d'un milieu ou d'une substance en fonction de la manière dont ces propriétés interagissent avec la lumière. Plusieurs domaines, dont la médecine, la science des matériaux, la télédétection, entre autres, utilisent la reconstruction des propriétés optiques.

Fondamentalement, la reconstruction des propriétés optiques utilise les façons spécifiques dont la lumière réagit avec divers matériaux. Cette interaction donne lieu à des phénomènes tels que l'absorption, la diffusion, la réflexion et la transmission, chacun fournissant des informations cruciales sur les propriétés du matériau. Il s'agit pour l'essentiel d'identifier l'indice de réfraction, le coefficient d'absorption, le coefficient de diffusion et le facteur d'anisotropie. Pour reconstruire les propriétés optiques, diverses approches d'imagerie et spectroscopiques peuvent être appliquées. Ces approches utilisent fréquemment des technologies avancées, telles que des spectromètres, des lasers, des détecteurs et des algorithmes complexes d'analyse de données. Selon l'application, les propriétés optiques peuvent être reconstruites en temps réel ou après traitement, et elles

peuvent fournir des informations précieuses sur les tissus biologiques, les échantillons environnementaux, les matériaux semi-conducteurs, et bien plus encore. La reconstruction des propriétés optiques a un énorme potentiel, mais elle présente également des difficultés. Les méthodes de reconstruction des paramètres optiques sont utilisées dans plusieurs domaines d'application [7, 8, 9, 10, 11, 12, 13].

Objectifs et méthodologie

La simulation des capteurs perceptifs dans le brouillard doit tenir compte de la modélisation de la propagation des ondes électromagnétiques à travers un milieu intermédiaire. Les caractéristiques optiques de ce milieu doivent être connues afin de simuler l'extinction du rayonnement. La distribution de la taille des gouttelettes pour le cas du brouillard est un paramètre clé qui détermine ces caractéristiques optiques en fonction de la longueur d'onde du rayonnement [14, 15, 5]. L'objectif de ce travail est de proposer une méthode pour identifier cette distribution à partir de mesures de rayonnement interprétées à l'aide de l'équation de transfert radiatif.

Dans ce travail de thèse, nous cherchons à identifier la distribution de taille des gouttelettes avec des modèles pouvant impliquer un opérateur de collision et ne nous limitant pas à la solution de Beer-Lambert. L'opérateur de collision représente les interactions entre les particules du milieu et la radiation électromagnétique. Ces interactions peuvent inclure l'absorption de photons par les particules du milieu, la diffusion de la radiation par ces particules, ainsi que l'émission de photons par les particules du milieu. Par conséquent, il est essentiel de développer des processus numériques pour résoudre l'équation de transfert radiatif complète. Nous utilisons ensuite ces procédures en utilisant une méthode basée sur la descente de gradient pour résoudre notre problème de minimisation : nous introduirons un problème adjoint à l'équation de transfert radiatif nous permettant de calculer facilement le gradient de la fonction de coût. Il est important de noter que le temps de calcul de ces procédures dépend davantage des paramètres de discrétisation pour résoudre l'équation de transfert radiative (ETR) et son problème adjoint que du nombre de paramètres décrivant la distribution de taille des gouttelettes. En effet, la méthode d'inversion que nous développons n'a pas besoin de modéliser la DSD inconnue comme cela a été fait dans [16, 17, 18, 19, 20], où les auteurs reconstruisent certains modèles de distributions de fréquences de volume (Loi Log-Normale et lois gamma qui dépendent de deux paramètres) en utilisant la loi de Beer-Lambert (sans le terme de diffusion). Avec notre méthode, nous sommes capables de fixer un nombre souhaité de classes de rayon pour définir la DSD sans impact sur le temps de calcul puisque nous utilisons une méthode de descente de gradient pour laquelle le gradient de la fonction de coût est calculé grâce à un problème adjoint du modèle de transfert radiatif dont la résolution numérique est très peu sensible au nombre de classes de rayon. Pour les applications numériques, nous utilisons les 60 classes de

rayon entre (0,15 μm-8,5 μm) de l'analyseur de particules PALAS Welas du Cerema.

Contributions de la thèse

Le résultat principal de ce manuscrit est l'identification des distributions de taille des gouttelettes (DSD) du brouillard par des mesures de rayonnement dans la plage de 350 nm à 2500 nm [21]. Pour le problème d'identification, une étude théorique et numérique de l'équation de transfert radiatif stationnaire unidimensionnelle est réalisée en utilisant la méthode de Yvon [22]. Nous prouvons la consistance du problème inverse, puis nous effectuons des expériences numériques en utilisant des données synthétiques. L'identification de la distribution N nous permet de calculer les propriétés optiques en utilisant la théorie de Lorenz-Mie [6]. Nous avons élaboré une méthode qui permet l'identification d'une large gamme de distributions rencontrées dans les brouillards naturels et ceux générés artificiellement dans la plateforme PAVIN. Dans cette étude, nous avons évalué notre méthode sur des DSD acquises par des mesures dans des conditions naturelles [23], des conditions artificielles [24], et via des modèles [3]. Les résultats numériques suggèrent que la méthode permet l'identification de la DSD avec différents modèles de transfert radiatif (Beer-Lambert, isotrope et opérateur de collision anisotrope).

Plan du manuscrit

Chapitre 1: Dans ce chapitre, nous commençons par introduire le cadre de la thèse dans la Section 1.1. Dans la Section 1.2, nous donnons la motivation pour identifier la distribution de la taille des gouttelettes et nous présentons également la plateforme "PAVIN Fog&Rain". Dans la Section 1.3, nous présentons la relation entre le brouillard et la visibilité et nous rappelons les quatre classes de visibilité routière. Un protocole de mesure de la visibilité est présenté dans la première partie de cette section. Dans la deuxième partie de la Section 1.3, nous définissons le brouillard et nous donnons quelques types de brouillard (le brouillard de radiation et le brouillard d'advection). Des distributions de tailles de gouttelettes artificielles mesurées sur la plateforme PAVIN au Cerema sont données pour différentes visibilités. Nous donnons également quelques modèles théoriques de la distribution de la taille des gouttelettes. Nous terminons la section avec la distribution réelle de la taille des gouttelettes mesurée lors de la campagne Paris-Fog en 2007. Les principaux objectifs de cette thèse sont discutés, ainsi que notre méthodologie de recherche dans la Section 1.4. Dans la Section 1.5, nous résumons l'organisation de ce manuscrit. À la fin de ce chapitre, nous abordons les contributions scientifiques dans la Section 1.6.

Chapitre 2: Ce chapitre commence avec la Section 2.1 qui offre un aperçu des recherches antérieures sur la reconstruction directe des propriétés optiques pour diverses applications. La Section 2.2 présente une revue de l'état actuel de la recherche sur l'identification de la distribution des tailles de particules dans le brouillard. Cette section est divisée

en deux parties. Dans la première partie, la méthode d'identification de la distribution est présentée en utilisant l'équation LiDAR. La deuxième partie présente la méthode d'identification en utilisant un modèle simplifié de l'équation de transfert radiatif, en particulier le modèle de Beer-Lambert.

Chapitre 3: Dans ce chapitre, nous présentons une introduction générale au transfert radiatif et à ses différents domaines d'application dans la Section 3.1. Dans la Section 3.2, nous donnons la dérivation de l'équation de transfert radiatif et le processus d'absorption, de diffusion et d'émission. Nous terminons cette section par le bilan de l'équation de transfert radiatif dépendant du temps. Les différents types de fonctions de phase utilisés dans l'équation de transfert radiatif (telles que les fonctions de Rayleigh, de Mie et de Henyey-Greenstein) sont présentés dans la Section 3.3. Dans la Section 3.4, nous discutons de la théorie de la diffusion de Lorenz-Mie. Cette théorie explique comment les ondes électromagnétiques interagissent avec les petites particules. Nous donnons également dans cette section l'expression des propriétés optiques en fonction de la distribution de la taille des gouttelettes de brouillard. Dans la Section 3.5, nous rappelons l'existence et l'unicité de la solution de l'équation de transport dépendante et indépendante du temps donnée par plusieurs auteurs. Une estimation L^∞ de la solution est également donnée dans cette section. Nous terminons ce chapitre par la Section 3.6 qui récapitule la formulation intégrale de la théorie du transport.

Chapitre 4: La Section 4.1 présente une introduction générale à l'équation de transfert radiatif stationnaire unidimensionnelle et à son calcul à partir de l'équation de transfert radiatif tridimensionnelle. Ensuite, dans la Section 4.2, nous passons en revue l'existence et l'unicité de la solution de cette équation. Nous fournissons des solutions exactes dans certains cas pour l'équation de transfert radiatif stationnaire dans la Section 4.3. Ces cas sont utilisés par la suite pour vérifier nos approximations numériques. La Section 4.4 présente différentes méthodes utilisées par plusieurs auteurs pour approximer l'équation de transfert radiatif. Nous étudions dans la Section 4.5 les approximations numériques présentées dans la Section 4.4 avec une analyse de leur convergence sur les cas explicites donnés dans la Section 4.3.

Chapitre 5: Ce chapitre commence avec la Section 5.1 qui présente les différentes distributions des gouttelettes utilisées dans notre méthode de reconstruction. Dans la Section 5.2, nous présentons également les problèmes inverses mal posés et la méthode de décomposition en valeurs singulières (SVD) pour résoudre le problème mal posé, et nous détaillons la DSD que nous utiliserons pour tester la méthode de reconstruction. Le problème inverse basé sur la descente de gradient et la fonction de coût sont présentés, ainsi que leurs propriétés, dans la Section 5.3. Nous donnons également dans cette section l'expression du gradient de la fonction de coût en termes d'un problème adjoint à l'équation de transfert radiatif (ETR), et nous rappelons l'algorithme de Barzilai-Borwein pour minimiser la fonction de coût.

Chapitre 6: Dans la Section 6.1, nous présentons les résultats numériques sur l'identification de la distribution de taille des gouttelettes (DSD) avec une source lambertienne en utilisant des mesures synthétiques (résultats de simulations avec de vraies DSD et certains modèles de DSD en entrée) dans le cas de la modélisation de Beer-Lambert (sans diffusion multiple), ainsi que dans les cas d'opérateurs de collision isotropes et anisotropes. Nous étudions également dans cette section la robustesse de notre méthode d'identification en ajoutant plusieurs niveaux de bruit à nos mesures synthétiques. Cette section se conclut par une étude de l'effet du bruit sur le coefficient d'extinction calculé à partir de la distribution approchée. De manière similaire à la Section 6.1, nous présentons dans la Section 6.2 l'identification de la distribution de taille des gouttelettes en utilisant une source collimatée, et une étude de robustesse est également présentée. Dans la Section 6.3, nous présentons les résultats d'identification dans le cas anisotrope avec des sources lambertienne et collimatée en utilisant la fonction de phase de Henyey-Greenstein.
Chapitre 7: La Section 7.1 offre une revue de l'équation de transfert radiatif stationnaire tridimensionnelle et explique la méthode numérique utilisée pour l'approximer en utilisant le simulateur SWEET développé au Cerema. La caractérisation de la source utilisée dans nos mesures expérimentales sur la plateforme PAVIN est décrite dans la Section 7.2. Nous terminons ce chapitre avec la Section 7.3, dans laquelle nous comparons les données numériques obtenues grâce à l'utilisation du simulateur SWEET avec les données expérimentales réalisées dans la plateforme PAVIN du Cerema.
Chapitre 8: Ce chapitre constitue une conclusion des travaux de la thèse et donne des perspectives pour de nouveaux travaux.

Nomenclature

D	platform PAVIN length, m	N_0, N_1	initial DSDs for the minimization algorithm
f	positive function which explodes for small radii	Q^{λ}_{abs}	absorption efficiency
G	number of measurement points	Q^{λ}_{ext}	extinction efficiency
I_{λ}	radiation intensity, W $\mathrm{m}^{-2}\mathrm{sr}^{-1}\mathrm{m}^{-1}$	Q^{λ}_{sca}	scattering cross section
J_{ε}	cost function with the regularization term	r	particle radius, μm
J_1	cost function without regularization term	RC	relative cost
k	kth iteration	RE	relative error on DSD
L	number of wavelengths	U	random variable with uniform law on $(0, 1)$
M^{synth}_{λ}	synthetic measurements, W $\mathrm{m}^{-2}\mathrm{sr}^{-1}\mathrm{m}^{-1}$	V_m	meteorological visibility, m
N	droplet size distribution (DSD), $\mathrm{cm}^{-3}\mu\mathrm{m}^{-1}$	x	spatial position, m
$N^{\star}$	target droplet size distribution, $\mathrm{cm}^{-3}\mu\mathrm{m}^{-1}$		

Greek Symbols

α	aperture angle of sensor	σ^{λ}_{abs}	absorption coefficient, m^{-1}
δ	Dirac function	σ^{λ}_{ext}	extinction coefficient, m^{-1}
ε	regularization parameter	σ^{λ}_{sca}	scattering coefficient, m^{-1}
η	noise level	τ	optical thickness
θ'	position angle of the sensor	Φ_{λ}	scattering phase function
λ	wavelength, nm	ψ_{λ}	Mie scattering phase function
μ	cosine of polar angle θ		

Subscripts/Superscripts

abs	absorption	sca	scattering
ext	extinction	synth	synthetic

Contents

Chapter 1

Introduction

The development and implementation of optical devices for Intelligent Transport Systems (ITS) are heavily impacted by the optical characteristics of the road scene (including atmosphere). The way that light interacts with the matter in the air (e.g. fog, rain, snow) is directly influenced by optical characteristics such as light scattering, absorption, and refraction. The knowledge of these characteristics in the context of ITS is essential for the effective operation of many technologies employed in contemporary transportation. In the development of automated vehicles, for instance, it is essential to correctly identify the optical properties of the surrounding environment so that the sensors and cameras can detect and recognize the road conditions, barriers and other vehicles. Using this knowledge, one can then move safely while driving. Additionally, optical properties are important in the construction of intelligent traffic management systems that use real-time data to improve traffic flow, reduce congestion, and improve overall safety. By applying our understanding of optical properties, ITS can transform transportation by creating safer, more practical solutions that benefit both people and society as a whole.

In this chapter, we start by introducing the thesis framework in Section 1.1. In section 1.2 we give the motivation for identifying the droplet size distribution. We also present the "PAVIN Fog&Rain" platform. The major objectives of this thesis are discussed together with our research methodology in Section 1.4. In Section 1.5, we conclude by summarizing the organization of this manuscript.

1.1 Thesis Framework

The University of Clermont Auvergne has obtained the label "initiatives of excellence" (I-SITE) of the program "investments of the future", which aims to establish a limited number of French universities to promote all their research and training activities internationally.
The work done in this thesis is part of a research activity related to autonomous transports for the Center of International Research on Innovation Transportation and Production Systems (CIR-ITPS) in the domain of Intelligent Automated Transport, funded by the I-Site CAP 20-25 Project. Additional information are available in the official website: `https://cap2025.fr/`. The theme of Intelligent Automated Transport aims to increase

the intelligence, functionality, and automation of robotic systems (mobile robots and collaborative robots) by taking into account both their adaptability and ergonomics, and the almost unavoidable interactions they have with humans.
Cerema, a public institution under the supervision of the Ministry of Ecological Transition and Territorial Cohesion, supports the State and local authorities in the development, deployment and evaluation of public policies for development, including transportation systems. Additional information are available in the official website: `https://www.cerema.fr/fr`. The activities of Cerema are organized around six complementary areas of action aimed at assisting local stakeholders in the realization of their projects.
The research domain of this thesis is focused on "Mobility" in the area of "Intelligent Transport Systems (ITS), Traffic, and Regulation: autonomous Vehicles". This research is done within the ITS research team of Cerema [25].
Regardless of the mode of transportation, the autonomous vehicle is upending existing transportation structures. Experiments are frequently required due to the field of intelligent transportation's ongoing developments. Several autonomous transport projects are being carried out for this purpose. For example, the SCOOP project [26] is a national project to deploy a Cooperative Intelligent Transport Systems (C-ITS) technology system that enables the exchange of information between vehicles and between vehicles and infrastructure, with the aim of improving safety for road users and staff, developing new services and preparing for the vehicles of the future. The C-ROADS project [27] is also a continuation of the SCOOP projects, whose use cases were extended by integrating urban situations and opening up technologies to new modes of communication between vehicles and infrastructure and between vehicles. In this context, we also mention several projects such as InDiD [28], SAM [29] or PRISSMA [30].

1.2 Context and Motivation

The progress in autonomous vehicle technology requires the integration of multiple driving assistance technologies utilizing optical equipment such as RADAR (Radio Detection and Ranging), LiDAR (Light Detection and Ranging), cameras, and other sensors. These technologies play vital roles in tasks like obstacle identification, pedestrian detection, recognizing traffic signs, and adjusting vehicle trajectory.
As mentioned in [31], LiDAR systems operate by measuring the time it takes for a pulsed light emitted from a laser to travel to an emitter. The emitted light falls within the infrared spectrum, specifically at wavelengths of 905 nm or 1550 nm which is specific to the domain of application. The choice between these wavelengths is influenced by energy considerations, as emissions at 905 nm require less energy than those at 1550 nm. This difference in energy absorption is attributed to water in the atmosphere, which begins absorbing energy beyond 1400 nm. In 2014, the authors in [32] studied the effect of

adverse weather on LiDAR sensor performance. The 905 nm wavelength, constrained by safety power limits, provides a detection range of approximately 100 meters. In contrast, the 1550 nm wavelength extends the detection range to 200-300 meters.
RADAR systems [33], functioning as an electromagnetic sensor, are capable of detecting, locating, tracking, and identifying various objects over long distances. Its operation involves emitting electromagnetic radiation towards targets, evaluating the reflected waves. Targets can include aircraft, ships, satellites, cars and even astronomical objects. As well as detecting the presence, position and speed of these objects, RADAR can in some cases provide details of their size and shape.
The development of fully autonomous vehicles is dependent on extensive sensor testing and validation, which includes subjecting these sensors to a series of experiments that simulate various extreme weather conditions. It is worth noting that the current state of automotive sensors suggests that they may face difficulties in identifying objects under such conditions. It is worth noting that the performance of the sensors may be limited in certain weather conditions, which could pose a risk. Therefore, it is important to conduct comprehensive studies of these sensors, particularly in adverse weather conditions.
Adverse weather conditions, such as snow, fog, and rain, provide a serious challenge for drivers, especially automated systems. This becomes much more difficult when developing software for self-driving cars, as it must be capable of adapting to a wide range of external situations, reflecting how humans deal with similar challenges [34, 35, 31, 36].
The World Meteorological Organization (WMO) [37] defines fog (presented at the left of Figure 1.1) as a suspension of very small, usually microscopic water droplets in the air, reducing visibility at the Earth's surface [38]. The term is used when the horizontal visibility is reduced to less than 1 km. Furthermore, the WMO defines rain (presented at the right of Figure 1.1) as precipitation of drops of water that falls from a cloud. The number density and size distribution of raindrops vary considerably with the intensity and nature of the precipitation.

Figure 1.1: Fog with visibility about 100 m (left). Illustration of the relative size of drops of rain and of drizzle (right) [37].

The reduction in visibility depends on the structure of the fog, and especially on the number density and size distribution of the droplets. The structure can vary considerably

over time and space.
Due to the visibility reduction, fog can affect human activities in many fields like free-space optical (FSO) communication, aviation or ground transportation [39, 40, 41]. In this latter field, adverse weather conditions are issues for the development of intelligent vehicle and autonomous driving since perceptive sensors like camera, RADAR and LiDAR are largely employed [42, 43, 44, 45, 46, 47]. Hasirlioglu [48] conducted a study of the influence of rain and fog on the detection of objects by camera, LiDAR and RADAR. Fog and rain were simulated in real world. His results highlight that the three sensors are affected by rain with more or less severity. Reduced contrast affects camera images. The main effect of adverse weather conditions on camera is the loss of contrast making it more difficult to identify or detect objects in the images. Also, LiDAR has a poor detection range and also blocks visibility in powder snow, strong fog, and heavy rain [49, 50]. Compared to LiDAR, the RADAR performs better in adverse weather. As mentioned in [51], weather affects RADAR in two ways, which are the attenuation and the backscattering. Attenuation decreases the signal's received strength, while backscattering increases interference at the receiver. In [52], the authors demonstrate the complementary characteristics of cameras and RADARs, and Singh [53] illustrate these characteristics in Figure 1.2.

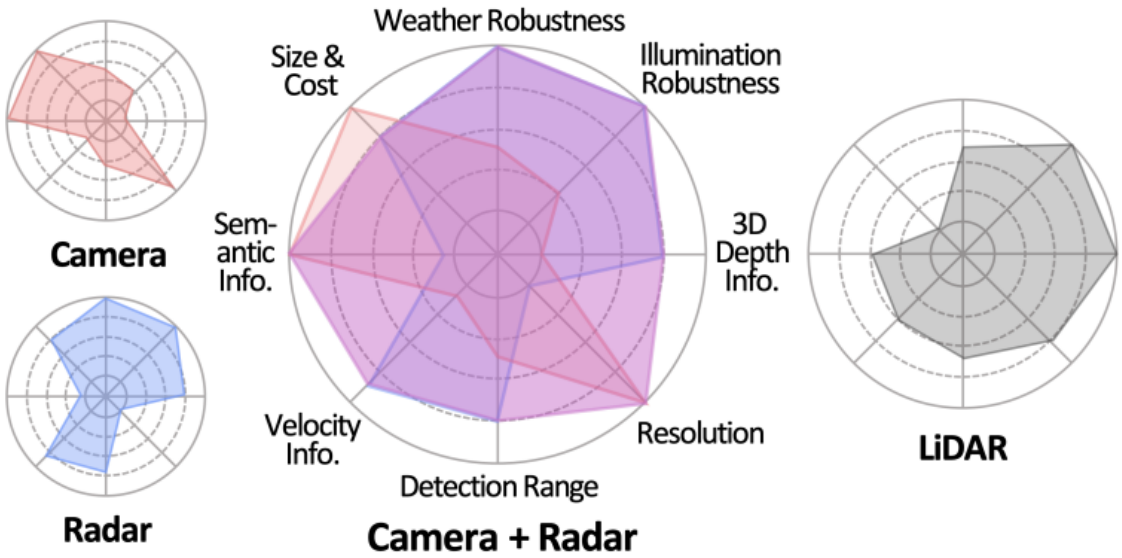

Figure 1.2: Sensor characteristics (presented in [53]) of camera, RADAR, and LiDAR.

It is important to know the impact of fog on the artificial perception of autonomous vehicles, particularly in challenging weather conditions, in order to guarantee the safety and efficacy of these developing technologies. Researchers and engineers are exploring solutions to enhance the robustness of perception systems in challenging conditions. This will further improve the reliability and adaptability of autonomous vehicles when

faced with various environmental challenges.
Many roadmaps [54, 4] of European and worldwide institutions responsible for transportation public policies highlight the driving scenario approach to demonstrate the safety of automated road transport systems, including scenarios based on realistic digital simulation taking into account adverse weather conditions.
The main issue with the numerical simulation tools used concerns their realism, even more so when they are used for autonomous driving safety assessment. The simulation of automotive perceptive sensors in fog conditions must take into account the modelling of the propagation of electromagnetic waves through a participating medium. For these optical sensor simulators, we can recall the Ansys AVxcelerate simulator [55], which provides physics-based accurate sensor simulation. It comes with a complete set of parametric physics-based sensor models. There are also several other simulators such as Electro-Optics Sensor Simulation [56], Mitsuba [57], AVSimulation [58], Carla Simulator [59]. These simulators use different types of modelling. For example, in [38] the authors present a comparison between a simple model using Koschmieder's theory based on the Beer-Lambert law (exponential attenuation of the light in fog w.r.t. the distance between emitter and receiver) and the full modelling of the radiative transfer equation by using Cerema's SWEET simulator based on the Ray-tracing method [38]. This comparison is illustrated in Figure 1.3 for night and day conditions.

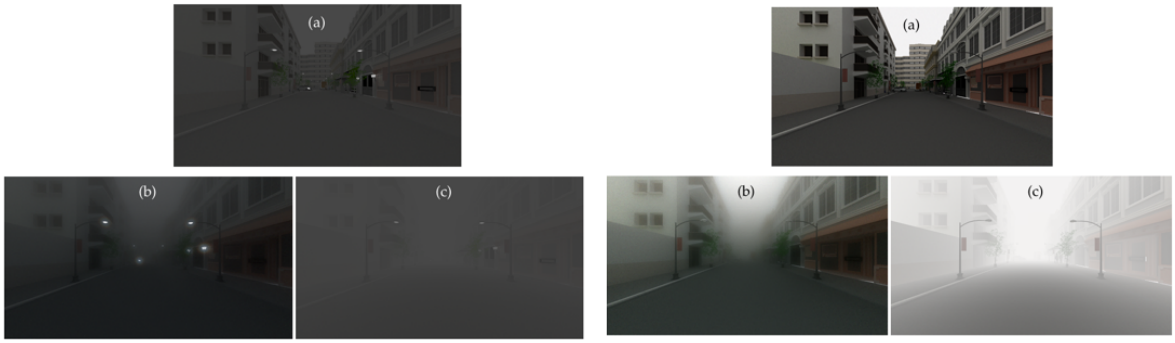

Figure 1.3: Simulated images for the intra-urban scene with the Cerema SWEET simulator [38] without fog (a) and with fog for visibility 20m (b) and with the Koschmieder model (c) in the night condition (left), and in the day conditions (right).

In addition, the images in Figure 1.4 show a section of the French A75 highway, at the Col de la Fageole point, without fog (a) and with fog (b) (see [60] for a detailed description of the database). Figure 1.4 with fog can be compared to the simulated images (Figure 1.3b in the left and right). Although the latter is not made in the same scene, it still allows us to observe a similarity in the visual aspect of the fog in all these images (i.e., blurry effects). This confirms the realism of the rendering performed by SWEET.

Figure 1.4: Real camera images taken from a section of the French A75 highway (at the Col de la Fageole point) without fog (a) and with fog (for visibility 156 m, (b)), both images are in grayscale (see [60]).

As shown in [38], more relevant modelings are needed to capture the contrast attenuation in foggy conditions close to the ones observed in real conditions, which is all the more true when the fog is dense. It is then necessary to take into account the in-scattering term (collision operator) which represents the interactions between the particles of the medium and electromagnetic radiation. These interactions may include the absorption of photons by the particles of the medium, the scattering of radiation by these particles, as well as the emission of photons by the particles of the medium.

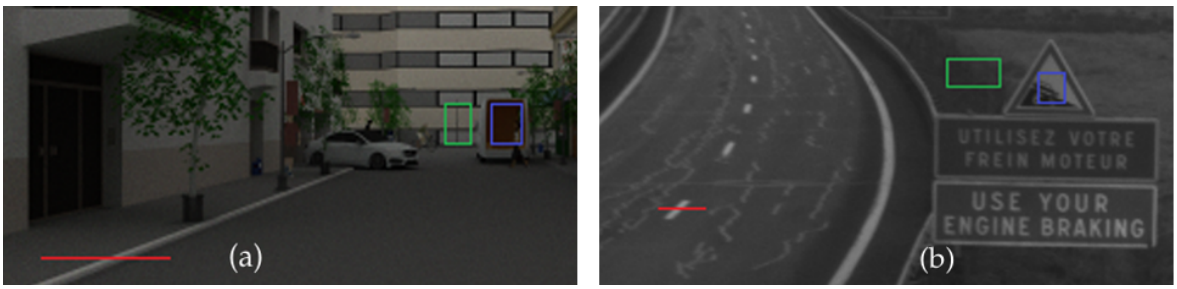

Figure 1.5: Pixel lines (in red) and contrast polygons (in blue/green) for the urban simulated scene (a) and the real one from a section of the French A75 highway (at the Col de la Fageole point) (b).

In addition, the authors in [38] analyze the evolution of the pixel lines. In the bottom of Figure 1.6, the peak in all the curves without fog (solid lines) represents the studied object, marking the ground in the case of real camera images (Figure 1.5b) and the edge of the sidewalk in the case of the intra-urban road simulated scene (Figure 1.5a). The presence of fog in the scene was simulated by SWEET, and in the real road scene, it attenuates the peak representing the object (ground markings, edge of the sidewalk) and slightly lighten the scene around as can be seen through the curves in the broken line of Figure 1.6 (left and right). However, in the case of the Koschmieder model, the

behavior is completely different, and this again confirms that this model excessively brightens the whole image as can be seen in the bottom of Figure 1.6.

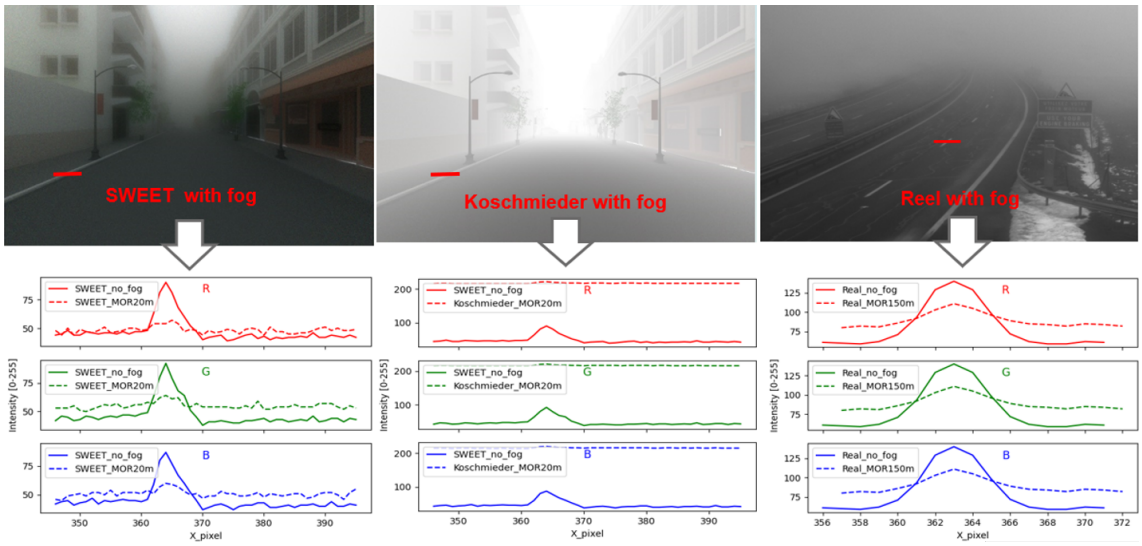

Figure 1.6: Comparing the intensity of a pixel line for images coming from SWEET (left), Koschmieder (middle) and real camera images (right) [38].

The simulation of perceptive sensors in fog conditions must take into account the modelling of the propagation of electromagnetic waves through a participating medium. The optical characteristics of this medium must be known in order to simulate the extinction of the radiation. These optical characteristics are computed from the droplet size distribution (DSD) by using the Lorenz-Mie scattering theory [6]. Then, the droplet size distribution of fog is a key parameter that governs these optical characteristics depending on the radiation wavelength [14, 15, 5]. A DSD is a function $N(r)$ (cm^{-3} $\mu\mathrm{m}^{-1}$) such that $N(r)\,dr$ represents the number of water droplets contained in a volume of 1 cm^3 whose radii belong to $(r, r+dr)$. There is an extensive literature on modeled or measured fog droplet size and other characteristics like liquid water content, total concentration of drops, mean diameter [39, 61, 62, 63, 64, 65, 66, 62, 67, 68, 69, 70, 71, 72, 73, 74, 75, 76, 77, 24, 78]. All the experimental studies show that fog droplet size ranges from a few tenths of a micron to a few tens of microns [79, 80, 39, 81, 40, 82, 83, 84]. Other studies attempt to characterize the droplet size distribution (DSD) by modeling them. Two main categories of laws are used for fitting: shifted gamma laws [85, 86, 87, 88] and log normal laws [89, 67].

To evaluate the impact of the adverse conditions on optical sensors, the French research and technical center Cerema operates the European Rain and Fog PAVIN platform [90], presented in Figure 1.7. In front of the control station, the track is divided into two parts (a solid tunnel and a greenhouse with a removable opaque cover), allowing tests to be conducted in both daylight and nighttime conditions, following a wide range of scenarios.

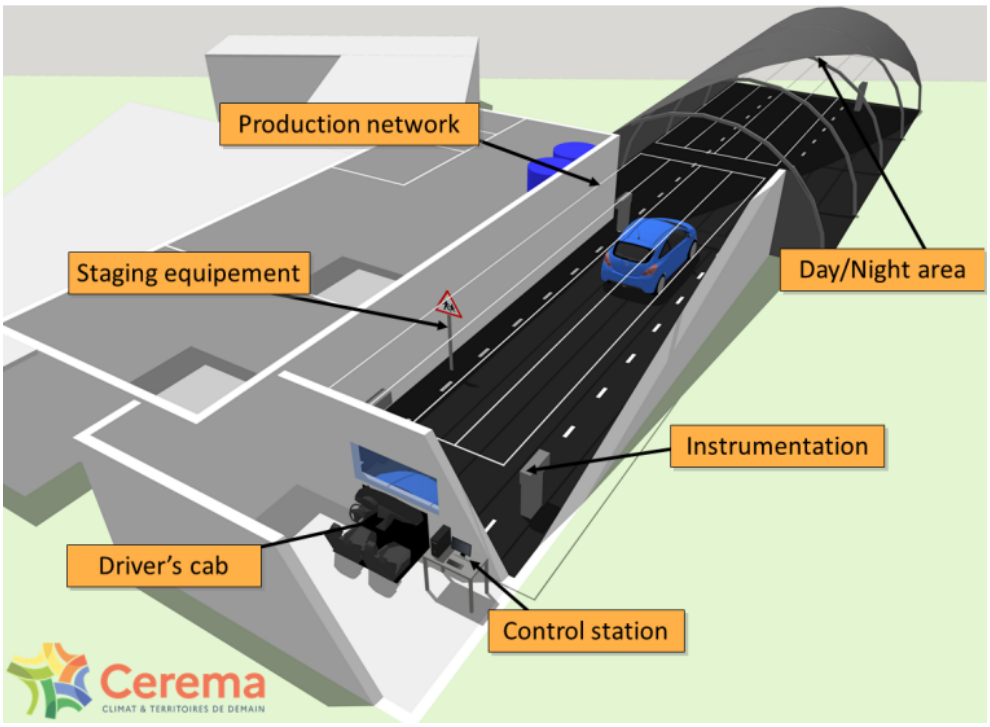

Figure 1.7: Overall structure of Cerema Adverse Weather platform [1].

The installation consists of a covered track that is 30 meters (see Table 1.1) long and is specially constructed using a number of elements, including a rain and fog generator, weather sensors, and reference vision sensors.

	Fixed section (Tunnel)	Greenhouse
Length	15 m	16 m
Wide	5.5 m	5.5 m
High	2.25 m	2.25 m

Table 1.1: Geometric characteristics of the Fog and Rain platform.

As presented in Figure 1.8, the optical sensors and cars can be exposed to controlled artificial fog and rain [1, 62, 91, 5]. This platform allows to study human perception in adverse conditions [92, 93], vision system capabilities in fog or rain conditions [94, 95, 96, 97, 98] or computer vision algorithms for object and weather detection [99, 100, 60]. Regarding the assessment of how adverse weather conditions affect the functionality of vehicle perception systems, as mentionned in [90] , the first public work was conducted in the context of the AWARE project "All Weather All Roads Enhanced vision" from 2014 to 2017 which develop an "all weather/conditions" visibility sensor, especially for use in adverse conditions such as at night and in fog, in order to see the vehicle's surroundings and detect risks, as part of an effort to provide an affordable solution. Its applications target the automotive and aerospace industries. This topic was then continued in the

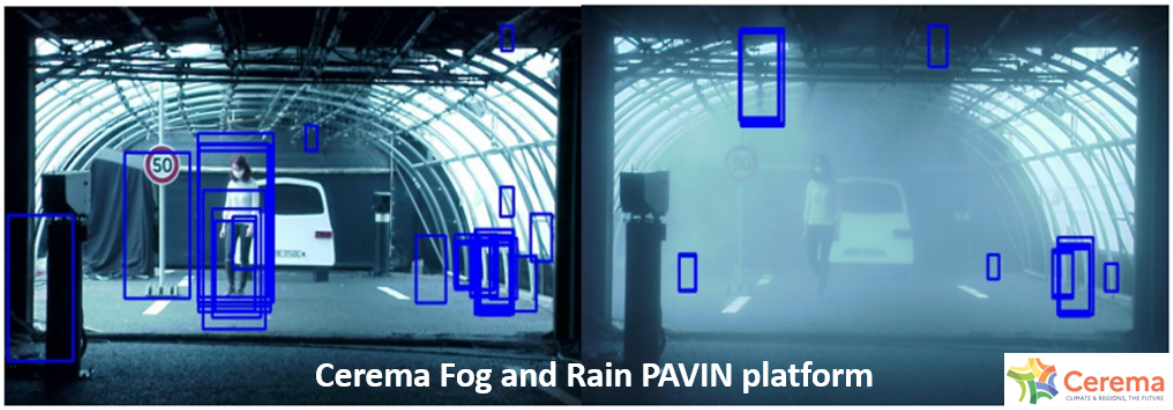

Figure 1.8: Representation of the evolution of optical sensors at the Cerema's platform in presence of fog.

DENSE project [101] "aDverse wEather eNvironmental Sensing systEm", launched in 2016, with the objective to eliminate one of the most pressing problems of automated driving: the inability of current systems to sense their surroundings under all weather conditions.
We summarize the types of studies that can be conducted in PAVIN platform:

1. Validation of sensors and products to be deployed outdoors.
2. Performance measurement of driver assistance systems/ ADAS (pedestrian and obstacle detectors).
3. Performance measurement of innovative road signalling and lighting systems.
4. Study of driver perception in conditions of reduced visibility.
5. Development of new imaging technologies adapted to fog and rain conditions (infrared, laser, RADAR).
6. Comparison between artificial vision systems and humans.
7. Design of 3D image and point cloud analysis and processing algorithms.

The reproducible weather conditions available in the PAVIN platform are:

1. Dense to light fog by dissipation (not stabilized), weather visibility 10 m to 1000 m.
2. Dense fog at a stabilized level; weather visibility from 10 m to 80 m.
3. There are two types of fog particle size: radiation (0.8 microns) and advection (0.8 to 8 microns), as shown in the top of Figure 1.10.

4. Steady-state heavy rain: rain intensity from 20 mm/h (maximum duration is 100 minutes) to 180 mm/h (maximum duration is 9 minutes) as shown in the bottom of Figure 1.9.

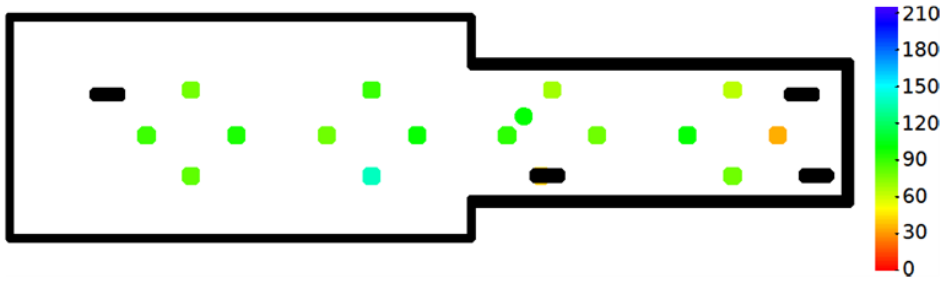

Figure 1.9: Rain intensity measured within the PAVIN platform (mm/h) [90].

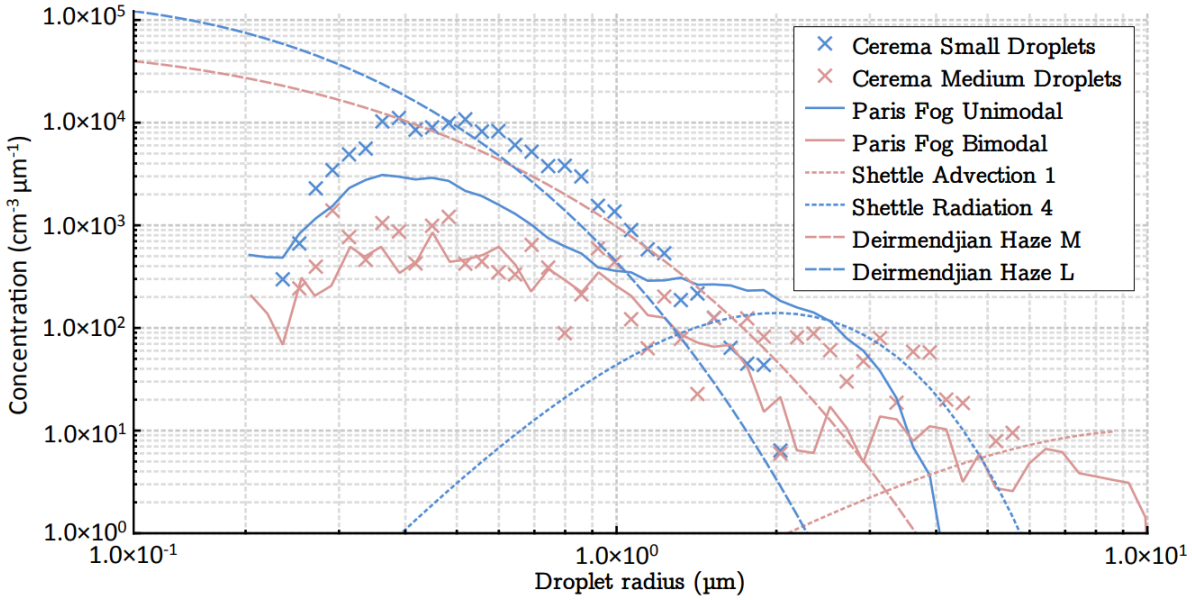

Figure 1.10: Particle size distribution of the PAVIN platform fogs compared to different models [24].

We give in Figure 1.11 various experimental tests of the sensor detection in the presence of fog in day and night conditions [90]. From the figures in the middle of Figure 1.11, we can observe how the presence of fog limits the visibility and the detection of obstacles.

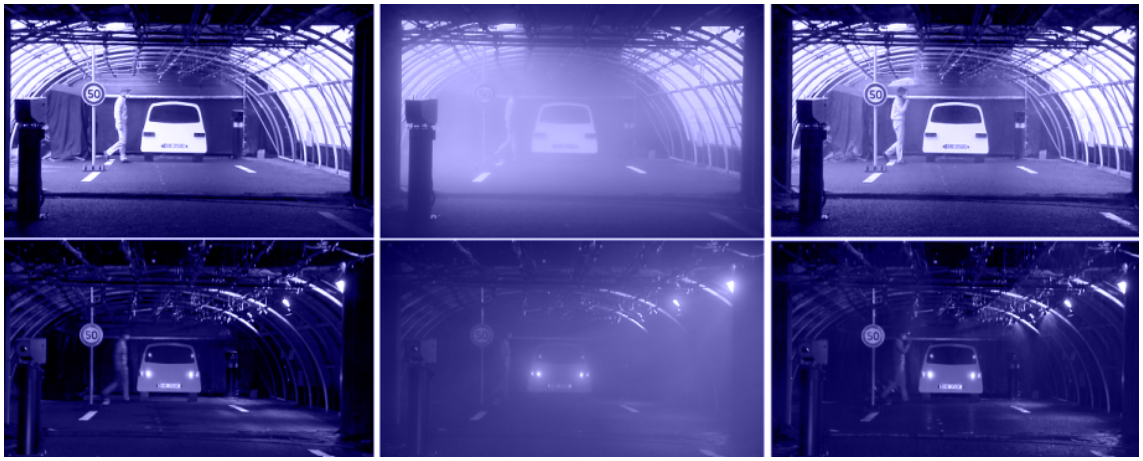

Figure 1.11: Some tests of sensor detection in both daylight and nighttime conditions in the presence of fog.

1.3 Fog and visibility

The safety and vision of drivers on the roadways can be significantly impacted by the road fog. It happens when the vision is lowered due to tiny water droplets suspended in the air, which is unsafe for drivers. High-traffic locations, coastal regions, and lowlands where humidity and cold temperatures are prevalent, can be particularly difficult due to this weather phenomena. When air humidity and relatively low temperatures mix, it frequently results in road fog. Fast cooling hot, humid air approaches its saturation threshold, where moisture condenses into minute droplets of suspended water. This procedure produces a dense haze that reduces vision, making driving challenging and sometimes hazardous.
Road fog has several negative effects. As drivers have less time to respond to barriers, other cars, and rapid changes in traffic, reduced vision dramatically raises the probability of traffic accidents. In conclusion, road fog is a complicated meteorological phenomenon that may have detrimental effects on the safety of the road.

1.3.1 Visibility

The meteorological visibility, noted by V_m (expressed in meters), is defined by the World Meteorological Organization (WMO) [37] as the greatest distance at which a black object of suitable dimensions can be seen and recognized against the horizon sky during daylight or could be seen and recognized during the night if the general illumination were raised to the normal daylight level.
Different methods to estimate the meteorological visibility distance have been developed in the field of transportation. One family of methods estimates the contrast of objects in the scene and assigns a distance, usually assuming the road is flat. Bush et Debes [102]

use a wavelet transform to detect the highest edge in the image with a contrast above 5% in a region of interest that encompasses the road pavement. A system for estimating the meteorological visibility distance with the same principles is proposed by Zhao-Zheng et al. [103], except that it uses the algorithm proposed by Hautière and al. [104] to estimate the contrast. In the field of transport, various techniques have been devised to estimate meteorological visibility distance. One type of approach involves measuring the contrast of objects in a visual image and then determining distance, often under the assumption of a level road surface. Bush and Debes [102] employs a wavelet transform to identify the most prominent edge in the image, considering a contrast threshold of at least 5% within a predefined region of interest that encompasses the road pavement. A comparable methodology for estimating meteorological visibility distance, based on the same principles, is presented by Zhao-Zheng and al. [103]. However, in their approach, they utilize the contrast estimation algorithm introduced by Hautière and al. [104].
The visibility is written more commonly, for a contrast threshold of 5%:

$$\text{for } \lambda = 550nm,\ V_m = -\frac{1}{\sigma_{ext}^{\lambda}} \ln\left(\frac{5}{100}\right) = \frac{3}{\sigma_{ext}^{\lambda}}, \tag{1.1}$$

where σ_{ext}^{λ} is the extinction coefficient.
In meteorology, the presence of fog is considered when meteorological visibility drops below 1000 meters. In a road context, fog becomes critical when meteorological visibility drops below 400 meters. In [105], four classes of road visibility are defined as presented in Table 1.2.

Visibility class	Meteorological visibility distance (V_m in meter)
Class 1	between 200 and 400 m
Class 2	between 100 and 200 m
Class 3	between 50 and 100 m
Class 4	less than 50 m

Table 1.2: Fog classes in a road context according to [105].

Based on these information, a road visibility sensor must affect to one of these four visibility classes and detect the origin of the visibility reduction.
The meteorological visibility distance is measured by using different types of instruments, which make it possible to detect fog by measuring the extinction coefficient, for example, we have the transmissiometers and scatterometers. The PAVIN Fog&Rain Platform is equipped with the transmissiometer DEGREANE HORIZON TR30 presented in Figure 1.12.

Figure 1.12: The transmissiometer DEGREANE HORIZON TR30 used in the PAVIN Fog&Rain Platform

Their basic principle consists of measuring the attenuation of a light beam as it passes through a fluid over a given distance [37]. Transmissometers are used mainly in aeronautical meteorology, but they find applications in other fields, such as oceanography. Visibility is calculated using the extinction coefficient over the known distance between the two instruments. In general, transmissometers measuring visibility in the atmosphere using a wavelength of about 550 nanometers, roughly in the middle of the visible spectrum. The extinction coefficient σ_{ext}^{λ} is given by using the Beer-Lambert law

$$I = I_0 e^{-\sigma_{ext}^{\lambda} d} \Longleftrightarrow \sigma_{ext}^{\lambda} = -\frac{1}{d} \ln\left(\frac{I}{I_0}\right), \tag{1.2}$$

where I_0 is the emitting luminous flux and I is the luminous flux received at distance d. Figure 1.13 represents the protocol to measure visibility by using the Beer-Lambert law.

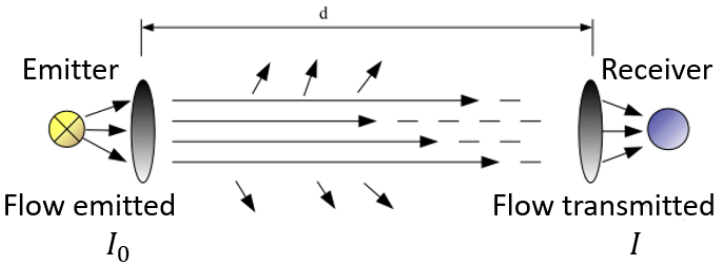

Figure 1.13: Protocol to measure the visibility

1.3.2 Types of Fog

By definition, fog is the suspension in the atmosphere of very small water droplets reducing visibility on the ground to less than one kilometer. Fog is actually a cloud whose base touches the ground. The World Meteorological Organization (WMO) explains several types of fog [37]. The two most common types of fog are the following:

1. Radiation fog: Radiation fog usually forms at night, when the earth's surface is cooled by radiation and in turn cools the adjacent air which reaches its saturation temperature. This type is made up of "small droplets", with diameters distributed around a mode between 1 and 10 μm.

2. Advection fog: Advection fog forms when relatively warm moist air moving over a colder surface cools on contact with that surface until it reaches its saturation temperature. This is the case, for example, when relatively warm moist air moves over a cold sea ("sea fog") or frozen or snow-covered ground. This type is made up of "large droplets", with diameters distributed around a mode between 10 and 20 μm.

Figure 1.14: Radiation fog (left) and Advection fog (right). Official website (WMO)

The Cerema, from its PAVIN Fog&Rain platform, can produce artificial fog. The fog production process consists of spraying pressurized water from injector rails suspended from the ceiling. The qualification of this equipment has made it possible to establish a mode of the particle size distribution of the order of a micron in diameter whatever the concentration [106].

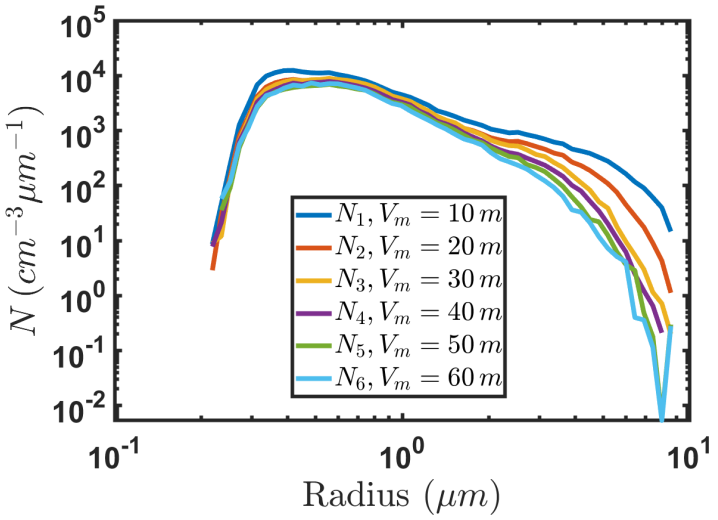

Figure 1.15: Droplet size distributions N for the artificial fog measured at PAVIN platform of Cerema for different visibility.

We note that the droplet size distribution DSD is the number of water particles per cm^3 for each radius r. The DSD is expressed in $cm^{-3}\mu m^{-1}$ as a function of the radius r of water particles expressed in μm, and is denoted by N. We present in Figure 1.15 various droplet size distributions measured in the PAVIN platform at Cerema [1].

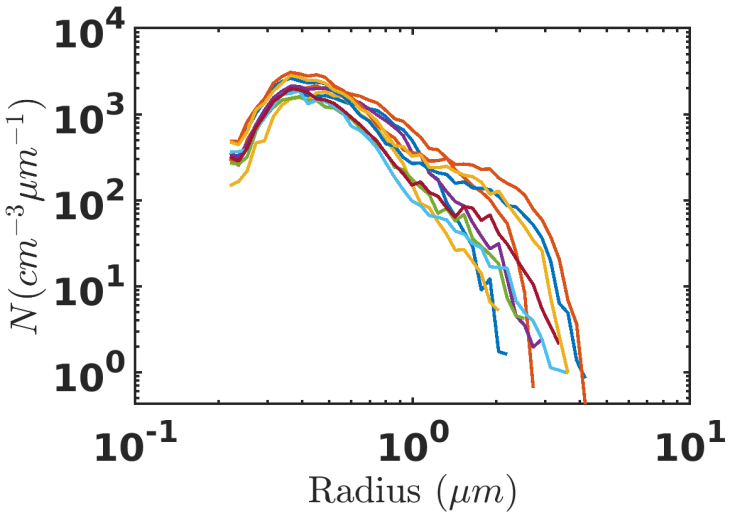

Figure 1.16: Droplet size distributions for a real fog (Paris-Fog campaign [2])

There is another type of particle size distribution, we give in Figure 1.16 the particle size distribution of natural fog. These distributions were measured during an episode of fog on the night of March 13 to 14, 2007 on the French Palaiseau site (Paris-Fog campaign [2]). Several comparisons between these distributions and artificial distributions measured in PAVIN platform are already carried out in [24]. We observe that the natural distribution of fog has forms similar to that of the distribution of the artificial fog presented in Figure

1.15. In addition, for these two types of fog, it is noted that the greatest number of concentration is for the particle of the radius varied between 0.3 μm and 0.6 μm.
Most studies dealing with the propagation of light in scattering media are based on granulometric models [107], with one of the reasons being the extreme difficulty of collecting experimental data. Among the various laws used to model the granulometric distribution of a natural polydisperse medium [86, 87, 88, 89, 67], the modified gamma distribution proposed by Deirmendjian [6] is the most widely applied to fog [108, 109]:

$$N(r) = c\, r^{\beta} e^{-d r^{\gamma}},\ r \geqslant 0, \tag{1.3}$$

where $N(r)$ is the number of particles per radius class, and c, β, d, and γ are parameters used to fit the model to observations. Shettle and Fenn [3] proposed a typology of different types of fog into four classes for which they provide values for the parameters in equation (1.3). Table 1.3 presents the coefficients given in [3] for modified Gamma laws (1.3) to represent the particle size distributions of natural fog where r_m represents the peak position for each model.

Types of fog	Model	$r_m(\mu m)$	c	β	d	γ
Advection fog	1	10	0.027	3	0.3	1
Advection fog	2	8	0.06592	3	0.375	1
Radiation fog	3	4	2.37305	6	1.5	1
Radiation fog	4	2	607.5	6	3.0	1

Table 1.3: Coefficients given in [3] for modified Gamma laws (1.3) to represent the particle size distributions of natural fog.

Figure 1.17 represents the modified gamma law fog particle size models proposed by Shettle and Fenn [3] and given in Table 1.3.

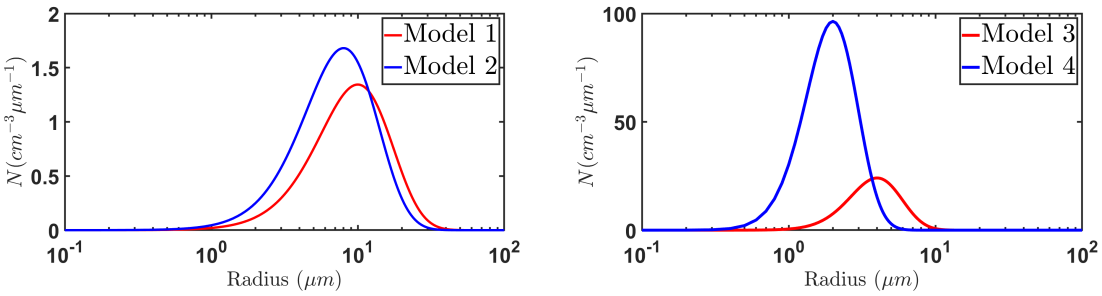

Figure 1.17: Modified gamma law fog particle size models proposed by Shettle and Fenn [3]

Shettle models always tend to overestimate the size of drops. These models are used to characterize fog of large drops (highest concentration for drops of radius 2 and 4 micron). Natural and platform mists are quite close. Comparison in terms of extinction for the wavelength 550 nm was made in [24].

1.4 Objectives and Methodology

As already mentionned, the simulation of perceptive sensors in fog must take into account the modelling of the propagation of electromagnetic waves through an intervening medium. The optical characteristics of this medium must be known in order to simulate the extinction of the radiation. The droplet size distribution for the fog case is a key parameter that determines these optical characteristics depending on the radiation wavelength [14, 15, 5].

The PAVIN Fog&Rain platform is a tool for evaluating perceptive sensor simulators by performing physical tests of wave propagation based on radiation measurements. In this platform, we already use particle size analyzers PALAS WELAS 2100, presented in Figure 1.18, to measure the DSD. These measurements are very local (1 cm^3) and may not be representative at the whole platform scale (400 m^3 of fog).

Figure 1.18: Aerosol Sensor welas 2100. Equipped with a small measurement volume and are used for coincidence-free measurement with a maximum number concentrations of up to 500,000 particles/cm3. Measuring range: 0.2 – 10 μm / 0.3 – 17 μm / 0.6 – 40 μm.

Therefore, our objective is to identify representative droplet size distributions of fogs produced in the platform thanks to radiance or irradiance measurements performed in Cerema's PAVIN platform. Figure 1.19 shows a diagram of experimental protocols allowing to perform the identification: a spectrally continuous light source illuminates the foggy medium and spectral measurements are made in forescattering (left) and backscattering (right) situations.

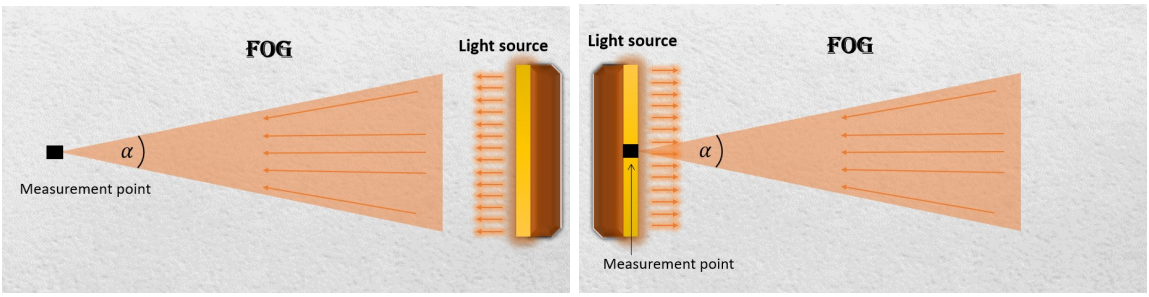

Figure 1.19: Diagram of the protocol for the experimental measurements.

The aim of this thesis works is then to propose a method for identifying the DSD from radiation measurements interpreted using the one-dimensional stationary radiative transfer equation. The reconstruction method is done by minimizing a cost function which corresponds to the error between the measurements and the digital model output. We aim to examine the identification of the DSD with radiative transfer models that can take into account the in-scattering term and do not limit us to the basic Beer-Lambert solution as mentioned by several authors. Consequently, it is essential to develop numerical processes to solve the complete radiative transfer equation. Several finite difference methods are used by several authors to approximate the one-dimensional stationary radiative transfer equation. In our work, this equation is approximated by using a decomposition method on the double Legendre basis and the optical properties are computed by using the Lorenz-Mie scattering theory from the fog droplet size distribution. We then use these procedures in a gradient descent-based method to solve our minimisation problem: we will introduce an adjoint problem to the radiative transfer equation allowing us to easily calculate the cost function gradient. It is important to note that the computation time of these procedures depends more on the discretisation parameters to solve the one-dimensional stationary radiative transfer equation and its adjoint problem than the number of parameters describing the DSD: the inversion method we develop does not need to model the unknown DSD as made in [16, 17, 18, 19, 20] where the authors reconstruct some models of volume frequency distributions (Log-Normal and gamma laws that depend on two parameters) by using Beer-Lambert law (without the in-scattering term). With our method, we are able to fix a desired number of radius classes to define the DSD without impact on the computing time since we use a gradient descent method for which the gradient of the cost function is calculated thanks to an adjoint problem of the radiative transfer model whose numerical resolution is very low sensitive to the number of radius classes. For numerical applications, we use the 60 radius classes (0.15 μm-8.5 μm).

The main result of our works is the identification of the droplet size distributions (noted also by retrieval of droplet size distributions) of fog by radiation measurements in the range 350 nm - 2500 nm [21]. For the identification problem (or retrieval problem), a theoretical and numerical study of the one-dimensional stationary radiative transfer

equation was carried out by using the Yvon method [22] to solve the RTE (double Legendre method). We prove the well-posedness of the underlying inverse problem of the RTE and then we conduct some numerical experiments using synthetic data. The identification of the distribution N enables us to calculate the optical properties using the Lorenz-Mie theory [6]. We have devised a method that allows identification of a broad range of distributions encountered in natural fogs and those artificially generated in the PAVIN platform. In this study, we evaluated our method on DSD acquired through measurements in natural conditions [23], artificial conditions [24], and via models [3]. The numerical results suggest that the method allows the identification of the DSD with different models of 1D radiative transfer (Beer-Lambert, isotropic in-scattering operator and anisotropic in-scattering operator).

1.5 Manuscript Plan

This thesis is structured as follows. A literature review on the optical properties and the droplet size distribution identification are presented in Chapter 2. In Chapter 3, a literature review is presented, covering the radiative transfer equation, its derivation, and their field of application. Also, the Lorenz-Mie scattering theory, which enables the expression of optical properties regarding fog droplet size distributions, is presented in this Chapter. Next, a 1D case of the stationary radiative transfer equation is presented in Chapter 4 with the existence and uniqueness of the solution and its theoretical and numerical resolution. In Chapter 5, we detail the DSD we will use to test the reconstruction method. Additionally, the gradient descent-based inverse problem and the cost function are presented along with their properties. This chapter discusses the expression of the cost function gradient in terms of an adjoint problem to the RTE. The numerical results on the DSD identification using synthetic measurements (output of simulations with real DSDs and some DSD models as input) in the Beer-Lambert modelling case (without multiple scattering), isotropic, and anisotropic collision operator cases are presented in Chapter 6. In Chapter 7, a detailed account of the experimental procedure used for the measurements performed on the PAVIN platform is presented. This chapter also presents a comparison between 3D numerical simulation of radiative transfer equation and experimental data acquired in the PAVIN platform. The manuscript is concluded in Chapter 8 with suggestions for future study subjects.

1.6 Scientific Contribution

Publication:

- A. Krayem, F. Bernardin, and A. Münch, "Identification of fog Particle Size Distribution by a radiative transfer equation inversion". Journal of Quantitative Spectroscopy and Radiative Transfer JQSRT, 2024. Click here.

Communication:

- Krayem, A., Bernardin, F., and Münch, A.: Identification of fog Particle Size Distributions by inverting the radiative transfer equation, EGU General Assembly 2023, Vienna, Austria, 24–28 Apr 2023, EGU23-7634, Abstract.
- Krayem, A., Bernardin, F., and Münch, A.: IDENTIFICATION OF FOG PARTICLE SIZE DISTRIBUTION BY A RADIATIVE TRANSFER EQUATION INVERSION, Proceeding of Proceedings of the 10th International Symposium on Radiative Transfer, RAD-23 Thessaloniki, Greece, 12–16 June 2023, 2023, (Click here).

Poster and presentations:

- 28 September 2023, Presentation in the international research center CIR ITPS "Innovative Transportation and Production Systems" of I-SITE CAP20-25, Clermont-Ferrand, France.
- 12-16 June 2023, 10th International Symposium on Radiative Transfer, RAD-23, Thessaloniki, Greece
- 24-28 April 2023, EGU General Assembly 2023, Vienna, Austria.
- 06 April 2023, International research center "Innovative Transportation and Production Systems" CIR ITPS, Institut Pascal, Clermont Ferrand, France.
- 12 January 2023, Journée d'équipe EDPAN, LMBP, Clermont-Ferrand, France.
- 21 August-02 September 2022, Summer school, IX Partial differential equations Optimal Design and numerics, Centro de Ciencias de Benasque "Pedro Pascual", Spain.
- 13-17 June 2022, CANUM 2020, 45eme Congrès National d'Analyse Numérique, Evian-les-Bains, France.
- 23 November 2021, Journée de doctorant, LMBP, Clermont-Ferrand, France.
- 29 June 2021, Poster à la journée scientifique de l'ecole doctorale des sciences pour l'ingénieur, Clermont-Ferrand, France.
- 21-25 June 2021, SMAI 2021, 10 ième Biennale Française des Mathématiques Appliquées et Industrielles, Grande-Motte, France.
- 04 June 2021, Présentation dans le défi « Véhicules et Machines Intelligents » of LabEx IMobS3 CAP 20-25, Clermont-Ferrand, France.

Chapter 2

State of the art on the particle size distribution identification

The identification (or the reconstruction) of particle size distribution of a participating medium is an important step in many scientific domains, including physics, meteorology, chemistry, and biology. We recall that our objective is to characterise the fog produced in the PAVIN platform by an average DSD compatible with both radiation measurements and a physical modelling of electromagnetic propagation. This is the definition of what we mean in our work by fog droplet size distribution identification, i.e. the search for a DSD compatible with experimental measurements interpreted by a given model. We can note that this identification leads to the quantification of some medium's characteristics calculated from the DSD, such as the extinction coefficient or meteorological visibility, or more generally optical properties expressed thanks to the particle size distribution by using the Lorenz-Mie scattering theory. For many applications, these optical properties allow to understand the fundamental characteristics of the systems under study, in order e.g. to optimize industrial operations and to obtain greater understanding of natural phenomena.
This chapter starts with Section 2.1, which provides an overview of previous research on the direct reconstruction of optical properties for various applications. Section 2.2 presents a comprehensive review of the current state of research on identifying particle size distribution in fog. In a first part, the identification of the distribution is presented using the LiDAR equation. The second part concerned a simplified model of the radiative transfer equation, specifically the Beer-Lambert model.

2.1 Review on the identification of optical properties

In the fields of optics and imaging, optical properties reconstruction is an important area. It consists of the extraction and study of significant properties from a medium or substance based on how those properties interact with light. Several fields, including medicine, materials science, remote sensing, and others use the optical properties reconstruction. Optical properties reconstruction enables to explore the composition, structure, and behavior of things at both the micro and macro scales by using the laws of light-matter interaction.

Fundamentally, optical properties reconstruction makes use of the specific ways that light reacts with various materials. This interaction results in phenomena like absorption, scattering, reflection, and transmission, each of which provides crucial information about the material's properties. To reconstruct optical properties, a variety of imaging and spectroscopic approaches can be applied. These approaches frequently use advanced technology, including spectrometers, lasers, detectors, and complex data analysis algorithms. Depending on the application, optical properties can be reconstructed in real-time or after processing, and they can provide valuable information about biological tissues, environmental samples, semiconductor materials, and more. Optical properties reconstruction has huge potential, but it also has difficulties. Research challenges include the actual difficulty of light-matter interactions, the requirement for precise measurements, and the creation of intricate mathematical models. But as the subject continues to develop, thanks to improvements in technology, computational capability, and multidisciplinary collaborations, we can investigate previously unknown parts of materials and biological systems. The optical properties reconstruction is employed in several application areas to learn more about the composition, structure, and optical characteristics of the samples or objects under study [110, 7, 111, 8, 9, 10, 11, 12, 13]. In Figure 2.1, we give some fields of use for optical properties reconstruction.

Figure 2.1: Various applications for optical properties reconstruction

We now go into more detail concerning the ways optical characteristics are used in various fields:

1. Meteorology [111]: The relationship between meteorology and optical property conversion is crucial to improve the precision and reliability of remote sensing data and derivative products used in several applications, including weather forecasting, environmental monitoring, agriculture, and climate research.

2. Remote sensing [110]: Refers to the acquisition of information about an object or area from a distance, typically using sensors on aircraft or satellites. Remote sensing is the study of electromagnetic radiation's interactions with the Earth's surface and atmosphere, particularly visible and near-infrared light, in the context of optical characteristics.

3. Astrophysics [112]: The reconstruction of optical properties is an important approach in astronomy that allows scientists to derive critical information about objects based on the light that they produce, absorb, or disperse. Astrophysicists can get a better knowledge of the universe's nature and features by employing various spectroscopic and detection techniques.

4. Optical tomography[11, 12]: This imaging technique uses light to create cross-sectional pictures of a sample or object. To discover more about the sample's internal structures and optical properties, measurements and examinations of how light interacts with the sample are required. Absorption and scattering are key optical properties in this context.

In summary, the identification of optical properties is essential in optical tomography, remote sensing, and biomedical imaging. These techniques exploit the interactions of light with different materials and tissues to provide valuable insights and information in their respective fields of application.
To reconstruct these properties, it is necessary to introduce the inverse problem of RTE, which is studied by several authors [113, 114]. RTE is a fundamental radiometric equation that defines how light propagates, reflects, and diffuses in a material. However, due to the non-linear and ill-posed character of the problem, as well as uncertainty in the observed data, inversion of the radiative transfer equation can be difficult. To achieve reliable estimates of optical characteristics, inversion procedures frequently include complex numerical techniques such as optimization methods, regularization algorithms, and light scattering models. This type of equation was introduced in astrophysics, nuclear reactors, and atmospheric science [115, 116, 117]. We are interested in the reconstruction of the optical properties (scattering coefficient, absorption coefficient, and phase function) in a time-independent case. Concerning the time-dependent case, we mention [118, 119, 120]. We present in Figures 2.2 various reconstruction methods for optical properties. Some authors use an exact method to reconstruct these properties [121] based on the knowledge of the Albedo operator which maps, for a given domain, the incoming flux to the outgoing flux under some conditions based on these properties. In [121], the authors only reconstruct the absorption and scattering coefficients in two dimensions, while in three dimensions, they reconstruct all these properties. In dimension $n \geqslant 3$, Bal and Jollivet [122] investigated the stability of the reconstruction of the scattering and absorption coefficients from the knowledge of the full Albedo operator.
There are authors who reconstruct these properties using numerical approximation methods. We mention the work of Klose, Netz, Beuthan, and Hielscher [123], where they evaluated the radiative transfer equation in two dimensions. The authors present a number of tissue phantoms to investigate the sensitivity of the fluence (the integral of radiance) calculated using the radiative transfer equation and compare it with ex-

perimental measurements. In their work, they used the Henyey–Greenstein scattering function (for the phase function). After several tests on various optical properties, the authors observe that without an accurate knowledge of the anisotropy factor of the phase function, the measured data cannot be properly predicted. After this study, the authors have introduced the reconstruction of the absorption and scattering coefficients [124] by assuming that the anisotropy factor of the phase function was known.

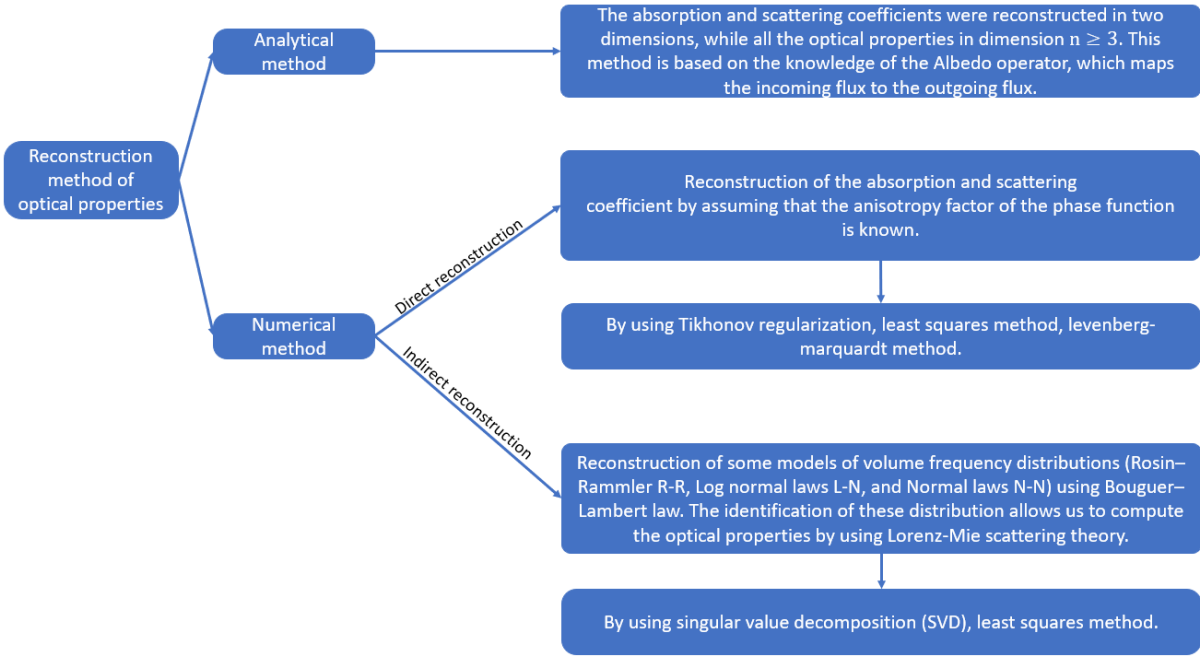

Figure 2.2: Representation of different reconstruction methods of optical properties.

Egger and Schlottbom [125] identify the scattering and absorption properties by assuming that the phase function is known in three dimensions. These authors use the Tikhonov regularization [126] in Banach spaces to provide a solution to this reconstruction problem. We also mention [127, 128], where the authors reconstruct the optical properties by assuming that one or two of these properties are known, and by using a reconstruction algorithm based on the Levenberg-Marquardt regularization [129].
Finally, we mention [16, 130, 131, 132, 18], where the authors reconstruct some models of volume frequency distributions (Rosin–Rammler R-R, Log normal laws L-N, and Normal laws N-N) using Bouguer–Lambert law, $I = I_0 e^{\sigma_{ext}\, d}$, which expresses the attenuation of the luminous flux I_0 at the value of I as a function of the distance d and the extinction coefficient σ_{ext}^{λ}. Chapter 5 provides more information about the reconstruction of optical properties by using the particle size distributions.
To obtain the optical properties, one can use the LiDAR inversion theory rather than the radiative transfer inversion theory. For example, we mention the Klett-Fernald inversion for the authors James Klett 1985 [133] and Fernald [134]. This method is based on

an inversion of the LiDAR signal by considering each wavelength independently. This type of inversion requires an a priori knowledge of the aerosols by imposing the LiDAR ratio (ratio between the extinction coefficient and the backscattering coefficient of the aerosol, which does not depend on its concentration but on its microphysics), as well as a boundary condition, a range in which the optical properties of the molecules and aerosols are known. The LiDAR ratio has units of steradians (sr) and can vary for common atmospheric scatterers from as low as 5 to about 100 sr, depending on the size distribution, shape, and chemical composition of the particles. [135, 136]. However, these measurements are difficult in some cases and there is no system to obtain the LiDAR ratio in the infrared.

2.2 Review on the identification of fog DSD

2.2.1 Identification by using LiDAR equation

As mentioned previously, some authors reconstruct the optical properties and then the droplet size distribution by using the LiDAR equation and not directly the radiative transfer equation. For example, we mention the Klett-Fernald inversion for the authors James Klett 1985 [133], Fernald [134] and others [135, 137, 138, 139, 136]. This method is based on a LiDAR signal inversion by considering each wavelength independent of the others. Figure 2.3 represents a laser transmitter emitting light pulses in the atmosphere; an optical assembly, usually a telescope, collects part of the scattered radiation, which, after being filtered, is brought onto a photo-detector; the detected signal is then amplified, digitized and processed to retrieve atmospheric parameters [140].

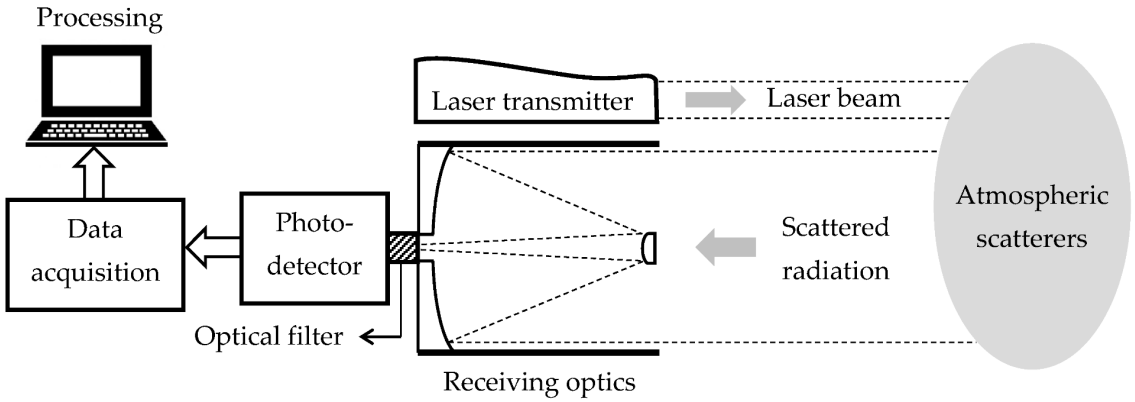

Figure 2.3: Basic schematics of a LiDAR system (see [140]).

The LiDAR power, denoted by $P^\lambda(x)$ (expressed in W), for a given wavelength λ and at distance x is given by the following LiDAR equation:

$$P^\lambda(x) = P_0^\lambda \, E^\lambda A \, \frac{c}{2} \frac{F(x)}{x^2} \, \beta^\lambda(x) \, \exp\left[-2 \int_0^x \alpha^\lambda(z')dz'\right] \tag{2.1}$$

where

1. P_0^λ represents the initial energy of the pulses emitted;
2. E^λ is system efficacity;
3. A the surface area (in m^2) of the optical reception system;
4. c is the speed of light in vacuum;
5. $F(x)$ is the overlap function between the emitted laser beam and the reception cone of the LiDAR at distance x (with a value between 0 and 1);
6. $\alpha^\lambda(x)$ represents the extinction coefficient (or attenuation, in m^{-1}) at x altitude for a wavelength λ, it conditions the transmission of the atmosphere;
7. $\beta^\lambda(x)$ represents the backscatter coefficient (in $m^{-1}.sr^{-1}$) at altitude x for a wavelength λ.

It should be noted that the extinction and backscattering coefficients are the sum of particle contributions (noted p) and molecular (noted m) evolving differently with wavelength and altitude:

$$\begin{cases} \alpha^\lambda(x) = \alpha_p^\lambda(x) + \alpha_m^\lambda(x), \\ \\ \beta^\lambda(x) = \beta_p^\lambda(x) + \beta_m^\lambda(x). \end{cases} \tag{2.2}$$

Klett and Fernald [133, 134] simplify this equation by assuming $F(x) = x^2$. Then the equation becomes

$$P^\lambda(x) = K^\lambda \beta^\lambda(x) \, \exp\left[-2 \int_0^x \alpha^\lambda(x')dz'\right], \tag{2.3}$$

where

$$K^\lambda = P_0^\lambda \, \frac{c}{2} \, E^\lambda A.$$

They proposed a resolution of this equation by making the hypothesis that α and β are linked by the lidar ratio

$$\mathrm{R}^\lambda = \frac{\alpha^\lambda(x)}{\beta^\lambda(x)}, \tag{2.4}$$

constant as a function of altitude and assumed known. According to the calculation carried out in [141], the backscatter coefficient $\beta^\lambda(x)$ obtained by the following form:

$$\beta_p^\lambda(x) = \frac{P^\lambda(x)x^2 \exp\left[-2\left(\mathrm{R}^\lambda - \mathrm{R}_m^\lambda\right)\int_0^x \beta_m^\lambda(x)dx\right]}{K^\lambda - 2\,\mathrm{R}^\lambda \int_0^x P^\lambda(x')x'^2 \exp\left[-2\left(\mathrm{R}^\lambda - \mathrm{R}_m^\lambda\right)\int_0^{x'} \beta_m^\lambda\left(x''\right)dx''\right]dx'} - \beta_m^\lambda(x) \tag{2.5}$$

where R_m is the ratio between extinction and molecular backscatter. This ratio is constant and its equal to

$$R_m = \frac{8\pi}{3}.$$

Then, the extinction and backscatter coefficient are given by

$$\begin{cases} \alpha_m^\lambda(x) = 1.17 \times 10^{-5} \times \left(\frac{\lambda}{0.55}\right)^{4.09} \left(\frac{288\,p}{1013\,T}\right), \\ \\ \beta_m^\lambda(x) = \frac{3}{8\,\pi}\alpha_m^\lambda(x), \end{cases} \tag{2.6}$$

where p, λ and T represent the pressure (in hectopascal "hPa"), the wavelength (in μm) and the temperature (in K), respectively. Then, by using (2.4)-(2.5), we can compute the extinction $\alpha_p^\lambda(x)$ and the backscatter $\beta_p^\lambda(x)$ coefficient of particles.
After the reconstruction of the optical properties, Mueller-Quenzel [139] laid the foundations of the inverse problem by showing numerically the feasibility of recovering the distribution function of aerosol. For several years now, numerical studies have been carried out on inversion algorithms, in particular by studying different regularization methods. For additional details, interested readers can refer to the following references [142, 143, 144].

2.2.2 Identification by using Beer-Lambert modelling

The Beer-Lambert law relates the attenuation of light to the properties of the material through which the light is traveling. When a beam of parallel monochromatic radiation light of intensity I_0 passes through a suspension of particle system (thickness x_0) with a refraction index different from that of the dispersed medium, the scattering and absorption will lead to an attenuation of the transmitted light intensity. According to the Lambert–Beer law, the transmitted light intensity I is defined as follows [145]:

$$\ln\left(\frac{I(\lambda)}{I_0(\lambda)}\right) = -x_0\sigma_{ext}(N), \tag{2.7}$$

where N denotes the particle size distribution. If the suspended particles are spherical, and the multiple scattering and interaction effects are neglectable, the transmitted light intensity I is expressed by the following integral equation:

$$\ln\left(\frac{I(\lambda)}{I_0(\lambda)}\right) = -x_0\,\pi \int_{r_{\min}}^{r_{\max}} Q_{ext}^\lambda(r)\,r^2\,N(r)\,dr, \tag{2.8}$$

where Q_{ext}^λ represents the extinction efficiency at the wavelength λ for a particle radius r. Various authors retrieve the particle size distribution by using model as the

Rosin–Rammer (R–R) distribution, the normal (N–N) distribution and the logarithmic normal (L–N) distribution. These distributions depend on two variables and are expressed as follow [146, 147]:

$$f_{\mathrm{R-R}}(r) = \frac{k_1}{D_1} \times \left(\frac{2\,r}{D_1}\right)^{k_1-1} \exp\left(-\left(\frac{2\,r}{D_1}\right)^{k_1}\right), \tag{2.9}$$

$$f_{\mathrm{L-N}}(r) = \frac{1}{2\,\sqrt{2\pi} r \ln k_1} \exp\left(-\frac{(\ln(2\,r) - \ln D_1)^2}{2(\ln k_1)^2}\right), \tag{2.10}$$

$$f_{\mathrm{N-N}}(r) = \frac{1}{\sqrt{2\pi} k_1} \exp\left(-\frac{(2\,r - D_1)^2}{2k_1^2}\right), \tag{2.11}$$

where r is the radius, D_1 is the characteristic diameters of these distribution functions and k_1 the narrowness indices of the distribution.
The matrix equation describes the discrete form of (2.8), without loss of generality, is:

$$AN = F, \tag{2.12}$$

where $A = (a_{lj})_{1\leqslant l\leqslant G,\, 1\leqslant j\leqslant R}$,

$$a_{lj} = -\pi\, x\, Q_{ext}^{\lambda_l}(r_j)\, r_j^2\, \Delta r,$$

and

$$F = \left(ln\left(\frac{I_{\lambda_1}(x)}{I_{\lambda}(0)}\right), \cdots, ln\left(\frac{I_{\lambda_G}(x)}{I_{\lambda_G}(0)}\right)\right), N = (N(r_1), \cdots, N(r_R))\,.$$

To solve our identification problem, the authors in [148, 10, 130, 18] introduce an objective function which is the L^2-norm of the residual between the real measured data, F_{obs}, and our forward modeled data, F. This objective function was minimized by using Genetic Algorithms (GA) [17, 149], Fruit Fly Optimization Algorithm (FOA) [150], and Particle Swarm Optimization (PSO) [151, 18]. Other algorithms are used, for example, the conjugate gradient method (CG) [152].
A first look at (2.12) may make one believe that size distribution retrieval is simple since typical methods for solving (2.12) are accessible [153]. This is true when the matrix A is well-conditioned. Unfortunately, this is not the case with our problem. The fundamental problem comes from the well-known ill-posedness of the original integral equation. The ill-posedness is frequently defined by a condition number $\kappa_2(A)$ that is greatly more than 1. Methods for solving this ill-posed linear problem are given by several authors [154, 155, 156, 157, 158, 159, 160].
In this thesis, we introduce an inversion method aimed at reconstructing the particle size distribution and, consequently, the optical properties via Mie theory. This approach addresses ill-posed problems by incorporating a regularization term. Furthermore, our inversion method is based on a complete modelling of the radiative transfer equation including the collision operator. To the best of our knowledge, this approach is new and has not been explored previously.

Chapter 3

Review on the radiative transfer equation

In this chapter, we provide a general introduction to radiative transfer and its different application domains in Section 3.1. In Section 3.2, we give the derivation of the radiative transfer equation and the process of absorption, scattering, and emission. We end this section with the equation balance of the time-dependent radiative transfer equation. Different types of phase functions used in the radiative transfer equation (such as Rayleigh, Mie, and Henyey-Greenstein phase function) are given in Section 3.3. In Section 3.5, we recall the existence and uniqueness of the solution of both the time-dependent and time-independent transport equation given by several authors. An L^∞-estimate of the solution is also given in this section. We end this chapter with Section 3.6 which recapitulates the integral formulation of the transport theory.

3.1 General introduction

The radiative transfer is an important theory in physics and astronomy. The radiative transfer equation explains the propagation of radiation through a material. Knowledge of how photons transfer energy through many substances, including the Earth's atmosphere, stars, planets, and even space clouds, requires solving of this equation. The radiative transfer equation is a valuable mathematical tool for modelling and predicting light-matter interactions in these various situations. This equation finds applications in various fields, including:

1. Meteorology and Climatology: This equation, by studying how sunlight is absorbed, reflected, and emitted into the Earth's atmosphere, helps to understand the mechanisms of atmospheric heating and cooling and their role in climate change.

2. Astrophysics: The radiative transfer is a fundamental theory in astrophysics. Radiation from an astrophysical object has been conducted by that object via radiative transfer. In order to comprehend the interpretation of data with regards to an object's structure, temperature, dynamics, and composition, it is important

to have a clear understanding of the mechanics behind this radiative transfer technique.

3. Medical and Environmental Research: The interaction between light and biological tissues and the oceans is modeled using the radiative transfer equation. Understanding light scattering within the human body as well as keeping a focus on environmental health and water quality can all benefit through it.

4. Optical Instrument Design: The radiative transfer has been used by engineers to design optical devices such as telescopes, radiation sensors, and lasers, optimizing the way light is guided, focused, and detected.

Understanding and applying the radiative transfer equation is crucial for the study of the universe and resolving practical challenges in areas such as meteorology, astronomy, and biomedical research. The radiative transfer equation is an important mathematical tool for simulating and forecasting interactions between light and matter in various domains.
The radiation theory was established between 1890 and 1905 through the works of Khvolson in 1890 and Schuster in 1905. Thereafter, the radiative theory was revisited in the context of astrophysics, notably by Chandrasekhar [116]. This book examines radiative transfer theory and its applications in astrophysics, covering topics ranging from scattering to the numerical solution of radiative transfer equations. In the realm of astrophysics, we reference [161] as an explanation of light's passage through interstellar space, stars, and galaxies. Within the domain of neutron transport in nuclear reactors, Case and Zweifel [115] highlighted a similar theoretical framework in 1967. At present, the ETR theory (Energy Transport and Radiation) is extensively used to investigate radiative transfers that involve thermally emitting substances within partially transparent materials. Additionally, we would like to mention [162], where the authors provide a basis in both the theoretical and practical aspects of radiative transfer. The transmission of solar and infrared radiation through dense clouds, the aerosol layer, and the oceanic mixed layer is demonstrated with the application of heuristic models of scattering and absorption, as well as a methodical approach to formulating and solving the radiative transfer equation.

3.2 Derivation of the radiative transfer equation

The fundamental principles of radiative transfer rest upon our comprehension of how energy propagates via radiation across space and materials. Electromagnetic radiation spans various wavelengths comprising gamma and X-rays, visible light, microwaves, and radio waves. The radiance is a fundamental aspect of radiative transfer theory. This is

the power per unit area of radiation that either travels or is emitted in a given direction u at a point s in $\mathbb{R}^3$ during a time period t. The unit sphere $\mathbb{S}^2$ (refer to Figure 3.1 (left)) defines the direction u.

$$\mathbb{S}^2 = \{\,(\cos\theta, \sin\theta\cos\varphi, \sin\theta\sin\varphi),\ 0 \leqslant \theta \leqslant \pi,\ \leqslant 0 \leqslant \varphi \leqslant 2\pi\}. \tag{3.1}$$

The specific intensity (or radiance) is denoted by I_λ typically expressed in watts per square meter per steradian ($Wm^{-2}sr^{-1}$), and is given by the formula:

$$I(t, s, u) = \frac{d\phi(t, s, u)}{\vec{u} \cdot \vec{n}\, dA\, d\Omega dv}, \tag{3.2}$$

where $d\phi$ is the radiant energy passing through an infinitesimal area dA in an infinitesimal solid angle $d\Omega$ centered around a direction in the frequency interval $[v, v + dv]$ (see Figure 3.1(right)).

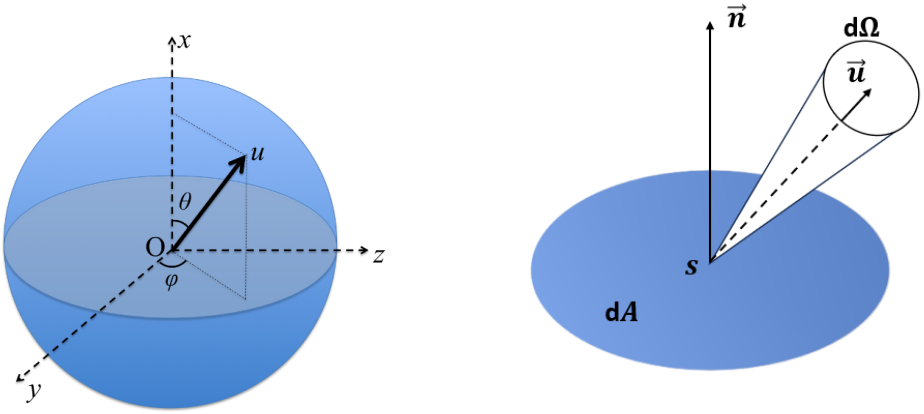

Figure 3.1: The spherical coordinates (left) and the geometric representation to define the intensity (right).

We also can define the radiative flux vector q_λ, for a wavelength λ as a function of the intensity and the relation is given as follows:

$$q_\lambda(t, s) = \int_{\mathbb{S}^2} I_\lambda(t, s, u)\, u\, d\Omega. \tag{3.3}$$

3.2.1 Extinction process

In radiative transfer, the absorption process involves how radiation and matter interact with each other leading to the transfer of energy from the radiation to the material. Let I be the intensity flux in the direction u. We obtain, by noting that $r = u \cdot s$ is the abscissa in the direction of flow, the following relation:

$$\frac{\partial I_\lambda}{\partial r}(t, r, u) = -\sigma^\lambda_{abs}\, I_\lambda(t, r, u). \tag{3.4}$$

This intensity decreases because of the processes of absorption where σ_{abs} represents the absorption coefficient.
The same relation is true in the case of extinction by scattering:

$$\frac{\partial I_\lambda}{\partial r}(t, r, u) = -\sigma^\lambda_{sca} I_\lambda(t, r, u). \tag{3.5}$$

Then, we can introduce the extinction coefficient by the following form:

$$\sigma^\lambda_{ext} = \sigma^\lambda_{abs} + \sigma^\lambda_{sca}, \tag{3.6}$$

and we introduce the Beer-Lambert law with the solution $I = I_0 e^{-\sigma^\lambda_{ext} r}$, which expresses the attenuation of the luminous flux I_0 at the value of I as a function of the distance r and the extinction coefficient σ^λ_{ext}.
We note that the albedo a is defined from the relation between the extinction and scattering coefficient. This relation is given as follows:

$$a = \frac{\sigma^\lambda_{sca}}{\sigma^\lambda_{ext}},$$

where σ^λ_{ext} is defined in (3.6). From this relation, the albedo is therefore a quantity between 0 and 1. We can say that if $a = 1$ the medium is totally scattering, and if $a = 0$ the medium is totally absorbent.

3.2.2 Transfer equation (Energy balance)

To give the radiative transfer equation balance, it is important to describe the detail of the scattering process. Scattering is the process, by which a photon's direction changes when it interacts with matter. This process may lead light to scatter (isotropic scattering) or be angle-dependent (anisotropic scattering) leading to specific directional changes. Finally, transmission occurs when electromagnetic radiation passes through a material without being absorbed or scattered.

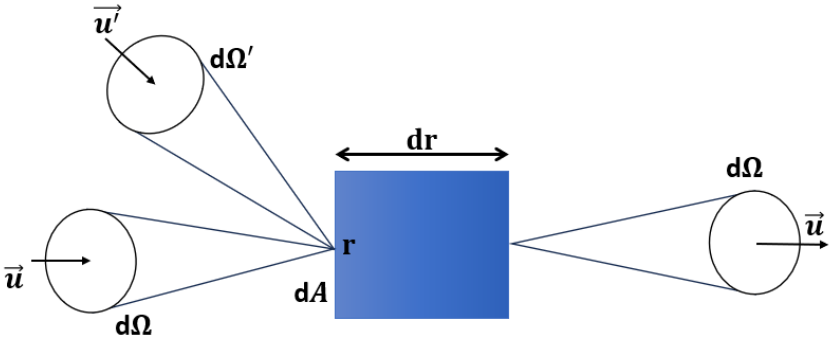

Figure 3.2: Geometric representation to describe the RTE

Figure 3.2 represents the system to describe the radiative transfer equation, an intensity flux enters a surface dA at a point r with a direction u and crosses a distance dr while continuing in the same direction u with a loss of energy due to the process of extinction described in the previous part. Other intensity flux enters the surface dA with a direction u' and continues with a direction u. In this case, it is important to add the phase function which describes the probability of this phenomenon. This phase function is denoted by Φ_λ and normalized as follows

$$\forall (u,u') \in \mathbb{S}^2 \times \mathbb{S}^2,\ \frac{1}{4\,\pi}\int_{\mathbb{S}^2} \Phi_\lambda(u,u')d\Omega' = 1. \tag{3.7}$$

The isotropic case corresponds to a phase function Φ_λ constant equal to one. The increase in flux due to scattering between r and $r+dr$ is then written:

$$\frac{\partial I_\lambda}{\partial r}(t,r,u) = \frac{\sigma^\lambda_{sca}}{4\pi}\ \int_{\mathbb{S}^2} I_\lambda(t,r,v)\Phi_\lambda(r,v,u)\,dv. \tag{3.8}$$

In this case, and taking into account the extinction, the absorption and the scattering, we obtain the following equation of radiative transfer equation:

$$\frac{1}{c}\frac{\partial I_\lambda}{\partial t}(t,r,u)+u.\nabla_r I_\lambda(t,r,u)+\sigma^\lambda_{ext} I_\lambda(t,r,u) = \frac{\sigma^\lambda_{sca}}{4\pi}\ \int_{\mathbb{S}^2} I_\lambda(t,r,v)\Phi_\lambda(r,v,u)\,dv+q_\lambda(t,r,u), \tag{3.9}$$

where c is the light speed in the host medium, q_λ is the source term, $\sigma^\lambda_{ext} = \sigma^\lambda_{sca} + \sigma^\lambda_{abs}$ and σ^λ_{sca} denote the extinction coefficient and the scattering coefficient, respectively.

3.3 Different types of phase functions for the radiative transfer equation

Phase functions play an important role in the radiative transfer equation because they describe the angular distribution of radiation. The phase functions are used depending on the context of the radiative transfer problem and the characteristics of the particles or surfaces involved in the process. The choice of the appropriate phase function is crucial to obtain accurate results when modeling radiative transfer in different media.
In the case of spherical particles (or an ensemble of randomly oriented non spherical particles), the phase function then only depends on $u\cdot u'$, where u and u' are two different vectors. In addition, we can express the value of $\cos\Theta$ as a function of the spherical coordinate of u and u' (see Figure 3.1 left). This relation is given by the following equality:

$$\cos\Theta = \mu\mu' + \sqrt{1-\mu^2}\sqrt{1+\mu'^2}\,\cos(\varphi-\varphi'), \tag{3.10}$$

where $\mu = \cos\theta$ and $\mu' = \cos\theta'$.
In general, the phase function can be written in terms of the Legendre polynomial basis

as follows:

$$\Phi(\cos\Theta) = \sum_{k=0}^{K} \alpha_k \, P_k(\cos\Theta), \tag{3.11}$$

where P_k represents the Legendre polynomial of order k and α_k is the coefficient determined according to the phase function. The determination of the integer K depends on the anisotropy of the phase function.
We present in the following some types of phase functions commonly used in this equation

3.3.1 Henyey-Greenstein phase function

This phase function is often used in radiative transfer models to represent anisotropic scatterong, that is, scatterong that preserves a certain preferred direction. It is characterized by a single parameter, the anisotropy factor g, which determines the degree of anisotropy of the scatterong.
The phase function that we want to represent has azimuthal symmetry: it is therefore a function of the only scattering angle Θ or its cosine. The function is expressed as follows [163]:

$$\Phi(\cos\Theta) = \frac{1}{4\pi} \frac{1-g^2}{(1+g^2-2g\,\cos(\Theta))^{\frac{3}{2}}},$$

verifies the following condition

$$\frac{1}{4\,\pi} \int_{\mathbb{S}^2} \Phi(u \cdot u')\, du' = 1.$$

The anisotropy coefficient (or factor) g (dimensionless), is a measure of the amount of forward direction retained after a single scattering event and has a probability density with a single scattering direction as a parameter

$$g = \langle \cos\Theta \rangle = \frac{1}{4\,\pi} \int_{\mathbb{S}^2} \Phi(u \cdot u')\, u \cdot u' du'.$$

For example, if we develop the Henyey-Greenstein phase function on the Legendre basis as mentioned in equation (3.11), we obtain $\alpha_k = g^k$. Figure 3.3 shows a polar diagram of the Henyey-Greenstein phase function as a function of the polar angles for three different anisotropic factors g.

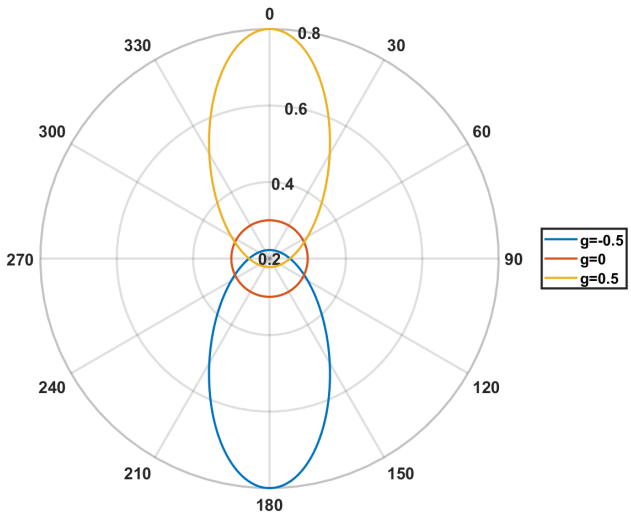

Figure 3.3: Diagram of polar Henyey-Greenstein phase function

In addition, the case $g = 0$ corresponds to isotropic scattering. The value $g = -1$ represents the strictly backscattering case and $g = 1$ represents the strictly forescattering case.

3.3.2 Rayleigh phase function

This phase function is used to represent scattering by particles much smaller than the incident radiation's wavelength (a particle known as Rayleigh), it behaves like an electric dipole. In the case where the incident wave is unpolarized, the phase function is then:

$$\Phi(\cos\Theta) = \frac{3}{4}(1 + \cos^2\Theta),$$

where Θ is the scattering angle.
Figure 3.4 represents the Rayleigh scattering intensity for a particle where the incident wave is coming from the left.

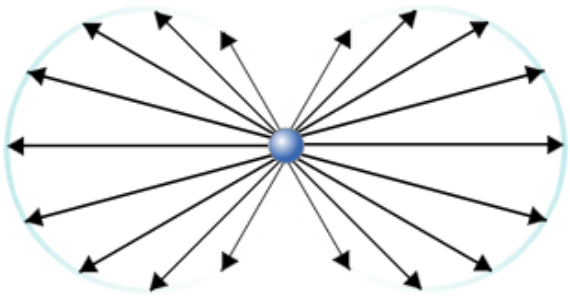

Figure 3.4: Rayleigh scattering intensity for a particle depending on the direction.

3.3.3 Lorenz-Mie phase function

The Lorenz-Mie phase function [164, 6, 165] is used to describe how light is scattered in different directions by particles of sizes comparable to the wavelength of light. It is widely used to model radiative transfer in media containing particles such as water droplets in clouds, dust particles in the atmosphere, and particles of various types of materials. The phase function of Mie is determined by the optical properties of the particle and the wavelength of the incident light. Figure 3.5 represents the Mie scattering intensity for small particles and for large particles where the incident wave is coming from the left.

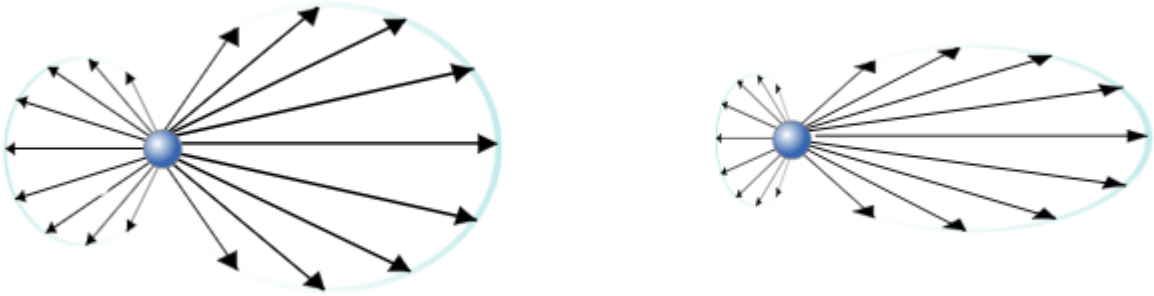

Figure 3.5: Mie scattering intensity for small particles (left), and for large particles (right) depending on the direction.

We detail the Lorenz-Mie scattering theory in the next section.

3.4 Lorenz-Mie scattering theory

The electromagnetic theory known as the "Mie theory" was introduced in 1908 by a German scientist Gustav Mie [164] and extended by Mie in 1912. This theory describes the scattering of light by conducting or dielectric spherical particles when their size is similar to the wavelength of the incident light. The interaction of light with particles in a medium results in light scattering. The dispersion of light in various directions can be influenced by these particles' sizes. The physical mechanism by which spherical particles scatter light is explained by Lorenz-Mie theory. The principal outcomes of Lorenz-Mie theory are formulae for figuring out scattering cross-section, and extinction coefficients based on variables like particle size, material refractive index, and wavelength of incoming light.
The Lorenz-Mie theory is used in many different fields of science and engineering. It has been used to analyze and explain many optical phenomena seen in many situations. For example, this theory is used in astronomy to study the scattering of solar light by atmospheric particles, in meteorology to explain cloud light scattering, in optics to

design particles for controlled light scattering, and in nanotechnology to characterize nanoparticles and nanostructures. In conclusion, it is a fundamental theory for understanding how light interacts with particles of a similar size to its wavelength.
The Mie solution (also known as the Lorenz–Mie solution or Mie scattering) [164, 166] solves the electromagnetic equations of Maxwell

$$\Delta\psi + k^2 m^2 \psi = 0,$$

by describing the elastic scattering of an electromagnetic wave by a spherical particle with its diameter and its complex refractive index, $m = n + ik$, with n and k denoting the real and imaginary part of the refractive index, the latter being linked to absorption properties. Figure 3.6 presents the refractive indices of pure water given by Segelstein indices [167] as a function of the wavelengths.

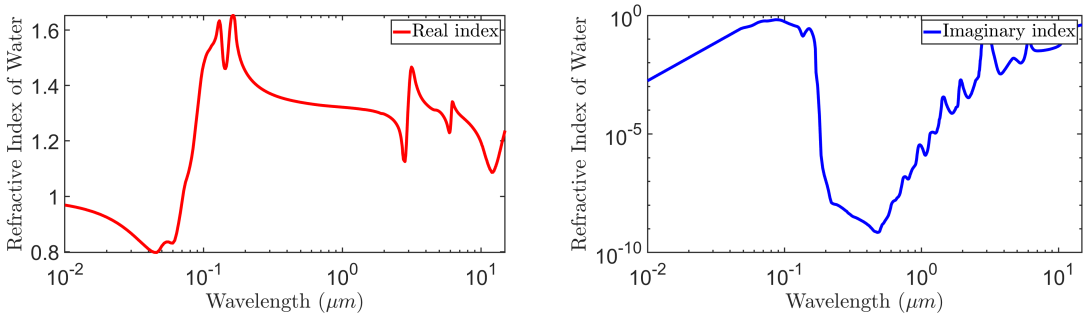

Figure 3.6: Representation of the complex refractive index of pure water [167].

3.4.1 Particles in an absorbing medium

In light scattering solved by Lorenz-Mie theory, as shown in Figure 3.7, a monochromatic plane wave with a wave vector $k = 2\pi/\lambda$ propagates in a medium with a refractive index m_1. This incident wave encounters a sphere of radius r and refraction indices m. As a result of the interaction, a wave is scattered by the sphere throughout space. Lorenz-Mie theory allows us to compute the scattering properties of a single homogeneous, spherical particle embedded in a homogeneous medium.

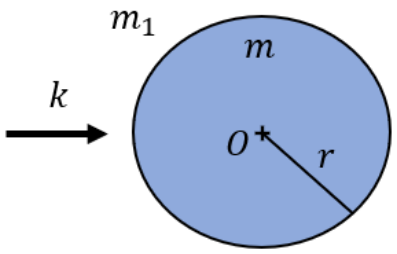

Figure 3.7: A diagram to present the notations used in the scattering by a sphere.

The scattering properties are computed using the scattering amplitude functions S_1 and S_2, which describe the scattering of an electromagnetic wave from a spherical particle [164, 165]:

$$S_1(\mu) = \sum_{n=1}^{+\infty} \frac{2n+1}{n(n+1)} \left(a_n(r,\lambda)\pi_n(\mu) + b_n(r,\lambda)\tau_n(\mu)\right), \tag{3.12}$$

$$S_2(\mu) = \sum_{n=1}^{+\infty} \frac{2n+1}{n(n+1)} \left(b_n(r,\lambda)\pi_n(\mu) + a_n(r,\lambda)\tau_n(\mu)\right), \tag{3.13}$$

where the function π_n and τ_n are related to the Legendre polynomials P_n as follows [168]:

$$\pi_n(\mu) = \frac{d}{d\mu}P_n(\mu) \qquad ; \qquad \tau_n(\mu) = \mu\pi_n(\mu) - (1-\mu^2)\frac{d}{d\mu}\pi_n(\mu). \tag{3.14}$$

Equation (3.14) can be rewritten by the following recurrences:

$$\begin{cases} \pi_0(z) = 0,\ \pi_1(z) = 1, \\ \forall\, n \geqslant 2\,, \pi_n(z) = z\dfrac{2n-1}{n-1}\,\pi_{n-1}(z) - \dfrac{n}{n-1}\,\pi_{n-2}(z), \end{cases}$$

$$\begin{cases} \tau_0(z) = 0,\ \tau_1(z) = z, \\ \forall\, n \geqslant 2\,, \tau_n(z) = z(\tau_n(z) - \tau_{n-2}(z)) - (2n-1)(1-z^2)\,\tau_{n-1}(z) + \tau_{n-2}(z). \end{cases}$$

The Lorenz-Mie coefficients a_n and b_n in equations (3.12) and (3.13) are complex numbers which are composed of the spherical Bessel functions $j_n(z)$ and $y_n(z)$ in the following way [166, 6]:

$$a_n(r,\lambda) = \frac{\psi_n'(y)\psi_n(x) - m\,\psi_n(y)\,\psi_n'(x)}{\psi_n'(y)\zeta_n(x) - m\,\psi_n(y)\,\zeta_n'(x)} \quad \forall n \geqslant 1, \tag{3.15}$$

$$b_n(r,\lambda) = \frac{m\,\psi_n'(y)\,\psi_n(x) - \psi_n(y)\,\psi_n'(x)}{m\,\psi_n'(y)\,\zeta_n(x) - \psi_n(y)\,\zeta_n'(x)} \quad \forall n \geqslant 1, \tag{3.16}$$

where m is the complex refractive index of the medium, λ is the wavelength in the host medium, and

$$x = \frac{2\pi\, r}{\lambda} \qquad , \qquad y = \frac{2\pi\, r\, m}{\lambda},$$

r is the radius of a spherical particles and

$$\begin{cases} \psi_n(z) = z\, j_n(z) = \sqrt{\frac{\pi\, z}{2}}\, j_{n+\frac{1}{2}}(z), \\ \\ \zeta_n(z) = z\,(j_n(z) - i\, y_n(z)) = \sqrt{\frac{\pi\, z}{2}}\left(j_{n+\frac{1}{2}}(z) + (-1)^n\, i\, j_{-n-\frac{1}{2}}(z)\right). \end{cases} \tag{3.17}$$

The Lorenz-Mie coefficients can be rewritten by

$$a_n(r,\lambda) = \frac{(\frac{A_n(y)}{m} + \frac{n}{x})Re(w_n(x)) - Re(w_{n-1}(x))}{(\frac{A_n(y)}{m} + \frac{n}{x})w_n(x) - w_{n-1}(x)}, \tag{3.18}$$

$$b_n(r,\lambda) = \frac{(m\, A_n(y) + \frac{n}{x})Re(w_n(x)) - Re(w_{n-1}(x))}{(m\, A_n(y) + \frac{n}{x})w_n(x) - w_{n-1}(x)}, \tag{3.19}$$

where

$$\begin{cases} A_n(y) = \dfrac{n}{y} - \dfrac{y}{n - y\, A_{n-1}(y)}, \\ \\ A_0(y) = \cot(y). \end{cases} \qquad \begin{cases} w_n(x) = \dfrac{2n-1}{x}\, w_{n-1}(x) - w_{n-1}(x), \\ \\ w_0(x) = \sin(x) - i\, \cos(x), \\ \\ w_{-1}(x) = \cos(x) - i\, \sin(x). \end{cases} \tag{3.20}$$

3.4.2 Optical properties

The extinction and scattering coefficients are expressed in terms of the droplet size distribution N as follows [169]:

$$\sigma^{\lambda}_{ext}(N) = \int_0^{+\infty} Q^{\lambda}_{ext}(r)\, \pi\, r^2\, N(r)\, dr \qquad ; \qquad \sigma^{\lambda}_{sca}(N) = \int_0^{+\infty} Q^{\lambda}_{sca}(r)\, \pi\, r^2\, N(r)\, dr. \tag{3.21}$$

Similarly, the phase function can be expressed by the following form:

$$\sigma^{\lambda}_{sca}(N)\, \phi_{\lambda}(\mu, N) = \int_0^{+\infty} Q^{\lambda}_{sca}(r) \psi_{\lambda}(r,\mu)\, \pi\, r^2\, N(r)\, dr, \tag{3.22}$$

where the scattering and extinction efficiencies are given by:

$$Q^{\lambda}_{sca}(r) = \frac{\lambda^2}{2\,\pi^2\, r^2} \sum_{n=1}^{+\infty} (2n+1)\left(|a_n(r,\lambda)|^2 + |b_n(r,\lambda)|^2\right), \tag{3.23}$$

$$Q^{\lambda}_{ext}(r) = \frac{\lambda^2}{2\,\pi^2\, r^2} \sum_{n=1}^{+\infty} (2n+1) Re\left(a_n(r,\lambda) + b_n(r,\lambda)\right). \tag{3.24}$$

For the Mie series presented in (3.12), (3.13), (3.23) and (3.24). Dave's procedure [170] consists of stopping summation when $|a_n|^2 + |b_n|^2 < 10^{-14}$. We denote by E the number of terms in these series. Analysis of the convergence behavior of these series reveals that it is only slightly influenced by refractive index and that $E \sim x$. In order to get a more

precise estimate, we followed the suggestion of Khare [171] that $E \sim x + cx^{1/3}$, where the $x^{1/3}$ term accounts for edge wave contributions. Upon generating a large amount of data on E as a function of x using a convergence criterion like Dave's [170], Wiscombe [172] found that these data could be excellently fit by:

$$E(x) = \begin{cases} x + 4x^{1/3} + 1 & \text{if} \quad 0.02 \leqslant x \leqslant 8, \\ x + 4.05x^{1/3} + 2 & \text{if} \quad 8 < x \leqslant 4200, \\ x + 4x^{1/3} + 2 & \text{if} \quad 4200 < x \leqslant 20000, \end{cases} \tag{3.25}$$

where E is the truncation function of the size parameter $x = 2\pi r/\lambda$.
The extinction efficiency Q_{ext} and the absorbing efficiency Q_{abs} are represented as a function of the particle radius r at the top of Figure 3.8 for different wavelengths (one in the visible $0.55\,\mu m$ and three in infrared $8, 10, 12\,\mu m$). At the bottom of Figure 3.8, we represent these functions for different particle radii as a function of wavelengths on the band $[350\,nm, 2500\,nm]$. The coefficient Q_{ext} is dimensionless and depends on the droplet size and the wavelength varies between 0 and 4 and stabilizes around 2 for drops with a radius of a few microns.

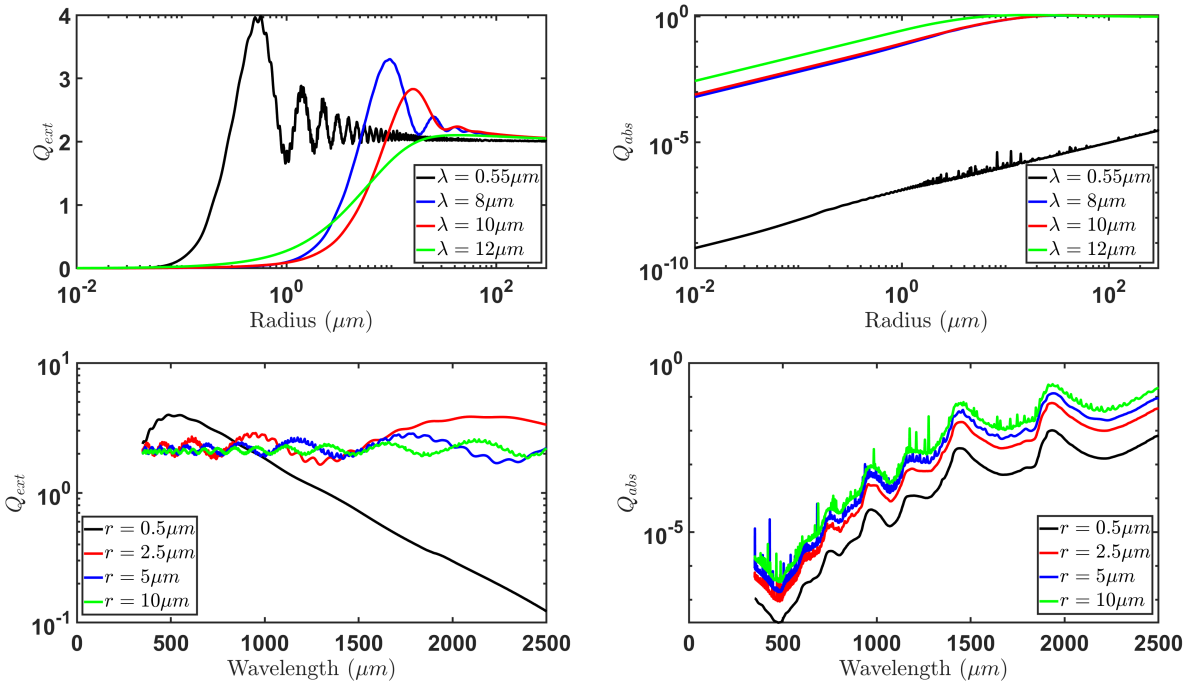

Figure 3.8: Extinction efficiency (top left) and absorption efficiency (top right) for four wavelengths (one in the visible and three in the thermal infrared), as a function of the radius of the sphere. Extinction efficiency (bottom left) and absorption efficiency (bottom right) for four particle radii as a function of the wavelength in the band 350-2500 μm.

Also, ψ_λ, is the Lorenz-Mie phase function for a particle of radius r as presented in Figure 3.9 where $\mu = \cos\theta$.

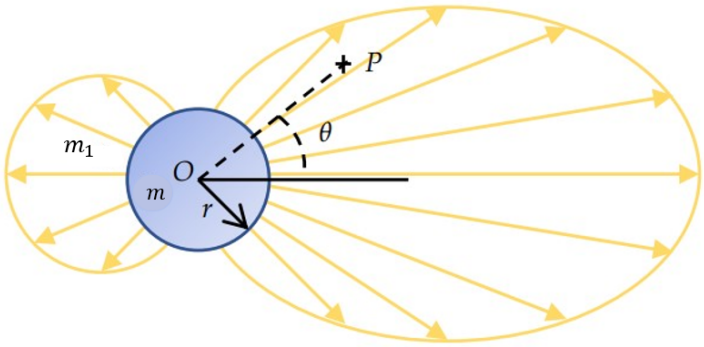

Figure 3.9: Representation of the Lorenz-Mie scattering phase function ψ_λ.

This function is given by

$$\psi_\lambda(r,\mu) = \frac{\lambda^2}{2\,\pi^2\,r^2\,Q^\lambda_{sca}(r)}\left(|S_1(\mu)|^2 + |S_2(\mu)|^2\right). \tag{3.26}$$

We present in Figure 3.10 the Lorenz-Mie scattering phase functions for various particle radii (0.5, 2.5, 5, 10 μm) and different wavelengths (0.55, 8, 12 μm). For the particle of radius, $r = 0.55\mu m$, we do not observe a variation of the ψ_λ as a function of the scattering angle for wavelengths in the infrared (8, 12 μm), which is not the case where the particle radius increases.

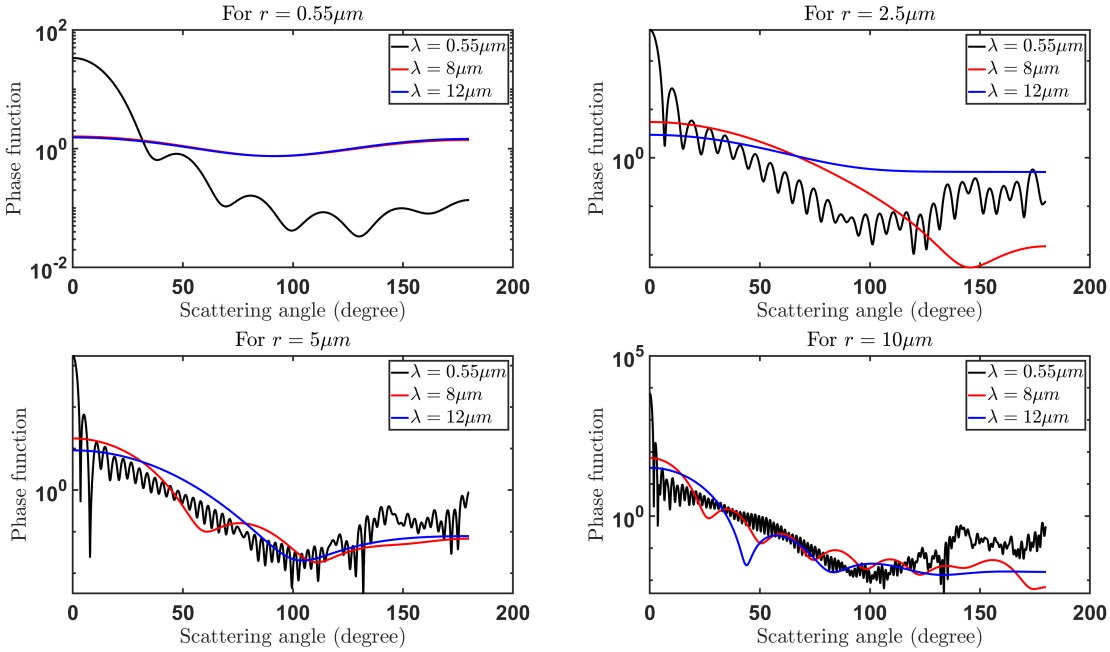

Figure 3.10: Lorenz-Mie scattering phase functions for various particle sizes and for different wavelengths.

In addition, for the visible wavelength 0.55 μm, we notice that as the particle size increases, this function exhibits oscillations with respect to the scattering angle. Finally, all of the curves in Figure 3.10 take into account the change in the complex refractive index of water as a function of wavelength.

3.5 Existence and uniqueness of solution for the transport equation

In this section, we analyze the time-dependent transport equation from a mathematical perspective. We recall that the most known existence and uniqueness results of this equation are obtained by Case-Zweifel [115] in 1967, Dautray-Lions [173], and other authors [174, 175, 176]. We present in this section the existence and uniqueness of solutions for two different types of boundary conditions which are homogeneous and nonhomogeneous boundary conditions. We have other types of boundary conditions such as the specular reflection condition, diffuse reflection condition, rotation condition, and translation condition (See Duderstadt-Martin [177] and Bell-Glasstone [178] for more information on these types of boundary conditions).
Before starting to present the results of the existence and uniqueness of the solution for the RTE equation, we introduce some notations used in this section. Let X an open domain in $\mathbb{R}^3$ where its boundary is denoted by ∂X, and $V \in \mathbb{S}^2$ where $\mathbb{S}^2$ is the unit sphere. We define the following sets:

$$\begin{cases} \Gamma = \partial X \times V, \\ \Gamma_0 = \{(x,v) \in \Gamma, \vec{v} \cdot \vec{n} = 0\}, \\ \Gamma_- = \{(x,v) \in \Gamma, \vec{v} \cdot \vec{n} < 0\}, \\ \Gamma_+ = \{(x,v) \in \Gamma, \vec{v} \cdot \vec{n} > 0\}. \end{cases} \tag{3.27}$$

Γ_- and Γ_+ presented in (3.27) represent the set of points in phase space corresponding to incoming and outgoing particles, respectively. We denote by n the unit normal vector at the point $x \in \partial X$ pointing outside X.
We also define the following Hilbert space:

$$\forall 1 \leqslant p < +\infty,\ W^p \equiv W^p(X \times V) := \{u \in L^p(X,V); v \cdot \nabla u \in L^p(X,V)\}.$$

3.5.1 Time-dependent case

We are interested in this part in the solution of the solution to time-dependent transport equation given by the following form:

$$\begin{cases} \dfrac{\partial u}{\partial t}(t,x,v) + v\cdot\nabla_x u(t,x,v) + a(x,v)u(t,x,v) = \displaystyle\int_V u(t,x,v')\,k(x,v,v')\,dv' \\ \qquad\qquad + q(t,x,v),\ \text{in}\ ]0,T[\times X\times V, \\ u(t,.,.)_{|\Gamma_-} = 0,\ t\in]0,T[, \\ u(0,x,v) = u_0,\ \text{on}\ X\times V. \end{cases} \tag{3.28}$$

We recall in Theorem 3.1 the existence and uniqueness obtained by Dautray-Lions [173, ChapterXXI, paragraph 2].

Theorem 3.1. *[173, ChapterXXI]*
Suppose that the data of problem (3.28) satisfy:

1. *k is a positive function satisfying*

$$\begin{cases} \displaystyle\int_V k(r,v',v)\,dv \leqslant M_1,\ \forall\,(x,v')\in X\times V, \\ \displaystyle\int_V k(r,v,v')\,dv' \leqslant M_2,\ \forall\,(x,v)\in X\times V, \end{cases} \tag{3.29}$$

   where M_1 and M_2 are two constant positives;

2. *$a\in L^\infty(X\times V)$,*

3. *$q\in L^p(]0,T[\times X\times V)$, $p\in[1,+\infty[$,*

4. *$u_0\in L^p(X\times V)$, $p\in[1,+\infty[$.*

Then, problem (3.28) *has a unique weak solution u in*

$$\mathcal{W}^p := \{u\in L^p(]0,T[\times X\times V);\ \frac{\partial u}{\partial t} + v\cdot\nabla u\in L^p(]0,T[\times X\times V);\ u(.,.,0)\in L^p(X\times V);\ u_{|\Gamma_-}\in L^p(]0,T[\times\Gamma_-)\}.$$

In addition, if u_0 verifies

$$v\cdot\nabla u_0\in L^p(X\times V),\ u_{0|\Gamma_-} = 0,$$

and $q\in C^1([0,T];L^p(X\times V))$, Then u is a strong solution of problem (3.28) *which satisfies, $\forall\,t\in[0,T]$,*

$$u\in C^1([0,T];L^p(X\times V)),\ v\cdot\nabla u\in C^1([0,T];L^p(X\times V)), u(t,.,.)_{|\Gamma_-} = 0.$$

Proof. The Theorem and its proof are presented in a more general form notably [173, ChapterXXI, paragraph 2]. □

3.5.2 Time-independent case

Homogeneous boundary condition: We are interested in this part in the solution of the time-independent transport equation where the source term q does not depend on the time t given by the following form:

$$\begin{cases} v \cdot \nabla_x u(x,v) + a(x,v)u(x,v) = \displaystyle\int_V u(x,v')\, k(x,v,v')\, d\mu(v') + q(x,v), \text{ in } X \times V, \\ u_{|\Gamma_-} = 0. \end{cases} \tag{3.30}$$

Theorem 3.2. *[173] Suppose that the data of problem* (3.30) *satisfies:*

1. *Assume that there exist two positive constants M_1 and M_2, such that the positive function k satisfies*

$$\begin{cases} \displaystyle\int_{\mathcal{V}} k(r,v',v)\, dv \leqslant M_1, \forall\, (x,v') \in X \times V, \\ \displaystyle\int_{\mathcal{V}} k(r,v,v')\, dv' \leqslant M_2, \forall\, (x,v) \in X \times V. \end{cases} \tag{3.31}$$

2. *For $\alpha > 0$, a and k satisfy (a.e in $X \times V$)*

$$\begin{cases} a(x,v) - \displaystyle\int_V k(x,v',v)\, dv' \geqslant \alpha, \\ a(x,v) - \displaystyle\int_V k(x,v,v')\, dv' \geqslant \alpha. \end{cases} \tag{3.32}$$

3. *$a \in L^\infty(X \times V)$.*

4. *$q \in L^p(X \times V)$, $p \in [1, +\infty[$.*

Then, for any $p \in [1, +\infty[$, problem (3.30) *has a unique solution u in W^p such that $u = 0$ on Γ_-.*

Nonhomogeneous boundary condition: The time-independent transport equation with a nonhomogeneous boundary condition is given by the following system:

$$\begin{cases} v \cdot \nabla_x u(x,v) + a(x,v)u(x,v) = \displaystyle\int_V u(x,v')\, k(x,v,v')\, d\mu(v') + q(x,v), \forall\, (x,v) \in X \times V, \\ u_{|\Gamma_-} = g. \end{cases} \tag{3.33}$$

Proposition 3.1. *[173] Suppose that the data of problem* (3.33) *satisfy:*

1. *a and k satisfy a.e in $X \times V$*
$$\alpha\, a(x,v) \geqslant \int_V k(x,v',v)\, dv \quad \textit{where} \quad 0 \leqslant \alpha < 1,$$
2. $a(x,v) \geqslant a_0 > 0$,
3. $\forall\, p \in [1, +\infty[,\ q \in L^p(X \times V)$,
4. $g \in L^\infty(\Gamma_-)$.

Then, the problem (3.33) *has a unique solution u in $L^\infty(X \times V)$ which verifies the following estimation:*
$$\|u\|_{L^\infty(X\times V)} \leqslant C(\|q\|_{L^\infty(X\times V)}, \|g\|_{L^\infty(\Gamma_-)}),$$
where C is a positive constant.

3.6 Integral formulation of the transport equation

In this section, we are interested in the computation of the integral formulation of transport equations in both time-dependent and time-independent cases. Several authors have worked on these types of formulations, such as Dautray-Lions [173], and G.Allaire [176]. We present in this part the integral formulation obtained by G.Allaire [176].
In this section, we suppose also that a and k depend on time t and the following assumptions are made:
$$\begin{cases} 0 \leqslant a \in C_b(\mathbb{R}^+ \times X \times \mathbb{R}^n), \\ \\ 0 \leqslant k \in C_b(\mathbb{R}^+ \times X \times \mathbb{R}^n \times \mathbb{R}^n), \\ \sup\limits_{(t,x,v)\in\mathbb{R}^+\times X\times\mathbb{R}^n} \displaystyle\int_{\mathbb{R}^n} k(t,x,v,v')\, dv' < \infty. \end{cases} \tag{3.34}$$
We denote by $\tau_{x,v}$ the exit time of X in the direction $-v$ starting from $x \in X$. $\tau_{x,v}$ is given as follows
$$\tau_{x,v} = inf\{\, t \geqslant 0 \,/\, x - tv \notin \bar{X}\}.$$

3.6.1 Integral formulation for time-dependent case

We are interested in this part in the integral formulation of the time-dependent transport equation given by the following form:
$$\begin{cases} \frac{\partial u}{\partial t}(t,x,v) + v \cdot \nabla_x u(t,x,v) + a(t,x,v)u(t,x,v) = \displaystyle\int_V u(t,x,v')\, k(x,v,v')\, dv' \\ \qquad\qquad + q(t,x,v), \text{ in }]0,T[\times X \times V, \\ u(t,.,.)_{|\Gamma_-} = g,\ t \in]0,T[, \\ u(0,x,v) = u_0, \text{ on} \quad \Gamma_-. \end{cases} \tag{3.35}$$

Definition 1. *Let $q \equiv q(t,x,v)$ be a continuous function on $]0,T[\times\Omega\times\mathbb{R}^n$. A function $u \equiv u(t,x,v)$ that is continuous on $]0,T[\times\Omega\times\mathbb{R}^n$ is a generalized solution of the time-dependent transport equation (3.35) if and only if, for all $(t,x,v)\in]0,T[\times\Omega\times\mathbb{R}^n$, the function*

$$s \mapsto u(t+s, x+sv, v)$$

is of class C^1 for $x+sv\in\Omega$, and it satisfies, for all $s\in\mathbb{R}$ such that $x+sv\in\Omega$,

$$\frac{d}{ds}u(t+s,x+sv,v) + a(t+s,x+sv,v)u(t+s,x+sv,v) = (\mathcal{K}u+q)(t+s,x+sv,v),$$

where

$$\mathcal{K}u(t,x,v) = \int_V u(t,x,v')\,k(t,x,v,v')\,dv'.$$

We have the following results:

Theorem 3.3. *Suppose that $u_0 \in C_b(\bar{X}\times\mathbb{R}^n)$ and $g\in C_b([0,T]\times\Gamma_-)$ such that*

$$\forall\,(x,v)\in\Gamma_-,\quad g(0,x,v) = u_0(x,v),$$

and $q\in C_b([0,T]\times\bar{X}\times\mathbb{R}^n)$. Then, problem (3.35) admits a unique generalized solution $u\in C_b([0,T]\times X\times\mathbb{R}^n)$. In addition, for all $(t,x,v)\in\mathbb{R}^+\times X\times\mathbb{R}^n$, the integral formulation verified by the solution u is given by:

$$\begin{aligned} u(t,x,v) = {} & \mathbb{1}_{t\leqslant\tau_{x,v}}\,u_0(x-tv,v)\,\exp\left(-\int_0^t a(s,(x+(s-t)v,v)\,ds\right) \\ & + \mathbb{1}_{t>\tau_{x,v}}\,g(t-\tau_{x,v}v, x-\tau_{x,v}x, v)\,\exp\left(-\int_{t-\tau_{x,v}}^t a(s,(x+(s-t)v,v)\,ds\right) \\ & + \int_{\max(t-\tau_{x,v},0)}^t \exp\left(-\int_s^t a(\theta,x+(\theta-t)v,v)\,d\theta\right)\times(\mathcal{K}u+q)(s,x+(s-t)v,v)\,ds, \end{aligned} \tag{3.36}$$

where

$$\mathcal{K}u(t,x,v) = \int_V k(t,x,v,v')\,u(t,x,v')\,dv'.$$

Theorem 3.4. *Under the same hypotheses of the previous theorem, suppose that u is the unique generalized solution of (3.35). Then*

- *If $u_0\geqslant 0$ on $\bar{X}$, $g\geqslant 0$ on $[0,T]\times\Gamma_-$, and $Q\geqslant 0$ on $[0,T]\times\bar{X}\times\mathbb{R}^N$, then $u\geqslant 0$ on $[0,T]\times X\times\mathbb{R}^n$;*
- *In addition, $\forall\,(t,x,v)\in[0,T]\times\bar{X}\times\mathbb{R}^n$,*

$$u(t,x,v) \leqslant \max\left(\|u_0\|_{L^\infty(X\times\mathbb{R}^n)}, \|g\|_{L^\infty([0,T]\times\Gamma_-)}\right)e^{Dt} + T\|q\|_{L^\infty([0,T]\times X\times\mathbb{R}^n)}e^{Dt},$$

where

$$D = \sup_{(t,x,v)\in\mathbb{R}^+\times X\times\mathbb{R}^n} \max\left(\int_{\mathbb{R}^n} k(t,x,v,v')\,dv' - a(t,x,v),\quad 0\right).$$

The proofs of these theorems can be found in [176, Chapter 3].

3.6.2 Solution of time-independent transport equation

According to the results presented in the previous part, we give in this part the existence and uniqueness of the time-independent case and a L^∞-estimate obtained from the L^∞-estimate of the time-dependent case by using the Laplace transform.
The time-independent transport equation with a nonhomogeneous boundary condition is given by the following system:

$$\begin{cases} (\lambda + v\cdot\nabla_x + a(x,v))\,\tilde{u}(x,v) = \mathcal{K}\tilde{u}(x,v) + q(x,v), \quad (x,v)\in X\times\mathbb{R}^n, \\ \tilde{u}_{|\Gamma_-} = g, \end{cases} \tag{3.37}$$

where

$$\mathcal{K}\tilde{u}(x,v) = \int_{\mathbb{R}^n} k(x,v,v')\tilde{u}(x,v')dv'.$$

Theorem 3.5. *[176, Chapter 3, Section 4]*
Let

$$D = \left\|\max(\mathcal{K}1 - a, 0)\right\|_{L^\infty(X\times\mathbb{R}^n)}.$$

For all $\lambda > D$, Problem (3.37) *admits a unique solution which verifies:*

$$\|\tilde{u}\|_{L^\infty(X\times\mathbb{R}^n)} \leqslant \frac{1}{\lambda - D}\max\left(\|q\|_{L^\infty(X\times\mathbb{R}^n)}, \lambda\,\|g\|_{L^\infty(\Gamma_-)}\right).$$

Proof. The problem expressed in system (3.37) can be derived from the time-dependent problem by using the Laplace transform:

$$\tilde{u}(x,v) = \int_0^{+\infty} e^{-\lambda t}u(t,x,v)\,dt,$$

where

$$\begin{cases} \left(\dfrac{\partial}{\partial t} + v\cdot\nabla_x + a(x,v)\right)u(t,x,v) = \mathcal{K}u(t,x,v), \quad (t,x,v)\in\mathbb{R}_+\times X\times\mathbb{R}^n, \\ u_{\Gamma_-} = \lambda g, \\ u_{|t=0} = q, \end{cases}$$

By Theorem 3.4, this time-dependent problem admits a solution u and verifies a L^∞-estimate. Then, we obtain the existence and uniqueness of the solution $\tilde{u}$ of the problem (3.37). □

As presented in this chapter, we discuss the Lorenz-Mie scattering theory that explains how electromagnetic waves interact with small particles. We also give the expression of optical properties according to the size distributions of the fog droplets. The existence and uniqueness of the radiative transfer equation was presented with the different estimates existing in the literature. In the following sections of the manuscript, our focus is directed towards the examination of the existence and uniqueness of the solution as provided by the referenced Theorem 3.5.

Chapter 4

One-dimensional stationary radiative transfer equation

This chapter is organized as follows. Section 4.1 presents a general introduction to the one-dimensional stationary radiative transfer equation and its computation from the 3D radiative transfer equation. Then, in section 4.2 we review the existence and uniqueness of the solution of this equation. We provide exact solutions in some cases for the stationary radiative transfer equation in section 4.3. These cases are used in the sequel to check our numerical approximations. Section 4.4 presents different methods used by several authors to approximate the radiative transfer equation. We study in section 4.5 the numerical approximations presented in Section 4.4 with an analysis of their convergence on the explicit cases given in Section 4.3.

4.1 General introduction

Slab modeling of radiative transfer refers to a simplified approach used in the field of atmospheric and environmental science to analyze the interaction of radiation with a medium (such as the Earth's atmosphere) that can be approximated as a plane-parallel slab. This approach can be particularly useful when dealing with scenarios where the medium's properties vary mainly in one direction (usually vertically) and do not change significantly in the other directions. The basic concept involves dividing the medium into thin horizontal layers or slabs, assuming that the radiative properties (like absorption, scattering, and emission) within each layer are uniform. Each layer is then treated as an individual unit, and the interactions of radiation with these layers are calculated and modeled.
In the "slab modelling", the dependence of the intensity is w.r.t x only (x is the spatial position), and not on y and z, denoted as $r = (x, y, z)$. In order, for this modeling, to be compatible with (2.5), it is sufficient to provide boundary conditions that satisfy the assumption of independence with respect to y and z. Considering the spatial domain of study (where the light source is positioned at $x = 0$):

$$X = \left\{ r = (x, y, z) \in \mathbb{R}^3, x \geqslant 0 \right\},$$

with the variables (x, θ, φ), the time-independent radiative transfer equation can be written, for a given wavelength λ, as:

$$\cos(\theta)\frac{\partial \bar{I}_\lambda}{\partial x}(x,\theta,\varphi) = -\sigma^\lambda_{ext}(N)\bar{I}_\lambda(x,\theta,\varphi) + \frac{\sigma^\lambda_{sca}(N)}{4\pi}\int_{\theta'=0}^{\pi}\int_{\varphi'=0}^{2\pi}\bar{I}_\lambda\left(x,\theta',\varphi'\right)\phi_\lambda\left(\cos\theta\cos\theta' + \sin\theta\sin\theta'\cos\left(\varphi-\varphi', N\right)\right)\sin\theta' d\varphi' d\theta'. \tag{4.1}$$

In this work, we will focus on an intensity average over the angles φ, defined as:

$$\forall x \geqslant 0, \forall 0 \leqslant \theta \leqslant \pi, I_\lambda(x,\theta) = \frac{1}{2\pi}\int_0^{2\pi}\bar{I}_\lambda(x,\theta,\varphi)d\varphi. \tag{4.2}$$

Then, we obtain:

$$\cos(\theta)\frac{\partial I_\lambda}{\partial x}(x,\theta) + \sigma^\lambda_{ext}(N)I_\lambda(x,\theta) = \frac{\sigma^\lambda_{sca}(N)}{4\pi}\frac{1}{2\pi}\int_0^{\pi}\int_0^{2\pi} I_\lambda(x,\theta') \times\left(\int_0^{2\pi}\phi_\lambda\left(\cos\theta\cos\theta' + \sin\theta\sin\theta'\cos\left(\varphi-\varphi'\right), N\right)d\varphi\right)\sin\theta' d\varphi' d\theta'. \tag{4.3}$$

Due to the 2π-periodicity of the cosine function and denoted by $w = \varphi - \varphi'$ we have:

$$\int_0^{2\pi}\phi_\lambda\left(\cos\theta\cos\theta' + \sin\theta\sin\theta'\cos\left(\varphi-\varphi'\right), N\right)d\varphi = \int_0^{2\pi}\phi_\lambda\left(\cos\theta\cos\theta' + \sin\theta\sin\theta'\cos(w), N\right)dw. \tag{4.4}$$

Then,

$$\cos(\theta)\frac{\partial I_\lambda}{\partial x}(x,\theta) + \sigma^\lambda_{ext}(N)I_\lambda(x,\theta) = \frac{\sigma^\lambda_{sca}}{2}\int_0^{\pi} I_\lambda\left(x,\theta'\right)\left(\frac{1}{2\pi}\int_0^{2\pi}\phi_\lambda\left(\cos\theta\cos\theta' + \sin\theta\sin\theta'\cos(w), N\right)dw\right)\sin\theta' d\theta'. \tag{4.5}$$

By introducing the variable $\mu = \cos\theta \in [-1,1]$, with $d\mu = -\sin\theta d\theta$, the previous equation can be rewritten as:

$$\mu\frac{\partial I_\lambda}{\partial x}(x,\mu) + \sigma^\lambda_{ext}(N)I_\lambda(x,\mu) = \frac{\sigma^\lambda_{sca}(N)}{2}\int_{-1}^{1} I_\lambda\left(x,\mu'\right)\Phi_\lambda\left(\mu,\mu',N\right)d\mu', \tag{4.6}$$

where:

$$\Phi_\lambda\left(\mu,\mu',N\right) = \frac{1}{2\pi}\int_0^{2\pi}\phi_\lambda\left(\mu\mu' + \sqrt{1-\mu^2}\sqrt{1-\mu'^2}\cos(w), N\right)dw. \tag{4.7}$$

Then, we have the following equation for a wavelength λ:

$$\mu\frac{\partial I_\lambda}{\partial x}(x,\mu) + \sigma^\lambda_{ext}(N)I_\lambda(x,\mu) = \mathcal{K}I_\lambda(x,\mu,N),\ (x,\mu) \in [0,+\infty)\times[-1,1], \tag{4.8}$$

with the following boundary conditions:

$$I(0,\mu) = I^+(\mu) \quad \text{for} \quad \mu > 0 \quad ; \quad \lim_{x\to+\infty} I(x,\mu) = 0 \quad \text{for} \quad \mu < 0, \tag{4.9}$$

where $\mu = \cos(\theta)$ denotes the cosine of the propagation angle, $N \in L^2(\mathbb{R}^+)$ is the droplet size distribution, and

$$\begin{cases} \sigma^\lambda_{ext}(N) = \sigma^\lambda_{abs}(N) + \sigma^\lambda_{sca}(N), \\ \mathcal{K}I_\lambda(x,\mu,N) = \dfrac{\sigma^\lambda_{sca}(N)}{2} \displaystyle\int_{-1}^{1} \Phi_\lambda(\mu,\mu',N)\, I_\lambda(x,\mu')\, d\mu', \\ \forall\, (\mu,\mu') \in [-1,1]^2,\ \Phi_\lambda(\mu\cdot\mu',N) \equiv \Phi_\lambda(\mu,\mu',N) = \dfrac{1}{2\pi}\displaystyle\int_0^{2\pi} \phi_\lambda(\mu\cdot\mu',N)\, d\omega, \\ \text{where, } \forall\omega \in [0,2\pi],\ \mu\cdot\mu' = \mu\mu' + \sqrt{1-\mu^2}\sqrt{1-\mu'^2}\cos(\omega) \end{cases} \tag{4.10}$$

The condition (3.7) in one-dimensional space becomes

$$\forall\, \mu \in [-1,1], \quad \frac{1}{2}\int_{-1}^{1} \Phi_\lambda(\mu,\mu',N)\, d\mu' = 1.$$

4.2 Existence and uniqueness of solutions of the 1D stationary radiative transfer equation

In this section, we review the existence and uniqueness of the solution of stationary radiative transfer equation obtained by Case-Zweifel [115]. We introduce the following radiative transfer equation:

$$\mu\,\frac{\partial I}{\partial x}(x,\mu) + I(x,\mu) = c\int_{-1}^{1} \Phi(\mu\cdot\mu',N)\, I(x,\mu')\, d\mu', \tag{4.11}$$

We consider a region where a is constant and look for solutions of the homogeneous equation there. These solutions will depend only on local properties. The idea is to construct special solutions appropriate to various boundary conditions in terms of superposition of the elementary solutions. We note that this problem is equivalent to problem (4.8) by applied $a = \sigma_{sca}(N)/\sigma_{ext}(N)$ and the change of variable $\tilde{x} = \sigma_{ext}(N)\, x$. Suppose that the phase function can be decomposed as follow:

$$\Phi(\mu\cdot\mu',N) = \sum_{k=0}^{K} \frac{2k+1}{4\pi}\Phi_k(N)P_k(\mu\cdot\mu'), \tag{4.12}$$

where P_k represents the Legendre polynomials defined for all $\mu \in [-1,1]$ by the following recurrence (see [168]):

$$\begin{cases} P_0(\mu) = 1 \quad , \quad P_1(\mu) = \mu, \\ \forall\, k \geqslant 1,\ P_{k+1}(\mu) = \dfrac{(2k+1)}{(k+1)}\,\mu\, P_k(\mu) - \dfrac{k}{(k+1)}\, P_{k-1}(\mu). \end{cases} \tag{4.13}$$

By combining the equation (4.12) in (4.11) and by using the addition theorem for spherical harmonics (See Appendix A in [115]), we obtain the following equation:

$$\mu \frac{\partial I}{\partial x}(x,\mu) + I(x,\mu) = \frac{c}{2}\sum_{k=0}^{K}(2k+1)\Phi_k(N)P_k(\mu)\int_{-1}^{1} P_k(\mu')\, I(x,\mu')\, d\mu'. \tag{4.14}$$

Translational invariance suggests trying (See Appendix F in [115]):

$$I(x,\mu) = e^{-x/\nu}\,\zeta_\nu(\mu).$$

In analogy with ordinary terminology, the authors call that ζ_ν by the "eigenfunctions" and the corresponding ν "eigenvalues" of the radiative transfer equation. Then using (4.14), we get the following equation which verifies ζ_ν:

$$(\nu-\mu)\zeta_\nu(\mu) = \frac{c\nu}{2}\sum_{k=0}^{K}(2k+1)\Phi_k(N)P_k(\mu)\int_{-1}^{1}\zeta_\nu(\mu')P_k(\mu')\, d\mu'. \tag{4.15}$$

Our goal now is to find a solution to the equation represented by (4.15). To do this, we multiply the equation by the Legendre polynomial P_l and we integrate over [-1,1]. Equation becomes (4.15):

$$\int_{-1}^{1}(\nu-\mu)\zeta_\nu(\mu)P_l(\mu)d\mu = \int_{-1}^{1}\frac{c\nu}{2}\sum_{k=0}^{K}(2k+1)\Phi_k(N)P_k(\mu)P_l(\mu)\left(\int_{-1}^{1}\zeta_\nu(\mu')P_k(\mu')\, d\mu'\right)d\mu. \tag{4.16}$$

We make the following notation:

$$\zeta_{\nu,k} = \int_{-1}^{1}\zeta_\nu(\mu)\, P_k(\mu)d\mu, \tag{4.17}$$

and we note the following relations:

$$\begin{cases} \displaystyle\int_{-1}^{1} P_k(\mu)\, P_l(\mu)\, d\mu = \frac{2}{2l+1}\delta_{lk}, \\ \mu\, P_l(\mu) = \dfrac{1}{2l+1}[(l+1)P_{l+1}(\mu) + lP_{l-1}(\mu)], \end{cases} \tag{4.18}$$

where δ_{lk} represents the Kronecker delta. Consequently, we derive the following relationships:

$$\begin{cases} \nu(1-c\,\Phi_k(N))\zeta_{\nu,k} - \dfrac{k+1}{2k+1}\,\zeta_{\nu,k+1} - \dfrac{k}{2k+1}\,\zeta_{\nu,k-1} = 0, \\ \zeta_{\nu,0} = 1, \\ \zeta_{\nu,1} = \nu(1-c), \\ \zeta_{\nu,2} = \dfrac{3\nu^3}{2}(1-c\nu_1)(1-c) - \dfrac{1}{2}. \end{cases} \tag{4.19}$$

Now, by using equation (4.15) and (4.17), we obtain:

$$(\nu-\mu)\zeta_\nu(\mu) = \frac{c\nu}{2}\sum_{k=0}^{K}(2k+1)\Phi_k(N)P_k(\mu)\,\zeta_{\nu,k} \tag{4.20}$$

By injecting (4.19) in (4.20), the solution of (4.15) is given by:

$$\begin{cases} \zeta_\nu(\mu) = \dfrac{c\nu}{2}\, PV\, \dfrac{\displaystyle\sum_{k=0}^{K}(2k+1)\Phi_k(N)\,\zeta_{\nu,k}\,P_k(\mu)}{\nu-\mu} + \lambda(\nu)\,\delta(\nu-\mu) \quad \text{if} \quad \nu \in [-1,1], \\ \zeta_\nu(\mu) = \dfrac{c\nu}{2}\, PV\, \dfrac{\displaystyle\sum_{k=0}^{K}(2k+1)\Phi_k(N)\,\zeta_{\nu,k}\,P_k(\mu)}{\nu-\mu} \quad \text{else}, \end{cases} \tag{4.21}$$

subject to the normalization condition

$$\int_{-1}^{1} \zeta_\nu(\mu) d\mu = 1.$$

PV in (4.21) indicates that principal values is to be understood when integrating an expression involving ζ_ν.
$\lambda(\nu)$ defined in (4.21) can always be chosen such that the equation (4.22) is satisfied

$$\lambda(\nu) = 1 - \frac{c\nu}{2}\sum_{k=0}^{K}(2k+1)\Phi_k(N)\zeta_{\nu,k}\int_{-1}^{1}\frac{P_k(\mu)}{\nu-\mu}\,d\mu'. \tag{4.22}$$

This equation is obtained by using the normalization condition.
According to these results of Case-Zweifel [115], the problem (4.8)-(4.9) has a unique solution which decreases exponentially towards 0 as x tends to infinity. In the sequel, we restrict the space domain to $[0, D]$, as shown in Figure 4.1, and the radiative transfer equation (4.8) posed in $[0, D]$ is given by the following problem [179, 176]:

$$\begin{cases} \mu\dfrac{\partial I_\lambda}{\partial x}(x,\mu) + \sigma_{ext}^{\lambda}(N) I_\lambda(x,\mu) = (\mathcal{K}I_\lambda)(x,\mu,N) + q_\lambda(x,\mu),\ (x,\mu) \in X, \\ I_\lambda(0,\mu) = I_\lambda^+(\mu) \quad \text{for} \quad \mu > 0 \quad \text{and} \quad I_\lambda(D,\mu) = I_\lambda^-(\mu) \quad \text{for} \quad \mu < 0, \end{cases} \tag{4.23}$$

where $X = [0, D] \times ([-1, 0) \cup (0, 1])$. I_λ^- is the spectral radiance value at $x = D$ which is small if D is large enough. For the numerical applications, we will use $I_\lambda^- = 0$.

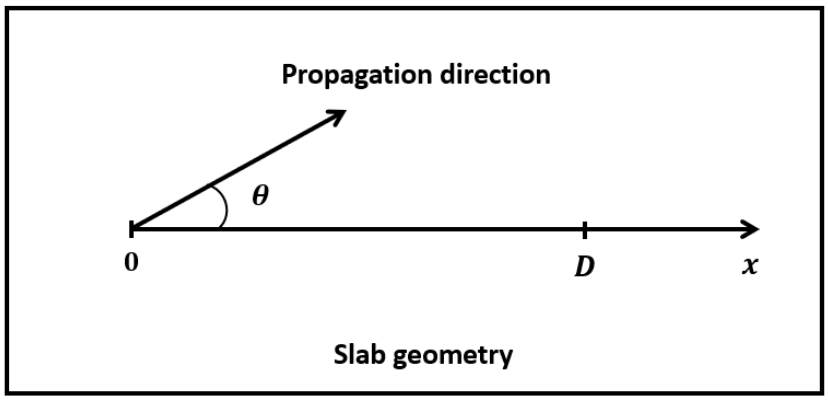

Figure 4.1: The geometry of the 1D slab for the investigated radiative transfer problem.

Theorem 4.1. *[176] Assume* $\sigma_{abs}^{\lambda}(N) > 0$ *and suppose that* $\frac{\sigma_{sca}^{\lambda}(N)}{2}\,\Phi_{\lambda} \in C_b(([-1,0)\cup(0,1])^2 \times \mathbb{R}^+)$ *and*

$$q_{\lambda} \in L^{\infty}(X) \quad , \quad I_{\lambda}^{+} \in L^{\infty}((0,1]), I_{\lambda}^{-} \in L^{\infty}([-1,0)),$$

where C_b *is the space of bounded continuous functions. The problem (4.23) has a unique solution in* $C_b(X)$ *which satisfies the following estimate*

$$\|I_{\lambda}\|_{L^{\infty}(X)} \leqslant \max\left(\|I_{\lambda}^{-}\|_{L^{\infty}([-1,0))}, \|I_{\lambda}^{+}\|_{L^{\infty}((0,1])}, \frac{1}{\sigma_{abs}^{\lambda}(N)}\|q_{\lambda}\|_{L^{\infty}(X)}\right). \tag{4.24}$$

4.3 Some explicit solutions of the 1D radiative transfer equation

In some cases, we provide exact solutions for the stationary radiative transfer equation used in the sequel to check our numerical approximations.

4.3.1 Case without collision operator ($\mathcal{K}L_{\lambda} \equiv 0$) and $q_{\lambda} \equiv 0$

We are interested in the following system, with $\sigma_{ext}^{\lambda}(N) > 0$:

$$\begin{cases} \mu\dfrac{\partial L_{\lambda}}{\partial x}(x,\mu) + \sigma_{ext}^{\lambda}(N) I_{\lambda}(x,\mu) = 0,\ (x,\mu) \in X, \\ I_{\lambda}(0,\mu) = I_{\lambda}^{+}(\mu),\ \mu > 0 \quad \text{and} \quad L_{\lambda}(D,\mu) = 0, \mu < 0. \end{cases} \tag{4.25}$$

It is easy to show the solution of (4.25) is:

$$I_{\lambda}(x,\mu) = I_{\lambda}^{+}(\mu)\, e^{-\sigma_{ext}^{\lambda}(N)\frac{x}{\mu}} \mathbb{1}_{\mu>0}. \tag{4.26}$$

4.3.2 Case without collision operator ($\mathcal{K}L_{\lambda} \equiv 0$) with a source expressed by a Dirac function

We are interested in the following system, with $\sigma_{ext}^{\lambda}(N) > 0$ and $0 < d < D$ real numbers:

$$\begin{cases} \mu\dfrac{\partial I_{\lambda}}{\partial x}(x,\mu) + \sigma_{ext}^{\lambda}(N) I_{\lambda}(x,\mu) = f(\mu)\delta_d(x),\ (x,\mu) \in X \\ I_{\lambda}(0,\mu) = 0,\ \mu > 0 \quad \text{and} \quad I_{\lambda}(D,\mu) = 0,\ \mu < 0. \end{cases} \tag{4.27}$$

The solution of (4.27) is :

$$I_{\lambda}(x,\mu) = \frac{f(\mu)}{|\mu|} e^{-\sigma_{ext}^{\lambda}(N)\frac{(x-d)}{\mu}} \mathbb{1}_{(x-d)\mu>0}. \tag{4.28}$$

Proof of Equation (4.28). We multiply the first equation in (4.27) by $\exp(\sigma_{ext}^{\lambda}(N)x/\mu)$ to obtain:

$$\frac{\partial}{\partial x}\left(\exp(\sigma_{ext}^{\lambda}(N)x/\mu)I_\lambda\right) = \frac{f(\mu)}{\mu}\exp(\sigma_{ext}^{\lambda}(N)d/\mu)\delta_d(x),$$

which leads to the existence of a constant $k(\mu)$ such that:

$$I_\lambda(x,\mu) = \exp(-\sigma_{ext}^{\lambda}(N)(x-d)/\mu)\left(\frac{f(\mu)}{\mu}H_d(x) + K(\mu)\right),$$

where $H_d(x) = \mathbb{1}_{x\geqslant d}$ denotes the Heaviside function at d, the primitive of δ_d. If $x > d$, $H_d(x) = 1$, and therefore:

$$\forall\, \mu < 0,\ I_\lambda(D,\mu) = \exp(-\sigma_{ext}^{\lambda}(N)(D-d)/\mu)\left(\frac{f(\mu)}{\mu} + K(\mu)\right) = 0,$$

which implies:

$$\forall\, \mu < 0,\ K(\mu) = -\frac{f(\mu)}{\mu}.$$

If $x < d$, $H_d(x) = 0$, and therefore:

$$\forall\, \mu > 0,\ I_\lambda(0,\mu) = \exp(-\sigma_{ext}^{\lambda}(N)(-d)/\mu)K(\mu) = 0,$$

which implies:

$$\forall\, \mu > 0,\ K(\mu) = 0.$$

Thus, we obtain Equation (4.28).

4.3.3 Case with phase function $\Phi_\lambda \equiv 1$ and source term q_λ expressed by the Dirac function

We are interested in the problem discussed in paragraph 4 of [173] with $0 < c < 1$:

$$\begin{cases} \mu\dfrac{\partial I_\lambda}{\partial\tau}(\tau,\mu) + I_\lambda(\tau,\mu) = \dfrac{c}{2}\displaystyle\int_{-1}^{1} I_\lambda(\tau,\mu')d\mu' + \frac{1}{2}\delta(\tau),\ \tau\in\mathbb{R},\ \mu\in[-1,0)\cup(0,1], \\ I_\lambda(-\infty,\mu) = 0,\ \mu > 0 \quad ; \quad I_\lambda(+\infty,\mu) = 0,\ \mu < 0. \end{cases} \tag{4.29}$$

where $c = \dfrac{\sigma_{sca}}{\sigma_{ext}}$ is the albedo, and $\tau = \sigma_{ext}\, x$ with x is the spatial position.
The solution is expressed by applying the Fourier transform to the variable μ, and by using Cauchy's theorem of complex analysis.
The expression of $T(\tau) := \displaystyle\int_{-1}^{1} I_\lambda(\tau,\mu)\, d\mu$, according to [173] is:

$$\forall\, \tau > 0,\ T(\tau) = \frac{\xi_0}{c}\,\frac{1-\xi_0^2}{\xi_0^2+c-1}\,e^{-\xi_0\tau} + \int_1^{+\infty}\frac{e^{-t\tau}}{2t\left[\left(1-\frac{c}{2t}\log\frac{t+1}{t-1}\right)^2 + \left(\frac{c\pi}{2t}\right)^2\right]}\,dt, \tag{4.30}$$

where $0 < \xi_0 \leqslant 1$ verifies $i\xi_0 - c\,\mathrm{atan}(i\xi_0) = 0$. We give in table 4.1 some values of ξ_0 according to c.

c	0.25	0.5	0.75	0.9
ξ_0	9.993×10^{-1}	9.575×10^{-1}	$7.755\times\ 10^{-1}$	5.254×10^{-1}

Table 4.1: Approximation of ξ_0 for several values of c.

4.4 Numerical schemes to approximate the RTE.

In this section, we present some methods to approximate the radiative transfer equation. The first method is based on the finite difference method as the "Step scheme" or "Diamond scheme" [176], and the second on the decomposition in the double basis of Legendre [22]. In the sequel of this work, we use the decomposition method and we give some numerical verification in the case of explicit solution of the radiative transfer equation.

4.4.1 Finite difference method

We present here a method called 'Step scheme', which discretizes the problem by representing functions by a finite number of values. To simplify the notation, we set $I \equiv I_\lambda$.
The stationary radiative transfer equation with the boundary condition is given by the following equation:

$$\begin{cases} \mu\dfrac{\partial I}{\partial x}(x,\mu) + \sigma_{ext}(N)\, I(x,\mu) = \dfrac{\sigma_{sca}(N)}{2}\displaystyle\int_{-1}^{1} \Phi(\mu,\mu',N)\, I(x,\mu')d\mu',\ (x,\mu) \in X, \\ \\ I(0,\mu) = I^+(\mu) \qquad if \quad \mu \in (0,1], \\ \\ I(D,\mu) = I^-(\mu) \qquad if \quad \mu \in [-1,0). \end{cases} \tag{4.31}$$

For problem (4.31) to be well-posed (see Theorem 4.1) we make the assumption that the medium is sub-critical, that's to say $\sigma_{abs} = \sigma_{ext} - \sigma_{sca} > 0$.

Diamond scheme: We give the following discretizations:

$$\begin{cases} x_{j+1/2} = j\,\Delta x \quad , \quad j \in \{1,...,M\} \quad , \quad \Delta x = \frac{D}{M}, \\ \\ -1 \leqslant \mu_{-K} < \mu_{-K+1} < ... < \mu_{-1} < 0 < \mu_1 < .... < \mu_K \leqslant 1. \end{cases} \tag{4.32}$$

As presented in system 4.31, the right-hand side of equation contains an integral operator (collision operator) involving the direction μ. When we have to discretize transport

collision operators, it is necessary to evaluate integrals with respect to the speed μ. For this we introduce weights $\omega_k \in \mathbb{R}$ and, for any function f, we approach the exact integral by a Riemann sum

$$\int_{-1}^{1} f(\mu)\, d\mu \approx \sum_{k=-K, k\neq 0}^{K} \omega_k\, f(\mu_k), \tag{4.33}$$

where

$$\omega_{-k} = \omega_k \geqslant 0,\ \ \mu_{-k} = -\mu_k \text{ for all } k.$$

The mesh in space is always defined by the points $x_{j+1/2}$ defined in (4.74) and the symmetric discretizations in speed μ_k where the index k varies in $\{-K, ..., -1\} \cup \{1, ..., K\}$ but does not take the value 0 so that no speed μ_k is zero. The weights ω_k are also symmetric and positive and the quadrature formula is (4.33). For any index k we will denote I_j^k an approximation of $I(x_j, \mu_k)$, for $j \in \{1, ..., M\}$, and $I_{j+1/2}^k$ an approximation of $I(x_{j+1/2}, \mu_k)$, for $j \in \{0, ..., M\}$.
For $j \in \{1, ..., M\}$ and all the indices k, the diamond scheme is given by

$$\begin{cases} \mu_k \dfrac{I_{j+1/2}^k - I_{j-1/2}^k}{\Delta x} + \sigma_{ext}(N)\, I_j^k = \dfrac{\sigma_{sca}(N)}{2} \bar{I}_j^k, \\ \\ I_j^k = \dfrac{I_{j+1/2}^k + I_{j-1/2}^k}{2}, \end{cases} \qquad j \in \{1, ..., M\} \tag{4.34}$$

where $\bar{I}_j^k$ is defined by

$$\bar{I}_j^k = \sum_{l=-K, l\neq 0}^{K} \omega_l\, \Phi_{l,k}\, I_j^l. \tag{4.35}$$

In general, we prefer to use a very simple iterative method, known as **iteration on the sources** [176, Chapter 5, Section 2].
More precisely, we denote by $n \geqslant 0$ the iteration number. We initialize the algorithm (called iteration on the sources) by setting, for $n = 0$,

$$\bar{I}_j^{k,0} = 0, \tag{4.36}$$

then at iteration $n \geqslant 1$ we solve

$$\mu_k\, \frac{I_{j+1/2}^{k,n} - I_{j-1/2}^{k,n}}{\Delta x} + \sigma_{ext}(N)\, \frac{I_{j+1/2}^{k,n} + I_{j-1/2}^{k,n}}{2} = \frac{\sigma_{sca}(N)}{2} \bar{I}_j^{k,n-1} \qquad , j \in \{1, ..., M\} \tag{4.37}$$

and the angular mean

$$\bar{I}_j^{k,n-1} = \sum_{l=-K, l\neq 0}^{K} \omega_l\, \Phi_{l,k}\, \frac{I_{j+1/2}^{l,n-1} + I_{j-1/2}^{l,n-1}}{2} \qquad , j \in \{1, ..., M\}. \tag{4.38}$$

The resolution of (4.37)-(4.38) is very simple.

• For $\mu_k > 0$ one solves (4.37)-(4.38) according to the increasing values of j starting from the boundary condition

$$I^{k,1}_{1/2} = I^+(\mu_k), \tag{4.39}$$

and writing for $j \geqslant 1$, $k \in \{1, ..., K\}$

$$I^{k,n}_{j+1/2} = \frac{(2\,\mu_k - \sigma_{ext}(N)\,\Delta x)\,I^{k,n}_{j-1/2} + \sigma_{sca}(N)\,\Delta x\,\bar{I}^{k,n-1}_j}{(2\,\mu_k + \sigma_{ext}(N)\,\Delta x)}. \tag{4.40}$$

• For $\mu_k < 0$ one solves (4.37)-(4.38) according to the decreasing values of j starting from the boundary condition

$$I^{k,1}_{N+1/2} = I^-(\mu_k), \tag{4.41}$$

and writing for $j \leqslant M$, $k \in \{-K, ..., -1\}$

$$I^{k,n}_{j+1/2} = \frac{(-2\,\mu_k - \sigma_{ext}(N)\,\Delta x)\,I^{k,n}_{j-1/2} + \sigma_{sca}(N)\,\Delta x\,\bar{I}^{k,n-1}_j}{(-2\,\mu_k + \sigma_{ext}(N)\,\Delta x)}. \tag{4.42}$$

Lemma 4.1. *The sources iteration algorithm* (4.40)-(4.42) *converges, as n tends to infinity, to the discrete solution of scheme* (4.34).

Step scheme: We give the following discretizations:

$$\begin{cases} x_j = j\,\Delta x \quad , \quad j \in \{1, ..., M\} \quad , \quad \Delta x = \frac{D}{M}, \\ \\ -1 \leqslant \mu_{-K} < \mu_{-K+1} < ... < \mu_{-1} < 0 < \mu_1 < .... < \mu_K \leqslant 1. \end{cases} \tag{4.43}$$

We consider the "step" difference scheme which has the virtues of being extremely simple and of always producing positive solutions.

$$\begin{cases} \mu_k \dfrac{I^k_j - I^k_{j-1}}{\Delta x} + \sigma_{ext}(N)\,I^k_j = \dfrac{\sigma_{sca}(N)}{2}\bar{I}^k_j \qquad \mu_k > 0, \\ \\ \mu_k \dfrac{I^k_{j+1} - I^k_j}{\Delta x} + \sigma_{ext}(N)\,I^k_j = \dfrac{\sigma_{sca}(N)}{2}\bar{I}^k_j \qquad \mu_k < 0, \end{cases} \qquad j \in \{1, ..., M\} \tag{4.44}$$

where $\bar{L}^k_j$ is defined by

$$\bar{I}^k_j = \sum_{l=-K, l\neq 0}^{K} \omega_l\,\Phi_{l,k}\,I^l_j. \tag{4.45}$$

Once again we solve (4.44) for the increasing j when $\mu_k > 0$ and for the decreasing j when $\mu_k < 0$. In general, by using the **iteration on the sources** [176, Chapter 5,

Section 2]. More precisely, we denote by $n \geqslant 0$ the iteration number. We initialize the algorithm by setting, for $n = 0$,

$$\bar{I}_j^{k,0} = 0, \tag{4.46}$$

then at iteration $n \geqslant 1$:
• For $\mu_k > 0$ one solves (4.44) according to the increasing values of j starting from the boundary condition

$$I_0^{k,n} = I^+(\mu_k) \qquad \text{(boundary condition in } x = 0),$$

and writing for $j \in \{1, ..., M\}$, $k \in \{1, ..., K\}$

$$I_j^{k,n} = \frac{2\,\mu_k I_{j-1}^{k,n} + \sigma_{sca}(N)\,\Delta x\,\bar{I}_j^{k,n-1}}{(2\,\mu_k + 2\,\sigma_{ext}(N)\,\Delta x)} \quad , \quad \bar{I}_j^{k,n-1} = \sum_{l=-K, l\neq 0}^{K} \omega_l\,\Phi_{l,k}\,I_j^{l,n-1}. \tag{4.47}$$

• For $\mu_k < 0$ one solves (4.44) according to the decreasing values of j starting from the boundary condition

$$I_{N+1}^{k,n} = I^-(\mu_k) \qquad \text{(boundary condition in } x = D),$$

and writing for $j \in \{M, ..., 1\}$, $k \in \{-K, ..., -1\}$

$$I_j^{k,n} = \frac{-2\,\mu_k I_{j+1}^{k,n} + \sigma_{sca}(N)\,\Delta x\,\bar{I}_j^{k,n-1}}{(-2\,\mu_k + 2\,\sigma_{ext}(N)\,\Delta x)} \quad , \quad \bar{I}_j^{k,n-1} = \sum_{l=-K, l\neq 0}^{K} \omega_l\,\Phi_{l,k}\,I_j^{l,n-1}. \tag{4.48}$$

Lemma 4.2. *The Step scheme (4.44) checks the principle of the maximum discreet (without condition in the discretization steps). In addition, it is consistent and precise to order 1 only.*

We present in Figure 4.2 a comparison between the explicit and numerical solutions of system (4.31) in the Beer-Lambert case (Section 4.3.1) with different values of σ_{ext}. This figure confirms that the numerical solution of the RTE is well approximated by using the step scheme.

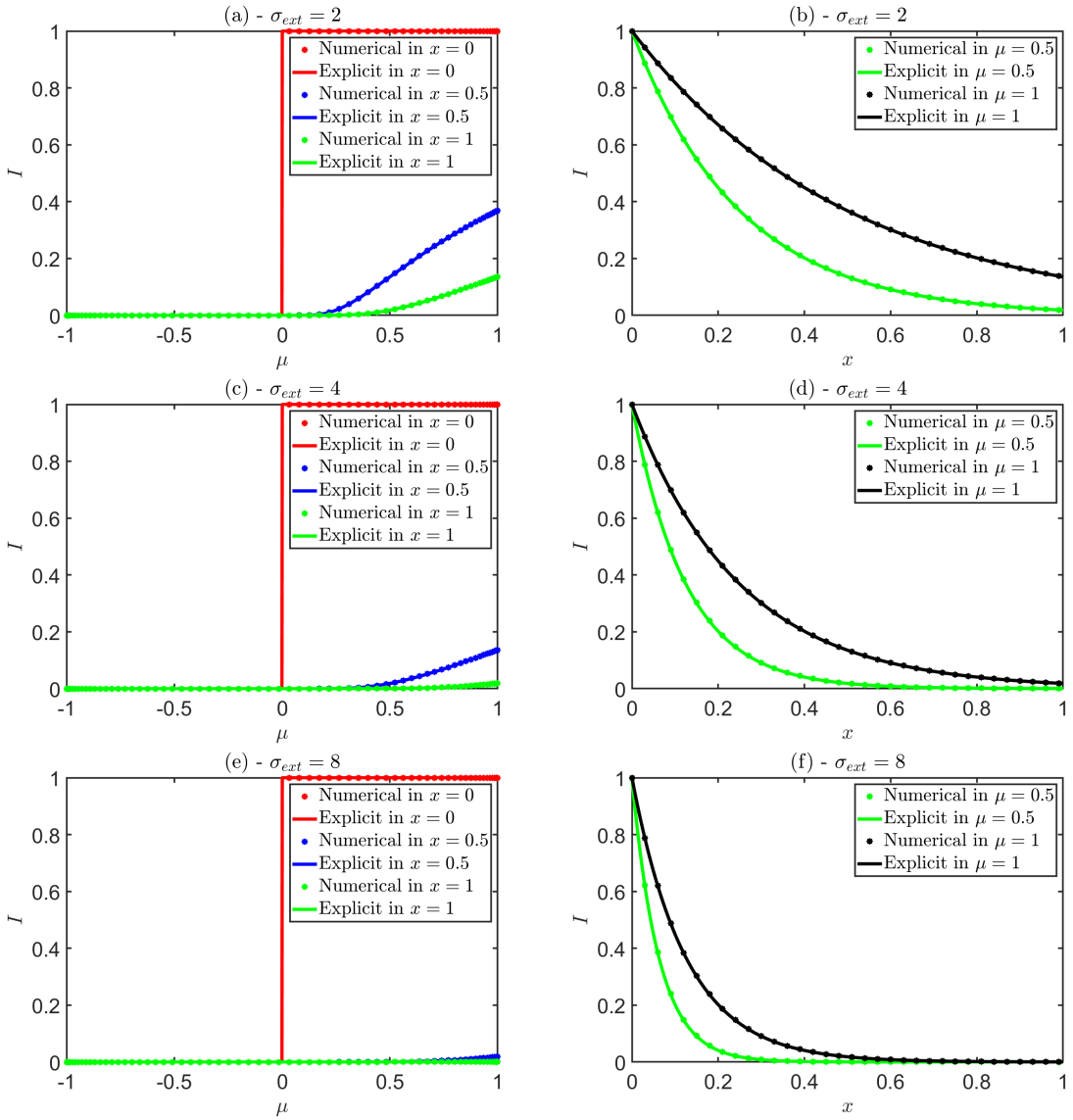

Figure 4.2: Numerical radiance by using the step scheme and the explicit radiance with respect to x and μ with $I^+(\mu) = 1$, $I^-(\mu) = 0$, $D = 1$, $\Delta x = 10^{-3}$, and $\Delta\mu = 10^{-3}$ for $\sigma_{sca} = 0$ and different values of σ_{ext}.

4.4.2 Decomposition in Legendre basis

As mentioned in the previous section, the one-dimensional stationary radiative transfer equation is approximated using the finite difference method, which takes a lot of time due to the decomposition on the spatial position and scattering angle. Therefore, in this section, we present the approximation of the one-dimensional stationary radiative transfer equation using Yvon's method [22]. In order to use this method, we need to decompose the phase function on the basis of Legendre polynomials. We recall that the Legendre polynomials are defined for all $\mu \in [-1, 1]$ by the following recurrence

(see [168]):

$$\begin{cases} P_0(\mu) = 1 \quad , \quad P_1(\mu) = \mu, \\ \forall\, n \geqslant 1,\, P_{n+1}(\mu) = \dfrac{(2n+1)}{(n+1)}\,\mu\, P_n(\mu) - \dfrac{n}{(n+1)}\, P_{n-1}(\mu). \end{cases} \tag{4.49}$$

The sequence defined in (4.49) verifies the following orthogonal properties:

$$\forall\, n \geqslant 1,\, \forall\, l \geqslant 1, \int_{-1}^{1} P_n(\mu)\, P_l(\mu)\, d\mu = \frac{2}{2n+1}\delta_{nl}. \tag{4.50}$$

To solve the stationary radiative transfer equation, we use Yvon's method [22] which is a decomposition method based on the double basis of Legendre polynomials $(P_n(2\cdot -1))_{n\geqslant 0}$ for $\mu \in [-1, 0)$ and $(P_n(2\cdot +1))_{n\geqslant 0}$ for $\mu \in (0, 1]$. Yvon's method consist in splitting the I_λ into two functions, one ℓ_λ^+ corresponds to photons having a $\mu > 0$, the other ℓ_λ^- corresponds to photons having a $\mu < 0$, and consider each of these parts as a separate function.
The intensity I_λ, for K Legendre polynomials, is decomposed as follows [22]:

$$I_\lambda(x,\mu) = \begin{cases} \displaystyle\sum_{j=0}^{K} (2j+1)\ell_{\lambda,j}^-(x,N)P_j(2\mu+1) \quad \text{if} \quad \mu < 0, \\ \displaystyle\sum_{j=0}^{K} (2j+1)\ell_{\lambda,j}^+(x,N)P_j(2\mu-1) \quad \text{if} \quad \mu > 0. \end{cases} \tag{4.51}$$

Suppose that the source term q_λ in (4.8) is decomposed as follows:

$$q_\lambda(x,\mu) = \sum_{i=0}^{K} q_{\lambda,i}(x)\, P_i(\mu). \tag{4.52}$$

In addition, the phase function Φ_λ is decomposed on Legendre polynomials basis as follows (see Lemma A.1 in Appendix A.2):

$$\Phi_\lambda(\mu,\mu',N) = \sum_{k=0}^{K} A_{\lambda,k}(N)\, P_k(\mu)\, P_k(\mu'). \tag{4.53}$$

By injecting (4.53), (4.51), and (4.52) into (4.23), we get two differential systems of size $K+1$ that verify the functions $\ell_{\lambda,j}^+$, $\ell_{\lambda,j}^-$ (see Appendix A.3):
$\forall\, 0 \leqslant j \leqslant K$,

$$\begin{cases} \dfrac{1}{2}\dfrac{j}{2j+1}\dfrac{d\ell_{\lambda,j-1}^+}{dx}(x,N) + \dfrac{1}{2}\dfrac{j+1}{2j+1}\dfrac{d\ell_{\lambda,j+1}^+}{dx}(x,N) + \dfrac{1}{2}\dfrac{d\ell_j^+}{dx}(x,N) + \sigma_{ext}^\lambda(N)\ell_j^+(x,N) \\ = \dfrac{1}{2}\sigma_{sca}^\lambda(N)\displaystyle\sum_{n=0}^{K}(2n+1)\left(\Gamma_{j,n}^{\alpha,\beta}\ell_{\lambda,n}^-(x,N) + \Gamma_{j,n}^{\alpha,\alpha}\ell_n^+(x,N)\right) + \sum_{n=0}^{K} q_{\lambda,n}(x)\alpha_{n,j}, \end{cases} \tag{4.54}$$

$$\left\{\begin{array}{l} -\frac{1}{2}\frac{j}{2j+1}\frac{d\overline{\ell}^-_{\lambda,j-1}}{dx}(x,N) - \frac{1}{2}\frac{j+1}{2j+1}\frac{d\overline{\ell}^-_{\lambda,j+1}}{dx}(x,N) - \frac{1}{2}\frac{d\ell^-_j}{dx}(x,N) + \sigma^\lambda_{ext}(N)\overline{\ell}^-_{\lambda,j}(x) \\ = \frac{1}{2}\sigma^\lambda_{sca}(N)\sum_{n=0}^{K}(2n+1)\left(\Gamma^{\beta,\beta}_{j,n}\overline{\ell}^-_{\lambda,n}(x,N) + \Gamma^{\beta,\alpha}_{j,n}\overline{\ell}^+_{\lambda,n}(x,N)\right) + \sum_{n=0}^{K} q_{\lambda,n}(D-x)\beta_{n,j}, \end{array}\right. \tag{4.55}$$

where

$$\left\{\begin{array}{l} \forall x\in[0,D], \left(\ell^-_{\lambda,K+1}\right)'(x,N) = \left(\ell^+_{\lambda,K+1}\right)'(x,N) = 0, \\ \left(\ell^+_{\lambda,j}(0,N)\right)_{0\leqslant j\leqslant K} \text{ and } \left(\ell^-_{\lambda,j}(D,N)\right)_{0\leqslant j\leqslant K} \text{ given (boundary condition),} \\ \overline{\ell}^\pm_{\lambda,k}(\cdot,N) = \ell^\pm_{\lambda,k}(D-\cdot,N). \end{array}\right. \tag{4.56}$$

with, for all $j\geqslant 0, \forall n\geqslant 0$, $\Gamma^{\alpha,\beta}_{j,n}$, and $\alpha_{n,j}, \beta_{n,j}$ are defined in (A.19)-(A.20) of Appendix A.3.
Eventually, systems (4.54)-(4.55) read in a compact form as follows:
$\forall\, 0<x<D$,

$$\left\{\begin{array}{l} A\,L'_\lambda(x) + B\,L_\lambda(x) = C_1\,L_\lambda(x) + C_2\,L_\lambda(D-x) + E(x), \\ \\ L_\lambda(0) \text{ given,} \end{array}\right. \tag{4.57}$$

with A, B, C_1 and C_2 some matrices of size $2(K+1)\times 2(K+1)$, A tridiagonal and B diagonal, $E(x)$ a vector of size $2K+2$.

$$\left\{\begin{array}{l} \forall 1\leqslant j\leqslant K,\ A(j,j-1) = -A(K+1+j,K+j) = \frac{1}{2}\frac{j}{2j+1}, \\ \forall 0\leqslant j\leqslant K,\ A(j,j) = A(K+1+j,K+1+j) = \frac{1}{2}, \\ \forall 0\leqslant j\leqslant K-1,\ A(j,j+1) = -A(K+1+j,K+j+2) = \frac{1}{2}\frac{j+1}{2j+1}, \end{array}\right. \tag{4.58}$$

$$\forall 0\leqslant j\leqslant K,\ B(j,j) = B(K+1+j,K+1+j) = \sigma^\lambda_{ext}(N), \tag{4.59}$$

and $\forall 0\leqslant j,n\leqslant K$,

$$\left\{\begin{array}{l} C_1(j,n) = \frac{1}{2}\sigma^\lambda_{sca}(N)\Gamma^{\alpha,\alpha}_{j,n}, \\ C_1(K+1+j,n) = \frac{1}{2}\sigma^\lambda_{sca}(N)\Gamma^{\beta,\beta}_{j,n}, \end{array}\right. \tag{4.60}$$

$$\left\{\begin{array}{l} C_2(j,n) = \frac{1}{2}\sigma^\lambda_{sca}(N)\Gamma^{\alpha,\beta}_{j,n}, \\ C_2(K+1+j,n) = \frac{1}{2}\sigma^\lambda_{sca}(N)\Gamma^{\beta,\alpha}_{j,n}. \end{array}\right. \tag{4.61}$$

$$\begin{cases} E(x)(j) = \sum_{n=0}^{K} q_{\lambda,n}(x)\alpha_{n,j} \\ E(x)(K+j+1) = \sum_{n=0}^{K} q_{\lambda,n}(D-x)\alpha_{n,j}. \end{cases} \tag{4.62}$$

In order to solve (4.57), we use the so-called "source iteration method" [176, Chapter 5, Section 2].

4.5 Numerical study of the 1D stationary radiative transfer equation discretization

In this section, we study the numerical approximations presented in Section 4.3 with an analysis of their convergence on the explicit cases given in Section 4.3. We start with a nondimensionalization step in order to reduce the number of parameters.

4.5.1 A nondimensionalization of the radiative transfer equation

The first step is to normalize in (4.23) the spatial domain $[0, D]$ by $[0, 1]$ thanks to the change of variable $\tilde{x} = x/D$ (this change of variable is valid since we are operating within slab modeling). Introducing the new functions:

$$\tilde{I}(x,\mu) = I(\tilde{x},\mu),\ \tilde{q}_\lambda(x,\mu) = q_\lambda(\tilde{x},\mu),\ \tilde{\sigma}^\lambda_{sca} = D\sigma^\lambda_{sca},\ \tilde{\sigma}^\lambda_{abs} = D\sigma^\lambda_{abs},\ \tilde{\sigma}^\lambda_{ext} = D\sigma^\lambda_{ext}, \tag{4.63}$$

then $\tilde{I}$ is the solution to:

$$\begin{cases} \mu\dfrac{\partial \tilde{I}_\lambda}{\partial x}(x,\mu,N) + \tilde{\sigma}^\lambda_{ext}(N)\tilde{I}_\lambda(x,\mu,N) = \tilde{\mathcal{K}}\tilde{I}_\lambda(x,\mu,N) + \tilde{q}_\lambda(x,\mu),\ (x,\mu) \in X, \\ \tilde{I}_\lambda(0,\mu,N) = I^+_\lambda(\mu) \quad \text{for} \quad \mu > 0 \quad \text{and} \quad \tilde{I}_\lambda(1,\mu,N) = I^-_\lambda(\mu) \quad \text{for} \quad \mu < 0, \end{cases} \tag{4.64}$$

where $X = [0,1] \times ([-1,0) \cup (0,1])$ and:

$$\tilde{\mathcal{K}}\tilde{I}_\lambda(x,\mu,N) = \frac{\tilde{\sigma}^\lambda_{sca}(N)}{2} \int_{-1}^{1} \Phi_\lambda(\mu,\mu',N)\, \tilde{I}_\lambda(x,\mu',N)\, d\mu'. \tag{4.65}$$

In this section, we will focus our numerical experiments on a Lambertian source, leading to put:

$$\forall\, \mu > 0,\ I^+_\lambda(\mu) = 1. \tag{4.66}$$

Moreover, we will use the following boundary condition in all the sequel:

$$\forall\, \mu < 0,\ I^-_\lambda(\mu) = 0. \tag{4.67}$$

To simplify the notations, all tildes will be removed.

4.5.2 Convergence error w.r.t. Legendre series truncation and spatial discretization

In our previous discussion of our numerical technique for approximating the solution of the radiative transfer equation, we explained our representation of intensity using a double Legendre basis. In Appendix A.2, we additionally displayed the decomposition of the phase function using the Legendre basis. Figure 4.3 displays a comparison of the phase function for varying numbers of Legendre polynomials, marked as K, as calculated using Lorenz-Mie theory. This calculation relies on a droplet size distribution displayed in Figures 1.15a. These findings are then compared with the phase function computed utilizing MiePlot [180] (employing the identical droplet size distribution). MiePlot is a software that uses Mie theory to simulate light scattering from spherical particles.
Figure 4.3a demonstrates that utilizing a decomposition with 50 Legendre polynomials leads to substantial oscillations in the phase function for larger scattering angles. Nevertheless, as showcased in Figures 4.3b, c, and d, these oscillations decrease gradually with an increase in the number of Legendre polynomials.

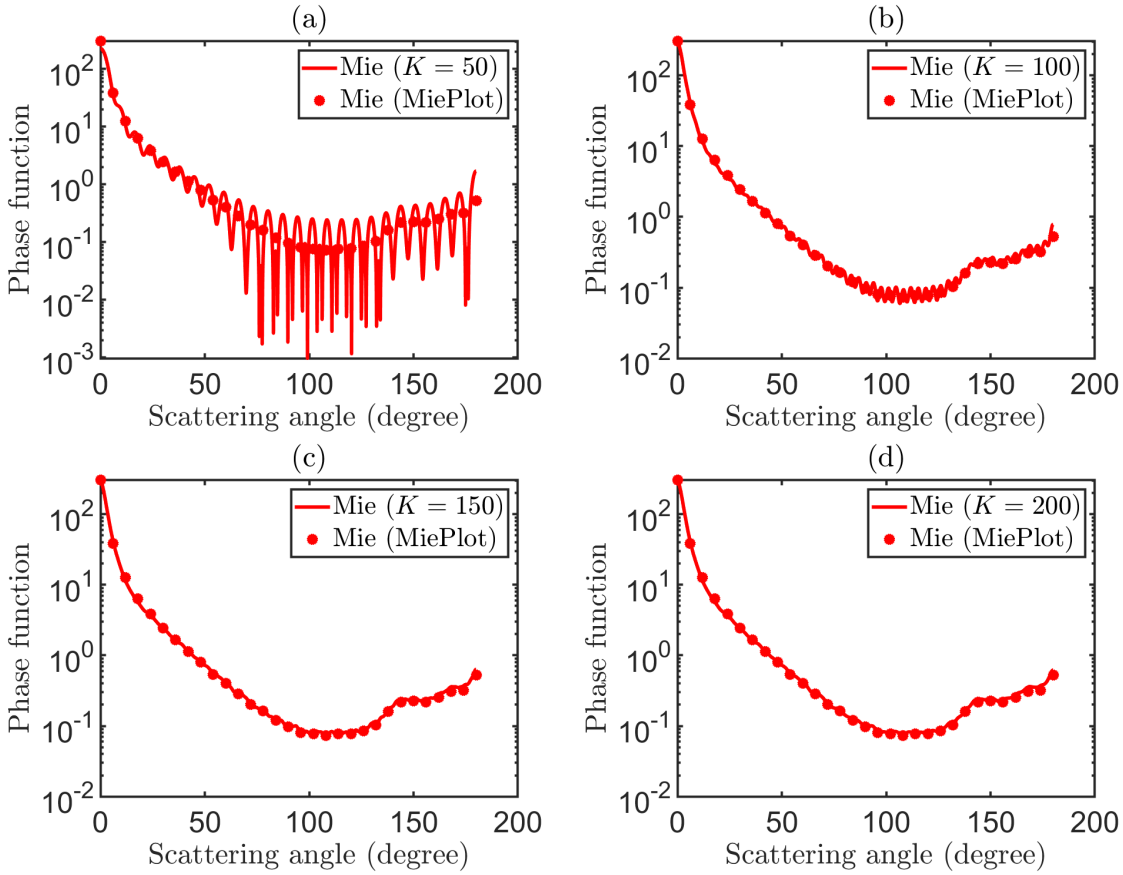

Figure 4.3: Comparison of the Lorenz-Mie phase function with MiePlot [180] in function of the wavelengths for : (a) $K = 50$, (b) $K = 100$, (c) $K = 150$, (d) $K = 200$.

To illustrate the negligible impact of oscillations on our numerical approximation, we have illustrated the concept in Figure 4.4. This figure depicts radiance measurements featuring distinctive numbers of Legendre polynomials at a specified wavelength λ_l. These measurements were executed at the x-axis, specifically $x = 0.5$, while referring to this formulation:

$$M_{\lambda_l}(x_i) = \int_a^b I^{\star}_{\lambda_l}(x_i, \mu)\, d\mu\,, \quad \forall\, 1 \leqslant i \leqslant G,\ 1 \leqslant l \leqslant L, \tag{4.68}$$

where

$$a = \cos\left(\frac{\pi}{360}\right),\ b = 1 \text{ (forescattering measurement with } 1^{\circ} \text{ aperture angle).} \tag{4.69}$$

Figure 4.4 confirms that the oscillations observed in Figure 4.3a do not have a significant impact on our measurement calculations. Specifically, for $K = 50$, our results closely resemble the solutions obtained for $K = 200$.

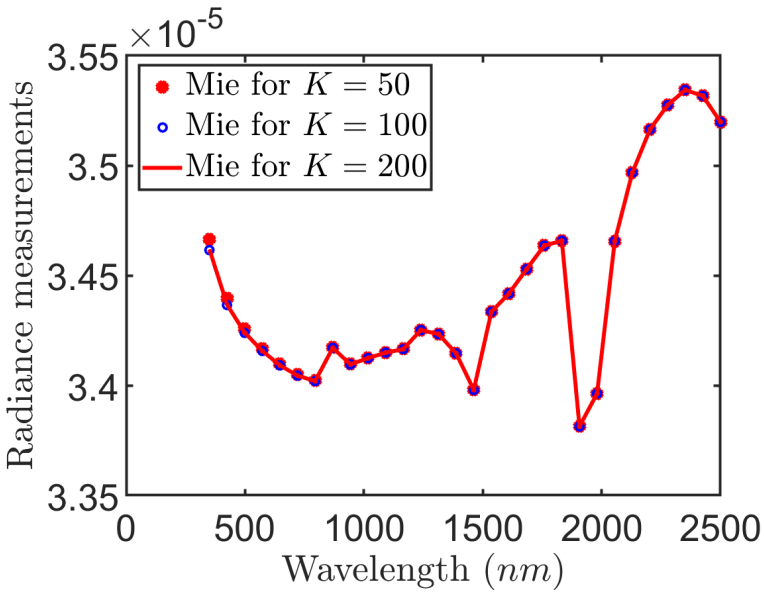

Figure 4.4: The radiance measurements presented in equation (4.68) for different Legendre polynomial numbers K in function of the wavelengths at a point $x = 0.5$.

The case of the Beer-Lambert solution (Section 4.3.1) is investigated here in order to analyze the convergence of our numerical procedure of Section 4.4. Considering the problem (4.64) with $\tilde{\mathcal{K}} = 0$, $\tilde{q}_\lambda = 0$ and with boundary conditions (4.66)- (4.67), the solution is then given by (4.26):

$$I(x, \mu) = \begin{cases} \exp(-\sigma_{ext} x/\mu) & \text{if } \mu > 0, \\ 0 & \text{if } \mu < 0. \end{cases} \tag{4.70}$$

For a stepsize Δx defining a partition

$$0 = x_0 < x_1 < \cdots < x_N = 1,$$

and a K-terms in the Legendre series truncation, we denote by $I^K_{\Delta x}$ the approximate radiance of I obtained by the numerical method of Section 4.4. We consider the following numerical error:

$$E(\sigma_{ext}, K, \Delta x) = \sup_{0 \leqslant i \leqslant N} \frac{\int_a^b \left| I(x_i, \mu) - I^K_{\Delta x}(x_i, \mu) \right| d\mu}{\int_a^b I(x_i, \mu) d\mu}. \tag{4.71}$$

For the numerical simulations, we will use a and b defined in equation (4.69). We plot in Figure 4.5 the relative error (4.71) for the following values:

$$\sigma_{ext} \in \{6.25 \times 10^{-2} m^{-1}, 1.0\, m^{-1}, 4.0\, m^{-1}, 16.0\, m^{-1}\},\ K \in \{10, 30, 50, 70, 90\}, \tag{4.72}$$

$$\Delta x \in \{2^{-i},\ 5 \leqslant i \leqslant 18\}. \tag{4.73}$$

In addition, we note that we choose these values of σ_{ext} for the problem posed on (0,1) using the change of variable presented in Section 4.5.1.

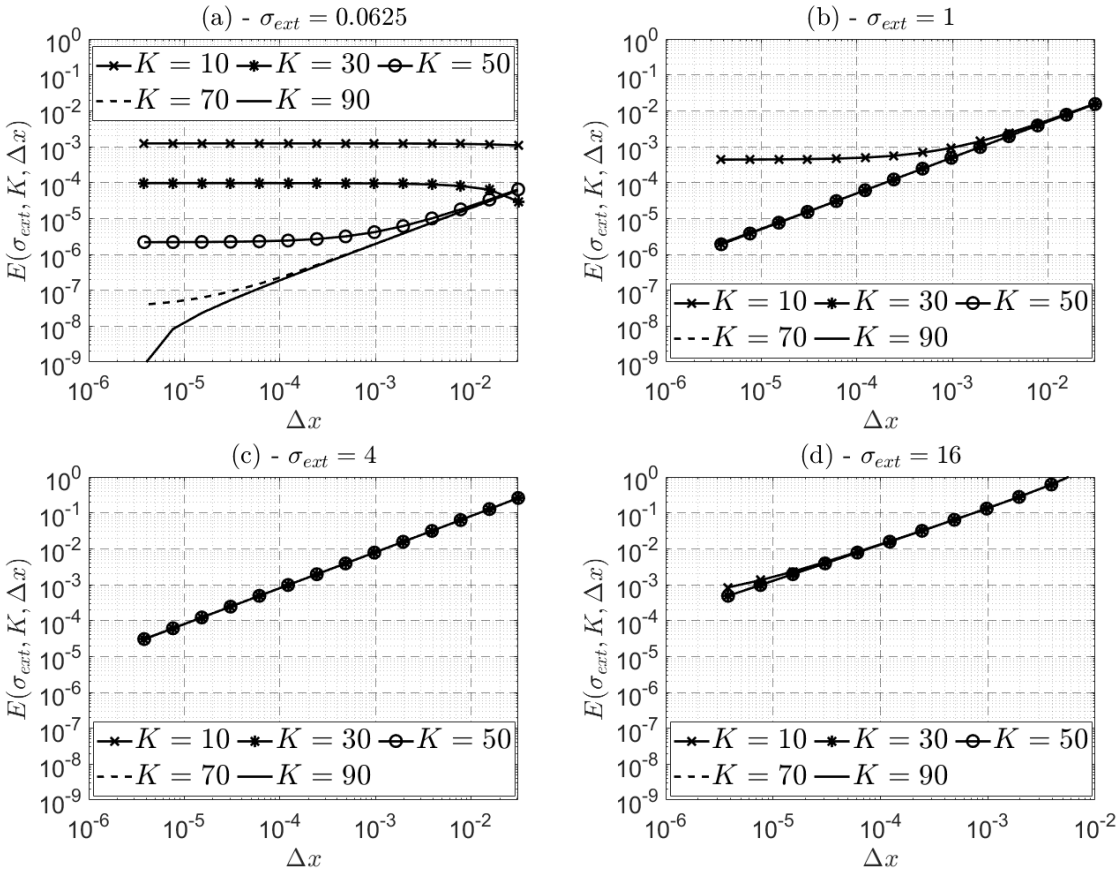

Figure 4.5: Error (4.71) in the Beer-Lambert case with σ_{ext} equal to $6.25\times\ 10^{-2}$ (a) , 1.0 (b), 4.0 (c) and 16.0 (d).

We can observe in Figure 4.5 that the error decreases as the step Δx decreases and as the truncation threshold K increases. The sensitivity to K is nevertheless very low

for high extinction coefficients. For the general case ($\mathcal{K} \neq 0$), we plot in Figure 4.6 the relative error (4.71). The calculations are done with one of the DSD measured at PAVIN platform. The "exact" solution, which is unknown, is assumed to be given by $I^K_{\Delta x}$ with $K = 100$ and $\Delta x = 2^{-18} \simeq 3.8 \times 10^{-6}$.

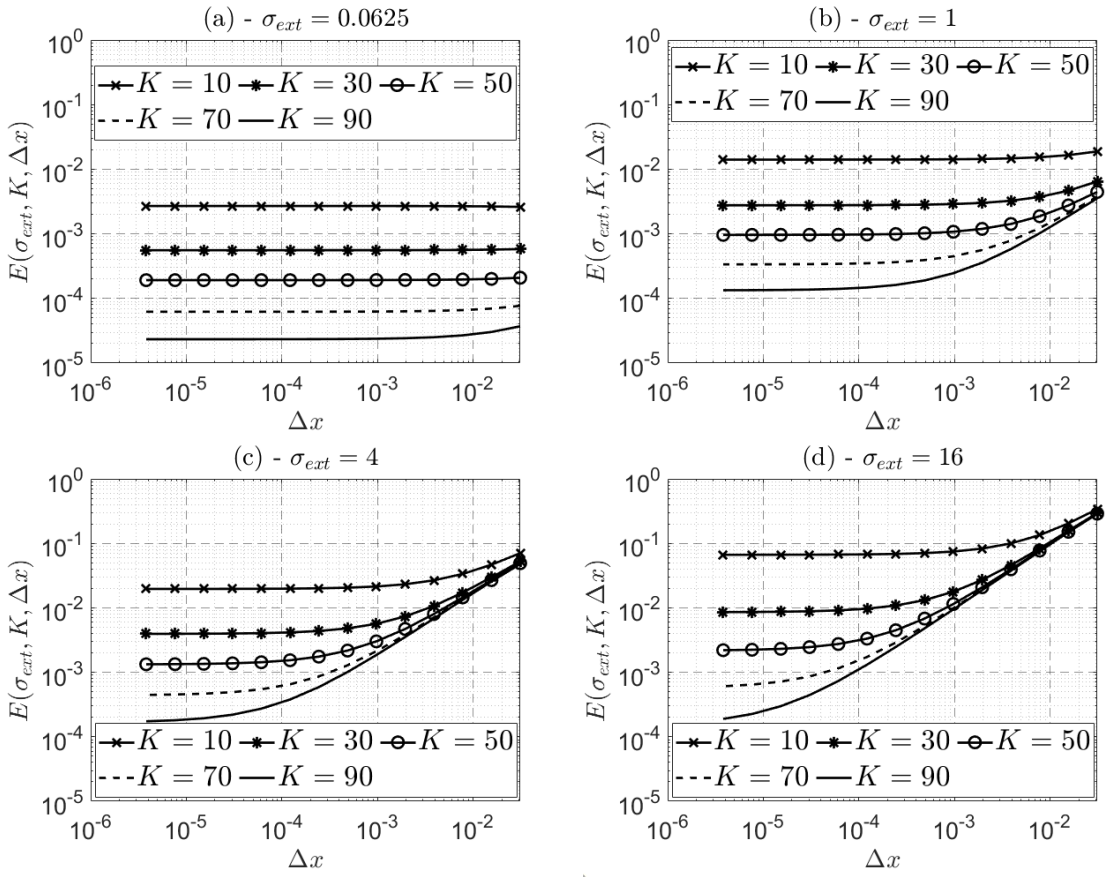

Figure 4.6: Error (4.71) in the general case with σ_{ext} equal to $6.25\times\ 10^{-2}$ (a) , 1.0 (b), 4.0 (c) and 16.0 (d).

We observe, from the Figures 4.5-4.6, that the relative error increases when the value of the extinction coefficient increases. This increase in error comes from a relation which expresses the convergence error of the numerical scheme as a function of the parameters of the differential equation [181, 182] which are Δx and σ^{λ}_{ext}. To show that, we use the Euler implicit scheme with the following discretizations:

$$\begin{cases} x_{j+1} = j\,\Delta x \quad , \quad j \in \{1, ..., M\} \quad , \quad \Delta x = \frac{D}{M}, \\ \\ 0 < \mu_1 < .... < \mu_K \leqslant 1. \end{cases} \tag{4.74}$$

The approximated solution L^k_j of Beer-Lambert problem can be written as follow:

$$L^k_{j+1} = \frac{\mu_k - \sigma^{\lambda}_{ext}\Delta x}{\mu_k} L^k_j. \tag{4.75}$$

In the other hand, by using the explicit solution (4.70), we have

$$L(x_{j+1},\mu_k) = \frac{\mu_k - \sigma_{ext}\Delta x}{\mu_k} L(x_j,\mu_k) + \frac{(\sigma_{ext}\Delta x)^2}{2\mu_k^2} L(x_j,\mu_k). \tag{4.76}$$

Let $e_{j+1} = L(x_{j+1},\mu_k) - L^k_{j+1}$, then

$$|e_{j+1}| \leqslant |e_j| + \frac{(\sigma_{ext}\Delta x)^2}{2\mu_k^2} \leqslant \cdots \leqslant |e_0| + \frac{D(\sigma_{ext})^2}{2\mu_k^2}\Delta x,$$

but $e_0 = 0$, then the error of the convergence is less than $\dfrac{D(\sigma_{ext})^2}{2\mu_k^2}\Delta x$.

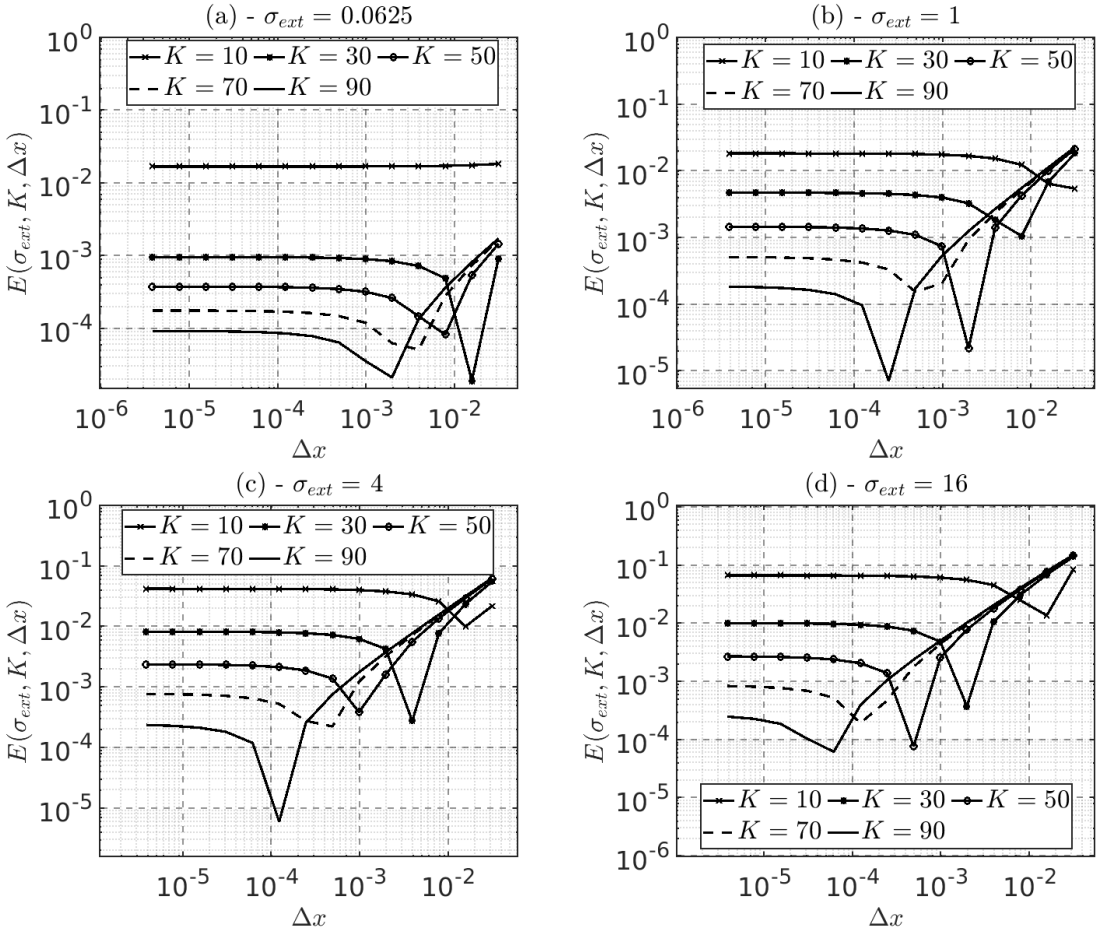

Figure 4.7: Error (4.71) in the general case with backscattering measurements for σ_{ext} equal to 6.25×10^{-2} (a) , 1.0 (b), 4.0 (c) and 16.0 (d).

Also, we plot in Figure 4.7, the relative error expressed in equation (4.71) for the backscattering case with an aperture angle of 1° (with $a = \cos\left(\pi + \dfrac{\pi}{360}\right)$ and $b = -1$) We can observe in Figures 4.6-4.7 a higher sensitivity to K, especially if the stepsize Δx is small. We will keep in the sequel:

$$K = 50 \text{ and } \Delta x = 10^{-3} \Longrightarrow E(\sigma_{ext}, k, \Delta x) \leqslant 10^{-2}. \tag{4.77}$$

Furthermore, we plot in Figure 4.8 the numerical and explicit radiance with respect to x and μ with $\Delta x = 10^{-3}$, and 50 Legendre polynomials, for the Beer-Lambert case and the collision case (in this latter, the explicit solution is given by $I^K_{\Delta x}$ with $K = 100$ and $\Delta x = 2^{-18} \simeq 3.8 \times 10^{-6}$).
Based on the numerical results derived in this section, we observe that our selection of $K = 50$ Legendre polynomials with a $\Delta x = 10^{-3}$ effectively approximates the solution.

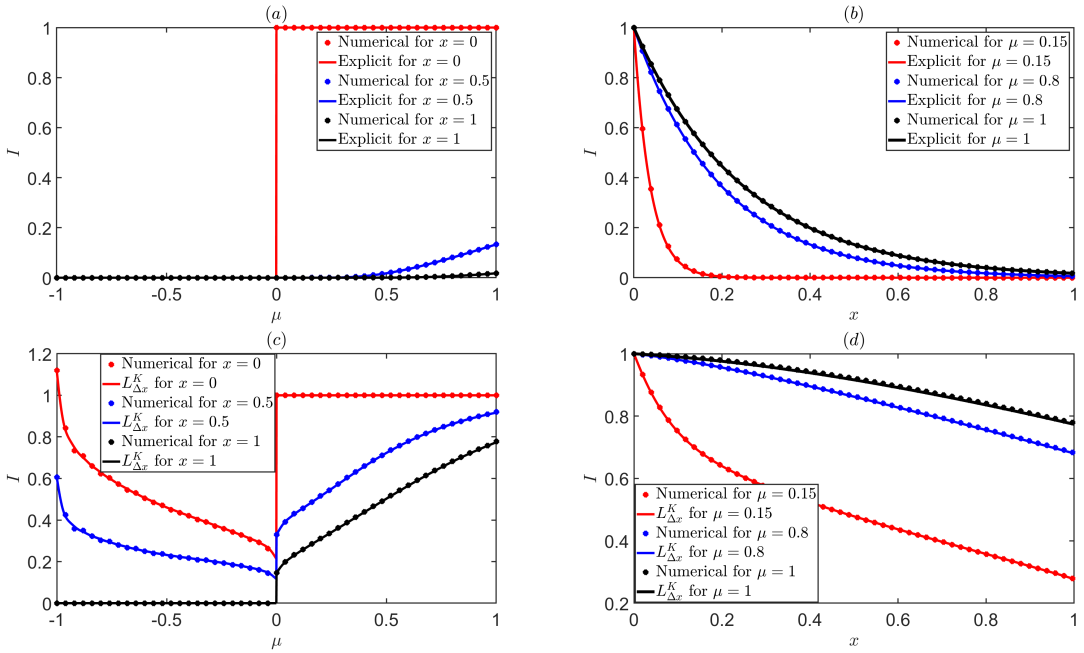

Figure 4.8: Numerical and explicit radiances with respect to x and μ with $\Delta x = 10^{-3}$, and 50 Legendre polynomials, for the Beer-Lambert case ((a) and (b)) and the collision case ((c) and (d)).

Now, we apply our numerical scheme on the simple model (4.27) whose solution is given by (4.28) with $f(\mu) = 1$ and $d = 1/2$.
We plot in Figure 4.9(a) the numerical and explicit radiances with respect to x and μ with $\Delta x = 10^{-3}$, and 50 Legendre polynomials for the problem (4.27) with $\sigma = 4.0$. We can observe a very good agreement between numerical and explicit solutions.
In order to take into account a collision operator which appears in the adjoint problem, we consider the Dautray-Lions solution (4.30) of problem (4.29). Since the Dautray-Lions solution (4.30) does not give the radiance but its integral over μ, we consider the following numerical error associated to the discretization of (4.29):

$$E(\Delta x, K, c) = \frac{\displaystyle\int_{\mathbb{R}}\int_{-1}^{1} \left| I(x,\mu) - I^K_{\Delta x}(x,\mu) \right| d\mu dx}{\displaystyle\int_{\mathbb{R}}\int_{-1}^{1} I(x,\mu) d\mu dx}, \tag{4.78}$$

where c is the parameter of the Dautray-Lions problem. We plot in Figure 4.9(b) the

numerical and explicit function T (see 4.30) with respect to τ with $\Delta\tau = 10^{-3}$, and 50 Legendre polynomials for the problem (4.29) with $c = 0.5$. In this case, we then find $E(2^{-16}, 100, 0.5) \approx 3.53 \times 10^{-2}$.

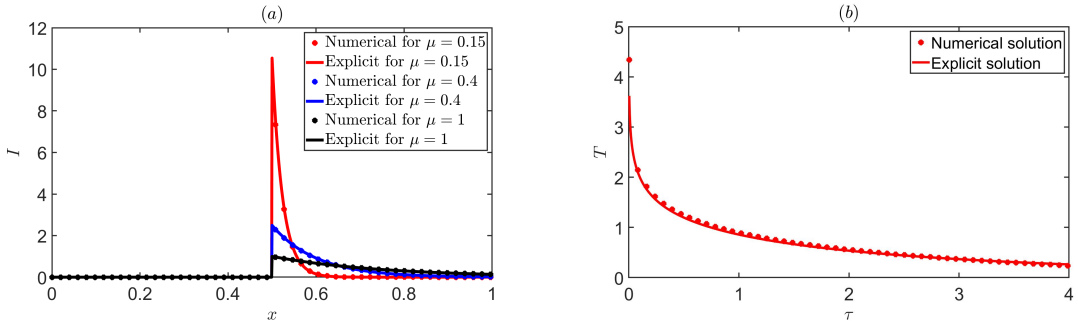

Figure 4.9: Numerical and explicit radiances with respect to x and μ with $\Delta x = 10^{-3}$, and 50 Legendre polynomials for the problem (4.27) with $\sigma = 4.0$ (a). Numerical and explicit function T (see 4.30) w.r.t. τ with $\Delta\tau = 10^{-3}$ and 50 Legendre polynomials for the problem (4.29) with $c = 0.5$.

Chapter 5

Droplet Size Distribution Identification

This chapter is organized as follows. In Section 5.1, we detail the different types of DSD used for our identification method. In section 5.2, we study the ill-posed inverse problems and singular value decomposition (SVD) method for resolving the ill-posed problem. The gradient descent-based inverse problem and the cost function are presented together with their properties in Section 5.3. We also give in this section the expression of the cost function gradient in terms of an adjoint problem to the RTE and we recall the Barzilai-Borwein algorithm to minimize the cost function.

5.1 The DSD used in the identification method

We will test our identification method on different fog droplet size distributions, which have been measured in the PAVIN platform or in natural conditions. We will also consider some common DSD models. The measurements were carried out with the PALAS WELAS particle size analyzer [24]. For numerical applications, all the DSD are normalized in order to have:

$$\tau \equiv D\sigma_{ext} = 4.0\, m^{-1} \text{ (on the domain } (0, D = 1\, m)) \Leftrightarrow V_m = 0.75\, m. \qquad (5.1)$$

The DSD of artificial fog produced in the PAVIN platform are represented in Figure 5.1(a). The DSD for a real fog (see Figure 5.1(b)) were acquired during an episode of fog in the night of March 13 to 14, 2007 on the French Palaiseau site (Paris-Fog campaign [2]).

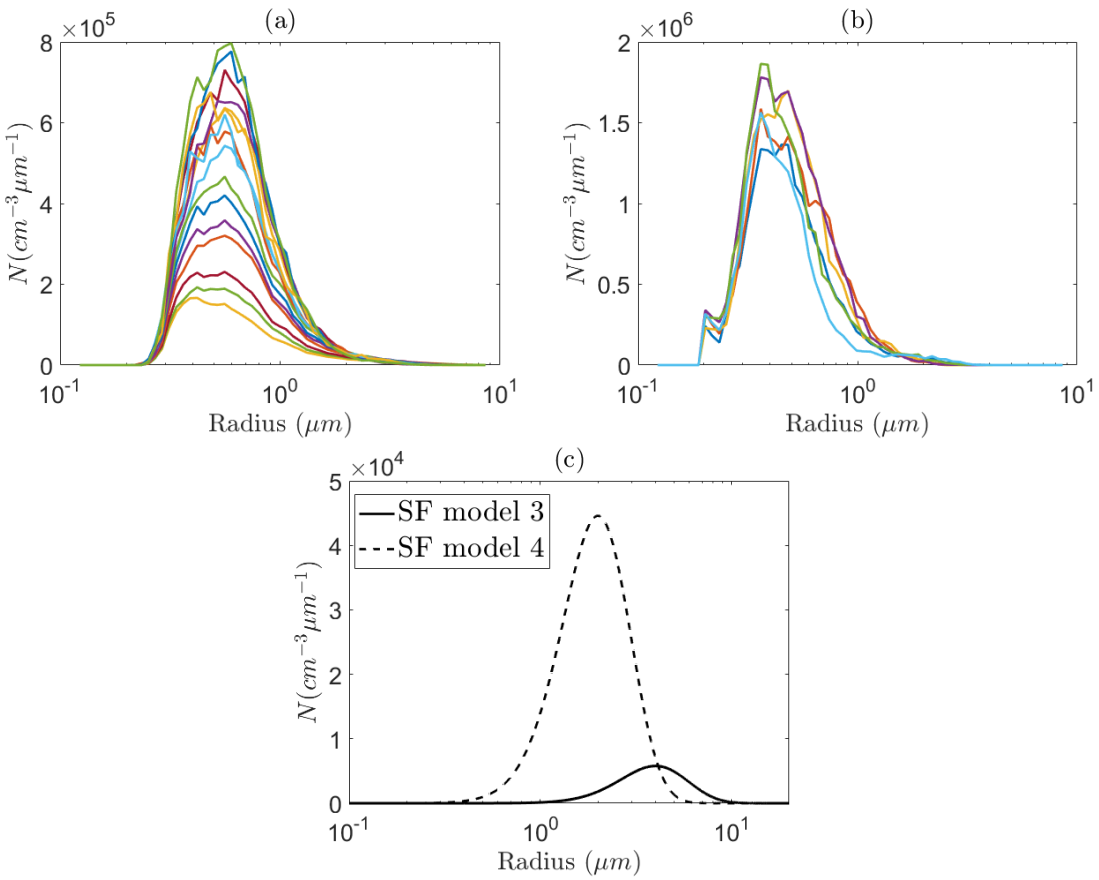

Figure 5.1: Droplet size distributions N (a) measured at Cerema PAVIN platform, (b) during the Paris-Fog campaign and (c) coming from Shettle and Fenn models.

In order to take into account DSD with bigger droplets, we consider in Figure 5.1(c) modified Gamma law based models of radiation fogs given by Shettle and Fen [3]) with the following coefficients:

Model	c	β	d	γ	$r_m(\mu m)$
3	428.15	6	1.5	1	4
4	211317	6	3.0	1	2

Table 5.1: Coefficients given in [3] for modified Gamma laws (1.3).

where r_m represents the peak position for each model.
To better show the reconstruction of the droplet size distributions, Figure 5.2 represents a 3D plot for various distribution of PAVIN platform (presented in Figure 5.1a), as a function of the radius of the particles. This figure will be compared, in the Chapter 6, with the reconstructed images.

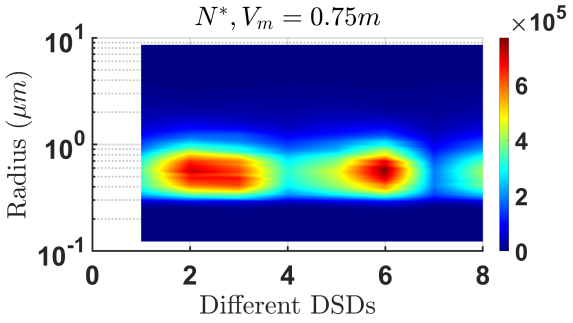

Figure 5.2: 3D plot of 8 different droplet size distributions N measured at Cerema PAVIN platform.

5.2 Ill-posed problems and SVD method

Most work on the reconstruction of this distribution is performed using a simple model of the radiative transfer equation, which is the Beer-Lambert law (as mentioned in Chapter 2). This model describes the light propagation assuming that there is no scattering. In this case, the problem can be considered as a Fredholm integral of the first kind:

$$F + e = \int_{r_{min}}^{r_{max}} A(r)N(r)\,dr, \tag{5.2}$$

where $F^\eta = (1 + \eta\, U)F = F + e$ represents the data with a relative noise level $\eta \geqslant 0$ and U a random variable with uniform law on $(0, 1)$ and F represents the true data corresponding to the target distribution $N^\star$. The difficulties in these types of problem are generally the ill-conditioned nature of discrete linear system [183, 184]. An illustrative example of Fredholm equation $F = AN$ was introduced by Shaw [185]. In order to comprehend and assess the ill-posed nature of this problem, we employ a significant tool, namely Singular Value Decomposition (SVD).
By adding a vector e of data affected by measurement errors, problem (2.8) can be written in matrix form as follows:

$$AN = F^\eta = (1 + \eta\, U)F, \tag{5.3}$$

where $A = (a_{lj})_{1\leqslant l\leqslant G,\, 1\leqslant j\leqslant R}$,

$$a_{lj} = -\pi\, x\, Q_{ext}^{\lambda_l}(r_j)\, r_j^2\, \Delta r_j,$$

and

$$F = \left(ln\left(\frac{L_{\lambda_1}(x)}{L_\lambda(0)}\right), \cdots, ln\left(\frac{L_{\lambda_G}(x)}{L_{\lambda_G}(0)}\right)\right), N = (N(r_1), \cdots, N(r_R)),$$

For $G = R = 60$, we compare in Figure 5.3 the approximated distribution N obtained by resolving the two problems $AN = F$ for $\eta = 0\%$ (figure a) and $AN = F^\eta$ for $\eta = 1\%$ (figure b).

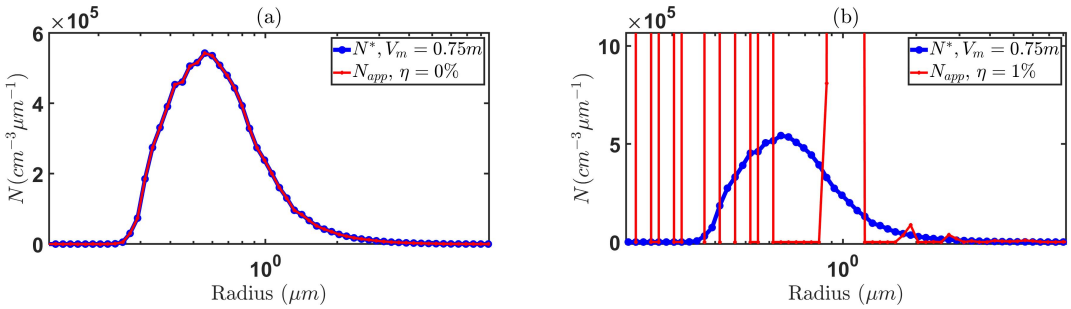

Figure 5.3: The approximated solution for $\eta = 0\%$ (a), for $\eta = 1\%$ (b).

It is clear that our attempt to estimate the distribution N has produced highly unsatisfactory results, despite the low noise level of 1%. The fundamental issue in identifying distribution N, specifically in the presence of noise, is due to the ill-posed nature of our linear system. The extent to which small perturbations in the input data affect the output is quantified by the condition number $\kappa_2(A) = \|A\|_2\|A^{-1}\|_2$. A problem with a small condition number is considered to be well-conditioned, whereas a problem with a high condition number is considered to be ill-conditioned. In the extreme case, A is so badly conditioned that it is almost singular ($\kappa_2(A) = +\infty$).
Theoretically, the relative error in the estimated solution is provided by an upper bound by

$$\frac{\|N - N_{app}\|_2}{\|N\|_2} \leqslant \kappa_2(A)\frac{\|F - F^\eta\|_2}{\|F\|_2}. \tag{5.4}$$

We present in Table 5.2 the value of $\kappa_2(A)$ in function of matrix dimension. We observe that the value of $\kappa_2(A)$ is always very large, which explains the ill-conditioned of our problem.

Matrix dimensions ($G \times R$)	10×10	20×20	40×40	60×60
$\kappa_2(A)$	1.36×10^6	6.68×10^{10}	1.35×10^{15}	1.75×10^{16}

Table 5.2: Condition number $\kappa_2(A)$ as a function of matrix dimensions.

To understand the ill-posed problem, several authors study the Singular value decomposition (SVD) of the identification problem. The authors in [158] study an illustrative example of Fredholm equation introduced by Shaw [185]. In our problem, we need to study the singular value decomposition of matrix A in (5.3) obtained by using the Lorenz-Mie theory [6]. According to the singular value decomposition, the matrix A can be decomposed as follows:

$$\begin{aligned} &A = USV^T, U = [u_1, \cdot\cdot, u_p] \in \mathbb{R}^{G\times G}, V = [v_1, \cdot\cdot, v_R] \in \mathbb{R}^{R\times R}, \\ &S = diag[\sigma_1, \cdot\cdot, \sigma_r, 0, \cdot\cdot, 0] \in \mathbb{R}^{G\times R}, \end{aligned} \tag{5.5}$$

where $r = rank(A)$, $U^T U = V^T V = I$, and $\sigma_1 \geqslant \sigma_2 \geqslant \cdot\cdot \geqslant \sigma_r \geqslant 0$ called the singular values of A, are the nonnegative square roots of the eigenvalues of $A^T A$.
By using (5.3), we have $N^{\eta}_{app} = A^{-1}F$, and by using that $A^{-1} = US^{-1}V^T$, we obtain

$$N^{\eta}_{app} = A^{-1}F^{\eta} = \sum_{n=1}^{r} \frac{u_n^T F^{\eta}}{\sigma_n} v_n = \sum_{n=1}^{r} \frac{u_n^T F}{\sigma_n} v_n + \sum_{n=1}^{r} \frac{u_n^T e}{\sigma_n} v_n = N^0_{app} + \sum_{n=1}^{r} \frac{u_n^T e}{\sigma_n} v_n, \quad (5.6)$$

where u_n, v_n are two columns of U and V, respectively. In this case, the condition number $\kappa_2(A) = \sigma_1 \sigma_r^{-1}$. To fully understand the influence of noise on the approximated solution N_{app}, we plot the quantities σ_n, $|u_n^T F|$ and $|u_n^T F|/\sigma_n$ as a function of n, also known as a Picard Plot [186].

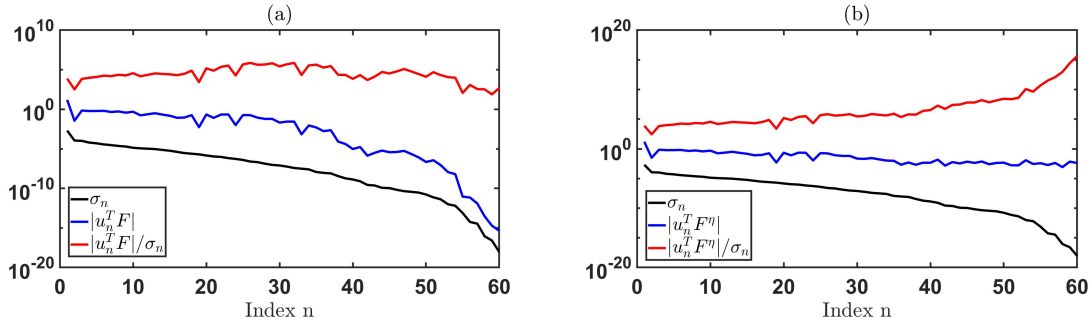

Figure 5.4: SVD components of the identification problem, for $\eta = 0\%$ (a), for $\eta = 1\%$ (b).

For the unperturbed system (Figure 5.4a), we observe that the two curves of the singular values and $|u_n^T F|$ decrease very quickly as a function of n. For the perturbed system (Figure 5.4b), we observe that the value of $|u_n^T F^{\eta}|$ decreases up to $n = 35$ and then it continues with an almost constant value. In fact, it can be observed in Figure 5.4b that there is an explosion in the value of $|u_n^T F^{\eta}|/\sigma_n$ leading to spurious solutions. This explosion indicates that starting from $n = 35$, the value of $u_n^T e/\sigma_n$, where e is the error that disturbs F, dominates the value of $u_n^T F/\sigma_n$.

Now, we present some identification results of distribution N by truncating the series (5.6) where the values of $u_n^T e/\sigma_n$ start to be dominant ($n = 35$ for the example in Figure 5.4). To evaluate the convergence, we compute the relative error between the target distribution $N^{\star}$ and the approximated solution N_{app}:

$$RE = \frac{\|N_{app} - N^{\star}\|_{L^2(\mathbb{R}^+)}}{\|N^{\star}\|_{L^2(\mathbb{R}^+)}} \times 100\,\%.$$

Figure 5.5 shows the approximated solution of the distribution N in case of $\eta = 1\%$ for different singular values number n. We observe that the best approximation uses only 35 singular values (Figure 5.5b) with a relative error $RE = 32\%$. For $n = 37$

(Figure 5.5c) and 40 (Figure 5.5d), where the value of error dominates (see figure 5.4b), our distribution N is poorly approximated.

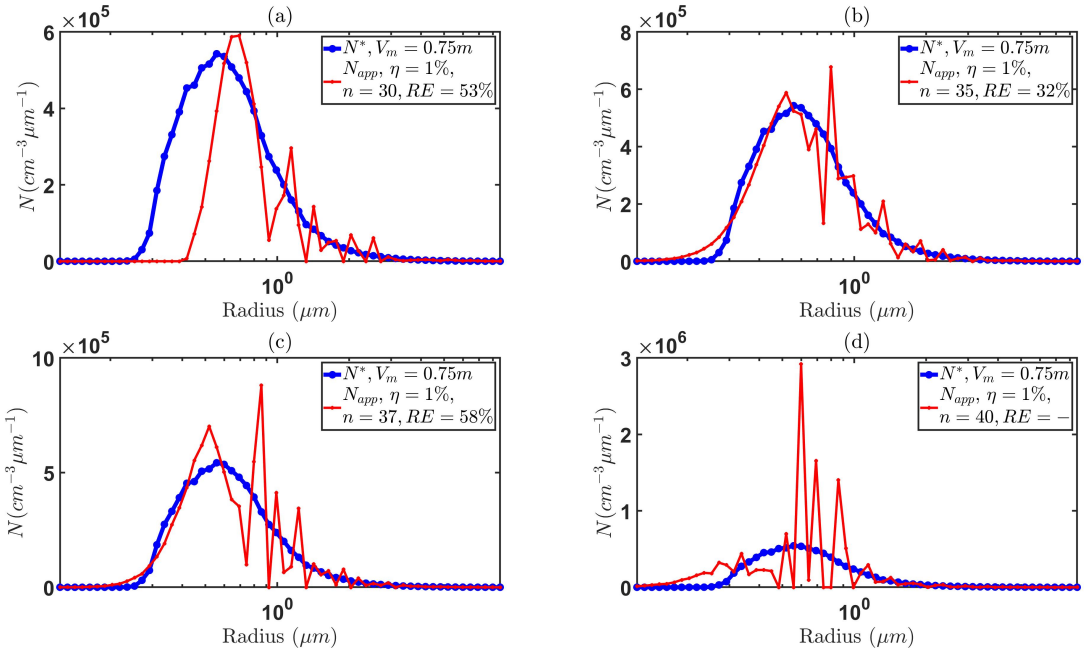

Figure 5.5: The approximated solution for $\eta = 1\%$ and $n = 30$ (a), $n = 35$ (b), $n = 37$ (c) and $n = 40$ (d).

Based on these findings, the solution N_{app} seems to be unstable. To solve this problem, we add a regularization term that serves to improve our approximate solution. We present in the following part a truncated SVD method [187, 188] with a regularization term ε as a solution to the ill-posedness of our identification problem. This method is based on the idea of truncating the series (2.2) where the values of $u_n^T e/\sigma_n$ start to be dominant.The TSVD solution is expresed by:

$$N_{app}^{\eta} = A^{-1}F^{\eta} = \sum_{n=1}^{r} t_n(\varepsilon)\frac{u_n^T F^{\eta}}{\sigma_n} v_n, \tag{5.7}$$

with $t_n(\varepsilon)$ called the filter factor [189, 186] is given by:

$$t_n(\varepsilon) = \begin{cases} 1 & \text{if} \quad n \leqslant \lfloor \varepsilon^{-1} \rfloor, \\ 0 & \text{else}, \end{cases} \tag{5.8}$$

where ε is the regularization parameter and $\lfloor \cdot \rfloor$ is the floor function.
For the results obtained in Figure 5.5, we find $\varepsilon = 0.0334$ (a), $\varepsilon = 0.0286$ (b), $\varepsilon = 0.0271$ (c) and $\varepsilon = 0.025$ (d).
In the following part, we present the reconstruction method of distribution N by using a least squares method and by adding a regularization term to solve the ill-posedness.

5.3 Identification of the DSD by a least-squares optimization method

5.3.1 The cost function and the minimization problem

The measurements at wavelength λ_l, at a point x_i of the x-axis is determined by:

$$M_l^i \equiv M_{\lambda_l}(x_i) = \int_a^b I^\star_{\lambda_l}(x_i,\mu)\,d\mu\,, \quad \forall\, 1 \leqslant i \leqslant G,\, 1 \leqslant l \leqslant L, \tag{5.9}$$

where L and G represent the numbers of measurement points and wavelengths, respectively. The two parameters a and b are defined as follows:

$$a = \cos\left(\theta' + \frac{\alpha}{2}\right) \qquad ; \qquad b = \cos(\theta') \tag{5.10}$$

where α designates the aperture angle of the sensor, and θ' is the position angle of the sensor relative to the source ($\theta' = 0°$ for forescattering measurements, and $\theta' = 180°$ for backscattering measurements).
$I^\star_\lambda(x,\mu)$ is the "real" spectral radiance in the direction μ, at point x and for the wavelength λ. For the numerical applications, we will use synthetic measurements obtained by (6.1) and by:

$$I^\star_\lambda(x,\mu) = I_\lambda(x,\mu,N^\star), \tag{5.11}$$

that is $I^\star_\lambda$ is the solution of the stationary radiative transfer equation (5.12) with a known droplet size distribution $N^\star$ measured in the PAVIN platform, in natural foggy conditions or coming from DSD modelling recalled in Section 2.2.

$$\begin{cases} \mu\dfrac{\partial I_\lambda}{\partial x}(x,\mu) + \sigma^\lambda_{ext}(N)L_\lambda(x,\mu) = \dfrac{\sigma^\lambda_{sca}(N)}{2}\displaystyle\int_{-1}^{1}\Phi(\mu,\mu',N)\,I_\lambda(x,\mu')d\mu', \quad (x,\mu)\in X \\ \\ I_\lambda(0,\mu) = I^+_\lambda(\mu) \quad \text{if} \quad \mu\in(0,1] \qquad \text{and} \qquad I_\lambda(D,\mu) = I^-_\lambda(\mu) \quad \text{if} \quad \mu\in[-1,0). \end{cases} \tag{5.12}$$

In order to identify the droplet size distribution N, we introduce for all $\varepsilon > 0$ the following least-squares problem:

$$\inf_{N\in\mathcal{H}(\mathbb{R}^+)} J_\varepsilon(N), \tag{5.13}$$

where

$$J_\varepsilon(N) = J_1(N) + \frac{\varepsilon}{2}\,\|\sqrt{f}\,N\|^2_{\mathcal{H}(\mathbb{R}^+)}, \tag{5.14}$$

and

$$J_1(N) = \frac{1}{2}\sum_{i=1}^{G}\sum_{l=1}^{L}\left(\frac{\displaystyle\int_a^b I_{\lambda_l}(x_i,\mu)\,d\mu - M_{\lambda_l}(x_i)}{M_{\lambda_l}(x_i)}\right)^2, \tag{5.15}$$

where

$$\mathcal{H}(\mathbb{R}^+) = \left\{ N \in L^2(\mathbb{R}^+), \int_{\mathbb{R}^+} r^2\, N^2(r) dr < +\infty \right\},$$

endowed with the inner product:

$$(N, \overline{N})_{\mathcal{H}(\mathbb{R}^+)} = \int_{\mathbb{R}^+} r^2\, N(r)\, \overline{N}(r)\, dr.$$

The cost function $J_\varepsilon(N)$ defined in (5.14) represents the difference between the measured radiation $M_{\lambda_l}(x_i)$ and the radiation calculated by the radiative transfer equation $F_{\lambda_l}(x_i)$ at point x_i for a wavelength λ_l; I and G represent the number of measurement points and wavelengths, respectively. The ε-term is a regularizing term as it ensures the well-posedness of the problem. Moreover, as a priori knowledge about the droplet size distribution N - almost zero for small radii - that we will identify, we introduce a positive function f that confirms that our approximated distribution is zero for small and large drops.

Theorem 5.1. *For all $\varepsilon > 0$, the least squares problem* (5.13)-(5.14) *admits a unique solution in $\mathcal{H}(\mathbb{R}^+)$.*

Proof. According to the results presented in Appendix B, the cost function J_ε defined in (5.14) is continuous, differentiable, and strictly convex. Then our problem (5.13)-(5.14) admits a unique minimum. □

5.3.2 The cost function gradient and the adjoint problem of the RTE

Here we show the differentiability of the cost function and express its gradient by using the adjoint problem associated to the radiative transfer equation.

Proposition 5.1. *For all $\varepsilon > 0$, the function J_ε is differentiable and its directional derivative in the direction $\overline{N} \in L^2(\mathbb{R}^+)$ is given by the following form:*

$$\forall \eta > 0, N \in L^2(\mathbb{R}^+),\ DJ_\varepsilon(N) \cdot \overline{N} := \lim_{\eta \to 0} \frac{J_\varepsilon(N + \eta\overline{N}) - J_\varepsilon(N)}{\eta} = (\nabla J_\varepsilon(N), \overline{N})_{\mathcal{H}(\mathbb{R}^+)},$$

where

$$\nabla J_\varepsilon(N) = -\pi \sum_{l=1}^{G} \left[Q_{ext}^{\lambda_l} W_{\lambda_l}(N) \right] + \frac{\pi}{2} \sum_{l=1}^{G} \left[Q_{sca}^{\lambda_l} R_{\lambda_l}(N) \right] + \varepsilon f N, \tag{5.16}$$

with for all wavelengths λ,

$$W_\lambda(N) = \int_{-1}^{1} \int_0^D p_\lambda(x, \mu)\, I_\lambda(x, \mu)\, dx\, d\mu, \tag{5.17}$$

$$R_\lambda(N) = \frac{1}{2\pi} \int_{\mu=-1}^{1} \int_0^D p_\lambda(x, \mu) \left(\int_{\mu'=-1}^{1} I_\lambda(x, \mu') \left(\int_0^{2\pi} \psi_\lambda(r, \mu_0) d\omega \right) d\mu' \right) dx\, d\mu.$$

I_λ verifies (4.23), and p_λ verifies the adjoint problem defined by

$$\begin{cases} -\mu \dfrac{\partial p_\lambda}{\partial x}(x,\mu) + \sigma_{ext}^{\lambda}(N)\, p_\lambda(x,\mu) = \mathcal{K} p_\lambda(x,\mu,N) + q_\lambda(x,\mu,N),\ (x,\mu) \in X \\ \\ p_\lambda(0,\mu) = 0,\ \mu < 0 \quad \textit{and} \quad p_\lambda(D,\mu) = 0,\ \mu > 0, \end{cases} \tag{5.18}$$

with

$$q_\lambda(x,\mu,N) = \sum_{i=1}^{G} \left(\frac{\displaystyle\int_a^b I_\lambda(x_i,\mu)\, d\mu - M_\lambda(x_i)}{(M_{\lambda_l}(x_i))^2} \right) \mathbb{1}_{(a,b)}(\mu)\, \delta_{x_i}(x). \tag{5.19}$$

Proof. The directional derivative of the cost function (5.14) according to $\overline{N}$ is given by the following form (see Appendix C):

$$\begin{aligned} DJ_\varepsilon(N)\cdot\overline{N} = &- \sum_{l=1}^{L} \left[\sigma_{ext}^{\lambda_l}(\overline{N}) \int_{-1}^{1}\int_0^D p_{\lambda_l}(x,\mu)\, I_{\lambda_l}(x,\mu)\, dx\, d\mu \right] \\ &+ \frac{1}{2} \sum_{l=1}^{L} \left[\sigma_{sca}^{\lambda_l}(\overline{N}) \int_{1}^{1}\int_0^D p_{\lambda_l}(x,\mu) \left(\int_{-1}^{1} I_{\lambda_l}(x,\mu') \Phi_{\lambda_l}\left(\mu,\mu',\overline{N}\right) d\mu' \right) dx d\mu \right] \\ &+ \varepsilon \int_0^{+\infty} r^2\, f(r)\, N(r)\, \overline{N}(r)\, dr. \end{aligned} \tag{5.20}$$

Moreover,

$$\sigma_{sca}^{\lambda_l}(\overline{N})\, \Phi_\lambda(\mu,\mu',\overline{N}) = \frac{1}{2\pi} \int_0^{2\pi} \sigma_{sca}^{\lambda_l}(\overline{N})\, \phi_\lambda(\mu\mu' + \sqrt{1-\mu^2}\sqrt{1-\mu'^2}\cos(\omega), \overline{N})\, d\omega, \tag{5.21}$$

by (3.22), and noting that $\mu_0 = \mu\mu' + \sqrt{1-\mu^2}\sqrt{1-\mu'^2}\cos(\omega)$, we have

$$\sigma_{sca}^{\lambda}\, \phi_\lambda(\mu_0,\overline{N}) = \int_0^{+\infty} Q_{sca}^{\lambda}(r) \psi_\lambda(r,\mu_0)\, \pi\, r^2\, \overline{N}(r)\, dr, \tag{5.22}$$

then

$$\sigma_{sca}^{\lambda_l}(\overline{N})\, \Phi_\lambda(\mu,\mu',\overline{N}) = \frac{1}{2\pi} \int_0^{2\pi} \int_0^{+\infty} Q_{sca}^{\lambda}(r) \psi_\lambda(r,\mu_0)\, \pi\, r^2\, \overline{N}(r)\, dr\, d\omega, \tag{5.23}$$

where ψ_λ is defined in (3.26).
By injecting (3.21) and (5.23) in (5.20), we get

$$\begin{aligned} DJ_\varepsilon(N)\cdot\overline{N} = &- \pi \sum_{l=1}^{G} \left[\int_0^{+\infty} Q_{ext}^{\lambda_l}(r)\, W_{\lambda_l}(N)\, r^2\, \overline{N}(r)\, dr \right] \\ &+ \frac{\pi}{2} \sum_{l=1}^{G} \left[\int_0^{+\infty} Q_{sca}^{\lambda_l}(r)\, R_{\lambda_l}(N) r^2\, \overline{N}(r)\, dr \right] + \varepsilon \int_0^{+\infty} r^2\, f(r)\, N(r)\, \overline{N}(r)\, dr, \end{aligned} \tag{5.24}$$

then, we obtain the formula (5.16). □

To use the same approximation method for the adjoint problem (5.18), we make a change of variable of $\tilde{x} = D - x$ to obtain a problem similar to the radiative transfer equation. Then, we obtain

$$p_\lambda(x,\mu) = \begin{cases} \displaystyle\sum_{k=0}^{K} (2\,k+1)\, d^-_{\lambda,k}(x,N) P_k(2\,\mu+1) & \text{if} \quad \mu < 0, \\ \\ \displaystyle\sum_{k=0}^{K} (2\,k+1)\, d^+_{\lambda,k}(x,N) P_k(2\,\mu-1) & \text{if} \quad \mu > 0. \end{cases} \tag{5.25}$$

where $d^-_{\lambda,k}$ and $d^+_{\lambda,k}$ are two problems similar to (4.55) and (4.54).

5.3.3 Approximation of the gradient

By injecting (4.51) and (5.25) into (5.16), and by using the trapezoidal rule for the integral in x, the gradient for K Legendre polynomials is given as follows:

$$\nabla J_\varepsilon(N) \approx -\,\pi \sum_{l=1}^{G} Q^{\lambda_l}_{ext}\, W_{\lambda_l}(N) + \frac{\pi}{2} \sum_{l=1}^{G} Q^{\lambda_l}_{sca}\, R_{\lambda_l}(N) + \varepsilon\, f\, N, \tag{5.26}$$

with $\forall\, 1 \leqslant l \leqslant G$

$$W_{\lambda_l}(N) \approx \sum_{i=0}^{S} w_i \left(\sum_{j=0}^{K} (2\,j+1) \, \left(d^-_{\lambda,j}(x_i,N)\, l^-_{\lambda,j}(x_i,N) + d^+_{\lambda,j}(x_i,N)\, l^-_{\lambda,j}(x_i,N) \right) \right),$$

$$R_{\lambda_l}(N) \approx \sum_{i=0}^{S} w_i \left(\sum_{j=0}^{K} (2\,j+1) \, \left(d^-_{\lambda_l,j}(x_i,N)\, B_{\lambda,j}(x_i,N) + d^+_{\lambda,j}(x_i,N)\, C_{\lambda,j}(x_i,N) \right) \right),$$

where ω_i is the weights, and $\forall\, 0 \leqslant i \leqslant S$, $\forall\, 0 \leqslant j \leqslant K$

$$B_{\lambda,j}(x_i,N) \approx \sum_{n=0}^{K} (2\,n+1) (\tilde{\Gamma}^{\beta,\beta}_{\lambda,j,n}\, l^-_{\lambda,j}(x_i,N) + \tilde{\Gamma}^{\alpha,\beta}_{\lambda,j,n}\, l^+_{\lambda,j}(x_i,N)),$$

$$C_{\lambda,j}(x_i,N) \approx \sum_{n=0}^{K} (2\,n+1) (\tilde{\Gamma}^{\alpha,\beta}_{j,n}\, l^-_{\lambda,j}(x_i,N) + \tilde{\Gamma}^{\alpha,\alpha}_{\lambda,j,n}\, l^+_{\lambda,j}(x_i,N)),$$

where $l^+_{\lambda,j}$, $l^-_{\lambda,j}$ is defined in (4.54)-(4.55), and $\tilde{\Gamma}^{u,v}_{\lambda,j,n}$ are defined by:

$$\forall j \geqslant 0, \forall n \geqslant 0, \tilde{\Gamma}^{u,v}_{\lambda,j,n} \equiv \tilde{\Gamma}^{u,v}_{\lambda,j,n}(r) = \sum_{k=0}^{K} \tilde{A}_{\lambda,k}(r)\, u_{k,j}\, v_{k,n},$$

with $\tilde{A}_{\lambda,k}$ is defined in (A.7), and u, v are defined in (A.20) of Appendix A.3.

5.3.4 Iterative minimization algorithm

The purpose of this part is to present the numerical algorithm to approximate the solution of the previously studied minimization problem (5.13)-(5.14). We consider the Barzilai-Borwein minimization algorithm [190]:

$$\begin{cases} N_0, N_1 \quad \text{given}, N_0 \neq N_1, \\ g_0 = \nabla J_\varepsilon(N_0) \quad \text{and} \quad g_1 = \nabla J_\varepsilon(N_1), \end{cases}$$

and for all $n \geqslant 1$

$$\begin{cases} \Delta N_{n-1} = N_n - N_{n-1} \quad ; \quad \Delta g_{n-1} = g_n - g_{n-1}, \\ N_{n+1} = N_n - \dfrac{(\Delta N_{n-1}, \Delta g_{n-1})_{\mathcal{H}(\mathbb{R}^+)}}{(\Delta g_{n-1}, \Delta g_{n-1})_{\mathcal{H}(\mathbb{R}^+)}} g_n, \\ g_{n+1} = \nabla J_\varepsilon(N_{n+1}). \end{cases}$$

We also mention the conjugate gradient method [152], as CG-Polak-Ribiere method [191] and CG-Daniel method [192] which is notably used by [124] in our context. The CG-Polak-Ribiere and CG-Daniel methods are considered as:

$$\begin{cases} N_0 \quad \text{given}, \\ \\ g_0 = \nabla J_\varepsilon(N_0) \quad \text{and} \quad d_0 = -g_0, \end{cases}$$

and for all $k \geqslant 0$:

$$\begin{cases} t_k = \arg\min\limits_{t \in \mathbb{R}^+} J_\varepsilon(N_k + t\, d_k), \\ N_{k+1} = N_k + t_k\, d_k, \quad t_k \in \mathbb{R}, \\ g_{k+1} = \nabla J_\varepsilon(N_{k+1}) \quad \text{and} \quad d_k = -g_k, \\ \beta_k^{PR} = \dfrac{(g_{k+1} - g_k, g_{k+1})_{\mathcal{H}(\mathbb{R}^+)}}{(g_k, g_k)_{\mathcal{H}(\mathbb{R}^+)}} \text{ for CG-Polak-Ribiere}, \\ \text{or} \quad \beta_k^{D} = \dfrac{(\nabla^2 J_\varepsilon(N_k) d_k, g_{k+1})_{\mathcal{H}(\mathbb{R}^+)}}{(\nabla^2 J_\varepsilon(N_k) d_k, d_k)_{\mathcal{H}(\mathbb{R}^+)}} \text{ for CG-Daniel}, \\ d_{k+1} = -g_{k+1} + \beta_k^{PR}\, d_k \quad \text{or} \quad d_{k+1} = -g_{k+1} + \beta_k^{D}\, d_k. \end{cases} \tag{5.27}$$

As presented in this chapter, our minimization problem for the identification of the droplet size distribution is ill-posed, necessitating the introduction of minimization problems with regularization terms. Our minimization problem with the regularization term is solved using the gradient descent method based on calculating the gradient of the cost function with respect to the direct problem and an adjoint problem with a point source term that depends on the measurement points taken. This minimization problem is numerically solved by using the Barzilai-Borwein algorithm, with a comparison to other algorithms. In the following chapter, we present in detail the different results of particle size distribution identifications.

Chapter 6

Numerical results of the Droplet Size Distribution Identification

The chapter is structured as follows. In Section 6.1, we present the numerical results on the DSD identification with a Lambertian source using synthetic measurements (output of simulations with real DSDs and some DSDs models as input) in Beer-Lambert modeling case (without multiple scattering), isotropic and anisotropic collision operator cases. We also study in this section the robustness of our identification method by adding several noise levels to our synthetic measurements. This section is concluded with a study of the effect of the noise on the extinction coefficient that is calculated from the approximated distribution. Similarly to section 6.1, we present in Section 6.2 the identification of droplet size distribution using a collimated source, along with an examination of its robustness. In Section 6.3, we present the identification results in the anisotropic case with both Lambertian and Collimated sources by using the Henyey-Greenstein phase function.

6.1 Droplet size distribution identification results with Lambertian source

In this part, we present some numerical identification of the distribution N by using synthetic measurements. We investigate the reconstruction method for different radiative transfer model and for the 3 types of DSD presented in Figure 5.1. The identification is done in the following four cases:

1. Beer-Lambert case with forescattering measurements ($\theta' = 0°$ and $\alpha = 1°$);
2. Isotropic collision operator case with forescattering measurements ($\theta' = 0°$ and $\alpha = 1°$);
3. Isotropic collision operator case with backscattering measurements ($\theta' = 180°$ and $\alpha = 1°$);
4. Anisotropic collision operator case with backscattering measurements ($\theta' = 180°$ and $\alpha = 1°$).

These four cases can serve as representative examples of real-world scenarios, each having diverse applications. For instance, the application of the Beer-Lambert law in identifying particle size distributions finds relevance in various fields such as environmental spectroscopy, atmospheric science, and remote sensing, as indicated by Huige [193]. Moreover, employing this law facilitates its application in water quality control, enabling the determination of pollutant concentrations in water, including dyes and chemicals, as noted by HE and al. [16, 130]. The isotropic case is applicable in optical tomography, as highlighted in Egger and Schlottbom's work [125]. Finally, we conclude by addressing the anisotropic case, specifically the multi-scattering scenario, which represents the general case where the collision operator is considered for backscattering measurements. This general case can be extended to a simple Lidar case with a phase function dependent only on a single scattering angle.

The measurement for wavelength λ_l and at a point x_i of the x-axis is denoted by $M_{\lambda_l}(x_i)$. We will test our method on synthetic measurements on which we add a noise, that is, given a target droplet size distribution $N^\star$, $M_{\lambda_l}(x_i) = (1+\eta\, U)\, M^{\text{synth}}_{\lambda_l}(x_i)$ with:

$$M^{\text{synth}}_{\lambda_l}(x_i) = \int_{\cos\left(\theta'+\frac{\alpha}{2}\right)}^{\cos(\theta')} I_{\lambda_l}(x_i,\mu,N^\star)\, d\mu\,, \quad \forall\, 1 \leqslant i \leqslant G,\ 1 \leqslant l \leqslant L, \tag{6.1}$$

where G and L denote respectively the number of measurement points and wavelengths, η denotes the noise level added to the synthetic measurement M^{synth}, U is a random variable with uniform law on $(0,1)$.

The wavelengths, for $\lambda_{min} = 350$ and $\lambda_{max} = 2500$, are chosen according to the following relationship:

$$\forall\, 1 \leqslant l \leqslant L,\ \lambda_l = \lambda_{min} + (l-1)\frac{(\lambda_{max}-\lambda_{min})}{G-1}\ \text{nm}. \tag{6.2}$$

In order to study the convergence of the minimization algorithm, we calculate at each iteration k the relative error RE of the minimizer and the relative cost RC

$$\begin{cases} RE(k) = 100 \times \dfrac{\|N_k - N^\star\|_{\mathcal{H}(\mathbb{R}^+)}}{\|N^\star\|_{\mathcal{H}(\mathbb{R}^+)}} = 100 \times \dfrac{\left(\displaystyle\sum_{i=1}^{R}[r_i(N_k(r_i)-N^\star(r_i))]^2\right)^{1/2}}{\left(\displaystyle\sum_{i=1}^{R}(r_i N^\star(r_i))^2\right)^{1/2}}, \\ \\ RC(k) = \dfrac{J_1(N_k)}{J_1(N_0)}, \end{cases}$$

where R denotes the number of sub-intervals which the particle size range $[r_{min}, r_{max}]$ is divided into; J_1 is defined in (5.15), $N^\star$ is the target DSD and N_0 is the initial DSD for the minimization algorithm. This algorithm is initialized by the two vectors $N_0 = (1,\cdots,1)$ and $N_1 = N_0 - 0.1\,\nabla J_\varepsilon(N_0)$ in all the numerical results shown in this section.

We perform our simulations with a Lambertian source, where the radiance at $x = 0$ is constant and is independent of μ (i.e we take $I(0,\mu) = I^+(\mu) = 1$ and $I(D,\mu) = I^-(\mu) = 0$). We fix two choices for the couple $(\varepsilon, f(r))$ depending on the locations of the DSD's peak. We refer to Table 6.1 for the $(\varepsilon, f(r))$ choices after some preliminar experiments.

Conditions	ε	$f(r)$
DSD with a peak location $r_m < 1\,\mu$m	10^{-14}	$1/r^9$
DSD with a peak location $r_m > 1\,\mu$m	10^{-6}	$1/r^4$

Table 6.1: Choices of the (ε, f) parameters of the cost function.

6.1.1 Determination of the best minimization algorithm

We determine the descent algorithm having the best performances by a comparison on the Beer-Lambert modelling case (see Section 4.3.1). Forescattering measurements are carried out ($\theta' = 0°, \alpha = 1°$). We recall, for all $\varepsilon \geqslant 0$, the cost function:

$$J_\varepsilon(N) = \frac{1}{2}\sum_{i=1}^{G}\sum_{l=1}^{L}\left(\frac{\displaystyle\int_{\cos\left(\theta'+\frac{\alpha}{2}\right)}^{\cos(\theta')} e^{-\sigma_{ext}^{\lambda_l}(N)\,\frac{x_i}{\mu}}\,d\mu - M_{\lambda_l}(x_i)}{M_{\lambda_l}(x_i)}\right)^2 + \frac{\varepsilon}{2}\,\|\sqrt{f}N\|^2_{\mathcal{H}(\mathbb{R}^+)}. \tag{6.3}$$

In this case (Beer-Lambert explicit solution to the RTE), we can simply compute the gradient of J_ε:

$$DJ_\varepsilon(N)\cdot\overline{N} = -\sum_{l=1}^{L}\sigma_{ext}^{\lambda_l}(\overline{N})\left(\sum_{i=1}^{G} x_i\,B^{\lambda_l}(x_i)\int_{\cos\left(\theta'+\frac{\alpha}{2}\right)}^{\cos(\theta')}\frac{1}{\mu}e^{-\sigma_{ext}^{\lambda_l}(N)\frac{x_i}{\mu}}\,d\mu\right) + \varepsilon\int_0^{+\infty} r^2 f(r)N(r)\overline{N}(r)\,dr, \tag{6.4}$$

with

$$B^{\lambda_l}(x_i) = \left(\frac{\displaystyle\int_{\cos\left(\theta'+\frac{\alpha}{2}\right)}^{\cos(\theta')} e^{-\sigma_{ext}^{\lambda_l}(N)\,\frac{x_i}{\mu}}\,d\mu - M_{\lambda_l}(x_i)}{(M_{\lambda_l}(x_i))^2}\right),\ 1\leqslant i\leqslant G\,;\ 1\leqslant l\leqslant L.$$

We then obtain:

$$\nabla J_\varepsilon(N) = -\pi\sum_{l=1}^{L} Q_{ext}^{\lambda_l}\left(\sum_{i=1}^{G} x_i\,B^{\lambda_l}(x_i)\int_{\cos\left(\theta'+\frac{\alpha}{2}\right)}^{\cos(\theta')}\frac{1}{\mu}\,e^{-\sigma_{ext}^{\lambda_l}(N)\,\frac{x_i}{\mu}}\,d\mu\right) + \varepsilon\,f\,N. \tag{6.5}$$

A Gauss's integration formula is used to compute the integral in (6.5).
A comparison between the Barzilai-Borwein minimization algorithm and the two conjugate gradient algorithms CG-Polak Ribière and CG-Daniel [152] is shown in Figure 6.1

for one of the DSD of Figure 5.1(a). In these results presented in Figure 6.2, we chose $G = 50$ wavelengths and one measurements point $x = 0.5$.

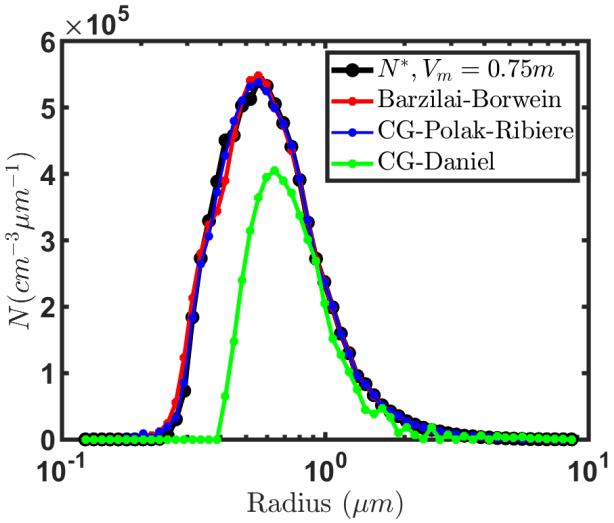

Figure 6.1: Reconstructed DSDs obtained by Barzilai-Borwein, CG-Polak Ribiere and CG-Daniel minimization algorithms after 30 000 iterations, and PAVIN platform target DSD with $\theta' = 0°$, $\alpha = 1°$, $x = 0.5$ and noise level $\eta = 0\%$.

Methods	$J_1(N)$	relative cost	relative error	times
Barzilai-Borwein	9.352×10^{-10}	8.247×10^{-13}	2.6 %	352 iterations/s
CG-Polak Ribiere	6.332×10^{-9}	5.583×10^{-12}	1.7 %	34 iterations/s
CG-Daniel	3.341×10^{-6}	5.541×10^{-5}	23%	25 iterations/s

Table 6.2: The cost J_1, the relative cost RC, and the relative error RE, after 30,000 iterations for various minimization algorithms with $\varepsilon = 10^{-14}$ and $f(r) = \frac{1}{r^9}$.

After 30,000 iterations, as indicated in Table 6.2, our approximated N using the Barzilai-Borwein algorithm exhibits an error of 2.5% compared to $N^\star$ a notably smaller error than the 23% error obtained with the CG-Daniel algorithm. The identification of N with the CG-Polak Ribiere algorithm (with an error of 1.7%) closely approaches the identification achieved with the Barzilai-Borwein algorithm. Figure 6.1 presents the identification of the distribution N by the Barzilai-Borwein algorithm and other used algorithms. We give in Figure 6.2, for the 50 wavelengths between 350 and 2500 nm used in the identification, the relative error:

$$E_\lambda = 100 \times \frac{\|L_\lambda^\star - L_\lambda^a\|_{L^\infty(X)}}{\|L_\lambda^\star\|_{L^\infty(X)}},$$

between the radiance $L_\lambda^\star$ calculated from $N^\star$, and the radiance L_λ^a calculated from the approximated distribution by the Barzilai-Borwein algorithm.

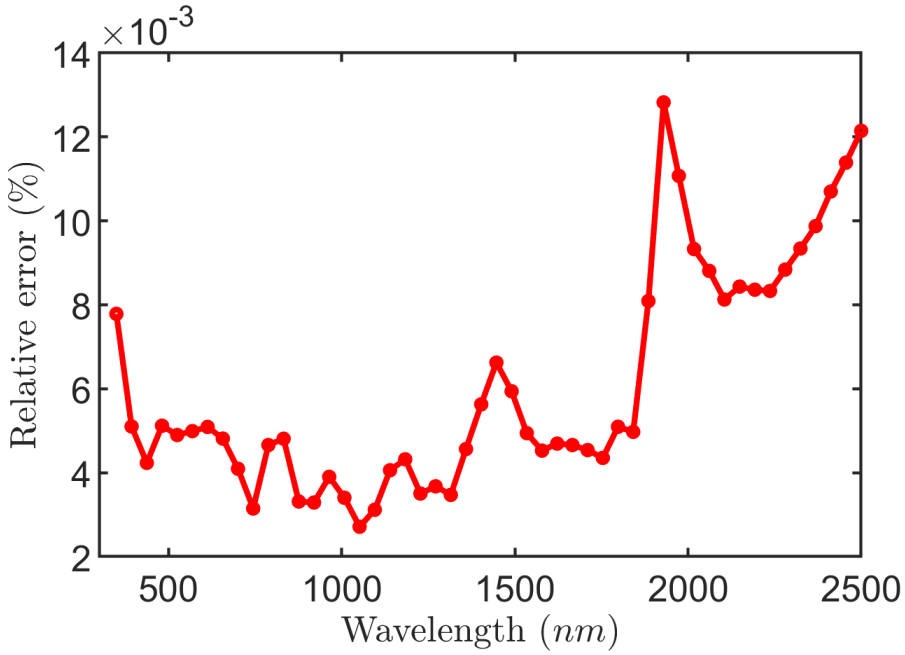

Figure 6.2: Relative error E_λ between the radiance calculated by $N^\star$ and by the approximated N (obtained by BB algorithm) w.r.t. wavelength λ.

A minimal difference is noted between the spectral radiance calculated from the target $N^\star$ and the approximated N. Furthermore, when considering computing time, the Barzilai-Borwein method is better than both conjugate gradient methods. In the case of CG-Polak-Ribière and CG-Daniel, we employ the Trichotomy method to estimate the value of t_n in equation (5.27), and this, consequently, has an impact on the overall calculation time. In the subsequent analysis, we will employ the Barzilai-Borwein algorithm for the identification of the distribution N.

6.1.2 Beer-Lambert case (see Section 2.2.2)

We present in this section the identification of the droplet size distribution by using the Beer-Lambert modeling. We show in Figure 6.3 the approximated distribution for two droplet size distributions presented in Figure 6.4. Table 6.3 presents the values of the relative cost and the relative error of these tests after 30,000 iterations, which suggest that the identification is satisfactory.

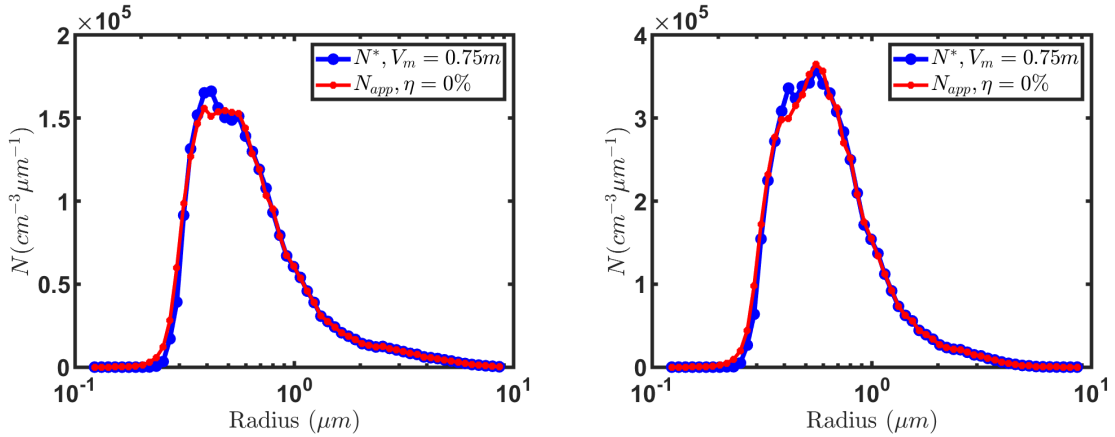

Figure 6.3: Identification results obtained after 30,000 iterations with $\theta' = 0°$, $\alpha = 1°$, $x = 0.5$ and the noise $\eta = 0\%$ for 2 PAVIN platform DSDs.

Tests	$J_1(N)$	relative cost	relative error
Test 1 (left)	2.735×10^{-10}	1.968×10^{-13}	2.3 %
Test 2 (right)	1.065×10^{-9}	5.629×10^{-13}	2.5 %

Table 6.3: The cost $J_1(N)$, the relative cost RC, and the relative error RE after 30 000 iterations with $\varepsilon = 10^{-14}$ and $f(r) = \frac{1}{r^9}$ corresponding to Figure 6.3.

To confirm the convergence of our identification method, we test the identification for more DSDs presented in Figure 6.4 (left). Figure 6.4 (right) represents the approximated distributions of these DSDs where we observe a good approximation of these distributions in this case. According to the figures, we notice that the surface of the red spot decreases (the red spot corresponds to the peaks of DSDs presented in 6.3) and is finally replaced by shades of yellow and blue near the value of the red spot.

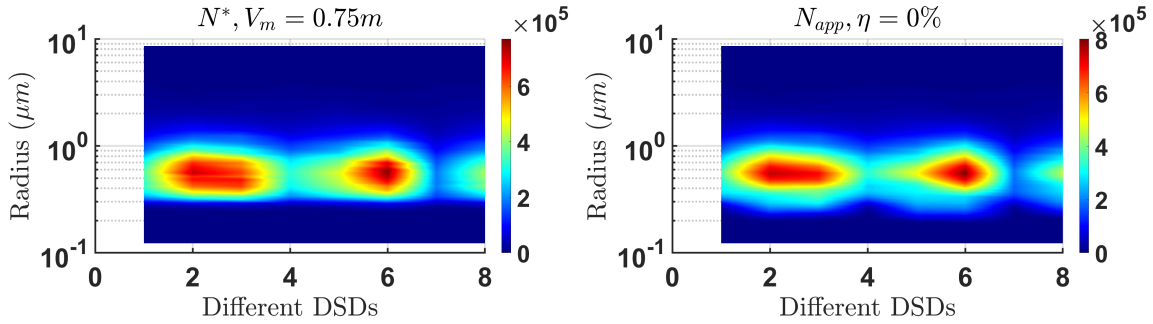

Figure 6.4: The target PAVIN DSDs (left) and the identification results obtained after 30,000 iterations with $\theta' = 0°$, $\alpha = 1°$, $x = 0.5$ and the noise $\eta = 0\%$.

Figure 6.5 shows the identification results for various droplet size distributions measured on Paris-Fog campaign [2] (see Figure 5.1(b)). Table 6.4 presents the values of the relative cost and the relative error of these tests after 100,000 iterations. These figures

and this table suggest that the identification is satisfactory with an error ranging between 4,7% and 8%.

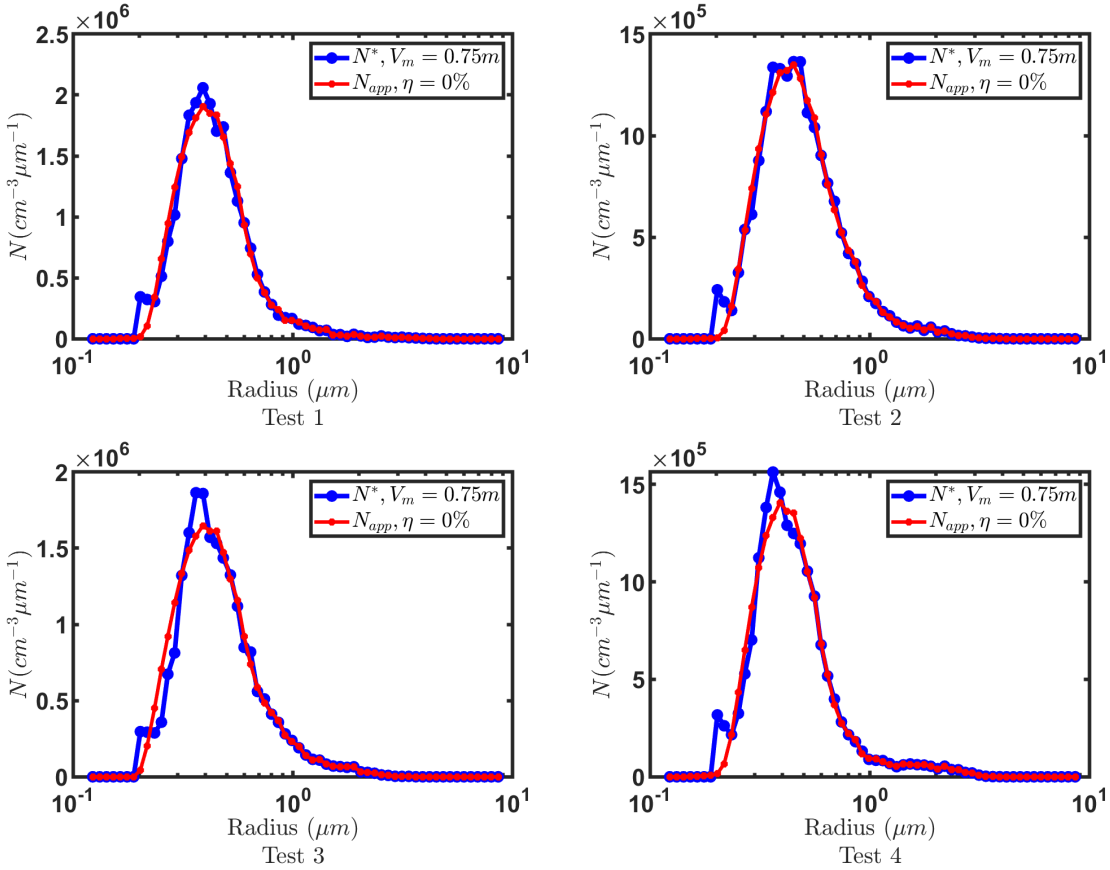

Figure 6.5: Identification results obtained after 100,000 iterations with $\theta' = 0°$, $\alpha = 1°$, $x = 0.5$ and the noise $\eta = 0\%$ for 4 Paris-Fog DSDs.

Tests	$J_1(N)$	relative cost	relative error
Test 1 (top left)	2.0137×10^{-7}	3.325×10^{-10}	7.6 %
Test 2 (top right)	4.924×10^{-8}	6.379×10^{-11}	4.7 %
Test 3 (bottom left)	3.917×10^{-7}	5.377×10^{-10}	8 %
Test 4 (bottom right)	1.410×10^{-7}	1.523×10^{-10}	7 %

Table 6.4: The cost $J_1(N)$, the relative cost RC, and the relative error RE after 100,000 iterations with $\varepsilon = 10^{-14}$ and $f(r) = \frac{1}{r^9}$ corresponding to Figure 6.5.

We now test the method on the Shettle and Fenn models of Table 5.1. The identification results are presented in Figure 6.6. Table 6.5 shows the relative cost and the relative error of the identifications presented in Figure 6.6. For these 2 models, we obtain a good approximation with relative error 0.43% and 2.6%, respectively. According to these tests, we can confirm that our identification method can be applied for the large drop distribution and not only for small drop distribution.

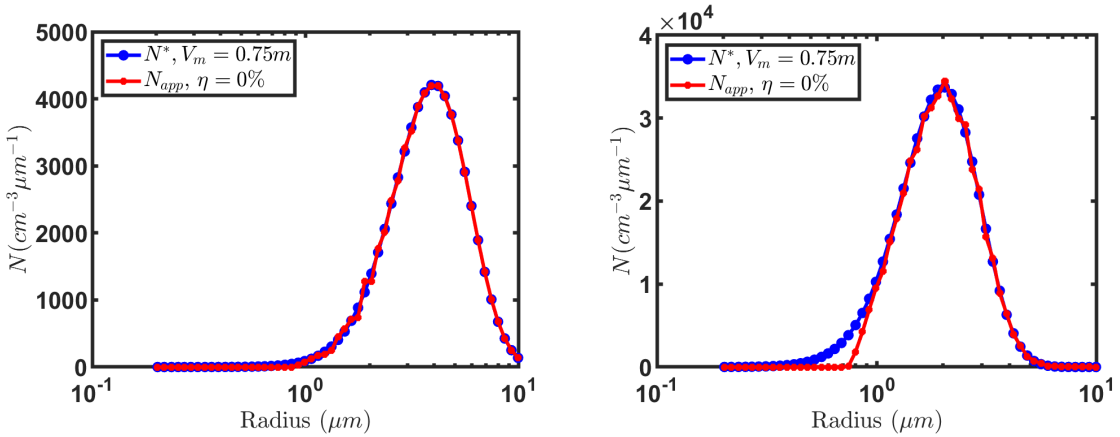

Figure 6.6: Identification results obtained after 10,000 iterations with $\theta' = 0°$, $\alpha = 1°$, $x = 0.5$ and the noise $\eta = 0\%$ for Shettle and Fenn DSD models.

Tests	$J_1(N)$	relative cost	relative error
Model 3 (left)	4.723×10^{-9}	4.680×10^{-8}	0.43 %
Model 4 (right)	6.828×10^{-6}	1.099×10^{-6}	2.6 %

Table 6.5: The cost $J_1(N)$, the relative cost RC, and the relative error RE after 10,000 iterations with $\varepsilon = 10^{-6}$ and $f(r) = \frac{1}{r^4}$.

6.1.3 Isotropic collision operator case

We introduce here a collision operator in the radiative transfer modelling thanks to the isotropic phase function $\Phi_\lambda \equiv 1$ and we then apply the DSD reconstruction method. Note that this case does not have a physical meaning since we prescribe a given phase function when it should depend on the DSD. Nevertheless, it has the merit of testing our method in a more complex case than the Beer-Lambert case allowing to consider backscattering measurements. According to Table 6.6 and Figure 6.7, we observe a good approximation of $N^\star$ with either forescattering or backscattering measurements with a relative cost less than 10^{-7} and a relative error less than 5 %.

Measurement type	$J_1(N)$	relative cost	relative error	time
Forescattering	4.980×10^{-7}	7.514×10^{-8}	3.4%	2 iterations/min
Backscattering	7.444×10^{-7}	2.985×10^{-8}	4.1%	2 iterations/min

Table 6.6: The cost $J_1(N)$, the relative cost RC, and the relative error RE after $2,000$ iterations for forescattering and backscattering measurements in the isotropic case.

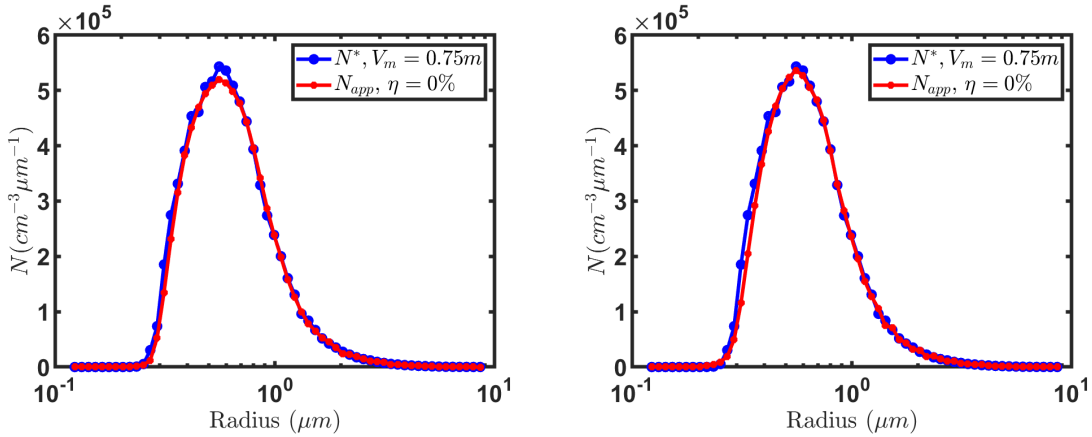

Figure 6.7: Identification results obtained after 2 000 iterations with forescattering measurements (left) and backscattering measurements (right) for a PAVIN platform DSD.

To confirm our identification method, we end this part with Figure 6.8, where we present the identification of various PAVIN DSDs presented in Figure 5.2. We observe that these distributions are well approximated and the peak (red spot) of these distributions is reached.

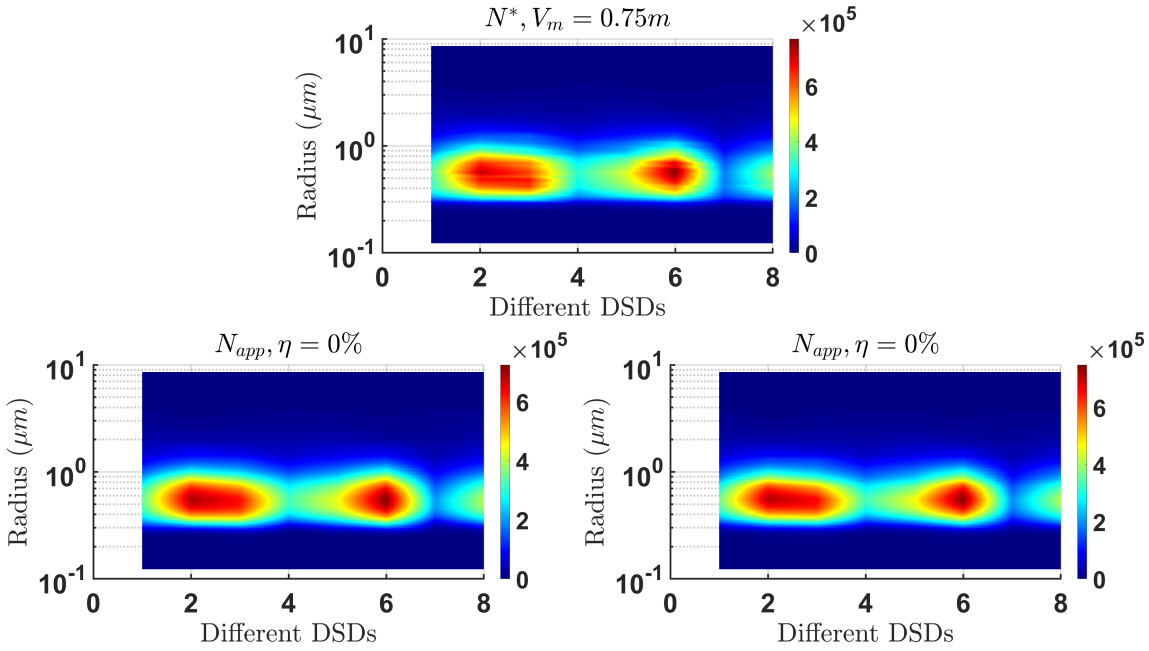

Figure 6.8: Identification results obtained with forescattering measurements (left) and backscattering measurements (right) for a PAVIN platform DSDs.

In this context, it is worth mentioning that the computation time is notably longer compared to what is achieved in the Beer-Lambert case, where we used directly the explicit solution. As an illustration, within a minute, the Beer-Lambert model enables 21,000 iterations, whereas the isotropic and anisotropic models allow only 2 iterations.

The reason for an extra computation time stems from the approach used to reconstruct the DSD. During each iteration of the Barzilai-Borwein algorithm, we perform calculations for 50 direct radiative transfer problems presented in (4.23) (depend on the choice of the number of the wavelength) and 50 adjoint problems presented in (5.18) associated with the radiative transfer equation. These 100 problems are subsequently solved using a fixed-point method as mentioned in Section 4.4.2.

6.1.4 Anisotropic collision operator case

In this part, we identify the distribution N in the anisotropic case when the phase function in the collision operator is calculated from the distribution N. From our numerical testing, the forescattering measurements do not properly identify the droplet size distribution. However, backscattering measurements allow us to well reconstruct the DSD. Figure 6.9 shows the identification of DSD in backscattering measurements after 5,000 iterations. The peak on 0.5 μm is reached.

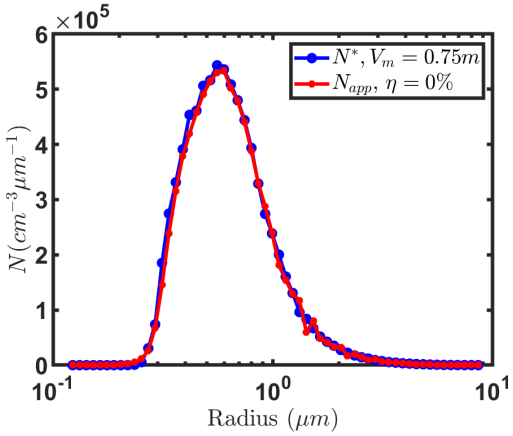

Figure 6.9: Identification results obtained after 5 000 iterations with backscattering measurements (right) for a PAVIN platform DSD in the anisotropic case with $J_1 \approx 1.212 \times 10^{-6}$, $RC \approx 5.143 \times 10^{-8}$, and $RE \approx 7.2\%$.

6.1.5 DSDs identification for different visibility

In this part, we explore the identification of droplet size distribution across different visibility and optical thicknesses, with no restriction to an optical thickness of $\tau = 4$. Table 6.7 represents the results obtained for distribution reconstruction under various visibility (0.25, 0.5, and 0.75 m), considering different modeling and measurement types. The relative error analysis indicates that our distribution is well approximated in these scenarios. Additionally, the table includes computed visibility values at the wavelength of 550 nm, derived from both the target and the approximated distributions.
Some researchers [193], when reconstructing the droplet size distribution, compare the

effective radius values obtained from the target and the approximated distribution. Table 6.7 provides the relative error between the target effective radius and the approximated effective radius, computed using the following formula:

$$E_{eff} = 100 \times \frac{|r^{\star}_{eff} - r^{app}_{eff}|}{r^{\star}_{eff}}, \tag{6.6}$$

where

$$r^{\star}_{eff} = \frac{\int_{r_{min}}^{r_{max}} r^3 N^{\star}(r) dr}{\int_{r_{min}}^{r_{max}} r^2 N^{\star}(r) dr} \quad \text{and} \quad r^{app}_{eff} = \frac{\int_{r_{min}}^{r_{max}} r^3 N_{app}(r) dr}{\int_{r_{min}}^{r_{max}} r^2 N_{app}(r) dr}. \tag{6.7}$$

Modelling	Measurement type	$V_m(N^{\star})$	RC	RE	E_{eff}	$V_m(N_{app})$
Isotropic	Forescattering	$0.25\,m$	6.379×10^{-6}	10.5%	1.16%	$2.511\times10^{-1}m$
Isotropic	Forescattering	$0.5\,m$	1.128×10^{-7}	5.7 %	0.3 %	$5.017\times10^{-1}m$
Isotropic	Forescattering	$0.75\,m$	6.169×10^{-8}	4 %	0.1 %	$7.516\times10^{-1}m$
Isotropic	Backscattering	$0.25\,m$	9.806×10^{-5}	10 %	1.4 %	$2.505\times10^{-1}m$
Isotropic	Backscattering	$0.5\,m$	8.266×10^{-8}	7 %	0.73%	$4.998\times10^{-1}m$
Isotropic	Backscattering	$0.75\,m$	3.193×10^{-8}	4.9 %	0.72%	$7.495\times10^{-1}m$
Anisotropic	Backscattering	$0.25\,m$	4.155×10^{-5}	10.8%	2.38%	$2.498\times10^{-1}m$
Anisotropic	Backscattering	$0.5\,m$	3.151×10^{-5}	10.5%	4.75%	$5.002\times10^{-1}m$
Anisotropic	Backscattering	$0.75\,m$	5.143×10^{-8}	7.2 %	1.42%	$7.488\times10^{-1}m$

Table 6.7: The relative cost RC, the relative error RE, relative effective radius E_{eff}, and the visibility (for $\lambda = 550nm$) for different modellings, measurement types and noise level $\eta = 0\%$ on the measurements.

6.1.6 Noise adding on the measurements

To study the robustness of the DSD identification method, we add to the measurements a noise level of 1% and 3%. We gather in Figures 6.10 and 6.11 the reconstructed DSD with different noises for the following cases: forescattering and Beer-Lambert case, forescattering and backscattering measurements in isotropic conditions, and backscattering measurements in anisotropic conditions.

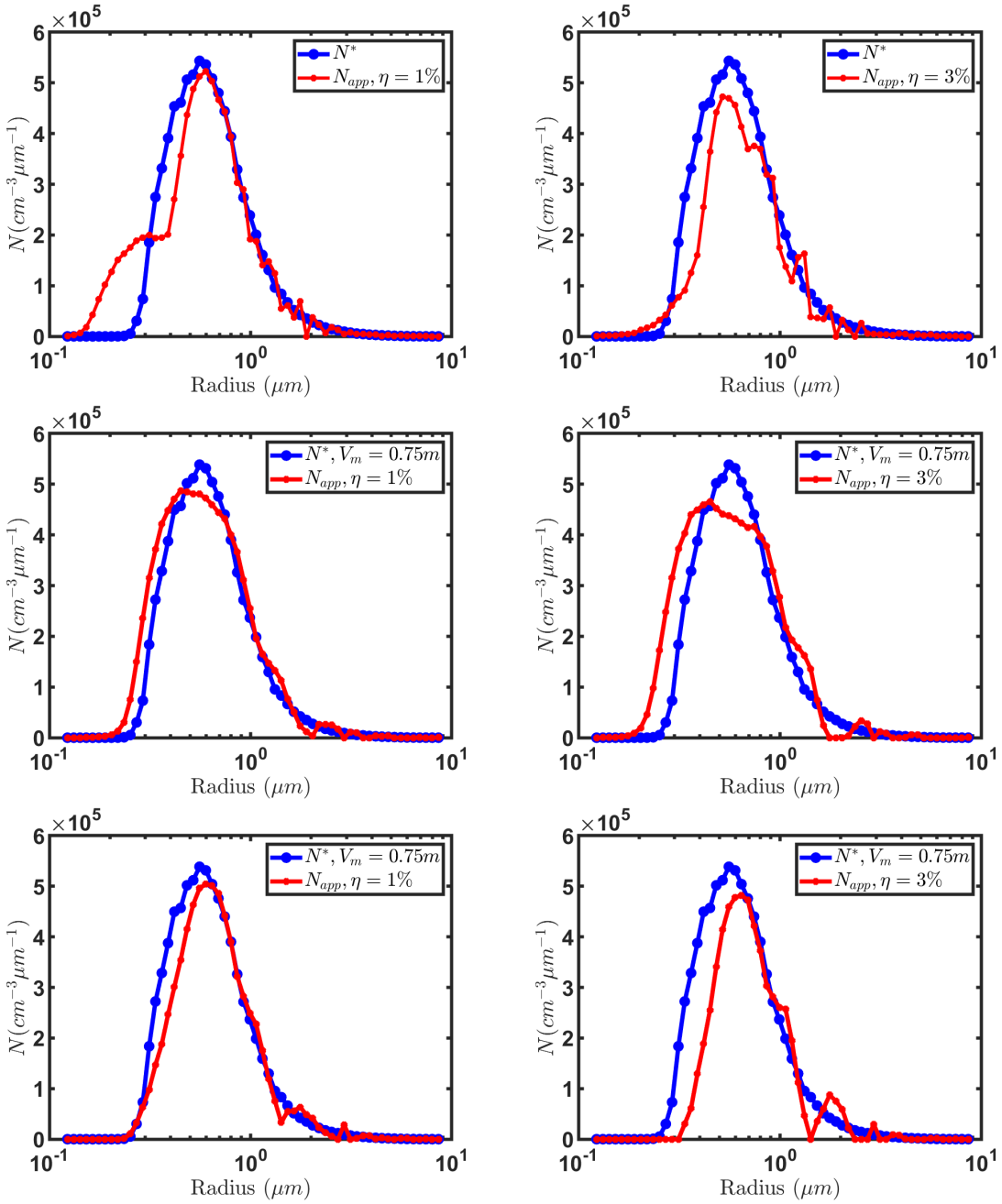

Figure 6.10: Identification results with noise adding (1% on the left, 3% on the right) in forescattering and Beer-Lambert case (first line), in forescattering and isotropic case (second line), backscattering and isotropic case (third line).

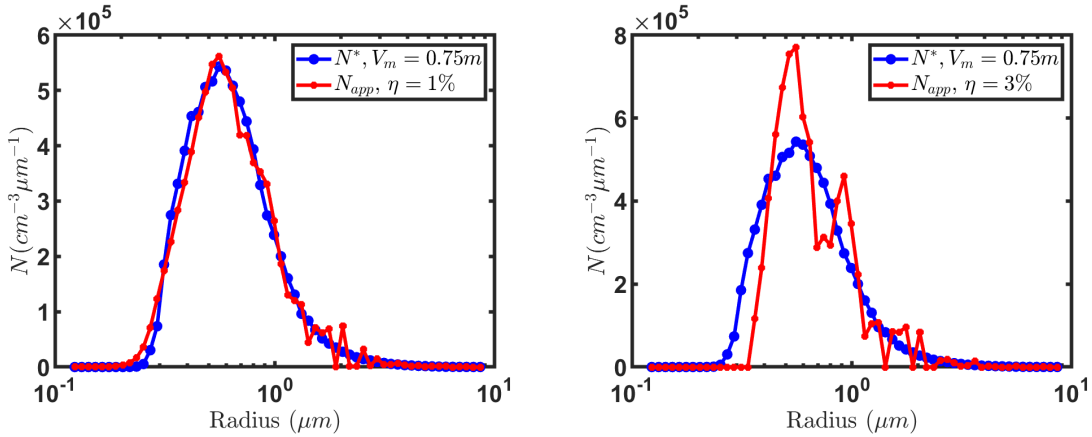

Figure 6.11: Identification results with noise (1% on the left, 3% on the right) in backscattering with anisotropic case.

Modelling	Measurement type	Noise η	relative cost	RE	E_{eff}	$V_m(N_{app})$
Beer-Lambert	Forescattering	0 %	8.247×10^{-13}	2.6%	0.062%	$7.501\times10^{-1}m$
Beer-Lambert	Forescattering	1 %	3.461×10^{-7}	19%	11%	$7.453\times10^{-1}m$
Beer-Lambert	Forescattering	3 %	3.451×10^{-6}	31%	28%	$7.478\times10^{-1}m$
Isotropic	Forescattering	0 %	6.169×10^{-8}	4%	0.1%	$7.516\times10^{-1}m$
Isotropic	Forescattering	1 %	9.735×10^{-5}	20%	0.75%	$7.474\times10^{-1}m$
Isotropic	Forescattering	3 %	9.959×10^{-4}	32%	1.91%	$7.402\times10^{-1}m$
Isotropic	Backscattering	0 %	3.193×10^{-8}	4.9%	0.72%	$7.495\times10^{-1}m$
Isotropic	Backscattering	1 %	2.304×10^{-5}	21%	1.83%	$7.597\times10^{-1}m$
Isotropic	Backscattering	3 %	2.327×10^{-4}	36%	4.30%	$7.845\times10^{-1}m$
Anisotropic	Backscattering	0 %	5.143×10^{-8}	7.2%	1.12%	$7.488\times10^{-1}m$
Anisotropic	Backscattering	1 %	2.171×10^{-5}	25%	1.27%	$7.554\times10^{-1}m$
Anisotropic	Backscattering	3 %	2.212×10^{-4}	46%	3.46%	$7.702\times10^{-1}m$

Table 6.8: The relative cost RC, the relative error RE, relative effective radius E_{eff}, and the approximated visibility (for $\lambda = 550nm$) for different modellings, measurement types and noise levels on the measurements.

Table 6.8 details values of the relative cost RC, the relative error RE, and the value of the visibility, for $\lambda = 550$ nm, obtained by the approximated DSD for different modellings, measurement types and noise levels on the measurements. According to Figures 6.10-6.11, the identification results are acceptable for 1% noise level: in particular, the peak at 0.5 μm is reached. For a noise level of 3%, the approximate distribution looks different from the target distribution. We note that in our identification method with a noise level 0%, we find an error between 3% and 7% on the approximated DSD which are errors similar to those found by other authors [19, 20]. Even in the cases with noise of 1% and 3%, we find that the errors are 25% and 30-46%, respectively.

It would be useful to study how the noise level influences the extinction value. Figure 6.12 illustrates the relative error $\tilde{E}_\eta^\lambda$ in extinction for the identification results obtained in the Beer-Lambert case (forescattering), Isotropic case (forescattering and backscattering), and the anisotropic case (forescattering). The relative error is calculated using the following formula:

$$\tilde{E}_\eta^\lambda = 100 \times \frac{|\sigma_{ext}^\lambda(N_{app}^\eta) - \sigma_{ext}^\lambda(N^*)|}{\sigma_{ext}^\lambda(N^*)}, \tag{6.8}$$

where N_{app}^η represents the approximated distribution for the noise level η=0,1, and 3. By examining Figure 6.12, we note that the maximum relative error for the identification of DSD by adding 3% of noise is 1% for the Beer-Lambert case, 8.6% for the isotropic case in forescattering, 4.6% for the isotropic case in backscattering, and 3% for the anisotropic case.

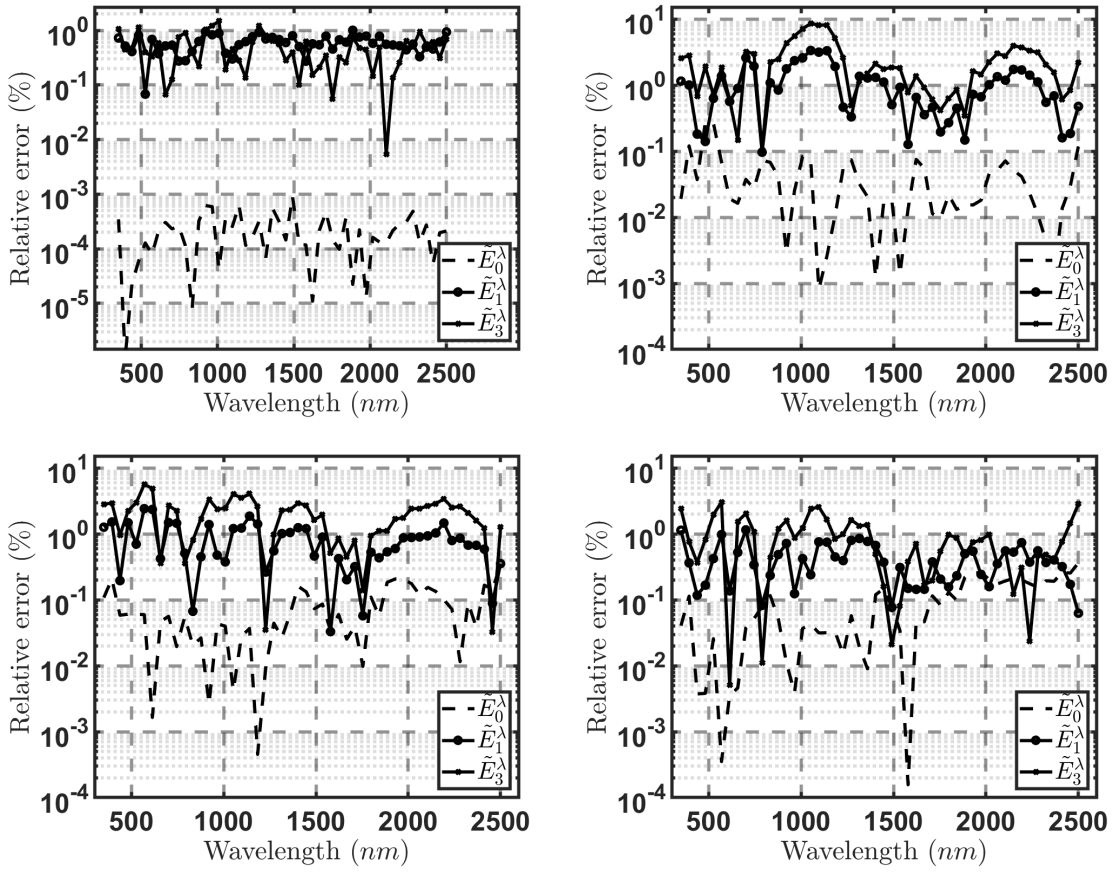

Figure 6.12: The relative error $\tilde{E}_\eta^\lambda$ on the extinction coefficient, obtained by (6.8), for the identification results in the Beer-Lambert case for forescattering (top left), Isotropic case for forescattering (top right), backscattering (bottom left), and the anisotropic case for backscattering (bottom right).

6.2 Droplet size distribution identification results with collimated source

In this section, we perform the same tests with PAVIN fog distribution presented in previous section but by using the irradiance measurements and a collimated source, where the radiance at $x = 0$ is dependent of μ (i.e we take $I(0, \mu) = I^+(\mu) = \delta_1(\mu)$ and $I(D, \mu) = I^-(\mu) = 0$).
In this case, the irradiance measurements can be approached by the following integral

$$\forall\, 1 \leqslant i \leqslant G,\, 1 \leqslant l \leqslant L, \quad M_{\lambda_l}(x_i) = \int_a^b \mu\, I^\star_{\lambda_l}(x_i, \mu)\, d\mu, \tag{6.9}$$

and the two coefficient a and b are given by the following form

$$a = \cos\left(\theta' + \frac{\pi}{2}\right) \qquad ; \qquad b = \cos(\theta'), \tag{6.10}$$

where $\theta' = 0$ for forescattering case and $\theta' = 180$ for the backscattering case. Then, our inverse problem becomes similar to problem posed in (5.13) and (5.14) where

$$J_1(N) = \frac{1}{2} \sum_{i=1}^{G} \sum_{l=1}^{L} \left(\frac{\int_a^b \mu\, I_{\lambda_l}(x_i, \mu)\, d\mu - M_{\lambda_l}(x_i)}{M_{\lambda_l}(x_i)} \right)^2. \tag{6.11}$$

J_ε is strictly convex, continuous and differentiable (the proof of these properties are similar to the proof presented in Appendix B for the problem (5.14)). Then, our updated problem admits a unique minimum. The gradient of J_ε (5.16) in Proposition 5.1 stays true where I_λ verifies (4.23), but p_λ verifies the adjoint problem defined by

$$\begin{cases} -\mu\, \dfrac{\partial p_\lambda}{\partial x}(x, \mu) + \sigma^\lambda_{ext}(N)\, p_\lambda(x, \mu) = \mathcal{K} p_\lambda(x, \mu, N) + q_\lambda(x, \mu, N),\ (x, \mu) \in X \\ \\ p_\lambda(0, \mu) = 0,\ \mu < 0 \quad \text{and} \quad p_\lambda(D, \mu) = 0,\ \mu > 0, \end{cases} \tag{6.12}$$

with

$$q_\lambda(x, \mu, N) = \sum_{i=1}^{G} \left(\frac{\int_a^b \mu\, I_\lambda(x_i, \mu)\, d\mu - M_\lambda(x_i)}{(M_{\lambda_l}(x_i))^2} \right) \mu\, \mathbb{1}_{(a,b)}(\mu)\, \delta_{x_i}(x). \tag{6.13}$$

As demonstrated in Figure 6.13, our identification results are deemed reliable when the noise level is set at 1%, notably achieving a peak at 0.5 μm. However, when the noise level is increased to 3%, the reconstruction starts to show noticeable changes. Table 6.9 provides a comprehensive overview of the values for the cost function $J_1(N)$, the relative cost RC, and the relative error RE for various modeling approaches, types of measurements, and different levels of noise added to the measurements.

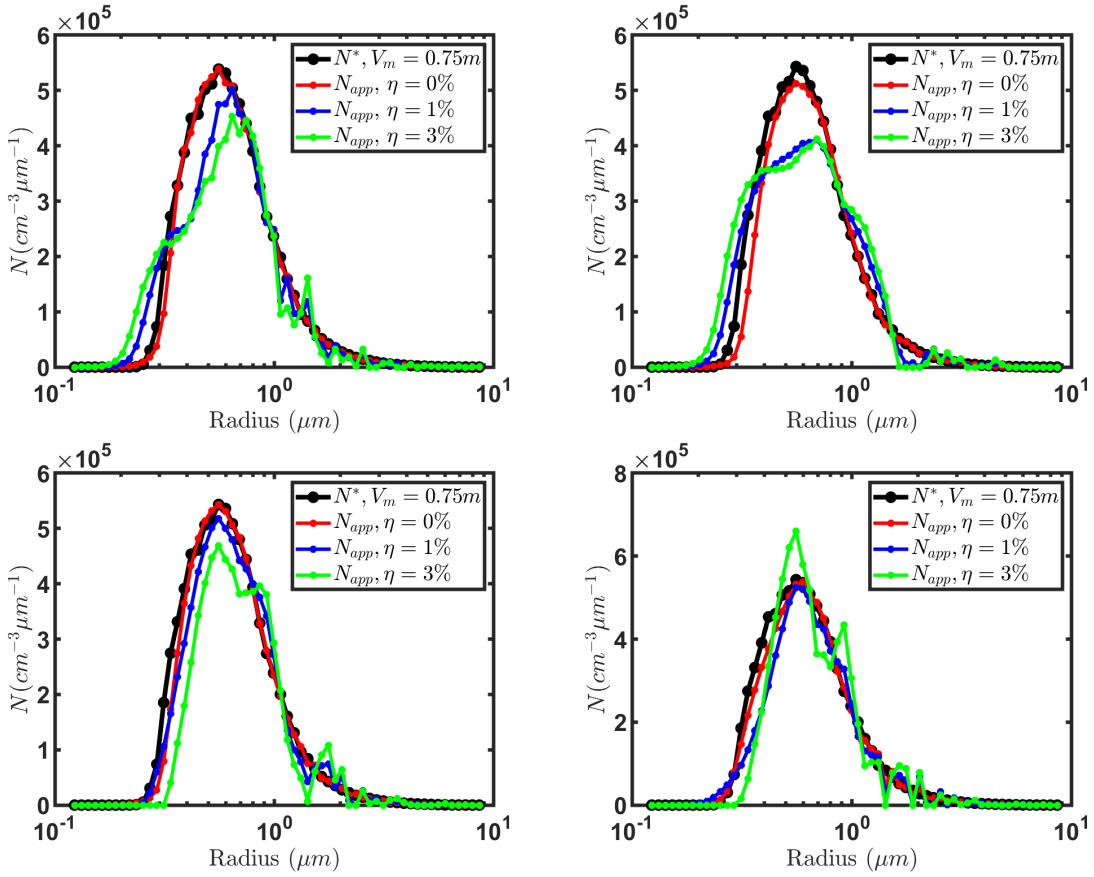

Figure 6.13: Identification results for collimated source obtained with forescattering measurements and Beer-Lambert modelling (top left) with forescattering measurements, isotropic modelling (top right), backscattering measurements and isotropic modelling (bottom left) and backscattering measurements and anisotropic modelling (bottom right) for a PAVIN platform DSDs.

Modelling	Measurement type	Noise η	$J_1(N)$	relative cost	relative error
Beer-Lambert	Forescattering	0 %	1.728×10^{-9}	2.374×10^{-12}	3.6 %
Beer-Lambert	Forescattering	1 %	9.488×10^{-4}	1.842×10^{-6}	16 %
Beer-Lambert	Forescattering	3 %	7.253×10^{-3}	7.135×10^{-6}	30 %
Isotropic	Forescattering	0 %	7.809×10^{-7}	2.434×10^{-7}	6 %
Isotropic	Forescattering	1 %	7.124×10^{-4}	2.224×10^{-4}	27 %
Isotropic	Forescattering	3 %	6.856×10^{-3}	2.136×10^{-3}	38 %
Isotropic	Backscattering	0 %	7.551×10^{-7}	3.027×10^{-8}	4 %
Isotropic	Backscattering	1 %	5.554×10^{-4}	2.227×10^{-5}	21 %
Isotropic	Backscattering	3 %	5.686×10^{-3}	2.279×10^{-4}	37 %
Anisotropic	Backscattering	0 %	3.529×10^{-6}	1.413×10^{-7}	10 %
Anisotropic	Backscattering	1 %	5.203×10^{-4}	2.084×10^{-5}	28 %
Anisotropic	Backscattering	3 %	5.258×10^{-3}	2.106×10^{-4}	38 %

Table 6.9: The cost $J_1(N)$, the relative cost RC and the relative error RE for different modellings, measurement types and noise levels on the measurements with collimated source.

Similar to the identification obtained in the case of Lambertian source, we present in Figure 6.14 the identification results of various DSDs obtained by using a Collimated source without noise levels on our measurements. According to this figure, we observe that our distribution is well approximated for the different modeling types.

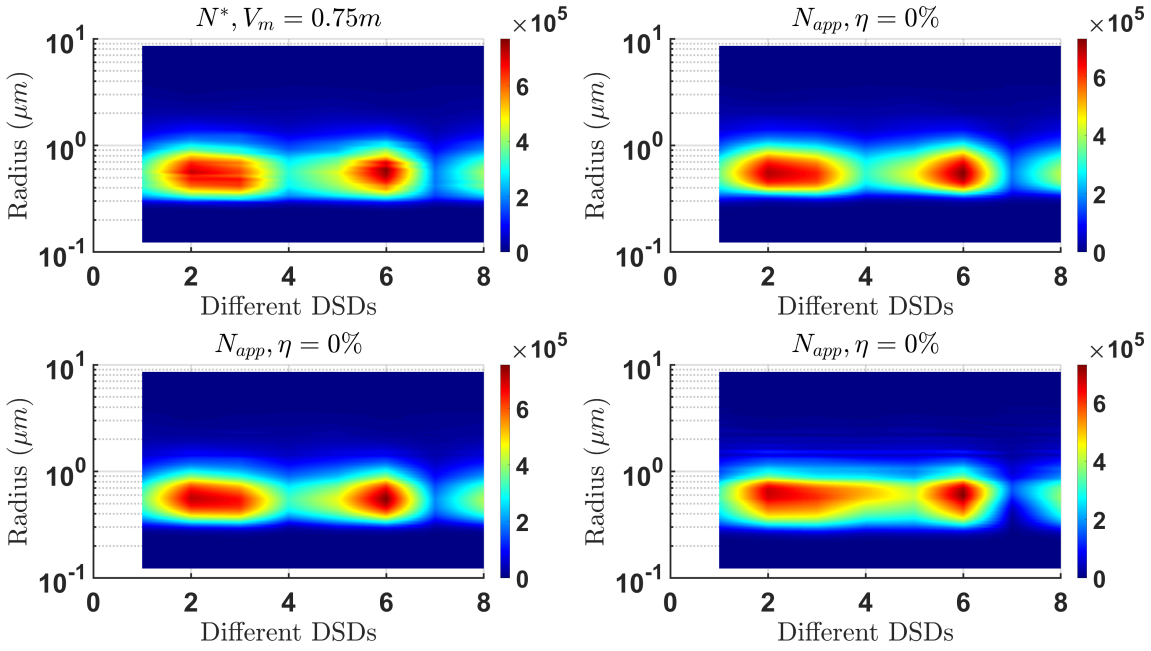

Figure 6.14: The target PAVIN DSDs (left top), the identification results, by using a collimated source, obtained with forescattering measurements, isotropic modelling (top right), backscattering measurements and isotropic modelling (bottom left), and backscattering measurements and anisotropic modelling (right bottom) for η=0%.

The robustness of the reconstruction in the isotropic case obtained in Figure 6.14 are also presented in Figure 6.15 for the noise level η=1% and 3%.

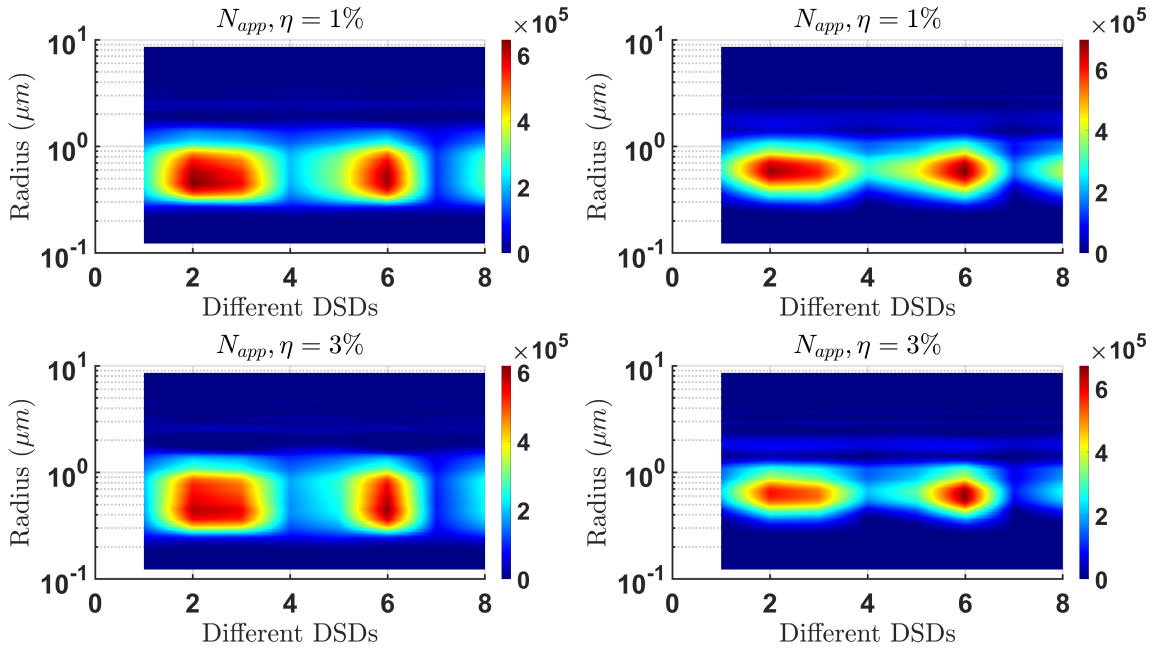

Figure 6.15: Identification results of various PAVIN DSDs, by using a collimated source, obtained with forescattering measurements, isotropic modelling (left), backscattering measurements and isotropic modelling (right) for η=1, and 3%.

6.3 Identification with Henyey-Greenstein phase function

In this section, we want to identify the DSDs by using the Henyey-Greenstein phase function for the collision operator

$$(\mathcal{K}I)_\lambda = \frac{\sigma^\lambda_{sca}(N)}{2} \int_{-1}^{1} \Phi_\lambda(\mu, \mu', N)\, I_\lambda(x, \mu') d\mu'. \tag{6.14}$$

The Henyey-Greenstein model, as described in [163], has a phase function that is not dependent on the droplet size distribution, unlike the Lorenz-Mie model. Instead, it depends on the anisotropy factor g. For additional details on this phase function, see Section 3.3.1 of Chapter 3.

$$\Phi(\cos\Theta) = \frac{1}{4\pi} \frac{1-g^2}{(1+g^2-2g\,\cos(\Theta))^{\frac{3}{2}}}, \tag{6.15}$$

where Θ is the scattering angle.
We compare the phase function produced by Lorenz-Mie theory for one droplet size

distribution in Figures 5.1a (with extinction coefficient $\sigma_{ext} = 4m^{-1}$) with the phase function of Henyey-Greenstein for different values of g in Figures 6.16. We use MiePlot [180] to compute the Lorenz-Mie phase function, which is a computer program for scattering light from a sphere using Mie theory. We observe, from Figures 6.16, that the Henyey-Greenstein for $g = 0.9$ is very close to the Mie phase function when the scattering angle closed to 0, this is not the case for the large scattering angles. But according to these curves, we can clearly see that the most important values of the phase function are for the smallest angles.

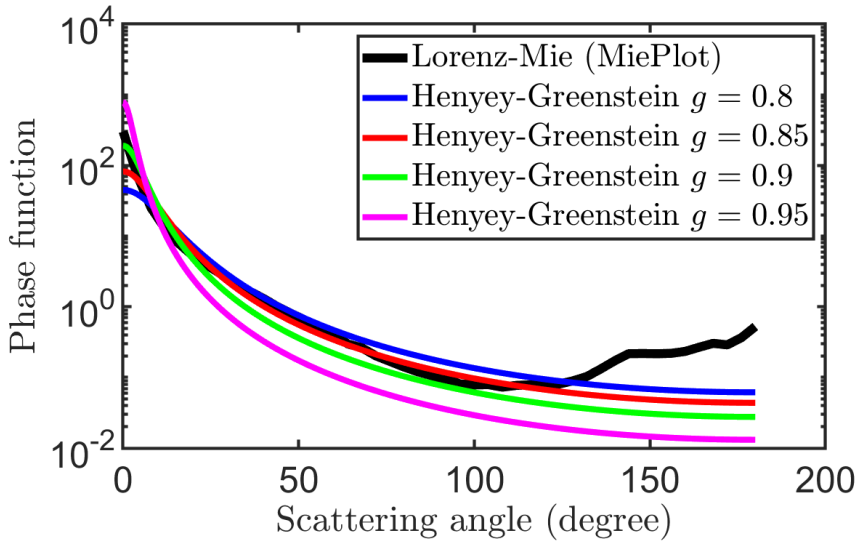

Figure 6.16: Comparison between the phase function computed by Lorenz-Mie theory (by using MiePlot [180]) for a one droplet size distribution in Figures 5.1a, and the phase function of Henyey-Greenstein for different values of g by using equation (6.15).

To identify the droplet size distributions by using these phase functions, we need to decompose them on a Legendre basis. For the decomposition of the Lorenz-Mie scattering phase function, we can see Lemma A.1 in Appendix A.2. similarly, for the decomposition of the Henyey-Greenstein phase function we can see equation (3.11) for Section 3.3 with $\alpha_k = g^k$. As mentioned in Section 4.5 of Chapter 4, to approximate the radiative transfer equation, we used 50 Legendre polynomials. We present in Figure 6.17 a comparison between the Lorenz-Mie phase function and the Henyey-Greenstein phase function obtained by using the decomposition on $K = 50$ the Legendre polynomials.
We observe in Figure 6.17 that the phase function obtained by decomposition on Legendre polynomials, both in Lorenz-Mie and Henyey-Greenstein, oscillate for large scattering angles. In relation to the numerical approximation of the radiative transfer equation, it is important to note that the oscillation does not have any impact on its values (see Section 4.5 of Chapter 4).

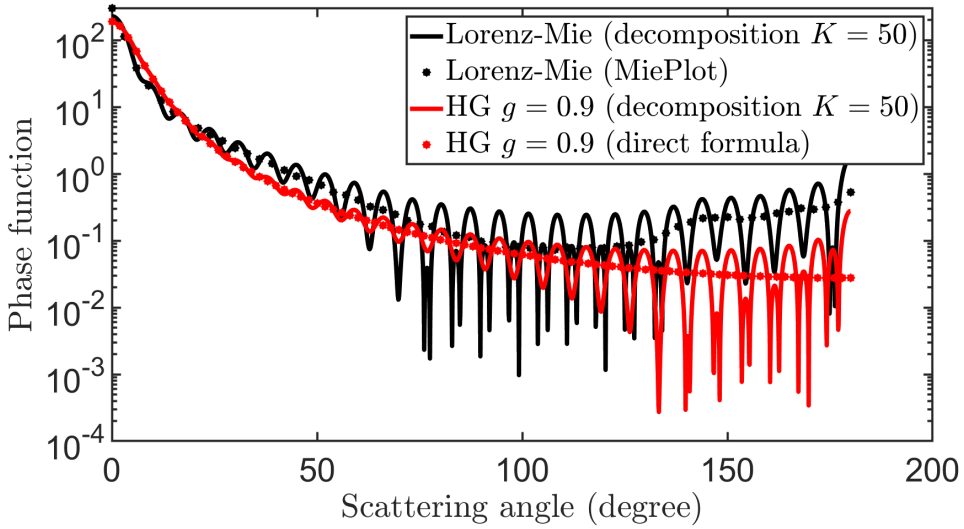

Figure 6.17: Comparison between the phase function computed by Lorenz-Mie theory by using MiePlot [180] and the decomposition with $K = 50$ for a one droplet size distribution in Figures 5.1a, and the phase function of Henyey-Greenstein for $g = 0.9$ by using equation (6.15), and by the decomposition with $K = 50$.

Figure 6.18 represents the approximation of one droplet size distribution by using the Henyey-Greenstein phase function for an anisotropy factor $g = 0.9$ for different noise level η. Furthermore, Table 6.10 details values of the relative cost RC, the relative error RE obtained for different source types, measurement types and noise levels on the measurements. These results obtained by using the Henyey-Greenstein phase function for the two types of source and different noise level are similar to the results obtained by using the Lorenz-Mie phase function presented in Tables 6.8-6.9.

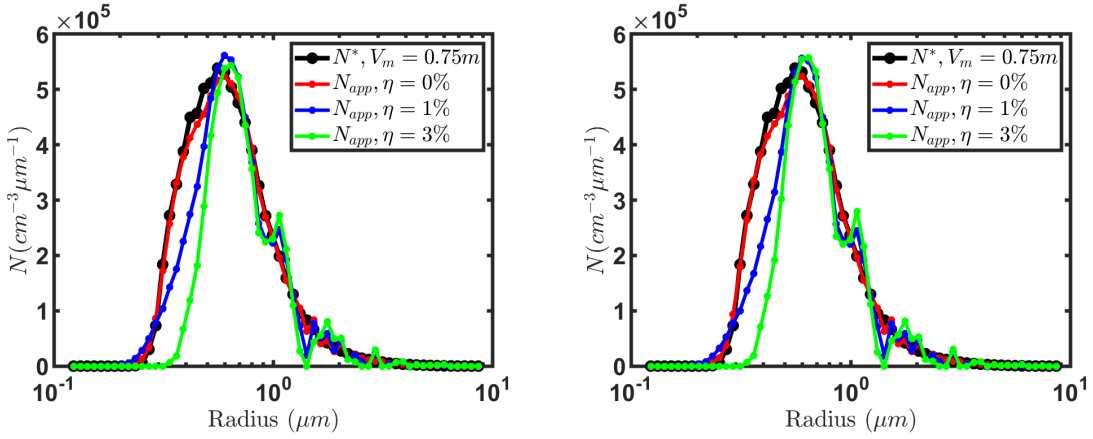

Figure 6.18: The approximated of the PAVIN DSDs in the case of: Lambertian source by using the radiance measurements (left), and Collimated source by using the irradiance measurements (right) with the decomposed Henyey-Greensterin phase function with $g = 0.9$ for different values of noise η.

Measurements type	Source type	Noise η	$J_1(N)$	relative cost	relative error
Radiance measurements	Lambertian	0 %	1.535×10^{-6}	6.151×10^{-6}	8.3 %
Radiance measurements	Lambertian	1 %	5.055×10^{-4}	2.025×10^{-5}	23 %
Radiance measurements	Lambertian	3 %	5.356×10^{-3}	2.145×10^{-4}	36 %
Irradiance measurements	Collimated	0 %	1.233×10^{-6}	4.938×10^{-8}	8 %
Irradiance measurements	Collimated	1 %	5.133×10^{-4}	2.055×10^{-5}	24 %
Irradiance measurements	Collimated	3 %	5.290×10^{-3}	2.118×10^{-4}	37 %

Table 6.10: The cost $J_1(N)$, the relative cost RC, and the relative error RE with $\varepsilon = 10^{-14}$ and $f(r) = \frac{1}{r^9}$ corresponding to Figure 6.18.

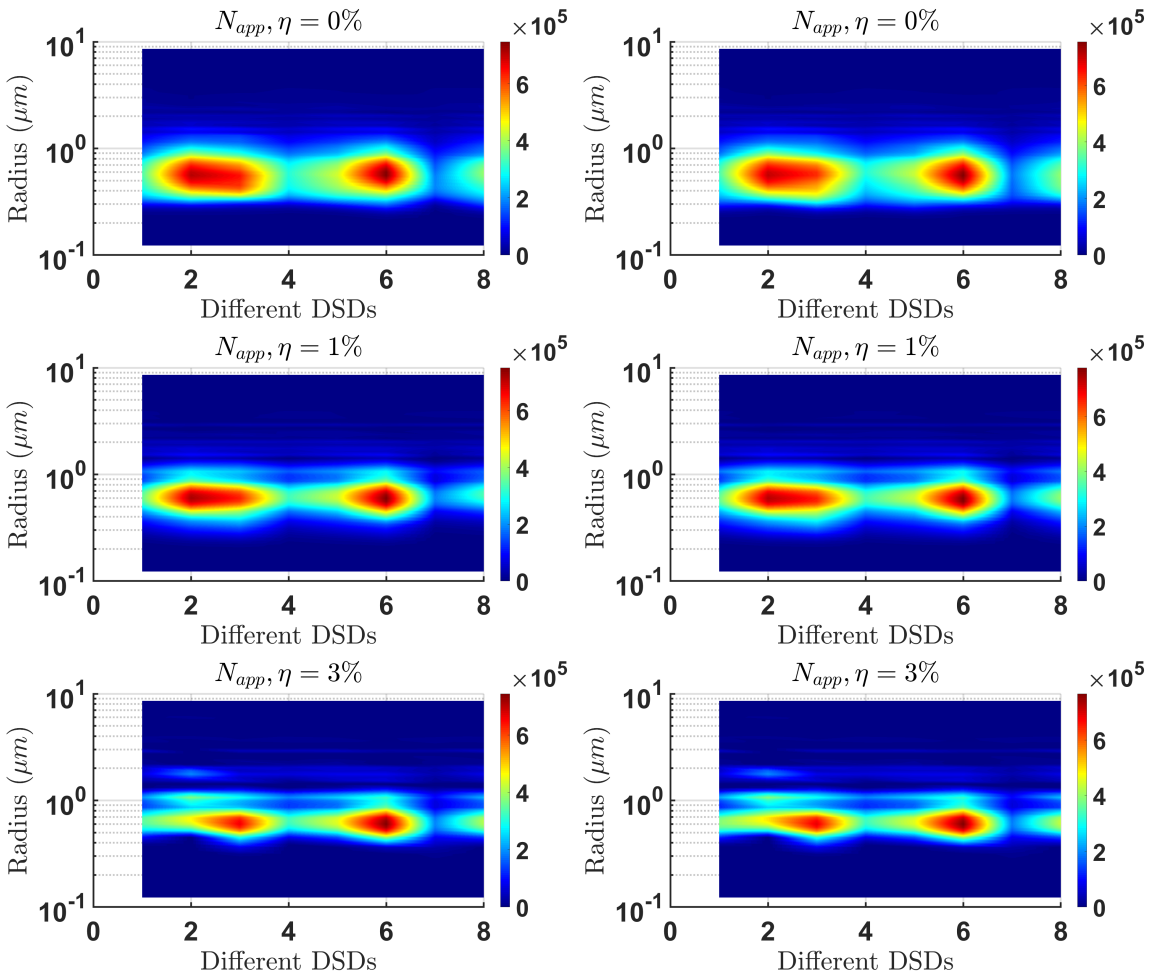

Figure 6.19: The approximation of the PAVIN DSDs for: Lambertian source by using the radiance measurements (left), and Collimated source by using the irradiance measurements (right) with the decomposed Henyey-Greensterin phase function with $g = 0.9$.

To be more general and to show the convergence of our identification method, we present in Figure 6.19 the approximation of various droplet size distribution presented in Figure 5.2 by using the Henyey-Greenstein phase function for an anisotropy factor $g = 0.9$.

Without a noise level, we observe a good approximation of the DSDs. For a noise $\eta = 1\%$, the red part (the peak of DSDs) begin to change but we obtain almost the same form of the results obtained without noise level. For a noise $\eta = 3\%$, we observe that the peak is reached for some distributions, but less well than that with 1%.
According to the results presented in this chapter, we deduce that the droplet size distribution identification method is tested for different model and measurements types. As we have seen, the reconstruction of the DSD in the anisotropic case requires measurements in backscattering. Additionally, the identification method is tested for different levels of visibility (0.25 m, 0.5 m, 0.75 m). These visibility levels are tested using the normalized problem in the spatial domain (0,1). Comparisons between the identification results of the granulometric distribution using the Mie phase function and the Henyey-Greenstein phase function have been obtained. In some cases, the robustness of our identification method has been studied with different levels of noise on synthetic measurements. The relative errors on our approximated distribution obtained are in the range of 30 to 40 %. Furthermore, the effect of different levels of noise on the value of various optical parameters (e.g., extinction coefficient, visibility) is studied. These results show that the relative errors on the extinction coefficient do not exceed 8 % for a noise level of 3 % (where the relative error in the approximate distribution is almost 40 %). Additionally, our identification method is tested for different types of distributions, such as the natural fog distribution measured in the Paris fog campaign in Paris in 2007, and also on models like the Shettle and Fenn model, which represents fog with large droplets.

Chapter 7

Experimental measurements and 3D numerical simulations

According to previous results presented in this thesis, the method of fog droplet size distribution identification was made using a 1D model of the radiative transfer equation and synthetic radiation measurements (as presented in Chapter 6). The next step towards achieving a higher goal is the identification of the droplet size distribution from experimental measurements collected in the PAVIN Fog&Rain platform of Cerema. To achieve this objective, we must understand cases where our developed 1D model is representative of the experiments. Recalling that the 1D slab model used in this work is in fact a 3D model in which the propagation depends only on one space dimension, it can be representative of experimental measurements in the case where measurements are made with an infinite planar Lambertian light source or very close to a sufficiently large source, which is difficult to access in the PAVIN platform of dimension $30\times5.5\times2.25$ m platform. The second possibility of applying our 1D identification method of the droplet size distribution is to use a collimated source and to perform measurements around its revolution axis. This latter option will be investigated in the future.
In the case where the source used is not large enough or collimated, which is the case of the source used at the PAVIN platform of Cerema (the characteristics of this source are given in detail in this chapter), we must go further from the identification of the droplet size distribution by a 1D model and develop an identification model based on a 3D radiative transfer equation. To achieve this objective, we present in this chapter a preliminary work based on comparisons of the 3D model simulated thanks to the SWEET simulator developed at Cerema and experimental measurements. In these comparisons, we used the droplet size distributions that are already measured in the platform PAVIN by particle size analyzers PALAS WELAS 2100 [24] presented in Figure 1.18. These comparisons are very preliminar and will serve as seminal works for further extensive studies.

This chapter is organised as follows. Section 7.1 provides a review of the three-dimensional stationary radiative transfer equation and explains the numerical method used to approximate them using the SWEET simulator developed at Cerema. The characterisation of the source used in our experimental measurements on the PAVIN platform is described in section 7.2. We end this chapter with Section 7.3, in which we compare the numerical

data procured through the use of the SWEET simulator with the experimental data performed in PAVIN platform.

7.1 Introduction

Our aim is to compare numerical simulations of the 3D radiative transfer equation with the experimental results obtained from the PAVIN platform. In the realm of three-dimensional modeling, complexity arises as boundary conditions are no longer established directly on the source and sensor. Instead, these conditions are applied to the walls, floor and ceiling of the fog platform. Measurements with the spectroradiometer leads to a reflectance below 4% for wavelengths ranging in [350 nm, 2500 nm]. This implies that the wall's albedo is zero, signifying complete absorption of light with no emission (we do not work in the thermal domain). We recall, from Chapter 3, the following three dimensional stationary radiative transfer equation.

$$u \cdot \nabla_r I_\lambda(r,u) + \sigma^\lambda_{ext}(N) I_\lambda(r,u) = \frac{\sigma^\lambda_{sca}(N)}{4\pi} \int_{\mathbb{S}^2} I_\lambda(r,v)\Phi_\lambda(r,v,u)\, dv, \tag{7.1}$$

where σ^λ_{ext} and σ^λ_{sca} are the extinction and scattering coefficients defined in (3.21) and Φ_λ is the phase function satisfying

$$\forall (u,v) \in \mathbb{S}^2 \times \mathbb{S}^2,\ \frac{1}{4\,\pi} \int_{\mathbb{S}^2} \Phi_\lambda(u,u')d\Omega' = 1. \tag{7.2}$$

The full Monte-Carlo simulator developed by Cerema, called SWEET [38] (Simulating WEather for intElligent Transportation systems) to calculate and simulate irradiances or radiances uses a Monte-Carlo method by Backward Ray-Tracing, i.e the photons are launched from the sensor and are traced back to the light source by going up the light path while taking into account the possible interactions with the water droplets present in the medium. The SWEET simulator developed by Cerema is a research-oriented and physically based simulator for internal use complementary to the Fog and Rain PAVIN platform. It is written in C++, runs on Linux and Microsoft Windows and uses OpenCL for GPU computing.

SWEET uses a Monte-Carlo method, specifically employing a backward approach, to solve the Radiative Transfer Equation (RTE) in a medium that participates. This technique is predicated on volumetric path tracing. To accomplish this, photons move in the medium and their interactions with droplets of fog are simulated through a stochastic process [194]. In detail, a photon is randomly sampled from the observation point and traced along a random direction at the speed of light. The duration of the trace is dictated by an exponential probabilistic law. If the photon reaches a light source, the random trajectory ends. Otherwise, if it interacts with an object, the reflective properties of the surface change the photon's direction. If neither a source nor an object

is encountered, the phase function is used to sample a new direction, representing a collision with a water droplet. This is combined with a new duration, and the process is repeated iteratively until either a source or an absorbing material is encountered.
In this chapter, we are focused on calculating the irradiance E_λ, which is the integration of radiance at $r \in \mathbb{R}^3$ for a given wavelength λ:

$$E_\lambda(r) = \int_0^{2\pi} \int_0^{\pi/2} I_\lambda(r, \theta, \varphi) \cos(\theta) \sin(\theta) \, d\theta \, d\varphi. \tag{7.3}$$

7.2 Representation of the source

In this section, we present the details of the source presented in Figure 7.1 (left) used for the experimental measurements carried out on 21 March 2023 on the PAVIN Fog&Rain platform at Cerema. The source used has a dimension of 36 cm $\times$ 36 cm and has been calibrated.
In photometry, luminous flux or luminous power is the measure of the perceived power of light. It differs from radiant flux, the measure of the total power of electromagnetic radiation (including infrared, ultraviolet, and visible light), in that luminous flux is adjusted to reflect the varying sensitivity of the human eye to different wavelengths of light. The SI unit of luminous flux is the lumen (lm). One lumen is defined as the luminous flux of light produced by a light source that emits one candela (cd) of luminous intensity over a solid angle of one steradian (sr). The total luminous flux obtained by our calibrated source is equal to 4003 lm with an efficiency of 80 lm/W. Also, we give in Figure 7.1 (right), the intensity of the source as a function of the wavelengths between 450 nm and 900 nm for different distance values. These data was sent by ARDOP Industrie [195].

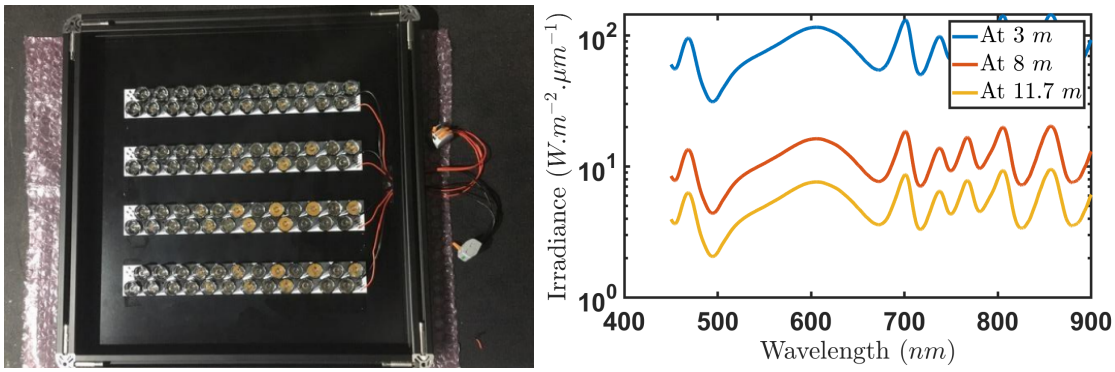

Figure 7.1: Representation of the source used in our experimental measurements obtained from ARDOP Industrie [195] (left), and the intensity in function of the wavelengths for different distance was sent by ARDOP Industrie (right).

7.3 Comparison between experimental and numerical data

We will begin this section by describing the experimental methodology used to carry out the measurements on the PAVIN platform of Cerema. The source of dimension 36 cm × 36 cm is positioned at the beginning of the platform. In addition, a PSR+ spectroradiometer (see Table 7.1) is positioned at a distance d from the source. The distance can be changed along the platform. The PSR series spectroradiometers are highly efficient portable devices, covering a very broad range of wavelengths from 320nm to 2500nm. As explained in Figure 7.2, this spectroradiometer is equipped with a silicon sensor for the UV-VIS-NIR range and two cooled InGaAs sensors for the SWIR range. These InGaAs sensors enhance performance in SWIR bands 1 and 2 and greatly improve the signal-to-noise ratio for optimal acquisition quality.

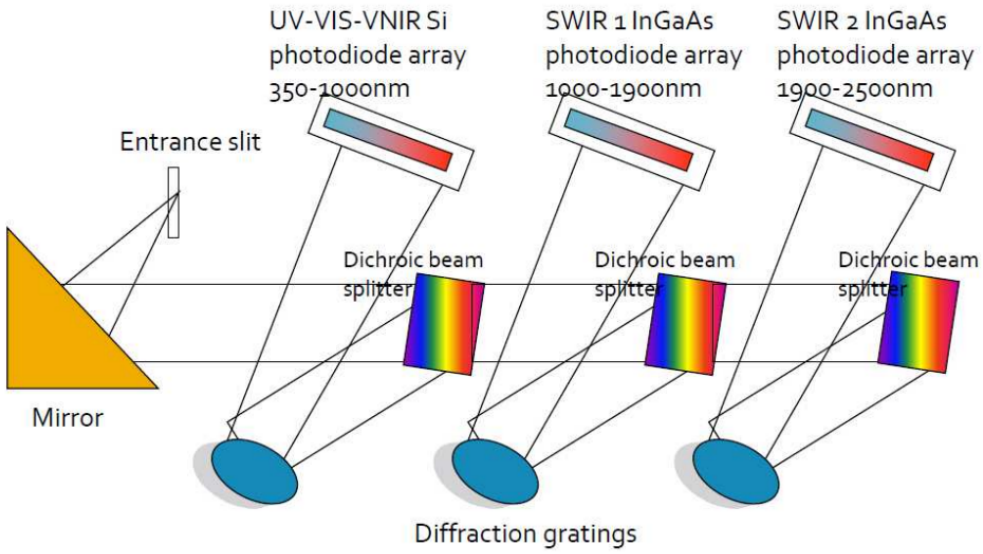

Figure 7.2: Diagram of the principle of operation of the spectroradiometer PSR+.

Model	PSR+	Spectrum	350-2500 nm
Dimension	21.6×29.2×8.25 cm^{-3}	Wavelength accuracy	±0.5nm bandwidth
weight	3.5 kg	Radiance Max	1,5×10^{-4} W/cm^2 /nm/sr

Table 7.1: Characterization of Cerema's PSR+ spectroradiometer.

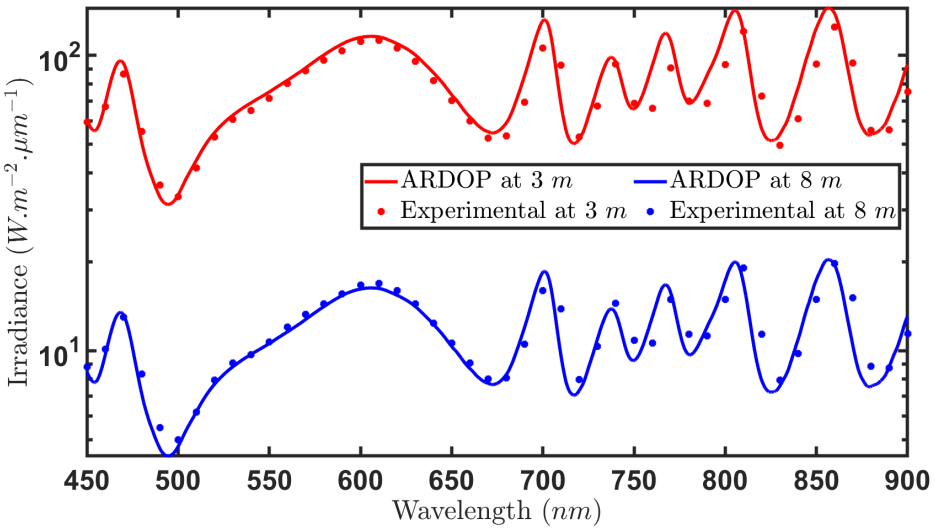

Figure 7.3: Comparaison between experimental data and ARDOP data for different distances without fog

To demonstrate the similarity between our experimental data and that sent by ARDOP, Figure 7.3 displays our results alongside ARDOP's original data. Now that it has been confirmed that the experimental measurements are consistent with the data provided by ARDOP for specific measurement points in non-foggy conditions, the next step is to verify the experimental data using numerical simulations.
We will describe the process of modelling the platform and measuring instruments. Initially, we need to create models in SketchUp software as shown in Figure 7.4, which will be fed into a 3D simulator specifically designed by Amine Ben Daoued.

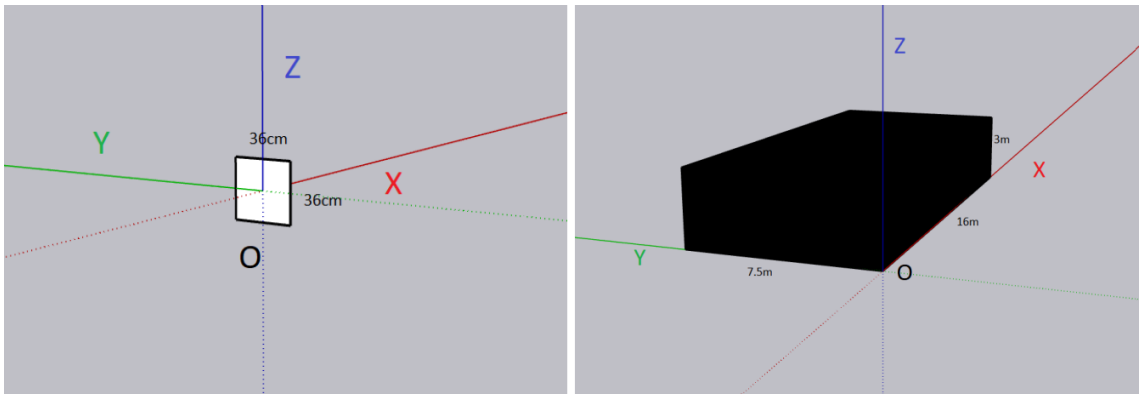

Figure 7.4: SketchUp modelling of the source (left), and of the PAVIN Fog&Rain platform (right)

This simulator will use the Monte-Carlo method for backward ray-tracing to calculate and simulate irradiances or radiances. The next step involves creating a model of the platform in SketchUp by adding materials on the walls, which will be utilized later to

apply our boundary conditions.
To facilitate a comparison between the numerical outcomes obtained through the Monte-Carlo algorithm and the experimental data, we evaluate a ratio based on measurement points and wavelengths employed.
Let

$$C(x,\lambda) = \frac{\text{Experimental}(x,\lambda)}{\text{Simulation}(x,\lambda)}. \tag{7.4}$$

For the case without fog, we present in Figure 7.5 the value of the ratio C as a function of different distances x and wavelengths λ. Based on this figure, it can be inferred that our numerical simulation closely matches the experimental measurements in non foggy conditions, indicating the accuracy of our simulation.

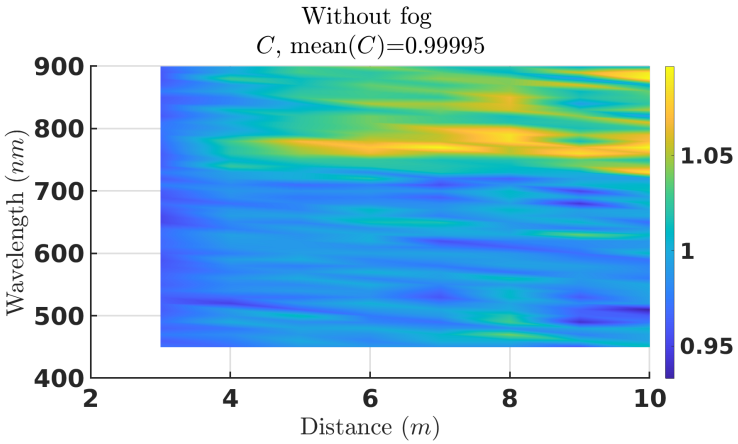

Figure 7.5: The ratio C in the case without fog.

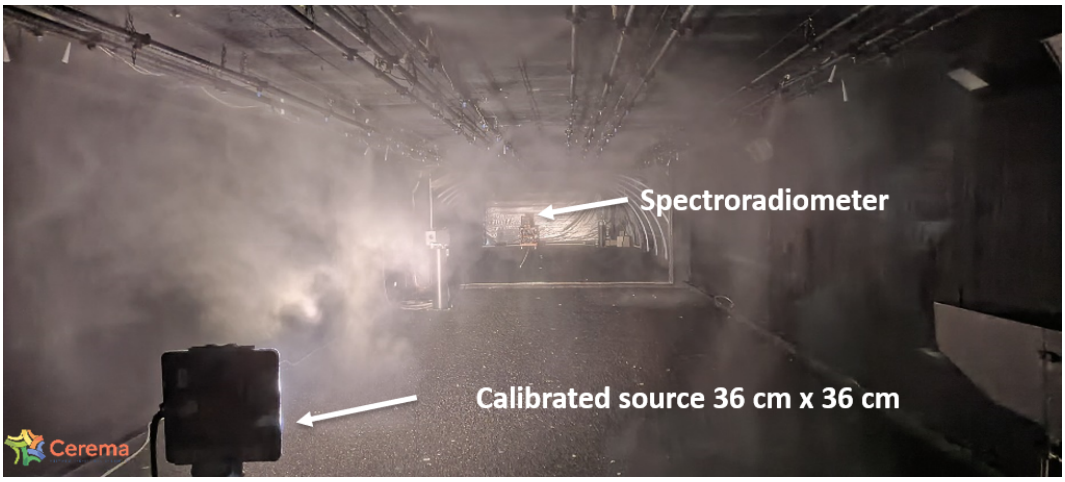

Figure 7.6: Experimental approach used to carry out the measurements on the PAVIN Fog&Rain platform of Cerema

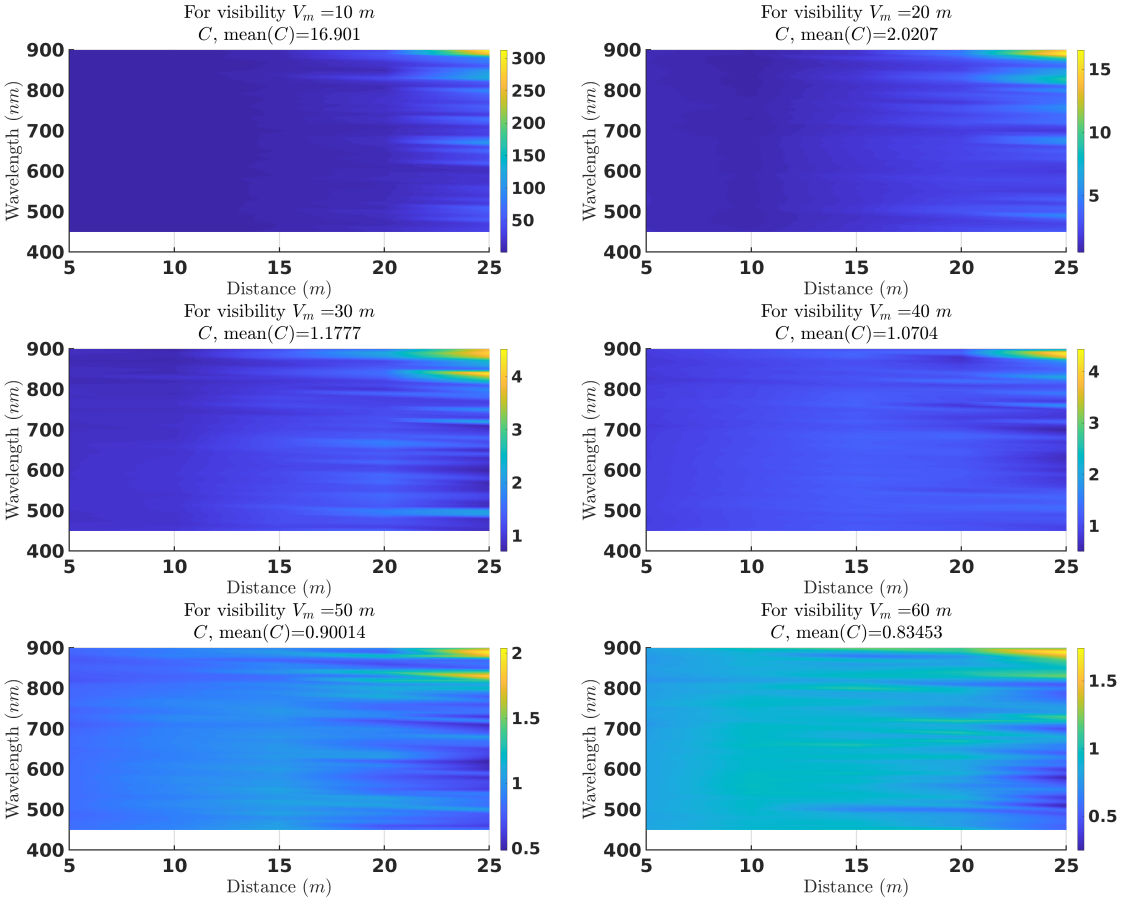

Figure 7.7: The ratio C in the case with fog for different visibility.

Our current goal is to assess the performance of our simulator under varying visibility conditions in fog. We conducted some tests according to the protocol depicted in Figure 7.6 in a case with fog. Figure 7.7 illustrates the C ratio, as defined in equation (7.4), across different particle size distributions corresponding to various levels of visibility presented in Figure 7.8.

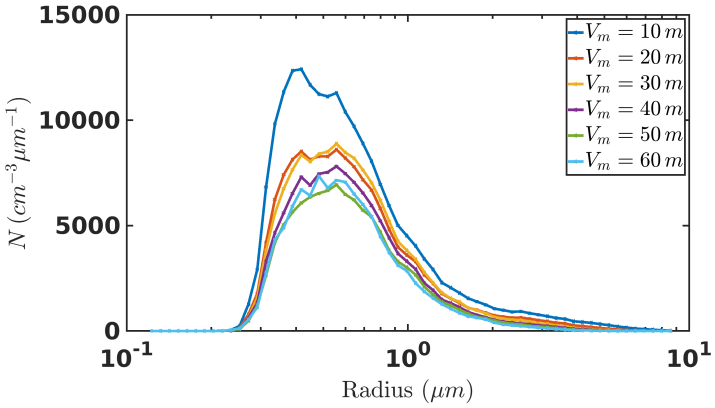

Figure 7.8: Artificial fog droplet size distributions used in the SWEET simulator measured at PAVIN platform of Cerema for different visibility.

Figure 7.7 demonstrates that the ratio C approaches 1 when the visibility in fog is 40, 50, or 60 meters. Furthermore, it can be observed that for greater distances with low visibility (as shown in the first three figures in Figure 7.7), there exists a disparity between the numerical simulation and the experimental data. This results can be confirmed in Figure 7.9 where we plotted mean on wavelength of C defined in (7.4).

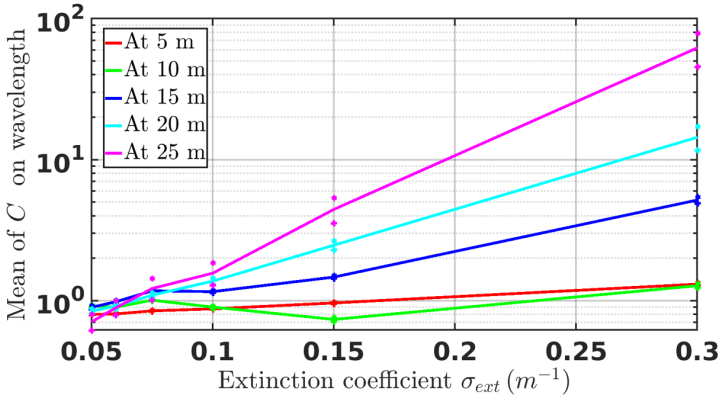

Figure 7.9: The mean of ratio C in the case with fog in function of different extinction coefficient.

According to the findings outlined in this chapter, it can be inferred that the results of 3D simulations closely align with experimental measurements conducted at the PAVIN platform, with the exception of specific situations involving measurements taken at a large distance from the source in conditions of dense fog.
These preliminary results are interesting since they show a roughly good agreement between 3D SWEET simulator and experimental measurements. Nevertheless they highlight some gaps which could be explained by the use of DSD measured locally in the platform with the PALAS device. This observation reinforces the decision to develop a droplet size distribution identification method based on a comprehensive 3D model of the radiative transfer equation. Moreover, it is essential to note that our methodology in this study assumes a homogeneous fog in which the DSD is constant over the whole platform and optical properties do not vary with spatial parameters. This assumption could contribute to the variation observed between simulations and experimental measurements is some cases. This highlights the motivation to expand the 3D model to take into account the optical properties that depend on spatial parameter.

Chapter 8

Conclusions and perspectives

8.1 Conclusion

The droplet size distribution (DSD) in a fog or cloud has an impact on the optical properties of the medium and its knowledge is therefore necessary to take into account clouds or fogs in meteorological models for example. We developped this work of identifying DSDs for another application than meteorology, namely the evaluation of optical sensors such as cameras, RADARs or LiDARs in adverse weather conditions for applications to intelligent transport systems.

We proposed an identification method based on radiation measurements at different wavelengths in the 350 nm - 2500 nm spectral band and the inversion of radiative transfer models. We assumed that the medium in which the measurements were made could be considered as optically homogeneous and that the radiative transfer within it could be modelled by a one-dimensional space equation. We then considered a complete modelling of the radiative transfer equation by taking into account a collision operator provided by the DSD via the Mie theory.

A least-squares method combined with the Barzilai Borwein algorithm has been used to identify the droplet size distribution (DSD) from radiation measurements. The minimization of the cost function required to calculate its gradient with respect to the DSD, what was done thanks to the resolution of an adjoint problem to the radiative transfer equation.

Inspired by Yvon's works, a decomposition method on the double Legendre basis has been used to approximate the stationary radiative transfer equation and its adjoint. The numerical method has been evaluated and validated on several explicit solutions of the stationary radiative transfer equation. In addition, an extensive numerical study was carried out to determine the convergence errors in the proposed numerical methods. A comparison between the Barzilai-Borwein algorithm and two algorithms based on the conjugate gradient was performed. It concluded that the Barzilai-Borwein method was more efficient than the other two and all numerical applications were performed with this algorithm.

Various models describing fog DSDs (Shettel and Fenn) and real DSD measured in natural conditions (Paris Fog campaign) or in artificial conditions (Cerema PAVIN platform) are used to compute synthetic radiation measurements via Mie theory and

the radiative transfer equation under different assumptions (Beer-Lambert modelling, isotropic or anisotropic collision operator).

Afterwards, the identification of the DSDs was carried out using these three radiative transfer modellings. In the Beer-Lambert case, the DSD reconstruction was successful by using forescattering measurements. In case of a modelling with an isotropic collision term, forescattering or backscattering measurements led to well reconstruct the DSD. From our numerical experiments, the identification method in the anisotropic case requires backscattering measurements. Furthermore, we test our identification method using other type of sources such as collimated sources by performing the irradiance measurements. We studied also the identification of DSD in the anisotopic case by using the Henyey-Greenstein function where we obtained a good approximation of the distributions.

We also explored in this thesis the robustness of the method by adding a several noise levels on our synthetic measurements and constated that the DSD reconstruction is very sensitive with respect to the noise adding on measurements. In some case, we compare the values of approximated extinction coefficient computed in function of wavelengths from the approximated DSD and the target extinction coefficient by using the Lorenz-Mie formula.

Particle size distribution identifications constitute a wide area of research, and numerous unresolved issues necessitate further exploration of light scattering theory and particle size distribution inversion approaches.

8.2 Perspectives

The improvement of the identification process for droplet size distribution (DSD) presents a promising direction for future exploration. This will involve investigating advanced optimization techniques, innovative algorithms, and integrating data from a range of sensor sources to enhance its precision and versatility.

Expanding the use of this methodology to other weather conditions, such as heavy rainfall, snow, smoke or dust offers valuable insights into its durability in different atmospheric contexts, allowing for crucial adjustments to enhance its wider applicability to automated transportation safety purposes. It is important to notice that the real-time identification of PSD could present a challenging objective for future works related to application for algorithms embedded in vehicles. It will enable continuous analysis for critical applications such as intelligent transport systems, which will require adaptations to accommodate dynamic atmospheric conditions.

Adapting the methodology to other areas, including environmental remote sensing or atmospheric monitoring, could be investigated. This evaluation of its versatility across different contexts positions the developed methodology in our works as a transdisciplinary

tool. Improvement of the methodology's accuracy remains a key trajectory through continual exploration of more sophisticated light scattering models, such as T-matrix method extending the Mie theory.

We detail below more precise perspectives.

8.2.1 Experimental validation of the identification method

The most important aspect is to validate our method through experiments in real conditions and not only, as made in this thesis, with synthetic measurements.

Field measurement campaigns would enable us to compare the results obtained with our method to real data, thereby reinforcing the credibility of our approach. As explained in Chapter 7, it would be necessary to perform experiments in the PAVIN platform for which a 1D modelling is relevant: the use of a collimated source could be useful in this way.

An other perspective is to pursue the works started in Chapter 7 concerning the comparison between real measurements and numerical simulations using a 3D Monte-Carlo method to approximate the RTE. The results show that 3D simulations performed by the SWEET simulator are close to real measurements in several cases. All the theoretical calculations made in Chapter 5 have to be adapted to the 3D case. The computing time necessary for the identification process will be an important issue to overcome. The measurements are local and then a Monte Carlo approach is relevant to simulate the radiance at local points, contrarily to deterministic methods, but the gradient expression of the cost function involves integral over the space domain of the radiance and the adjoint state: this will increase considerably the computing time. It will then be necessary to adopt particular numerical integration schemes in order to reduce this time.

8.2.2 Application in other fields

Exploring other application areas for our method offers an opportunity to broaden the impact and relevance of our work. For example, the application of the droplet size distribution reconstruction could be expanded in the future to other environments, such as dust, which is of interest for mobile agricultural robotics in the field of AgroTechnologies where the environment is often challenging to control. A project is already underway at Cerema in collaboration with the research unit Technologies and Information Systems for Agrosystems (TSCF), affiliated with the INRAE Clermont Auvergne-Rhône-Alpes Center. This unit conducts advanced research in key areas such as agriculture, environment, and food. It is also involved in research, expertise, and testing activities focused on the safety and performance of agro-equipment, contributing to improving safety in agriculture and reducing agricultural-origin pollution.

In addition, the work carried out in this thesis is under the hypothesis of non-polarized light, future work will be launched at Cerema using the polarization of light by the use of polarimetric camera. Light polarization is a property of light waves that depicts the direction of their oscillations. A polarized light vibrates or oscillates in only one direction. This is in contrast to a nonpolarized light that vibrates in many directions. A polarized light may be plane-polarized, circularly polarized or elliptical-polarized light based on the net direction of the vibrations. Experimental results have already been obtained on the characterization of the backscattering of polarized light in foggy environments, see e.g. [196, 197].

Appendix A

Decomposition on the basis of Legendre polynomial

A.1 Decomposition of S_1 and S_2 on the basis of Legendre polynomial

In order to approximate the solution of the radiative transfer equation by using the decomposition on the double of Legendre basis, it is necessary to compute the decomposition of the Lorenz-Mie scattering phase functions defined in (3.26). In the following section, we provide the decomposition of S_1 and S_2 as presented in equations (3.12)-(3.13). It is important to note that the Legendre polynomials are defined for all $\mu \in [-1, 1]$ and can be computed using the following recurrence (as described in [168]):

$$\begin{cases} P_0(\mu) = 1 \quad , \quad P_1(\mu) = \mu, \\ \forall\, n \geqslant 1,\ P_{n+1}(\mu) = \dfrac{(2n+1)}{(n+1)}\,\mu\, P_n(\mu) - \dfrac{n}{(n+1)}\, P_{n-1}(\mu). \end{cases} \tag{A.1}$$

To compute the decomposition

$$\forall\, \mu \in [-1, 1],\ S_1(\mu) = \sum_{i=0}^{+\infty} \alpha_i\, P_i(\mu) \quad ; \quad S_2(\mu) = \sum_{i=0}^{+\infty} \beta_i\, P_i(\mu) \tag{A.2}$$

of S_1 and S_2 on the basis of Legendre polynomial, we express the polynomials π_n and τ_n occurring in (3.12)- (3.13) in function of the Legendre polynomials $(P_n)_{n\geqslant 0}$ and we obtain the following decomposition:

$$\pi_0 = 0, \text{ and } \forall n \geqslant 1,\ \pi_{2n} = \sum_{k=0}^{n-1} (4k+3) P_{2k+1},\ \pi_{2n-1} = \sum_{k=0}^{n-1} (4k+1) P_{2k}, \tag{A.3}$$

$$\tau_0 = 0,\ \tau_1 = P_1,\ \tau_{2n} = (2n)^2 - \sum_{k=0}^{n-1} (4k+1) P_{2k},\ \tau_{2n-1} = (2n-1)^2 - \sum_{k=0}^{n-2} (4k+3) P_{2k+1}. \tag{A.4}$$

By injecting (A.3),(A.4) in (3.12),(3.13), and (A.10), we obtain after some computations:

$$\forall k \geqslant 0, \begin{cases} \alpha_{2k} = \sum_{n=k\vee 2}^{+\infty} p_1(n,k) + \left(\frac{3}{2}a_1 - \frac{5}{6}b_2\right)\delta_{k0} + \frac{10}{3}b_2\delta_{k1} \\ \alpha_{2k+1} = \sum_{n=(k+1)\vee 2}^{+\infty} i_1(n,k) + \left(\frac{3}{2}b_1 + \frac{5}{2}a_2\right)\delta_{k0} \end{cases}$$

$$\forall k \geqslant 0, \begin{cases} \beta_{2k} = \sum_{n=k\vee 2}^{+\infty} p_2(n,k) + \left(\frac{3}{2}b_1 - \frac{5}{6}a_2\right)\delta_{k0} + \frac{10}{3}a_2\delta_{k1} \\ \beta_{2k+1} = \sum_{n=(k+1)\vee 2}^{+\infty} i_2(n,k) + \left(\frac{3}{2}a_1 + \frac{5}{2}b_2\right)\delta_{k0} \end{cases}$$

with for $n \geqslant 2$:

$$\begin{cases} p_1(n,k) = -\frac{(4n+1)(4k+1)}{2n(2n+1)}b_{2n} + \frac{(4n-1)(4k+1)}{2n(2n-1)}a_{2n-1}, 0 \leqslant k \leqslant n-1 \\ p_1(n,n) = \frac{4n+1}{2n(2n+1)}(2n)^2 b_{2n} \end{cases}$$

$$\begin{cases} i_1(n,k) = -\frac{(4n+1)(4k+3)}{2n(2n+1)}a_{2n} - \frac{(4n-1)(4k+3)}{2n(2n-1)}b_{2n-1}, 0 \leqslant k \leqslant n-2 \\ i_1(n,n-1) = \frac{(4n+1)(4n-1)}{2n(2n+1)}a_{2n} + \frac{4n-1}{2n(2n-1)}(2n-1)^2 b_{2n-1} \end{cases}$$

$$\begin{cases} p_2(n,k) = -\frac{(4n+1)(4k+1)}{2n(2n+1)}a_{2n} + \frac{(4n-1)(4k+1)}{2n(2n-1)}b_{2n-1}, 0 \leqslant k \leqslant n-1 \\ p_2(n,n) = \frac{4n+1}{2n(2n+1)}(2n)^2 a_{2n} \end{cases}$$

$$\begin{cases} i_2(n,k) = -\frac{(4n+1)(4k+3)}{2n(2n+1)}b_{2n} - \frac{(4n-1)(4k+3)}{2n(2n-1)}a_{2n-1}, 0 \leqslant k \leqslant n-2 \\ i_2(n,n-1) = \frac{(4n+1)(4n-1)}{2n(2n+1)}b_{2n} + \frac{4n-1}{2n(2n-1)}(2n-1)^2 a_{2n-1}. \end{cases}$$

A.2 Decomposition of the phase function on Legendre basis

In this appendix, we present the decomposition of the phase function Φ_λ, defined in (4.25) in Chapter 4, on Legendre polynomials basis [198].

Lemma A.1. *The phase function Φ_λ defined in (4.25) can be decomposed as follows:* $\forall\,(\mu,\mu')\in[-1,1]^2$, $\forall\,N\in L^2(\mathbb{R}^+)$,

$$\Phi_\lambda(\mu,\mu',N)=\sum_{k=0}^{+\infty}A_{\lambda,k}(N)\,P_k(\mu)\,P_k(\mu'), \tag{A.5}$$

with

$$A_{\lambda,k}(N)=\frac{1}{\sigma^\lambda_{sca}(N)}\int_0^{+\infty}Q^\lambda_{sca}(r)\tilde{A}_{\lambda,k}(r)\,\pi\,r^2\,N(r)\,dr, \tag{A.6}$$

and

$$\forall\,r>0,\ \tilde{A}_{\lambda,k}(r)=\frac{\lambda^2(2k+1)}{4\,\pi^2\,r^2\,Q^\lambda_{sca}(r)}\sum_{i=0}^{+\infty}\sum_{j=0}^{+\infty}(\alpha_i\,\overline{\alpha}_j+\beta_i\,\overline{\beta}_j)\int_{-1}^{1}P_i(\mu)\,P_j(\mu)\,P_k(\mu)\,d\mu, \tag{A.7}$$

where $\alpha,\,\beta\in\mathbb{C}$ are determined in Appendix A.1. $\overline{\alpha},\overline{\beta}$ are the complex conjugates of $\alpha,\,\beta$ and we have [199]:

$$\int_{-1}^{1}P_i(\mu)\,P_j(\mu)P_k(\mu)d\mu=\begin{cases}0\ \textit{if } i+j<k\ \textit{ or } j+k<i\ \textit{ or } i+j+k\ \textit{ is odd}\\ 2\dfrac{(2s-2i)(2s-2k)(2s-2j)}{(2s-1)!}\left[\dfrac{s!}{(s-i)!(s-j)!(s-k)!}\right]\quad \textit{else,}\end{cases}$$

with $s=(i+j+k)/2$.

Proof. Let us assume that the functions S_1 and S_2 defined by

$$S_1(\mu)=\sum_{n=1}^{+\infty}\frac{2n+1}{n(n+1)}\left(a_n(r,\lambda)\pi_n(\mu)+b_n(r,\lambda)\tau_n(\mu)\right), \tag{A.8}$$

$$S_2(\mu)=\sum_{n=1}^{+\infty}\frac{2n+1}{n(n+1)}\left(b_n(r,\lambda)\pi_n(\mu)+a_n(r,\lambda)\tau_n(\mu)\right), \tag{A.9}$$

are decomposed on the Legendre basis $(P_k)_{k\geqslant0}$ as follows (see Appendix A.1):

$$\forall\,\mu\in[-1,1],\ S_1(\mu)=\sum_{i=0}^{+\infty}\alpha_i\,P_i(\mu)\quad;\quad S_2(\mu)=\sum_{i=0}^{+\infty}\beta_i\,P_i(\mu). \tag{A.10}$$

From (3.26) and by using equationA.10, we deduce that

$$\begin{aligned}\psi_\lambda(r,\mu)=&\frac{\lambda^2}{2\,\pi^2\,r^2\,Q^\lambda_{sca}(r)}\sum_{i=0}^{+\infty}\sum_{j=0}^{+\infty}(\alpha_i\,\overline{\alpha}_j+\beta_i\,\overline{\beta}_j)\,P_i(\mu)\,P_j(\mu)\\ =&\sum_{k=0}^{+\infty}\tilde{A}_{\lambda,k}(r)\,P_k(\mu).\end{aligned} \tag{A.11}$$

where $\tilde{A}$ defined in A.7.
Moreover,

$$\begin{aligned}\phi_\lambda(\mu, N) &= \frac{1}{\sigma^\lambda_{sca}(N)} \int_0^{+\infty} Q^\lambda_{sca}(r)\psi_\lambda(r,\mu)\,\pi\, r^2\, N(r)\, dr \\ &= \frac{1}{\sigma^\lambda_{sca}(N)} \int_0^{+\infty} Q^\lambda_{sca}(r) \left(\sum_{k=0}^{+\infty} \tilde{A}_{\lambda,k}(r)\, P_k(\mu)\right) \pi\, r^2\, N(r)\, dr \\ &= \sum_{k=0}^{+\infty} A_{\lambda,k}(N)\, P_k(\mu),\end{aligned} \tag{A.12}$$

where

$$A_{\lambda,k}(N) = \frac{1}{\sigma^\lambda_{sca}(N)} \int_0^{+\infty} Q^\lambda_{sca}(r)\tilde{A}_{\lambda,k}(r)\,\pi\, r^2\, N(r)\, dr. \tag{A.13}$$

Then,

$$\begin{aligned}\Phi_\lambda(\mu, \mu', N) &= \frac{1}{2\pi} \int_0^{2\pi} \phi_\lambda(\mu\mu' + \sqrt{1-\mu^2}\sqrt{1-\mu'^2}\cos(\omega), N)\, d\omega \\ &= \frac{1}{2\pi} \sum_{k=0}^{+\infty} A_{\lambda,k}(N) \int_0^{2\pi} P_k(\mu\mu' + \sqrt{1-\mu^2}\sqrt{1-\mu'^2}\cos(\omega)) d\omega,\end{aligned} \tag{A.14}$$

using Legendre's polynomial addition theorem [168]: for all $n \geqslant 1$,
$\forall\,(\mu,\mu') \in [-1,1]^2, \forall w \in [0,2\pi]$,

$$\begin{aligned}&P_n\left(\mu\mu' + \sqrt{1-\mu^2}\sqrt{1-\mu'^2}\cos w\right) \\ &\qquad = P_n(\mu)P_n\left(\mu'\right) + 2\sum_{m=1}^{n} \frac{(n-m)!}{(n+m)!} P_n^m(\mu)P_n^m\left(\mu'\right)\cos(mw).\end{aligned} \tag{A.15}$$

By integrating the equation (A.15) on [0,2π], we get:

$$\forall\,(\mu,\mu') \in [-1,1]^2, \frac{1}{2\,\pi}\int_0^{2\pi} P_n\left(\mu\mu' + \sqrt{1-\mu^2}\sqrt{1-\mu'^2}\cos w\right) dw = P_n(\mu)P_n\left(\mu'\right).$$

Then, from (A.14) and the addition theorem for Legendre functions, we obtain:

$$\Phi_\lambda(\mu, \mu', N) = \sum_{k=0}^{+\infty} A_{\lambda,k}(N)\, P_k(\mu)\, P_k(\mu').$$

□

A.3 Decomposition of the intensity on a double Legendre basis

To solve the stationary radiative transfer equation, we use Yvon's method [22] which is a decomposition method based on the double basis of Legendre polynomials. As

mentioned in equation (4.51) of Chapter 3, the intensity I_λ, for K Legendre polynomials, is decomposed as follows [22]:

$$I_\lambda(x,\mu) = \begin{cases} \sum_{j=0}^{K}(2j+1)\ell^-_{\lambda,j}(x,N)P_j(2\mu+1) & \text{if} \quad \mu<0, \\ \sum_{j=0}^{K}(2j+1)\ell^+_{\lambda,j}(x,N)P_j(2\mu-1) & \text{if} \quad \mu>0. \end{cases}$$

In this section, we search to compute the problems that verifies ℓ^-_λ and ℓ^+_λ. By injecting the decomposition presented in (4.53), (4.51), and (4.52) into (4.23), we obtain

$$\begin{aligned}
&\sum_{n=0}^{\infty}(2n+1)\left(\frac{d\ell^+_n}{dx}(x)\mu P^+_n(\mu)\right)+\sigma^\lambda_{ext}(N)\sum_{n=0}^{\infty}(2n+1)\ell^+_n(x)P^+_n(\mu)\\
&=\frac{\sigma^\lambda_{sca}(N)}{4\pi}\left(\int_{-1}^{0}\sum_{n=0}^{+\infty}(2n+1)\ell^-_n(x)P^-_n(\mu')\sum_{k=0}^{+\infty}A_k\int_0^{2\pi}P_k(\mu\mu'+\sqrt{1-\mu^2}\sqrt{1-\mu'^2}\cos w)dwd\mu'\right.\\
&\left.+\int_0^1\sum_{n=0}^{+\infty}(2n+1)\ell^+_n(x)P^+_n(\mu')\sum_{k=0}^{+\infty}A_k\int_0^{2\pi}P_k\left(\mu\mu'+\sqrt{1-\mu^2}\sqrt{1-\mu'^2}\cos w\right)dwd\mu'\right)\\
&+\sum_{n=0}^{+\infty}q_{\lambda,n}\,P_n(\mu).
\end{aligned}$$

Using Legendre's polynomial addition theorem (A.15), we have:

$$\begin{aligned}
&\sum_{n=0}^{\infty}(2n+1)\left(\frac{d\ell^+_n}{dx}(x)\mu P^+_n(\mu)\right)+\sigma^\lambda_{ext}(N)\sum_{n=0}^{\infty}(2n+1)\ell^+_n(x)P^+_n(\mu)\\
&\quad=\frac{1}{2}\sigma^\lambda_{sca}(N)\sum_{n=0}^{\infty}\sum_{k=0}^{\infty}(2n+1)A_kP_k(\mu)\left(\ell^-_n(x)+\ell^+_n(x)\right)\\
&\qquad\times\left(\int_{-1}^{0}P_k(\mu')\,P^-_n(\mu')\,d\mu'+\int_0^1P_k(\mu')\,P^+_n(\mu')\,d\mu'\right)+\sum_{n=0}^{+\infty}q_{\lambda,n}\,P_n(\mu).
\end{aligned}\tag{A.16}$$

Using recurrence (4.49) and orthogonality relations (4.50), we obtain:

$$\begin{aligned}
\mu P^+_n(\mu)&=\frac{1}{2}\left(\frac{n}{2n+1}P^+_{n-1}(\mu)+\frac{n+1}{2n+1}P^+_{n+1}(\mu)+P^+_n(\mu)\right),\ 0<\mu\leqslant 1,\\
\mu P^-_n(\mu)&=\frac{1}{2}\left(\frac{n}{2n+1}P^-_{n-1}(\mu)+\frac{n+1}{2n+1}P^-_{n+1}(\mu)-P^-_n(\mu)\right),\ -1\leqslant\mu<1,\\
\int_0^1\mu P^+_k(\mu)P^+_n(\mu)d\mu&=\frac{1}{2(2n+1)}\left(\frac{n}{2n-1}\delta_{k,n-1}+\frac{n+1}{2n+3}\delta_{k,n+1}+\delta_{k,n}\right),\\
\int_{-1}^0\mu P^-_k(\mu)P^-_n(\mu)d\mu&=\frac{1}{2(2n+1)}\left(\frac{n}{2n+1}\delta_{k,n-1}+\frac{n+1}{2n+3}\delta_{k,n+1}-\delta_{k,n}\right),\\
\int_0^1P^+_k(\mu)P^+_n(\mu)d\mu&=\frac{1}{2n+1}\delta_{k,n},\\
\int_{-1}^0P^-_k(\mu)P^-_n(\mu)d\mu&=\frac{1}{2n+1}\delta_{k,n}.
\end{aligned}\tag{A.17}$$

By multiplying equation (A.16) with $P_j^+(\mu)$ for all $j \geqslant 0$, integrating over $[0,1]$, and using formulas (A.17), we get:

$$\begin{aligned}&\frac{1}{2}\frac{j}{2j+1}\frac{d\ell_{j-1}^+}{dx}(x) + \frac{1}{2}\frac{j+1}{2j+1}\frac{d\ell_{j+1}^+}{dx}(x) + \frac{1}{2}\frac{d\ell_j^+}{dx}(x) + \sigma_{ext}^\lambda(N)\ell_j^+(x)\\ &= \frac{1}{2}\sigma_{sca}^\lambda(N)\sum_{n=0}^{\infty}(2n+1)\left(\ell_n^-(x)\sum_{k=0}^{\infty}A_k\alpha_{k,j}\beta_{k,n} + \ell_n^+(x)\sum_{k=0}^{\infty}A_k\alpha_{k,j}\alpha_{k,n}\right) + \sum_{n=0}^{+\infty}q_{\lambda,n}\alpha_{n,j}.\end{aligned}$$

This is equivalent to

$$\begin{aligned}&\frac{1}{2}\frac{j}{2j+1}\frac{d\ell_{j-1}^+}{dx}(x) + \frac{1}{2}\frac{j+1}{2j+1}\frac{d\ell_{j+1}^+}{dx}(x) + \frac{1}{2}\frac{d\ell_j^+}{dx}(x) + \sigma_{ext}^\lambda(N)\ell_j^+(x)\\ &= \frac{1}{2}\sigma_{sca}^\lambda(N)\sum_{n=0}^{\infty}(2n+1)\left(\Gamma_{j,n}^{\alpha,\beta}\ell_n^-(x) + \Gamma_{j,n}^{\alpha,\alpha}\ell_n^+(x)\right) + \sum_{n=0}^{+\infty}q_{\lambda,n}\alpha_{n,j},\end{aligned} \tag{A.18}$$

where

$$\forall j \geqslant 0, \forall n \geqslant 0, \Gamma_{\lambda,j,n}^{u,v} \equiv \Gamma_{\lambda,j,n}^{u,v}(N) = \sum_{k=0}^{K} A_{\lambda,k}(N)\, u_{k,j}\, v_{k,n}, \tag{A.19}$$

for any real families $(u_{p,q})_{p\geqslant 0,q\geqslant 0}$, $(v_{p,q})_{p\geqslant 0,q\geqslant 0}$ while $A_{\lambda,k}$ is defined in (A.6), and

$$\begin{aligned}\forall k \geqslant 0, \forall n \geqslant k, \alpha_{n,k} &= \int_0^1 P_n(\mu)P_k(2\mu-1)d\mu = \frac{1}{2}\int_{-1}^1 P_n\left(\frac{y+1}{2}\right)P_k(y)dy,\\ \forall k \geqslant 0, \forall n \geqslant k, \beta_{n,k} &= \int_{-1}^0 P_n(\mu)P_k(2\mu+1)d\mu = \frac{1}{2}\int_{-1}^1 P_n\left(\frac{y-1}{2}\right)P_k(y)dy.\end{aligned} \tag{A.20}$$

By using (A.17), we can show that for all $k \geqslant 0$ and $n \geqslant k$:

$$\alpha_{n+1,k} = \frac{1}{2}\frac{k+1}{2k+1}\frac{2n+1}{n+1}\alpha_{n,k+1} + \frac{1}{2}\frac{2n+1}{n+1}\alpha_{n,k} + \frac{1}{2}\frac{k}{2k+1}\frac{2n+1}{n+1}\alpha_{n,k-1} - \frac{n}{n+1}\alpha_{n-1,k},$$

which makes $\alpha_{n,k}$ computable through a recurrence on n, initialized with:

$$\begin{cases}\forall k \geqslant 0, \alpha_{0,k} = \delta_{0,k},\\ \forall k \geqslant 2, \alpha_{1,k} = 0, \alpha_{1,1} = \dfrac{1}{6}, \alpha_{1,0} = \dfrac{1}{2},\\ \alpha_{0,0} = 1, \alpha_{1,0} = \dfrac{1}{2}, \forall n \geqslant 2, \alpha_{n,0} = -\dfrac{n-2}{n+1}\alpha_{n-2,0}.\end{cases}$$

Similarly, we can show that for all $k \geqslant 0$ and $n \geqslant k$:

$$\beta_{n+1,k} = \frac{1}{2}\frac{k+1}{2k+1}\frac{2n+1}{n+1}\beta_{n,k+1} - \frac{1}{2}\frac{2n+1}{n+1}\beta_{n,k} + \frac{1}{2}\frac{k}{2k+1}\frac{2n+1}{n+1}\beta_{n,k-1} - \frac{n}{n+1}\alpha_{n-1,k},$$

which makes $\beta_{n,k}$ computable through a recurrence on n, initialized with:

$$\begin{cases}\forall k \geqslant 0, \beta_{0,k} = \delta_{0,k},\\ \forall k \geqslant 2, \beta_{1,k} = 0, \beta_{1,1} = \dfrac{1}{6}, \beta_{1,0} = \dfrac{1}{2},\\ \beta_{0,0} = 1, \beta_{1,0} = -\dfrac{1}{2}, \forall n \geqslant 2, \beta_{n,0} = -\dfrac{n-2}{n+1}\beta_{n-2,0}.\end{cases}$$

However, it is worth noting that it is enough to compute the $\alpha_{n,k}$ values and then use the following symmetry property of Legendre polynomials ($P_n(-\mu) = (-1)^n P_n(\mu)$ for $-1 \leqslant \mu \leqslant 1$):

$$\forall k \geqslant 0, \forall n \geqslant k, \beta_{n,k} = (-1)^{n+k}\alpha_{n,k}.$$

The same calculations can be carried out for $\mu < 0$, leading to a system analogous to (A.18) for ℓ^-. This gives to the following system to solve:

$$\begin{cases} \dfrac{1}{2}\dfrac{j}{2j+1}\dfrac{d\ell^+_{\lambda,j-1}}{dx}(x,N) + \dfrac{1}{2}\dfrac{j+1}{2j+1}\dfrac{d\ell^+_{\lambda,j+1}}{dx}(x,N) + \dfrac{1}{2}\dfrac{d\ell^+_j}{dx}(x,N) + \sigma^\lambda_{ext}(N)\ell^+_j(x,N) \\ = \dfrac{1}{2}\sigma^\lambda_{sca}(N)\displaystyle\sum_{n=0}^{K}(2n+1)\left(\Gamma^{\alpha,\beta}_{j,n}\ell^-_{\lambda,n}(x,N) + \Gamma^{\alpha,\alpha}_{j,n}\ell^+_n(x,N)\right) + \sum_{n=0}^{K} q_{\lambda,n}(x)\alpha_{n,j}, 0 \leqslant j \leqslant K, \\ \\ -\dfrac{1}{2}\dfrac{j}{2j+1}\dfrac{d\overline{\ell}^-_{\lambda,j-1}}{dx}(x,N) - \dfrac{1}{2}\dfrac{j+1}{2j+1}\dfrac{d\overline{\ell}^-_{\lambda,j+1}}{dx}(x,N) - \dfrac{1}{2}\dfrac{d\ell^-_j}{dx}(x,N) + \sigma^\lambda_{ext}(N)\overline{\ell}^-_{\lambda,j}(x) \\ = \dfrac{1}{2}\sigma^\lambda_{sca}(N)\displaystyle\sum_{n=0}^{K}(2n+1)\left(\Gamma^{\beta,\beta}_{j,n}\overline{\ell}^-_{\lambda,n}(x,N) + \Gamma^{\beta,\alpha}_{j,n}\overline{\ell}^+_{\lambda,n}(x,N)\right) + \sum_{n=0}^{K} q_{\lambda,n}(D-x)\beta_{n,j}, 0 \leqslant j \leqslant K, \\ \\ \forall x \in [0,D], \left(\ell^-_{\lambda,K+1}\right)'(x,N) = \left(\ell^+_{\lambda,K+1}\right)'(x,N) = 0, \\ \left(\ell^+_{\lambda,j}(0,N)\right)\right)_{0\leqslant j\leqslant K} \text{ and } \left(\ell^-_{\lambda,j}(D,N)\right)\Big)_{0\leqslant j\leqslant K} \text{ given,} \end{cases} \tag{A.21}$$

where we put $\overline{\ell}^\pm_{\lambda,k}(\cdot,N) = \ell^\pm_{\lambda,k}(D-\cdot,N)$.

Appendix B

Cost function properties

In this section, we examine the properties of the cost function J_ε, which is defined in equation (5.14) in Chapter 5 as:

$$J_\varepsilon(N) = J_1(N) + \frac{\varepsilon}{2} \|\sqrt{f}\, N\|^2_{\mathcal{H}(\mathbb{R}^+)},$$

where

$$J_1(N) = \frac{1}{2} \sum_{i=1}^{G} \sum_{l=1}^{L} \left(\frac{\int_a^b I_{\lambda_l}(x_i, \mu)\, d\mu - M_{\lambda_l}(x_i)}{M_{\lambda_l}(x_i)} \right)^2 .$$

Throughout this appendix, we denote by $I_{\lambda,1}$ and $I_{\lambda,2}$ two solutions of equation (5.12) corresponding to N_1 and N_2, respectively.

B.1 Strict convexity of the cost function

Let us show that J_ε (defined in (5.14)) is strictly convex, that is

$$\forall\, 0 < \beta < 1,\, \forall N_1, N_2 \in L^2(\mathbb{R}^+),\ \text{such that } N_1 \neq N_2,$$
$$J_\varepsilon(\beta\, N_1 + (1-\beta) N_2) < \beta\, J_\varepsilon(N_1) + (1-\beta) J_\varepsilon(N_2).$$

We have

$$\begin{aligned} & J_\varepsilon(\beta N_1 + (1-\beta) N_2) \\ & = \frac{1}{2} \sum_{i=1}^{G} \sum_{l=1}^{L} \frac{1}{M^2_{\lambda_l}(x_i)} \left(\int_a^b \beta\, I_{\lambda_l,1}(x_i, \mu) + (1-\beta)\, I_{\lambda_l,2}(x_i, \mu) d\mu - M_{\lambda_l}(x_i) \right)^2 \\ & \quad + \frac{\varepsilon}{2} \int_{\mathbb{R}^+} f(r)\, r^2\, (\beta N_1 + (1-\beta) N_2)^2 dr, \end{aligned} \tag{B.1}$$

where $I_{\lambda,1}$ and $I_{\lambda,2}$ verify (4.23) for N_1 and N_2 , respectively.
However,

$$M_{\lambda_l}(x_i) = \beta\, M_{\lambda_l}(x_i) + (1-\beta)\, M_{\lambda_l}(x_i).$$

By using the inequality $2cd \leqslant (c^2 + d^2)$, for $c = A$ and $d = B$ in the first term of the right hand side of equation (B.1) where

$$A = \left(\int_a^b I_{\lambda_l,1}(x_i, \mu) d\mu - M_{\lambda_l}(x_i) \right) \quad \text{and} \quad B = \left(\int_a^b I_{\lambda_l,2}(x_i, \mu) d\mu - M_{\lambda_l}(x_i) \right),$$

and for $c = N_1$ and $d = N_2$ where $c \neq d$ in the second term of the right hand side of equation (B.1), we can derive the following inequality:

$$
\begin{aligned}
&J_\varepsilon(\beta N_1 + (1-\beta)N_2) \\
&< \frac{1}{2}\sum_{i=1}^{G}\sum_{l=1}^{L}\frac{1}{M_{\lambda_l}^2(x_i)}\left(\beta^2 A^2 + (1-\beta)^2 B^2 + \beta(1-\beta)(A^2+B^2)\right) \\
&\quad + \beta^2\,\frac{\varepsilon}{2}\,\|\sqrt{f}\,N_1\|^2_{\mathcal{H}(\mathbb{R}^+)} + (1-\beta)^2\,\frac{\varepsilon}{2}\,\|\sqrt{f}\,N_2\|^2_{\mathcal{H}(\mathbb{R}^+)} \\
&\quad + \quad \frac{\varepsilon}{2}\,\beta\,(1-\beta)(\|\sqrt{f}\,N_1\|^2_{\mathcal{H}(\mathbb{R}^+)} + \|\sqrt{f}\,N_2\|^2_{\mathcal{H}(\mathbb{R}^+)}) \\
&= \beta\frac{1}{2}\sum_{i=1}^{G}\sum_{l=1}^{L}\frac{1}{M_{\lambda_l}^2(x_i)}\left(\int_a^b I_{\lambda_l,1}(x_i,\mu)d\mu - M_{\lambda_l}(x_i)\right)^2 + \beta\,\frac{\varepsilon}{2}\,\|\sqrt{f}\,N_1\|^2_{\mathcal{H}(\mathbb{R}^+)} \\
&\quad + (1-\beta)\frac{1}{2}\sum_{i=1}^{G}\sum_{l=1}^{L}\frac{1}{M_{\lambda_l}^2(x_i)}\left(\int_a^b I_{\lambda_l,2}(x_i,\mu)d\mu - M_{\lambda_l}(x_i)\right)^2 + (1-\beta)\frac{\varepsilon}{2}\|\sqrt{f}\,N_2\|^2_{\mathcal{H}(\mathbb{R}^+)} \\
&= \beta\,J_\varepsilon(N_1) + (1-\beta)J_\varepsilon(N_2).
\end{aligned}
$$

B.2 Continuity of the cost function

Let us show that:

$$J_\varepsilon(N_1) \longrightarrow J_\varepsilon(N_2) \;\text{ when }\; N_1 \longrightarrow N_2 \,\text{in}\, L^2(\mathbb{R}^+).$$

We have

$$
\begin{aligned}
&J_\varepsilon(N_1) - J_\varepsilon(N_2) \\
&= \frac{1}{2}\sum_{i=1}^{G}\sum_{l=1}^{L}\frac{1}{M_{\lambda_l}^2(x_i)}\left[\left(\int_a^b I_{\lambda_l,1}(x_i,\mu)\,d\mu\right)^2 - 2\,M_{\lambda_l}(x_i)\int_a^b I_{\lambda_l,1}(x_i,\mu)\,d\mu + M_{\lambda_l}(x_i)^2\right] \\
&\quad - \frac{1}{2}\sum_{i=1}^{G}\sum_{l=1}^{L}\frac{1}{M_{\lambda_l}^2(x_i)}\left[\left(\int_a^b I_{\lambda_l,2}(x_i,\mu)d\mu\right)^2 - 2M_{\lambda_l}(x_i)\int_a^b I_{\lambda_l,2}(x_i,\mu)d\mu + M_{\lambda_l}(x_i))^2\right] \\
&\quad + \frac{\varepsilon}{2}\left(\|\sqrt{f}\,N_1\|^2_{\mathcal{H}(\mathbb{R}^+)} - \|\sqrt{f}\,N_2\|^2_{\mathcal{H}(\mathbb{R}^+)}\right) \\
&= \frac{1}{2}\sum_{i=1}^{G}\sum_{l=1}^{L}\frac{1}{M_{\lambda_l}^2(x_i)}\left[\left(\int_a^b (I_{\lambda_l,1} - I_{\lambda_l,2})(x_i,\mu)\,d\mu\right)\left(\int_a^b (I_{\lambda_l,1} + I_{\lambda_l,2})(x_i,\mu)\,d\mu\right)\right] \\
&\quad + \sum_{i=1}^{G}\sum_{l=1}^{L}\left(\frac{1}{M_{\lambda_l}(x_i)}\int_a^b (I_{\lambda_l,2} - I_{\lambda_l,1})(x_i,\mu)d\mu\right) \\
&\quad + \frac{\varepsilon}{2}\left(\|\sqrt{f}\,N_1\|^2_{\mathcal{H}(\mathbb{R}^+)} - \|\sqrt{f}\,N_2\|^2_{\mathcal{H}(\mathbb{R}^+)}\right).
\end{aligned}
$$

Then,

$$
\begin{aligned}
&|J_\varepsilon(N_1) - J_\varepsilon(N_2)| \\
&\leqslant \frac{1}{2}\sum_{i=1}^{G}\sum_{l=1}^{L}\frac{1}{|M^2_{\lambda_l}(x_i)|}\left[\left(\int_a^b |(I_{\lambda_l,1} - I_{\lambda_l,2})(x_i,\mu)|d\mu\right)\left(\int_a^b |(I_{\lambda_l,1} + I_{\lambda_l,2})(x_i,\mu)|d\mu\right)\right] \\
&\quad + \sum_{i=1}^{G}\sum_{l=1}^{L}\left(\frac{1}{|M_{\lambda_l}(x_i)|}\int_a^b |(I_{\lambda_l,2} - I_{\lambda_l,1})(x_i,\mu)|d\mu\right) \\
&\quad + \frac{\varepsilon}{2}\left(\left|\|\sqrt{f}\,N_1\|^2_{\mathcal{H}(\mathbb{R}^+)} - \|\sqrt{f}\,N_2\|^2_{\mathcal{H}(\mathbb{R}^+)}\right|\right).
\end{aligned}
\tag{B.2}
$$

Let $I_{\lambda,1}$ and $I_{\lambda,2}$ be two solutions of (4.23) for N_1 and N_2 respectively. Then, $I_{\lambda,1} - I_{\lambda,2}$ is solution of the following system

$$
\begin{cases}
\mu\dfrac{\partial(I_{\lambda,1} - I_{\lambda,2})}{\partial x}(x,\mu) + \sigma^\lambda_{ext}(N_1)\,(I_{\lambda,1} - I_{\lambda,2})(x,\mu) \\
\qquad\qquad = \displaystyle\int_{-1}^{1} f_{\lambda,1}(\mu,\mu',N_1)\,(I_{\lambda,1} - I_{\lambda,2})(x,\mu')\,d\mu' + q(x,\mu), \\
(I_{\lambda,1} - I_{\lambda,2})(0,\mu) = 0 \qquad if \quad \mu \in (0,1], \\
(I_{\lambda,1} - I_{\lambda,2})(D,\mu) = 0 \qquad if \quad \mu \in [-1,0),
\end{cases}
\tag{B.3}
$$

where $q_\lambda(x,\mu) = q_{\lambda,1}(x,\mu) + q_{\lambda,2}(x,\mu)$, with

$$
q_{\lambda,1}(x,\mu) = (\sigma^\lambda_{ext}(N_2) - \sigma^\lambda_{ext}(N_1))\,I_{\lambda,2}(x,\mu),
$$

$$
q_{\lambda,2}(x,\mu) = \int_{-1}^{1}(f_{\lambda,1}(\mu,\mu',N_1) - f_{\lambda,2}(\mu,\mu',N_2))\;I_{\lambda,2}\,(x,\mu')\;d\mu'.
$$

According to Theorem 4.1, problem (B.3) admits a unique solution verifies the following estimation:

$$
\|I_{\lambda,1} - I_{\lambda,2}\|_{L^\infty(X)} \leqslant \frac{1}{\sigma^\lambda_{abs}(N_1)}\,\|q_\lambda\|_{L^\infty(X)}. \tag{B.4}
$$

Now we must determine the norm of $q_{\lambda,1}$ and $q_{\lambda,2}$.
For $q_{\lambda,1}$:

$$
\|q_{\lambda,1}\|_{L^\infty(X)} \leqslant \|\sigma^\lambda_{ext}(N_2) - \sigma^\lambda_{ext}(N_1)\|_{L^\infty(X)}\,\|I_{\lambda,2}\|_{L^\infty(X)},
$$

but $\sigma^\lambda_{ext}(N_2) - \sigma^\lambda_{ext}(N_1) = \pi\displaystyle\int_0^{+\infty} Q^\lambda_{ext}(r)\,r^2\,(N_1(r) - N_2(r))\,dr$. Then, using Holder's inequality and (4.24), we obtain

$$
\|q_{\lambda,1}\|_{L^\infty(X)} \leqslant C\,\|N_1 - N_2\|_{L^2(\mathbb{R}^+)}\,\max\left(\|I^-_\lambda\|_{L^\infty([-1,0))}, \|I^+_\lambda\|_{L^\infty((0,1])}\right), \tag{B.5}
$$

where $C = \left(\int_0^{+\infty} \pi^2 Q_{ext}^{\lambda}(r)^2\, r^4 dr\right)^{1/2}$.
For q_2:

$$\begin{aligned}|q_{\lambda,2}(x,\mu)| &\leqslant \int_{-1}^{1} |(f_{\lambda,1}(\mu,\mu',N_1) - f_{\lambda,2}(\mu,\mu',N_2))\; I_{\lambda,2}\,(x,\mu')|\; d\mu' \\ &\leqslant \left(\int_{-1}^{1} |(f_{\lambda,1}(\mu,\mu',N_1) - f_{\lambda,2}(\mu,\mu',N_2))|\; d\mu'\right)\; \tilde{I}_{\lambda,2}(x),\end{aligned}$$

with $\tilde{I}_{\lambda,2}(x) = \|I_{\lambda,2}(x,.)\|_{L^\infty([-1,1])}$.
But,

$$\begin{aligned}&f_{\lambda,1}(\mu,\mu',N_1) - f_{\lambda,2}(\mu,\mu',N_2) \\ &= \frac{1}{4}\int_0^{+\infty}\left(\int_0^{2\pi} r^2\, Q_{sca}^{\lambda}(r)\psi_\lambda(r,\mu\mu' + \sqrt{1-\mu^2}\sqrt{1-\mu'^2}\cos(w))dw\right)(N_1(r) - N_2(r))\, dr.\end{aligned}$$

Then, using the notation $\mu_0 = \mu\mu' + \sqrt{1-\mu^2}\sqrt{1-\mu'^2}\cos(w)$,

$$\begin{aligned}&\int_{-1}^{1} |f_{\lambda,1}(\mu,\mu',N_1) - f_{\lambda,2}(\mu,\mu',N_2)|\; d\mu' \\ &\quad= \frac{1}{4}\int_0^{+\infty}\left(\int_{-1}^{1}\int_0^{2\pi} r^2\, Q_{sca}^{\lambda}(r)\,\psi_\lambda(r,\mu_0)\, dw\, d\mu'\right)\,(N_1(r) - N_2(r))\, dr \\ &\quad\leqslant \frac{1}{4}\left(\int_0^{+\infty}\int_{-1}^{1}\int_0^{2\pi} |r^2\, Q_{sca}^{\lambda}(r)\,\psi_\lambda(r,\mu_0)\, dw\, d\mu'|^2\, dr\right)^{\frac{1}{2}} \|N_1 - N_2\|_{L^2(\mathbb{R}^+)}.\end{aligned}$$

Then, we obtain the following estimation for $q_{\lambda,2}$:

$$|q_{\lambda,2}(x,\mu)| \leqslant \frac{1}{4}\left(\int_0^{+\infty}\int_{-1}^{1}\int_0^{2\pi} |r^2 Q_{sca}^{\lambda}(r)\,\psi_\lambda(r,\mu_0)\, dw\, d\mu'|^2\, dr\right)^{\frac{1}{2}} \|N_1 - N_2\|_{L^2(\mathbb{R}^+)}.$$

Finally (B.4) becomes

$$\begin{aligned}&\|I_{\lambda,1} - I_{\lambda,2}\|_{L^\infty(X)} \\ &\leqslant \frac{1}{\sigma_{abs}^{\lambda}(N_1)}\left(C\,\max\left(\|I_\lambda^-\|_{L^\infty([-1,0))}, \|I_\lambda^+\|_{L^\infty((0,1])}\right) + \|g_\lambda\|_{L^\infty(X)}\right)\|N_1 - N_2\|_{L^2(\mathbb{R}^+)},\end{aligned}$$

where

$$g_\lambda(x,\mu) = \frac{1}{4}\tilde{L}_{\lambda,2}(x)\left(\int_0^{+\infty}\int_{-1}^{1}\int_0^{2\pi} |r^2 Q_{sca}^{\lambda}(r)\,\psi_\lambda(r,\mu_0)\, dw\, d\mu'|^2\, dr\right)^{\frac{1}{2}}.$$

Then $I_{\lambda,1} \longrightarrow I_{\lambda,2}$ in $L^\infty(\mathbb{R}^+)$ when $N_1 \longrightarrow N_2$ in $L^2(\mathbb{R}^+)$. By using equation (B.2), we obtain $J_\varepsilon(N_1) \longrightarrow J_\varepsilon(N_2)$.

B.3 Differentiability of the cost function

$\forall\, \eta > 0$, N and $\overline{N} \in L^2(\mathbb{R}^+)$ we compute, with $N_\eta = N + \eta\overline{N}$, the following function

$$J_\varepsilon(N_\eta) = J_\varepsilon(N) + \eta\, J_{\varepsilon,1}(N,\overline{N}) + \eta^2\, J_{\varepsilon,2}(N,\overline{N}),$$

where $J_{\varepsilon,1}$ and $J_{\varepsilon,2}$ are two functions defined as follows:

$$\begin{aligned} J_{\varepsilon,1}(N,\overline{N}) = &\sum_{i=1}^{G}\sum_{l=1}^{L}\frac{1}{M^2_{\lambda_l}(x_i)}\left(\int_a^b I_{\lambda_l}(x_i,\mu)d\mu - M_{\lambda_l}(x_i)\right)\left(\int_a^b \overline{I}_{\lambda_l}(x_i,\mu)d\mu\right) \\ &+\varepsilon\int_{\mathbb{R}^+} f(r)r^2 N\overline{N}dr, \end{aligned} \tag{B.6}$$

and

$$J_{\varepsilon,2}(N,\overline{N}) = \frac{1}{2}\sum_{i=1}^{G}\sum_{l=1}^{L}\frac{1}{M^2_{\lambda_l}(x_i)}\left(\int_a^b \overline{I}_{\lambda_l}(x_i,\mu)\,d\mu\right)^2 + \frac{\varepsilon}{2}\,\|\sqrt{f}\,\overline{N}\|^2_{\mathcal{H}(\mathbb{R}^+)}, \tag{B.7}$$

where I_λ satisfies problem (4.23) with $q_\lambda(x,\mu)=0$ and $\overline{I}_\lambda$ satisfies

$$\begin{cases} \mu\dfrac{\partial\overline{I}_\lambda}{\partial x}(x,\mu) + \sigma^\lambda_{ext}(N)\,\overline{I}_\lambda(x,\mu) = \displaystyle\int_{-1}^{1} f_\lambda(\mu,\mu',N)\,\overline{I}_\lambda(x,\mu')\,d\mu' \\ \qquad\qquad\qquad\qquad + \displaystyle\int_{-1}^{1} f_\lambda(\mu,\mu',\overline{N})\,I_\lambda(x,\mu')\,d\mu' - \sigma^\lambda_{ext}(\overline{N})\,I_\lambda(x,\mu), \\ \overline{I}_\lambda(0,\mu) = 0 \qquad if \quad \mu\in(0,1], \quad \overline{I}_\lambda(D,\mu) = 0 \qquad if \quad \mu\in[-1,0). \end{cases} \tag{B.8}$$

From the fact that I_λ satisfies (4.23) for N and N_η respectively, the system (B.8) can be derived by subtracting the two problems.
The function defined in (B.6) is linear w.r.t $\overline{N}$:

$$\begin{aligned} &J_{\varepsilon,1}(N,\overline{N}_1+\beta\overline{N}_2) \\ &= \sum_{i=1}^{G}\sum_{l=1}^{L}\frac{1}{M^2_{\lambda_l}(x_i)}\left(\int_a^b I_{\lambda_l}(x_i,\mu)d\mu - M_{\lambda_l}(x_i)\right)\left(\int_a^b (\overline{I}_{\lambda,1}+\beta\overline{I}_{\lambda,2})(x_i,\mu)d\mu\right) \\ &\quad +\varepsilon\int_{\mathbb{R}^+} f(r)\,r^2 N(\overline{N}_1+\beta\overline{N}_2)dr \\ &= \sum_{i=1}^{G}\sum_{l=1}^{L}\frac{1}{M^2_{\lambda_l}(x_i)}\left(\int_a^b I_{\lambda_l}(x_i,\mu)d\mu - M_{\lambda_l}(x_i)\right)\left(\int_a^b \overline{I}_{\lambda,1}(x_i,\mu)d\mu\right) \\ &\quad +\beta\sum_{i=1}^{I}\sum_{l=1}^{G}\frac{1}{M^2_{\lambda_l}(x_i)}\left(\int_a^b I_{\lambda_l}(x_i,\mu)d\mu - M_{\lambda_l}(x_i)\right)\left(\int_a^b \overline{I}_{\lambda,2}(x_i,\mu)d\mu\right) \\ &\quad +\varepsilon\int_{\mathbb{R}^+} f(r)\,r^2\,N\,\overline{N}_1\,dr + \beta\varepsilon\int_{\mathbb{R}^+} f(r)\,r^2\,N\,\overline{N}_2\,dr \\ &= J_{\varepsilon,1}(N,\overline{N}_1) + \beta\,J_{\varepsilon,1}(N,\overline{N}_2), \end{aligned}$$

where $\overline{I}_{\lambda,1}$, $\overline{I}_{\lambda,2}$ satisfy (B.8) for $\overline{N}_1$ and $\overline{N}_2$, respectively.
For the continuity, we have from (B.6)

$$\begin{aligned} |J_{\varepsilon,1}(N,\overline{N})| \leqslant &\left|\sum_{i=1}^{G}\sum_{l=1}^{L}\frac{1}{M^2_{\lambda_l}(x_i)}\left(\int_a^b I_{\lambda_l}(x_i,\mu)d\mu - M_{\lambda_l}(x_i)\right)\int_a^b \overline{I}_{\lambda_l}(x_i,\mu)d\mu\right| \\ &+\varepsilon\int_{\mathbb{R}^+}|r^2\,N\,\overline{N}|\,dr. \end{aligned}$$

By using Theorem 4.1, the following estimation for $\overline{I}_\lambda$ can be derived:

$$\|\overline{I}_\lambda\|_{L^\infty(X)} \leqslant \frac{1}{\sigma^\lambda_{abs}(N)} \|q_\lambda\|_{L^\infty(X)}, \tag{B.9}$$

with

$$q_\lambda(x,\mu) = \int_{-1}^{1} f_\lambda(\mu,\mu',\overline{N})\, I_\lambda(x,\mu')\, d\mu' - \sigma^\lambda_{ext}(\overline{N})\, I_{\lambda_l}(x,\mu),$$

$$f_\lambda(\mu,\mu',N) = \frac{1}{4}\int_0^{2\pi}\int_0^{+\infty} Q^\lambda_{sca}(r)\, \psi_\lambda(r, \mu\mu' + \sqrt{1-\mu^2}\sqrt{1-\mu'^2}\cos(w))\, r^2\, N(r)\, dr\, dw.$$

Then,

$$\begin{aligned} |q_\lambda(x,\mu)| &\leqslant \int_{-1}^{1} \left| f_\lambda(\mu,\mu',\overline{N})\, I_\lambda(x,\mu') \right| d\mu' - |\sigma^\lambda_{ext}(\overline{N})\, I_\lambda(x,\mu)| \\ &\leqslant \left(\int_{-1}^{1} \left| f_\lambda(\mu,\mu',\overline{N}) \right| d\mu' \right) \tilde{I}_\lambda(x) + \pi\, \|I_\lambda\|_{L^\infty(X)} \int_0^{+\infty} |Q^\lambda_{ext}(r)\, r^2\, N(r)|\, dr \\ &\leqslant \left(\int_{-1}^{1} \left| f_\lambda(\mu,\mu',\overline{N}) \right| d\mu' \right) \tilde{I}_\lambda(x) + C\, \|I_\lambda\|_{L^\infty(X)}\ \|N\|_{L^2(\mathbb{R}^+)}, \end{aligned} \tag{B.10}$$

where $C = \pi \left(\int_0^{+\infty} |r^2\, Q^\lambda_{ext}(r)|^2\, dr \right)^{\frac{1}{2}}$.

But

$$\begin{aligned} \int_{-1}^{1} |f_\lambda(\mu,\mu',\overline{N})| d\mu' &\leqslant \frac{1}{4}\int_0^{+\infty} \left(\int_{-1}^{1}\int_0^{2\pi} Q^\lambda_{sca}(r)\psi_\lambda(r,\mu_0) dw d\mu' \right) r^2 \overline{N}(r) dr \\ &\leqslant \frac{1}{4} \left(\int_0^{+\infty} \varphi_\lambda(r,\mu)^2\, dr \right)^{\frac{1}{2}} \|\overline{N}\|_{L^2(\mathbb{R}^+)}, \end{aligned}$$

where

$$\varphi_\lambda(r,\mu) = \int_{-1}^{1}\int_0^{2\pi} r^2\, Q^\lambda_{sca}(r)\, \psi_\lambda(r,\mu_0) dw\, d\mu' \ \text{ and } \ \mu_0 = \mu\mu' + \sqrt{1-\mu^2}\sqrt{1-\mu'^2}\cos(w).$$

Then, from (B.10), we get

$$\|q_\lambda\|_{L^\infty(X)} \leqslant \left(\|g_\lambda\|_{L^\infty(X)} + C\, \|I_\lambda\|_{L^\infty(X)} \right) \|\overline{N}\|_{L^2(\mathbb{R}^+)},$$

where

$$g_\lambda(x,\mu) = \left(\int_0^{+\infty} \varphi_\lambda(r,\mu)^2\, dr \right)^{\frac{1}{2}}\ \tilde{I}_\lambda(x).$$

Finally we obtain

$$\|\overline{I}_\lambda\|_{L^\infty(X)} \leqslant \frac{1}{\sigma^\lambda_{abs}(N)} \left(\|g_\lambda\|_{L^\infty(X)} + C\, \|I_\lambda\|_{L^\infty(X)} \right) \|\overline{N}\|_{L^2(\mathbb{R}^+)}. \tag{B.11}$$

By using equations (B.6)-(B.11), the continuity of $J_{\varepsilon,1}$ w.r.t $\overline{N}$ can be inferred. Additionally, by using equation (B.11), we can obtain that:

$$\lim_{\overline{N}\to 0} \frac{|J_{\varepsilon,2}(N,\overline{N})|}{\|\overline{N}\|_{L^2(\mathbb{R}^+)}} = 0. \tag{B.12}$$

where $J_{\varepsilon,2}$ is defined in (B.7).

Then, by the linearity and the continuity of $J_{\varepsilon,1}$, and by equation (B.12), we obtain the differentiability of the cost function.

Appendix C

Gradient of the cost function

The direction derivative of the cost function J_ε defined in (5.14) according to $\overline{N} \in L^2(\mathbb{R}^+)$ is given by

$$DJ_\varepsilon(N)\cdot\overline{N} = \sum_{i=1}^{G}\sum_{l=1}^{L} K(x_i,\lambda_l)\left(\int_a^b \overline{I}_{\lambda_l}(x_i,\mu,\overline{N})d\mu\right) + \varepsilon\int_{\mathbb{R}^+} r^2\, f(r)\, N(r)\,\overline{N}(r)\,dr, \tag{C.1}$$

where

$$K(x_i,\lambda_l) = \left(\frac{\displaystyle\int_a^b I_{\lambda_l}(x_i,\mu)\,d\mu - M_{\lambda_l}(x_i)}{M_{\lambda_l}(x_i)^2}\right),$$

and $\overline{I}_\lambda$ verifies the following problem

$$\begin{cases} \mu\dfrac{\partial\overline{I}_\lambda}{\partial x}(x,\mu) + \sigma^\lambda_{ext}(\overline{N})\, I_\lambda(x,\mu) + \sigma^\lambda_{ext}(N)\,\overline{I}_\lambda(x,\mu) = \displaystyle\int_{-1}^{1} I_\lambda(x,\mu')f_\lambda(\mu,\mu',\overline{N})d\mu' \\ \qquad\qquad\qquad\qquad\qquad\qquad + \displaystyle\int_{-1}^{1} \overline{I}_\lambda(x,\mu')f_\lambda(\mu,\mu',N)d\mu', \\ \overline{I}_\lambda(0,\mu) = 0 \qquad if \quad \mu\in(0,1], \qquad \text{and} \qquad \overline{I}_\lambda(D,\mu) = 0 \qquad if \quad \mu\in[-1,0). \end{cases} \tag{C.2}$$

where

$$f_\lambda(\mu,\mu',N) = \frac{1}{4}\int_0^{2\pi}\int_0^{+\infty} Q^\lambda_{sca}(r)\,\psi_\lambda(r,\mu\mu' + \sqrt{1-\mu^2}\sqrt{1-\mu'^2}\cos(w))\,r^2\,N(r)\,dr\,dw.$$

To obtain the gradient expression, we need to determine the first term of the right hand side in (C.1) in function of the direct problem I_λ and the adjoint problem p_λ. For that, we multiply (5.18) by $\overline{I}(x,\mu)$ and (C.2) by $p_\lambda(x,\mu)$ and by integrating on X, we obtain

$$\begin{aligned} -\int_{-1}^{1}\int_0^D \mu\,\frac{\partial p_\lambda}{\partial x}(x,\mu)\overline{I}_\lambda(x,\mu)\,dxd\mu + \int_{-1}^{1}\int_0^D \sigma^\lambda_{ext}(N)\,p_\lambda(x,\mu)\overline{L}(x,\mu)dxd\mu \\ = \int_{-1}^{1}\int_0^D \overline{I}_\lambda(x,\mu)\int_{-1}^{1} p(x,\mu')f_\lambda(\mu',\mu,N)d\mu'dxd\mu \\ + \int_{-1}^{1}\int_0^D \overline{I}_\lambda(x,\mu)\sum_{i=1}^{I} K(x_i,\lambda)\mathbb{1}_{(a,b)}(\mu)\,\delta_{x_i}(x)\,dx\,d\mu \end{aligned} \tag{C.3}$$

and

$$\begin{aligned}\int_{-1}^{1}\int_{0}^{D}\mu\, p_\lambda(x,\mu)\frac{\partial \overline{I}_\lambda}{\partial x}(x,\mu)\,dx\,d\mu + \int_{-1}^{1}\int_{0}^{D}\sigma_{ext}(\overline{N})\, p_\lambda(x,\mu)\, I_\lambda(x,\mu)\,dx\,d\mu \\ + \int_{-1}^{1}\int_{0}^{D}\sigma_{ext}^{\lambda}(N)\, p_\lambda(x,\mu)\,\overline{I}_\lambda(x,\mu)\,dx\,d\mu \\ = \int_{-1}^{1}\int_{0}^{D} p_\lambda(x,\mu)\int_{-1}^{1} I_\lambda(x,\mu')f_\lambda(\mu,\mu',\overline{N})d\mu'\,dx\,d\mu \\ + \int_{-1}^{1}\int_{0}^{D} p_\lambda(x,\mu)\int_{-1}^{1}\overline{I}_\lambda(x,\mu')f_\lambda(\mu,\mu',N)d\mu'\,dx\,d\mu\end{aligned} \tag{C.4}$$

by using the integration by part and that

$$\int_{-1}^{1}\int_{0}^{D} p_\lambda(x,\mu)\int_{-1}^{1} f_\lambda(\mu,\mu',N)\overline{I}_\lambda(x,\mu')d\mu' dx d\mu = \int_{-1}^{1}\int_{0}^{D}\overline{I}_\lambda(x,\mu)\int_{-1}^{1} p(x,\mu')f_\lambda(\mu',\mu,N)\,d\mu' dx d\mu$$

$$\int_{-1}^{1}\int_{0}^{D}\overline{I}_\lambda(x,\mu)\sum_{i=1}^{I} K(x_i,\lambda)\,\mathbb{1}_{(a,b)}(\mu)\,\delta_{x_i}(x)dx d\mu = \sum_{i=1}^{I} K(x_i,\lambda)\int_a^b \overline{I}_\lambda(x_i,\mu)d\mu$$

and by comparing (C.3) and (C.4), we obtain

$$\begin{aligned}\sum_{i=1}^{G}\sum_{l=1}^{L} K(x_i,\lambda_l)\int_a^b \overline{I}_{\lambda_l}(x_i,\mu)d\mu = \sum_{l=1}^{L}\left[-\int_{-1}^{1}\int_{0}^{D}\sigma_{ext}^{\lambda_l}(\overline{N})p_{\lambda_l}(x,\mu,)I_{\lambda_l}(x,\mu)dx d\mu\right] \\ + \sum_{l=1}^{L}\left[\int_{-1}^{1}\int_{0}^{D} p_{\lambda_l}(x,\mu)\int_{-1}^{1} I_{\lambda_l}(x,\mu')f_{\lambda_l}(\mu,\mu',\overline{N})d\mu' dx d\mu\right].\end{aligned} \tag{C.5}$$

Then, by (C.5) we obtain

$$\begin{aligned}DJ_\varepsilon(N)\cdot\overline{N} = \varepsilon\int_0^{+\infty} r^2\, f(r)N\,\overline{N}\,dr - \sum_{l=1}^{L}\left[\int_{-1}^{1}\int_{0}^{D} p_{\lambda_l}(x,\mu)\,\sigma_{ext}^{\lambda_l}(\overline{N})\, I_{\lambda_l}(x,\mu)\,dx\,d\mu\right] \\ + \sum_{l=1}^{L}\left[\int_{-1}^{1}\int_{0}^{D} p_{\lambda_l}(x,\mu)\int_{-1}^{1} I_{\lambda_l}(x,\mu')\, f_{\lambda_l}(\mu,\mu',\overline{N})\,d\mu'\,dx\,d\mu\right].\end{aligned} \tag{C.6}$$

List of Figures

List of Tables

Bibliography

[1] Cerema, "Adverse weather platform, available online: `https://www.cerema.fr/en/innovation-recherche/innovation/offres-technologie/simulation-platform-adverse-climate-conditions`."

[2] T. Bergot, M. Haeffelin, L. Musson-Genon, R. Tardiff, M. Colomb, C. Boitel, G. Bouhours, T. Bourriane, D. Carrer, J. Challet, P. Chazette, P. Drobinski, É. Dupont, J.-C. Dupont, T. Elias, C. Fesquet, O. Garrouste, L. Gomes, A. Guérin, F. Lapouge, Y. Lefranc, D. Legain, P. Morange, C. Pietras, A. Plana-Fattori, A. Protat, J. Rangognio, J.-C. Raut, S. Rémy, D. Richard, B. E. de. Romand, and X. Zhang, "Paris-fog : des chercheurs dans le brouillard," 2008.

[3] E. P. Shettle and R. W. Fenn, "Models for the aerosols of the lower atmosphere and the effects of humidity variations on their optical properties," 1979.

[4] "European ccam partnership, strategic research and innovation agenda 2021-2027, v1.4," 2022.

[5] P. Duthon, M. Colomb, and F. Bernardin, "Light Transmission in Fog: The Influence of Wavelength on the Extinction Coefficient," *Applied Sciences*, vol. 9, no. 14, p. 2843, 2019.

[6] D. Deirmendjian, *Electromagnetic Scattering on Spherical Polydispersions*. Santa Monica, CA: RAND Corporation, 1969.

[7] A. H. Hielscher and S. Bartel, "Use of penalty terms in gradient-based iterative reconstruction schemes for optical tomography.," *Journal of biomedical optics*, vol. 6 2, pp. 183–92, 2001.

[8] J. Tang, W. Han, and B. Han, "A theoretical study for rte-based parameter identification problems," *Inverse Problems*, vol. 29, p. 095002, aug 2013.

[9] S. R. Arridge, "Optical tomography in medical imaging," *Inverse Problems*, vol. 15, p. R41, apr 1999.

[10] C. Macdonald, S. Arridge, and S. Powell, "Efficient inversion strategies for estimating optical properties with monte carlo radiative transport models," *Journal of Biomedical Optics*, vol. 25, 08 2020.

[11] A. Klose, U. Netz, J. Beuthan, and A. Hielscher, "Optical tomography using the time-independent equation of radiative transfer-part 1: Forward model," *Journal of Quantitative Spectroscopy and Radiative Transfer*, vol. 72, pp. 691–713, 03 2002.

[12] S. R. Arridge and J. C. Schotland, "Optical tomography: forward and inverse problems," *Inverse Problems*, vol. 25, p. 123010, dec 2009.

[13] D. H. Chu M, "Image reconstruction in diffuse optical tomography based on simplified spherical harmonics approximation," *Opt Express*, dec 2009.

[14] K. Beier and H. Gemperlein, "Simulation of infrared detection range at fog conditions for enhanced vision systems in civil aviation," *Aerospace Science and Technology*, vol. 8, no. 1, pp. 63–71, 2004.

[15] M. Grabner and V. Kvicera, "The wavelength dependent model of extinction in fog and haze for free space optical communication," *Opt. Express*, vol. 19, pp. 3379–3386, Feb 2011.

[16] Z. He, H. Qi, Y. Yao, and L. Ruan, "Inverse estimation of the particle size distribution using the fruit fly optimization algorithm," *Applied Thermal Engineering*, vol. 88, pp. 306–314, 2015. Special Issue for International Heat Transfer Symposium 2014.

[17] X. Sun, H. Tang, and G. Yuan, "Anomalous diffraction approximation method for retrieval of spherical and spheroidal particle size distributions in total light scattering," *Journal of Quantitative Spectroscopy and Radiative Transfer*, vol. 109, no. 1, pp. 89–106, 2008.

[18] Y. Yuan, H.-L. Yi, Y. Shuai, F.-Q. Wang, and H.-P. Tan, "Inverse problem for particle size distributions of atmospheric aerosols using stochastic particle swarm optimization," *Journal of Quantitative Spectroscopy and Radiative Transfer*, vol. 111, no. 14, pp. 2106–2114, 2010.

[19] J. Vargas-Ubera, J. F. Aguilar, and D. M. Gale, "Reconstruction of particle-size distributions from light-scattering patterns using three inversion methods," *Appl. Opt.*, vol. 46, pp. 124–132, Jan 2007.

[20] P. Enerena, Y. T. Aksoya, Y. Zhub, E. Koosb, and M. R. Vetranoa, "Determination of particle size distribution in nanofluids using light extinction spectroscopy," 2020.

[21] A. Krayem, F. Bernardin, and A. Münch, "Identification of fog particle size distribution by a radiative transfer equation inversion," *Journal of Quantitative Spectroscopy and Radiative Transfer*, vol. 317, p. 108923, 2024.

[22] J. Yvon, "La diffusion macroscopique des neutrons une methode d'approximation," *Journal of Nuclear Energy (1954)*, 1957.

[23] M. Haeffelin, T. Bergot, T. Elias, R. Tardif, D. Carrer, P. Chazette, M. Colomb, P. Drobinski, E. Dupont, J.-C. Dupont, L. Gomes, L. Musson-Genon, C. Pietras, A. Plana-Fattori, A. Protat, J. Rangognio, J.-C. Raut, S. Rémy, D. Richard, J. Sciare, and X. Zhang, "PARISFOG: Shedding New Light on Fog Physical Processes," *Bulletin of the American Meteorological Society*, vol. 91, pp. 767–783, 2010.

[24] P. Duthon, M. Colomb, and F. Bernardin, "Fog classification by their droplet size distributions: Application to the characterization of cerema's platform," *Atmosphere*, vol. 11, no. 6, 2020.

[25] ITS-Cerema, "Systèmes de transports intelligents, pour l'infrastructure de demain, une assistance à la mobilité et au développement des véhicules autonomes, available online: `https://www.cerema.fr/fr/innovation-recherche/recherche/equipes/sti-systemes-transports-intelligents-infrastructure-demain`."

[26] SCOOP, "Scoop project, available online: `https://www.scoop.developpement-durable.gouv.fr/`."

[27] C-ROADS, "C-roads project, available online: `https://www.c-roads.eu/platform.html`."

[28] InDiD-Project, "Infrastructure digitale de demain, available online: `https://www.c-roads.eu/pilots/core-members/france/Partner/project/show/indid.html`."

[29] SAM-Project, "Security and acceptability for automated driving, available online: `https://www.vedecom.fr/sam-project-security-acceptability-for-automated-driving/?lang=en`."

[30] PRISSMA-Project, "Plateforme de recherche et d'investissement pour la sûreté et la sécurité de la mobilité autonome, available online: `https://prissma.univ-gustave-eiffel.fr/`."

[31] M. Kutila, P. Pyykönen, W. Ritter, O. Sawade, and B. Schäufele, "Automotive lidar sensor development scenarios for harsh weather conditions," in *2016 IEEE 19th International Conference on Intelligent Transportation Systems (ITSC)*, pp. 265–270, 2016.

[32] J. Wojtanowski, M. Zygmunt, M. Kaszczuk, Z. Mierczyk, and M. Muzal, "Comparison of 905 nm and 1550 nm semiconductor laser rangefinders' performance

deterioration due to adverse environmental conditions," *Opto-Electronics Review*, vol. 22, 06 2014.

[33] Y. Zhou, L. Liu, H. Zhao, M. López-Benítez, L. Yu, and Y. Yue, "Towards deep radar perception for autonomous driving: Datasets, methods, and challenges," *Sensors*, vol. 22, no. 11, 2022.

[34] M. Kutila, P. Pyykönen, W. Ritter, O. Sawade, and B. Schäufele, "Pedestrian detection and tracking using in-vehicle lidar for automotive application," in *IEEE Intelligent Vehicles Symposium (IV), BadenBaden. Initial system specification. RobustSENSE deliverable 2.1.*, pp. 734–739, 2011.

[35] N. A. M. Mai, P. Duthon, L. Khoudour, A. Crouzil, and S. A. Velastin, "3d object detection with sls-fusion network in foggy weather conditions," *Sensors*, vol. 21, no. 20, 2021.

[36] M. Bijelic, T. Gruber, F. Mannan, F. Kraus, W. Ritter, K. Dietmayer, and F. Heide, "Seeing through fog without seeing fog: Deep multimodal sensor fusion in unseen adverse weather," 2020.

[37] W. M. O. (WMO), *Guide to Instruments and Methods of Observation*.

[38] A. Ben-Daoued, P. Duthon, and F. Bernardin, "Sweet: A realistic multiwavelength 3d simulator for automotive perceptive sensors in foggy conditions," *Journal of Imaging*, vol. 9, no. 2, 2023.

[39] I. Gultepe, R. Tardif, S. C. Michaelides, J. Cermak, A. Bott, J. Bendix, M. D. Müller, M. Pagowski, B. Hansen, G. Ellrod, W. Jacobs, G. Toth, and S. G. Cober, "Fog research: A review of past achievements and future perspectives," *Pure and Applied Geophysics*, 2007.

[40] I. Gultepe, J. A. Milbrandt, and B. Zhou, *Marine Fog: A Review on Microphysics and Visibility Prediction*, pp. 345–394. Cham: Springer International Publishing, 2017.

[41] J. D. Price, S. Lane, I. A. Boutle, D. K. E. Smith, T. Bergot, C. Lac, L. Duconge, J. McGregor, A. Kerr-Munslow, M. Pickering, and R. Clark, "Lanfex: A field and modeling study to improve our understanding and forecasting of radiation fog," *Bulletin of the American Meteorological Society*, vol. 99, no. 10, pp. 2061 – 2077, 2018.

[42] J. Vargas, S. Alsweiss, O. Toker, R. Razdan, and J. Santos, "An overview of autonomous vehicles sensors and their vulnerability to weather conditions," *Sensors*, vol. 21, no. 16, 2021.

[43] R.-C. Miclea, V.-I. Ungureanu, F.-D. Sandru, and I. Silea, "Visibility enhancement and fog detection: Solutions presented in recent scientific papers with potential for application to mobile systems," *Sensors*, vol. 21, no. 10, 2021.

[44] F. Rosique, P. J. Navarro, C. Fernández, and A. Padilla, "A systematic review of perception system and simulators for autonomous vehicles research," *Sensors*, vol. 19, no. 3, 2019.

[45] J. Fayyad, M. A. Jaradat, D. Gruyer, and H. Najjaran, "Deep learning sensor fusion for autonomous vehicle perception and localization: A review," *Sensors*, vol. 20, no. 15, 2020.

[46] C. L. Walker, B. Boyce, C. P. Albrecht, and A. Siems-Anderson, "Will weather dampen self-driving vehicles?," *Bulletin of the American Meteorological Society*, vol. 101, no. 11, pp. E1914 – E1923, 2020.

[47] A. S. Mohammed, A. Amamou, F. K. Ayevide, S. Kelouwani, K. Agbossou, and N. Zioui, "The perception system of intelligent ground vehicles in all weather conditions: A systematic literature review," *Sensors*, vol. 20, no. 22, 2020.

[48] S. Hasirlioglu and A. Riener, "A model-based approach to simulate rain effects on automotive surround sensor data," *2018 21st International Conference on Intelligent Transportation Systems (ITSC)*, pp. 2609–2615, 2018.

[49] M. Jokela, M. Kutila, and P. Pyykönen, "Testing and validation of automotive point-cloud sensors in adverse weather conditions," *Applied Sciences*, vol. 9, no. 11, 2019.

[50] A. Carballo, J. Lambert, A. M. Cano, D. R. Wong, P. Narksri, Y. Kitsukawa, E. Takeuchi, S. Kato, and K. Takeda, "Libre: The multiple 3d lidar dataset," *2020 IEEE Intelligent Vehicles Symposium (IV)*, pp. 1094–1101, 2020.

[51] S. Zang, M. Ding, D. Smith, P. Tyler, T. Rakotoarivelo, and M. A. Kaafar, "The impact of adverse weather conditions on autonomous vehicles: How rain, snow, fog, and hail affect the performance of a self-driving car," *IEEE Vehicular Technology Magazine*, vol. 14, no. 2, pp. 103–111, 2019.

[52] Y. Kim, S. Kim, J. W. Choi, and D. Kum, "Craft: Camera-radar 3d object detection with spatio-contextual fusion transformer," 2022.

[53] A. Singh, "Vision-radar fusion for robotics bev detections: A survey," 02 2023.

[54] "United nations, economic and social council, economic commission for europe, new assessment/test method for automated driving (natm)," 2021.

[55] ANSYS, "Ansys avxcelerate sensors datasheet, 2022. available online: https://www.ansys.com/content/dam/resource-center/datasheet/ansys-avxcelerate-sensors-datasheet.pdf."

[56] . Electro-Optics Sensor Simulation, OKTAL, "Available online: https://www.oktal-se.fr/how-to-buy/packaged-solution/."

[57] W. Jakob, S. Speierer, N. Roussel, M. Nimier-David, D. Vicini, T. Zeltner, B. Nicolet, M. Crespo, V. Leroy, and Z. Zhang, "Mitsuba 3 renderer," 2022. https://mitsuba-renderer.org.

[58] "Avsimulation, 2022. available online: https://www.avsimulation.com/."

[59] A. Dosovitskiy, G. Ros, F. Codevilla, A. Lopez, and V. Koltun, "CARLA: An open urban driving simulator," in *Proceedings of the 1st Annual Conference on Robot Learning*, pp. 1–16, 2017.

[60] K. Dahmane, P. Duthon, F. Bernardin, M. Colomb, F. Chausse, and C. Blanc, "Weathereye-proposal of an algorithm able to classify weather conditions from traffic camera images," *Atmosphere*, vol. 12, no. 6, 2021.

[61] D. A. Stewart and O. M. Essenwanger, "A survey of fog and related optical propagation characteristics," 1982.

[62] M. Colomb, K. Hirech, P. André, J. Boreux, P. Lacôte, and J. Dufour, "An innovative artificial fog production device improved in the European project "FOG"," *Atmospheric Research*, vol. 87, pp. 242–251, mar 2008.

[63] J. Allen Zak, "Drop Size Distributions and Related Properties of Fog for Five," Tech. Rep. April 1994, NASA, 1994.

[64] F. García-García, U. Virafuentes, and G. Montero-Martínez, "Fine-scale measurements of fog-droplet concentrations: A preliminary assessment," *Atmospheric Research*, vol. 64, no. 1-4, pp. 179–189, 2002.

[65] B. A. Kunkel, "Microphysical Properties of Fog at Otis AFB," tech. rep., Air Force Geophysics Laboratory, Air Force Systems Command, United States Air Force, 1982.

[66] B. Thies, S. Egli, and J. Bendix, "The influence of drop size distributions on the relationship between liquid water content and radar reflectivity in radiation fogs," *Atmosphere*, vol. 8, no. 8, 2017.

[67] M. Colomb, F. Bernardin, and P. Morange, "Paramétrisation de la visibilité et modelisation de la distribution granulométrique à partir de données microphysiques," in *Séminaire AMA 2008 Météo France*, pp. 1–10, 2008.

[68] B. A. Kunkel, "Parameterization of droplet terminal velocity and extinction coefficient in fog models," *Journal of Climate and applied meteorology*, vol. 23, no. 1, pp. 34–41, 1984.

[69] T. Elias, J. C. Dupont, E. Hammer, C. R. Hoyle, M. Haeffelin, F. Burnet, and D. Jolivet, "Enhanced extinction of visible radiation due to hydrated aerosols in mist and fog," *Atmospheric Chemistry and Physics*, vol. 15, no. 12, pp. 6605–6623, 2015.

[70] J. A. Garland, "Some fog droplet size distributions obtained by an impaction method," *Quarterly Journal of the Royal Meteorological Society*, vol. 97, no. 414, pp. 483–494, 1971.

[71] M. Kumai, "Arctic Fog Droplet Size Distribution and Its Effect on Light Attenuation," *Journal of the Atmospheric Sciences*, vol. 30, no. 4, pp. 635–643, 1973.

[72] B. A. Kunkel, "Fog Drop-Size Distributions Measured with a Laser Hologram Camera," *Journal of Applied Meteorology*, vol. 10, no. 3, pp. 482–486, 1971.

[73] S. Fuzzi, M. Gazzi, C. Pesci, and V. Vicentini, "A linear impactor for fog droplet sampling," *Atmospheric Environment (1967)*, vol. 14, no. 7, pp. 797–801, 1980.

[74] J. Goodman, "The Microstructure of California Coastal Fog and Stratus," *Journal of Applied Meteorology*, vol. 16, no. 10, pp. 1056–1067, 1977.

[75] B. A. Kunkel, "Comparison of Fog Drop Size Spectra Measured by Light Scattering and Impaction Techniques," tech. rep., Air Force Geophysics Laboratory, Air Force Systems Command, United States Air Force, 1981.

[76] M. B. Meyer, J. E. Jiusto, and G. G. Lala, "Measurements of visual range and radiation- fog (haze) microphysics.," *Journal of the Atmospheric Sciences*, vol. 37, no. 3, pp. 622–629, 1980.

[77] Q. Liu, B. Wu, Z. Wang, and T. Hao, "Fog droplet size distribution and the interaction between fog droplets and fine particles during dense fog in tianjin, china," *Atmosphere*, vol. 11, no. 3, 2020.

[78] J. Li, C. Zhu, H. Chen, D. Zhao, L. Xue, X. Wang, H. Li, P. Liu, J. Liu, C. Zhang, Y. Mu, W. Zhang, L. Zhang, H. Herrmann, K. Li, M. Liu, and J. Chen, "The

evolution of cloud and aerosol microphysics at the summit of mt. tai, china," *Atmospheric Chemistry and Physics*, vol. 20, no. 22, pp. 13735–13751, 2020.

[79] R. G. Pinnick, D. L. Hoihjelle, G. Fernandez, E. B. Stenmark, J. D. Lindberg, G. B. Hoidale, and S. G. Jennings, "Vertical Structure in Atmospheric Fog and Haze and Its Effects on Visible and Infrared Extinction," *Journal of the Atmospheric Sciences*, vol. 35, no. 10, pp. 2020–2032, 1978.

[80] H. E. Gerber, "Microstructure of a radiation fog.," *Journal of the Atmospheric Sciences*, vol. 38, no. 2, pp. 454–458, 1981.

[81] J. He, X. Ren, H. Wang, Z. Shi, F. Zhang, L. Hu, Q. Zeng, and X. Jin, "Analysis of the microphysical structure and evolution characteristics of a typical sea fog weather event in the eastern sea of china," *Remote Sensing*, vol. 14, no. 21, 2022.

[82] M. Mazoyer, F. Burnet, and C. Denjean, "Experimental study on the evolution of droplet size distribution during the fog life cycle," *Atmospheric Chemistry and Physics*, vol. 22, no. 17, pp. 11305–11321, 2022.

[83] F. S. Boudala, D. Wu, G. A. Isaac, and I. Gultepe, "Seasonal and microphysical characteristics of fog at a northern airport in alberta, canada," *Remote Sensing*, vol. 14, no. 19, 2022.

[84] J. Price, "Radiation Fog. Part I: Observations of Stability and Drop Size Distributions," *Boundary-Layer Meteorology*, vol. 139, pp. 167–191, May 2011.

[85] D. Deirmendjian, "Electromagnetic Scattering on Spherical Polydispersions," 1969.

[86] E. P. Shettle and R. W. Fenn, "Models for the aerosols of the lower atmosphere and the effects of humidity variations on their optical properties," *Environmental Research Paperr*, vol. 676, no. 6, p. 89, 1979.

[87] J. V. Mallow, "Empirical fog droplet size distribution functions with finite limits," *Journal of the atmospheric sciences*, vol. 32, no. 2 (February, 1975), pp. 440–443, 1975.

[88] F. Tampieri and C. Tomasi, "Size distribution models of fog and cloud droplets in terms of the modified gamma function," *Tellus*, vol. 28, no. 4, pp. 333–347, 1976.

[89] F. Bernardin, M. Colomb, F. Egal, P. Morange, and J. Boreux, "Droplet distribution models for visibility calculation," in *5th International Conference on Fog, Fog Collection and Dew*, no. July, (Münster), pp. 2–5, 2010.

[90] S. Liandrat, P. Duthon, F. Bernardin, A. Ben Daoued, and J.-L. Bicard, "A review of Cerema PAVIN fog & rain platform: from past and back to the future," in *ITS World Congress*, (Los Angeles, United States), Sept. 2022.

[91] P. Duthon, F. Bernardin, F. Chausse, and M. Colomb, "Methodology used to evaluate computer vision algorithms in adverse weather conditions.," in *Proceedings of 6th Transport Research Arena*, (Warsaw, Poland), 2016.

[92] V. Cavallo, M. Colomb, and J. Doré, "Distance Perception of Vehicle Rear Lights in Fog," *Human Factors*, vol. 43, no. 3, pp. 442–451, 2001.

[93] B. Quétard, J.-C. Quinton, M. Colomb, G. Pezzulo, L. Barca, M. Izaute, O. K. Appadoo, and M. Mermillod, "Combined effects of expectations and visual uncertainty upon detection and identification of a target in the fog," *Cognitive processing*, vol. 16, no. 1, pp. 343–348, 2015.

[94] F. Bernardin, R. Bremond, V. Ledoux, M. Pinto, S. Lemonnier, V. Cavallo, and M. Colomb, "Measuring the effect of the rainfall on the windshield in terms of visual performance," *Accident Analysis and Prevention*, vol. 63, pp. 83–88, 2014.

[95] M. Marchetti, V. Boucher, J. Dumoulin, and M. Colomb, "Retrieving visibility distance in fog combining infrared thermography, Principal Components Analysis and Partial Least-Square regression," *Infrared Physics and Technology*, vol. 71, pp. 289–297, 2015.

[96] N. Pinchon, O. Cassignol, A. Nicolas, P. Leduc, J. P. Tarel, R. Bremond, G. Julien, N. Pinchon, O. Cassignol, A. Nicolas, F. Bernardin, N. Pinchon, O. Cassignol, A. Nicolas, F. Bernardin, P. Leduc, and J.-p. Tarel, "All-weather vision for automotive safety : which spectral band ?," in *SIA Vision 2016 - International Conference Night Drive Tests and Exhibition*, 2016.

[97] M. Kutila, P. Pyykönen, H. Holzhuter, M. Colomb, and P. Duthon, "Automotive lidar performance verification in fog and rain," *2018 21st International Conference on Intelligent Transportation Systems (ITSC)*, 2018.

[98] Y. Li, P. Duthon, M. Colomb, and J. Ibanez-Guzman, "What happens for a tof lidar in fog?," *IEEE Transactions on Intelligent Transportation Systems*, 2021.

[99] K. Dahmane, P. Duthon, F. Bernardin, M. Colomb, N. Essoukri Ben Amara, and F. Chausse, "The Cerema pedestrian database : A specific database in adverse weather conditions to evaluate computer vision pedestrian detectors," in *7th Conference on Sciences of Electronics, Technologies of Information and Telecommunications (SETIT)*, pp. 480–485, 2016.

[100] M. Bijelic, F. Mannan, T. Gruber, W. Ritter, K. Dietmayer, and F. Heide, "Seeing Through Fog Without Seeing Fog: Deep Sensor Fusion in the Absence of Labeled Training Data," *CoRR*, vol. abs/1902.0, 2019.

[101] DENSE, "Dverse weather environmental sensing system, available online: `https://www.dense247.eu/`."

[102] C. Busch and E. Debes, "Wavelet transform for analyzing fog visibility," *IEEE Intell. Syst.*, vol. 13, pp. 66–71, 1998.

[103] Z.-z. Chen, J. Li, and Q.-m. Chen, "Real-time video detection of road visibility conditions," vol. 5, pp. 472–476, 01 2009.

[104] N. Hautière, R. Labayrade, and D. Aubert, "Estimation of the visibility distance by stereovision: A generic approach.," *IEICE Transactions*, vol. 89-D, pp. 2084–2091, 01 2006.

[105] *Météorologie routière - Recueil des données météorologiques et routières - Terminologie. AFNOR (Paris La Défense). NF P 99-320, avril 1998.*

[106] M. Colomb, "Les salles de brouillard artificiel," 11 2002.

[107] e. I. O. K. L. P. VOLNISTOVA, A. S. DROFA, "Experimental study of object visibility in fog," *Izvestiya, Atmospheric and Oceanic Physics*, vol. 26(7), no. 524–529, 1990.

[108] R. E. Turner and P. Lambeck, "Natural and artificial illumination in optically thick atmospheres," 1975.

[109] A. Kokhanovsky, *Optics of Light Scattering Media: Problems and Solutions*. CSCW: Computer Supported Cooperative Work, Springer, 2001.

[110] L. Palacios-Peña, R. Baró, A. Baklanov, A. Balzarini, D. Brunner, R. Forkel, M. Hirtl, L. Honzak, J. M. Lopez-Romero, J. Camaño, G. Pirovano, R. García, W. Schröder, J. Werhahn, R. Wolke, R. Žabkar, and P. Jimenez-Guerrero, "An assessment of aerosol optical properties from remote sensing observations and regional chemistry-climate coupled models over europe," *Atmospheric Chemistry and Physics Discussions*, pp. 1–37, 09 2017.

[111] Y. Zhao, J. Ding, Y. Han, T. Lu, Y. Zhang, and H. Luo, "Aerosol physical–optical properties under different stages of continuous wet weather over the guangdong–hong kong–macao greater bay area, china," *Remote Sensing*, vol. 15, no. 5, 2023.

[112] R. Claes, J. Kluska, H. V. Winckel, and M. Min, "Neural network based image reconstruction with astrophysical priors," in *Optical and Infrared Interferometry and Imaging VII* (P. G. Tuthill, A. Mérand, and S. Sallum, eds.), vol. 11446, p. 114461U, International Society for Optics and Photonics, SPIE, 2020.

[113] N. J. McCormick, "Methods for solving inverse problems for radiation transport—an update," *Transport Theory and Statistical Physics*, 1986.

[114] N. J. McCormick, "Inverse radiative transfer problems: A review," *Nuclear Science and Engineering*, 1992.

[115] K. Case and P. Zweifel, *Linear Transport Theory.* (Addison-Wesley, Reading, Massachusetts, 1967).

[116] S. Chandrasekhar, *Radiative Transfer.* Dover, New York, 1960.

[117] F. Paletou, "Une introduction au transfert de rayonnement astrophysique." Apr. 2020.

[118] A. Addoum, O. Farges, and F. Asllanaj, "Optical properties reconstruction using the adjoint method based on the radiative transfer equation," *Journal of Quantitative Spectroscopy and Radiative Transfer*, vol. 204, 2018.

[119] J. Guan, S. Fang, and C. Guo, "Optical tomography reconstruction algorithm based on the radiative transfer equation considering refractive index: Part 2. inverse model," *Computerized Medical Imaging and Graphics*, 2013.

[120] Y. Qiao, H. Qi, Q. Chen, L. Ruan, and H. Tan, "An efficient and robust reconstruction method for optical tomography with the time-domain radiative transfer equation," *Optics and Lasers in Engineering*, 2016.

[121] M. Choulli and P. Stefanov, "Reconstruction of the coefficients of the stationary transport equation from boundary measurements," *Inverse Problems*, vol. 12, pp. L19–L23, oct 1996.

[122] G. Bal and A. Jollivet, "Stability estimates in stationary inverse transport," *Inverse Problems and Imaging*, vol. 2, no. 4, pp. 427–454, 2008.

[123] A. Klose, U. Netz, J. Beuthan, and A. Hielscher, "Optical tomography using the time-independent equation of radiative transfer-part 1: Forward model," *Journal of Quantitative Spectroscopy and Radiative Transfer*, vol. 72, pp. 691–713, 03 2002.

[124] A. D. Klose and A. H. Hielscher, "Optical tomography using the time-independent equation of radiative transfer—part 2: inverse model," *Journal of Quantitative Spectroscopy and Radiative Transfer*, 2002.

[125] H. Egger and M. Schlottbom, "Numerical methods for parameter identification in stationary radiative transfer jo - computational optimization and applications," *Journal of Mathematical Physics*, 2015.

[126] F. Lenzen and O. Scherzer, "Tikhonov type regularization methods: History and recent progress," *Proceeding Eccomas*, vol. 2004, 01 2004.

[127] B. Bo, H. B. H. Weimin, T. Jinping, and L. Li, "Image reconstruction for diffuse optical tomography based on radiative transfer equation," *Computational and Mathematical Methods in Medicine*, 2015.

[128] T. Feng, P. Edström, and M. Gulliksson, "Levenberg–marquardt methods for parameter estimation problems in the radiative transfer equation," *Inverse Problems*, mar 2007.

[129] K. Levenberg, "A method for the solution of certain non – linear problems in least squares," *Quarterly of Applied Mathematics*, vol. 2, pp. 164–168, 1944.

[130] Z. He, H. Qi, Z. Lew, L. Ruan, H. Tan, and K. Luo, "Application of the lsqr algorithm in non-parametric estimation of aerosol size distribution," *Optics Communications*, 2016.

[131] X. Sun, H. Tang, and G. Yuan, "Anomalous diffraction approximation method for retrieval of spherical and spheroidal particle size distributions in total light scattering," *Journal of Quantitative Spectroscopy and Radiative Transfer*, 2008.

[132] X. Sun, H. Tang, and J. Dai, "Inversion of particle size distribution from spectral extinction data using the modified beta function," *Powder Technology*, vol. 190, no. 3, 2009.

[133] J. Klett, "Lidar inversion with variable backscatter/extinction ratios," *Applied optics*, vol. 24, pp. 1638–43, 07 1985.

[134] F. FG., "Analysis of atmospheric lidar observations: some comments," *Appl Opt.*, vol. 24, 1984.

[135] A. Ansmann, U. Wandinger, M. Riebesell, C. Weitkamp, and W. Michaelis, "Independent measurement of extinction and backscatter profiles in cirrus clouds by using a combined raman elastic-backscatter lidar," *Appl. Opt.*, vol. 31, pp. 7113–7131, Nov 1992.

[136] I. Mattis, A. Ansmann, D. Müller, U. Wandinger, and D. Althausen, "Dual-wavelength raman lidar observations of the extinction-to-backscatter ratio of saharan dust," vol. 29, p. 1306, may 2002.

[137] B. Kaul, *Laser Sensing the Aerosol Pollution in the Atmosphere.* Thesis, Ph.D. Thesis, Institute of Atmospheric Optics, Tomsk State University, Tomsk, Russia, 1976. (In Russian), Dec. 1976.

[138] J. Hitschfeld, W.; Bordan, "Errors inherent in the radar measurement of rainfall at attenuating wavelengths," *J. Appl. Meteorol.*, vol. 11, no. 58–67, 1954.

[139] H. Mueller and H. Quenzel, "Information content of multispectral lidar measurements with respect to the aerosol size distribution," vol. 24, pp. 648–654, Mar. 1985.

[140] A. Comerón, C. Muñoz-Porcar, F. Rocadenbosch, A. Rodríguez-Gómez, and M. Sicard, "Current research in lidar technology used for the remote sensing of atmospheric aerosols," *Sensors*, vol. 17, no. 6, 2017.

[141] P. Lafrique, *Lidar multispectral pour la caractérisation des aérosols.* Theses, Institut Supérieur de l'Aéronautique et de l'Espace (ISAE), Dec. 2015.

[142] C. Böckmann, J. Biele, and R. Neuber, "Analysis of multi-wavelength lidar data by inversion with mollifier method," *Pure Applied Optics*, vol. 7, pp. 827–836, July 1998.

[143] I. Veselovskii, A. Kolgotin, V. Griaznov, D. Müller, U. Wandinger, and D. N. Whiteman, "Inversion with regularization for the retrieval of tropospheric aerosol parameters from multiwavelength lidar sounding," *Appl. Opt.*, vol. 41, pp. 3685–3699, Jun 2002.

[144] C. Böckmann, "Hybrid regularization method for the ill-posed inversion of multiwavelength lidar data in the retrieval of aerosol size distributions," *Appl. Opt.*, vol. 40, pp. 1329–1342, Mar 2001.

[145] A. K. Roy and S. K. Sharma, "A simple analysis of the extinction spectrum of a size distribution of mie particles," *Journal of Optics A: Pure and Applied Optics*, vol. 7, no. 11, p. 675, 2005.

[146] Z. He, H. Qi, Y. Yao, and L. Ruan, "An effective inversion algorithm for retrieving bimodal aerosol particle size distribution from spectral extinction data," *Journal of Quantitative Spectroscopy and Radiative Transfer*, vol. 149, pp. 117–127, 2014.

[147] Z. He, H. Qi, Q. Chen, and L. Ruan, "Retrieval of aerosol size distribution using improved quantum-behaved particle swarm optimization on spectral extinction measurements," *Particuology*, vol. 28, pp. 6–14, 2016.

[148] J. Vargas-Ubera, J. F. Aguilar, and D. M. Gale, "Reconstruction of particle-size distributions from light-scattering patterns using three inversion methods," *Appl. Opt.*, vol. 46, pp. 124–132, Jan 2007.

[149] X. Sun, H. Tang, and G. Yuan, "Determination of the particle size range in the visible spectrum from spectral extinction measurements," *Measurement Science and Technology*, vol. 18, p. 3572, oct 2007.

[150] Z. He, H. Qi, Y. Yao, and L. Ruan, "Inverse estimation of the particle size distribution using the fruit fly optimization algorithm," *Applied Thermal Engineering*, vol. 88, pp. 306–314, 2015. Special Issue for International Heat Transfer Symposium 2014.

[151] H. Qi, L. Ruan, M. Shi, W. An, and H. Tan, "Application of multi-phase particle swarm optimization technique to inverse radiation problem," *Journal of Quantitative Spectroscopy and Radiative Transfer*, vol. 109, no. 3, pp. 476–493, 2008.

[152] W. W. Hager and H. Zhang, "A survey of nonlinear conjugate gradient methods," 2005.

[153] C. Lawson and R. Hanson, *Solving Least Squares Problems*. Classics in Applied Mathematics, Society for Industrial and Applied Mathematics, 1995.

[154] S. B. Srinivasamurthy, "Methods of solving ill-posed problems," 2012.

[155] Y. Liu, W. P. Arnott, and J. Hallett, "Particle size distribution retrieval from multispectral optical depth: Influences of particle nonsphericity and refractive index," *Journal of Geophysical Research*, vol. 104, pp. 31753–31762, 1999.

[156] J. Mao, Y. Ren, J. Li, Q. Wang, and Y. Zhang, "Observation and inversion of aerosol particle size distribution over yinchuan area," *Atmosphere*, vol. 12, no. 8, 2021.

[157] E. D. Hirleman, "Optimal Scaling of the Inverse Fraunhofer Diffraction Particle Sizing Problem: The linear system produced by quadrature," *Presented at the International Symposium on Optical Particle Sizing: Theory and Practice*, 1987.

[158] G. Świrniak and J. Mroczka, "Forward and inverse analysis for particle size distribution measurements of disperse samples: A review," *Measurement*, vol. 187, p. 110256, 2022.

[159] E. Kazamarande and P. Comon, "Stabilité numérique de l'algorithme de Levinson," *M2AN - Modélisation mathématique et analyse numérique*, vol. 29, no. 2, pp. 123–170, 1995.

[160] Y. Wang, S. Fan, and X. Feng, "Retrieval of the aerosol particle size distribution function by incorporating a priori information," *Journal of Aerosol Science*, vol. 38, no. 8, pp. 885–901, 2007.

[161] A. Peraiah, "An introduction to radiative transfer: Methods and applications in astrophysics," *An Introduction to Radiative Transfer: Methods and Applications in Astrophysics, by Annamaneni Peraiah. Cambridge University Press, 2001, 492 pp.*, 11 2001.

[162] G. Thomas and K. Stamnes, *Radiative Transfer in the Atmosphere and Ocean*. 08 1999.

[163] L. C. Henyey and J. L. Greenstein, "Diffuse radiation in the galaxy," *The Astrophysical Journal*, vol. 93, pp. 70–83, 1940.

[164] G. Mie, *Beiträge Zur Optik Trüber Medien, Speziell Kolloidaler Metallösungen.* Annalen der Physik, 1908.

[165] L. Lorenz, *Lysbevaegelsen i og uden for en af plane Lysbølger belyst kugle*. 8Det-Kongelige Danske Videnskabernes Selskabs skrifter: Naturvidenskabelig og Mathematisk Afdeling, Luno, 1890.

[166] L. Lorenz, *Lysbevægelsen i og uden for en af plane Lysbølger belyst Kugle*. Kongelige Danske Videnskabernes Selskabs Skrifter: Naturvidenskabelig og Mathematisk Afdeling, 1890.

[167] D. J. Segelstein, *The Complex Refractive Index of Water*. Theses, M.S. Thesis, University of Missouri–Kansas City, 1981.

[168] R. Lagrange, *Polynômes et fonctions de Legendre*. Mémorial des sciences mathématiques, Gauthier-Villars, 1939.

[169] H. Van de Hulst, *Light Scattering by Small Particles*. John Wiley and Sons, New York; Chapman and Hall, London., 1957.

[170] J. V. Dave, "Scattering of electromagnetic radiation by a large, absorbing sphere," *IBM Journal of Research and Development*, vol. 13, no. 3, pp. 302–313, 1969.

[171] V. Khare, *Short-Wavelength Scattering of Electromagnetic Waves by a Homogeneous Dielectric Sphere*. Thesis, Ph.D. Thesis, U. Rochester, N.Y., (available from University Microfilms, Ann Arbor, Mich.), 1976.

[172] W. J. Wiscombe, *Improved mie scattering algorithms.* Appl. Opt., 19, 1980.

[173] J.-L. L. Robert Dautray, *Mathematical Analysis and Numerical Methods for Science and Technology: Volume 6 Evolution Problems II.* Berlin, Heidelberg: Springer Berlin Heidelberg, 2000.

[174] G. Bal, "Couplage d'equations et homogeneisation en transport neutronique," 1997.

[175] E.Bonneaux, "Résolution de problèmes de transport par fermeture non linéaire des Équa- tions de moments. application à la neutronique," 1997.

[176] G. Allaire and B. F.Golse, X.Blanc, *Transport et diffusion.* CMAP, Ecole Polytechnique, 2019.

[177] W. R. M. James J. Duderstadt, "Transport theory," 1979.

[178] G. I. Bell and S. Glasstone, "Nuclear reactor theory," *Nature*, 1970.

[179] V. Agoshkov and V. I. Agoškov, *Boundary value problems for transport equations.* Springer Science & Business Media, 1998.

[180] P. Laven, ""the optics of a water drop, mie scattering and the debye series": `http://www.philiplaven.com/mieplot.htm`."

[181] D. Griffiths and D. Higham, *Numerical Methods for Ordinary Differential Equations: Initial Value Problems.* 01 2010.

[182] G. Sewell and H. Gould, "The numerical solution of ordinary and partial differential equations," *Computers in Physics*, 1988.

[183] J. Mroczka, "Method of moments in light scattering data inversion in the particle size distribution function," *Optics Communications*, vol. 99, no. 3, pp. 147–151, 1993.

[184] J. M. Varah, "On the numerical solution of ill-conditioned linear systems with applications to ill-posed problems," *SIAM Journal on Numerical Analysis*, vol. 10, no. 2, pp. 257–267, 1973.

[185] C. Shaw, "Improvement of the resolution of an instrument by numerical solution of an integral equation," *Journal of Mathematical Analysis and Applications*, vol. 37, no. 1, pp. 83–112, 1972.

[186] P. C. Hansen, *Rank-deficient and discrete ill-posed problems: numerical aspects of linear inversion.* SIAM, 1998.

[187] P. C. Hansen, "The truncatedSVD as a method for regularization," *BIT Numerical Mathematics*, vol. 27, pp. 505–514, 11 1987.

[188] P. Xu, "Truncated SVD methods for discrete linear ill-posed problems," *Geophysical Journal International*, vol. 135, pp. 505–514, 11 1998.

[189] P. C. Hansen, "Numerical tools for analysis and solution of fredholm integral equations of the first kind," *Inverse Problems*, vol. 8, p. 849, dec 1992.

[190] J. Barzilai and J. M. Borwein, "Two-point step size gradient methods," *Ima Journal of Numerical Analysis*, vol. 8, pp. 141–148, 1988.

[191] E. Polak and G. Ribiere, "Note sur la convergence de méthodes de directions conjuguées," *Revue française d'informatique et de recherche opérationnelle. Série rouge*, vol. 3, no. R1, pp. 35–43, 1969.

[192] J. W. Daniel, "The conjugate gradient method for linear and nonlinear operator equations," *SIAM Journal on Numerical Analysis*, vol. 4, no. 1, pp. 10–26, 1967.

[193] H. Di, Z. Wang, and D. Hua, "Precise size distribution measurement of aerosol particles and fog droplets in the open atmosphere," *Opt. Express*, vol. 27, pp. A890–A908, Jun 2019.

[194] B. Lapeyre, É. Pardoux, R. Sentis, A. W. Craig, and F. Craig, "Introduction to monte-carlo methods for transport and diffusion equations," 2003.

[195] A. Industrie, "Cité de la photonique, available online: `http://www.ardop.com`."

[196] M. Ballesta-Garcia, S. Peña-Gutiérrez, P. García-Gómez, and S. Royo, "Experimental characterization of polarized light backscattering in fog environments," *Sensors*, vol. 23, no. 21, 2023.

[197] S. Peña-Gutiérrez, M. Ballesta-Garcia, P. García-Gómez, and S. Royo, "Quantitative demonstration of the superiority of circularly polarized light in fog environments," *Optics Letters*, vol. 47, 11 2021.

[198] B. W. Fowler, "Expansion of mie-theory phase functions in series of legendre polynomials," *J. Opt. Soc. Am.*, vol. 73, pp. 19–22, Jan 1983.

[199] J.-C. Adams, *On the expression of the product of any two Legendre's coefficients by means of a series of Legendre's coefficients.* Proc. R. Soc. Lond G. Tschirhart, Caract´eristiques physiques g´en´erales des brouillards, Monographies de la, 1878.